The Stability and Manufacturability of Emerging Thin Film Photovoltaic Technologies

Christopher David Bracher

Department of Physics and Astronomy

Faculty of Science

The University of Sheffield

Thesis submitted for the degree of Doctor of Philosophy

September 2016

Acknowledgements

I would like to take this opportunity to thank the people who have made getting to this point possible. First and foremost, I would like to thank my supervisor David Lidzey for giving me this opportunity, and the support and guidance you have provided over the past 4 years.

The members of the EPMM group and Ossila Ltd past and present also deserve thanks, both for academic reasons and the friendships over the years. In particular, I would like to thank Charlotte Nicolaou, Darren Watters, Jon Griffin, Max Reinhardt, Nick Scarratt, and Theo Grant; you've been great friends over the years and this Ph.D. would not have been as fun without you. Additionally, special thanks to Andrew Pearson for the training and assistance you provided me with during the first half of my Ph.D, and for being an all-around great guy.

I thank my family for the love and support you always give me. Without your support and encouragement I would never have made it this far. Thanks to my brother for all the weekends playing video games together, an excellent escape from work.

I would also like to thank my friends from undergraduate: Alice, Bob, Clifton, Emily, Emma, Liv, Luca, Medders, Moo, Nathan, Oli, and Rachel. Your continuing friendship is the best thing that I got out of university, and all the impromptu trips and holidays over the years since then have probably helped keep me sane. I'm sure we will continue to find ways to meet up, and I look forward to the next time I see you all.

Finally, I would like to thank Emperor Shen Nung for discovering tea in 2737 BCE, a drink without which none of this would have been possible.

Abstract

In order for a photovoltaic device to be commercially viable it must have a production cost and operational stability commensurate with its final application. Both of these properties are influenced by many factors, including the production of the active materials and the deposition techniques used to fabricate it. In this thesis, the stability and manufacturability of two emerging photovoltaic materials are examined: organic semiconducting polymers and organic-inorganic perovskites.

Organic semiconducting polymers are commonly synthesised through reactions utilising metal catalysts, which can remain with the polymer after synthesis, necessitating the investigation of their influence on photovoltaic devices. This work shows that the presence of the residual catalyst palladium in PCDTBT organic photovoltaic (OPV) devices caused significant reductions in power conversion efficiency and an additional increase in efficiency loss during the first 60 hours of operation. It is also shown, however, that only minor losses occurred in PFD2TBT-8 OPV devices at high Pd concentrations, highlighting the need to examine individual material systems.

Despite being a very new technology, perovskite solar cells (PSCs) have already achieved comparable performance to silicon solar cells, making it important to investigate the stability of such devices. The operational stability of PSCs in the inverted architecture was characterised, showing lifetimes of <300 hours. Using spectroscopic and device characterisation techniques, the major loss mechanisms were revealed to be reactions with water and oxygen, resulting the in the decomposition of the perovskite. It is also examined how the addition of hydroiodic acid to the perovskite precursor solution affects the performance and stability of spin and spray coated PSCs. Finally, the effects of deposition temperature and additional annealing on the operational stability of PSCs was investigated.

Publications

1. C. Bracher, H. Yi, N. W. Scarratt, R. Masters, A. J. Pearson, C. Rodenburg, A. Iraqi, D. G. Lidzey, The effect of residual palladium catalyst on the performance and stability of PCDTBT:$PC_{70}BM$ organic solar cells, Organic Electronics 27 (2015), 266-273.

2. D. K. Mohamad, J. Griffin, C. Bracher, A. T. Barrows, D. G. Lidzey, Spray-cast multilayer organometal perovskite solar cells fabricated in air, Advanced Energy Materials (2016), 1600994.

3. C. Bracher, B. Freestone, D. K. Mohamad, D. G. Lidzey, The operational stability of inverted architecture $CH_3NH_3PbI_{3-x}Cl_x$ perovskite solar cells, Journal of Materials Chemistry C, submitted.

Conference Presentations

UK Semiconductors (UKSC), Sheffield, UK, July 2013.
Poster presentation.

Hybrid-Organic Photovoltaics (HOPV), Lausanne, Switzerland, May 2014.
Poster presentation.

UK Semiconductors (UKSC), Sheffield, UK, July 2014.
Oral presentation.

European Optical Society Annual Meeting (EOSAM), Berlin, Germany, September 2014.
Oral presentation.

UK Semiconductors (UKSC), Sheffield, UK, July 2016.
Poster presentation.

Contents

Chapter 1

Introduction

Global electricity generation has grown from 21,600 TWh (~78 PJ) in 2012 to 23,300 TWh (~84 PJ) in 2013, an increase of 7.8%, and is predicted to grow by a further 57% by 2040 to 36,500 TWh (~131 PJ) [1,2]. In order to meet this predicted growth, new power plants will need to be constructed. Currently, the primary source of electricity is from burning fossil fuels (i.e. coal, oil, and natural gas), providing 64.7% of global generation, with coal being the single largest source of electricity at 41.3% of global generation [2]. Recently, however, fossil fuels have been becoming less desirable for two main reasons. Firstly, the finite nature of the resource means that they cannot be used indefinitely, and alternate forms of generation will be needed when the fuel runs out. Secondly, and arguably more pressingly, the negative environmental side effects of burning fossil fuels, releasing greenhouse gases (such as carbon dioxide and nitrous oxide) that lead to anthropogenic climate change and air pollution [3]. Nuclear power, accounting for 10.6% of global electricity generation in 2013, has also become less desirable to the general public due to increased fear about the safety of nuclear power plants since the Fukushima Daiichi disaster in 2011 [4]. This makes renewable energy sources, including solar, wind, geothermal, biomass, and hydroelectric, accounting for 22% of global generation in 2013 (74% of which was from hydroelectric), the most desirable for future electricity generation.

Of the various sources of renewable electricity, solar has arguably the largest potential for future energy generation as the total annual solar energy incident on the landmasses of the Earth is estimated to be 1,575 – 49,837 EJ, more than enough

to satisfy global energy needs [5]. Solar power generation exists in two forms, solar thermal and solar photovoltaic (PV). Solar thermal uses the energy of solar radiation to heat a fluid which can be used as direct heating, or to drive a turbine to generate electricity. Solar PV converts solar radiation directly into electricity through the use of semiconducting materials. Both of these technologies allow for the generation of electricity on a local basis. This can be important in areas without the grid infrastructure required for large scale generation, and can be integrated with pre-existing buildings through rooftop installation.

Whilst it may sound like a simple matter of just rolling out solar generation across the world, there are issues preventing the mass deployment of solar power. Firstly, solar power is a variable source of electricity, with generation affected by the weather, time of day, and seasonal variations in sunlight. Therefore, energy storage or alternate forms of generation are needed to provide electricity at times when sunlight is limited or not available. Secondly, whilst the price of commercial silicon solar PV panels, the most common form of solar panel, has been decreasing rapidly due to increased production quantities, the price of produced energy is still high relative to generation from fossil fuels [5]. For example, the US Energy Information Administration estimates the cost of solar PV to be 12.5 cents/kWh, and the cost of conventional coal to be 9.5 cents/kWh [6]. There are several ways in which costs can be further reduced, including using materials that can be processed more cheaply or improved conversion efficiency. However, pushes to higher performance can lead to the use of more expensive materials, such as gallium arsenide, which have achieved efficiencies of 28.8%, close to the Shockley–Queisser limit, or increased complexity, as seen in solar cells with multiple absorber layers [7,8]. Cadmium telluride solar cells have managed to achieve comparable performance to silicon, with lower processing costs [9]. Tellurium is, however, a relatively rare element, leading to uncertainty about the future of this technology [10].

All of the materials discussed above are inorganic semiconductors, the oldest and most studied class of PV materials. In the past few decades, an alternative class of material has seen increasing interest, the organic semiconductor. These are small organic molecules or organic polymers (i.e. containing carbon) that have several

advantages over traditional inorganic semiconductors. Firstly, the deposition of organic materials can be performed from solutions, allowing the use of a variety of printing and coating techniques that are already established in industry, such as inkjet printing, slot die coating, and spray coating [11]. The processing of organic materials is also performed at low temperatures, and can be done in ambient air, reducing the energy cost and enabling a greater range of substrates to be able to be used, such as glass and flexible plastics [12]. The optical and electronic properties of organic semiconductors can be easily tuned by changing the structure of the materials [13]. Such factors should reduce the energy payback time of organic solar cells, and allow for the production of very cheap, light-weight, and flexible solar cells that can be fabricated via rapid roll-to-roll processes [14–16].

Despite these advantages, there are still issues with the lifetime and scalability of organic solar cells. Whilst the peak power conversion efficiencies (PCE) for single junction (one absorbing layer) solar cells is currently at 12.2% using the polymer PBDB-T, (high enough to be considered for commercialisation) this has only been demonstrated on a laboratory scale with device areas of 13 mm^2 [17,18]. Higher efficiencies have been announced by Heliatek, achieving 13.2% in multi-junction (multiple absorbing layers) organic solar cells [19]. Much larger devices are required if organic solar cells are to be deployed, however, most efforts to increase their size have resulted in decreases in efficiency due to the magnification of detrimental effects, such as pinholes and parasitic resistances, as active areas increase [14,20]. The lifetimes of organic solar cells have also not been widely investigated, however, lifetimes of 7 – 11 years in laboratory scale PCDTBT based devices [21,22], and over 10,000 hours in P3HT based modules have been observed [23]. These are promising results for the future of organic solar cells, but further study is required to make them commercially viable, particularly for higher efficiency devices.

Another class of material for solar PV has emerged over the past decade, the perovskite, and has caused much excitement in solar cell research communities. Perovskites are materials with a particular crystal structure that can exhibit semiconducting properties. The common perovskites used in PV are hybrid materials, containing both organic and inorganic components, and seem to

combine the advantages of both types of semiconductor. As with organic semiconductors, perovskites can be processed at low temperatures, from solution, in ambient conditions, enabling the use of a wide variety of substrates and printing and coating techniques. Perovskite solar cell performance is, however, more comparable to inorganic solar cells due to the excellent optical and electronic properties they exhibit, such as ambipolar charge transport and long charge carrier lifetimes [24], with peak device efficiencies currently reaching 22.1% [25].

Despite these impressive properties perovskite solar cells are not yet ready for commercialisation. One major issue is that the most common perovskite materials that are being studied contain lead, a fact that potentially prevents deployment due to health and safety regulation [24,26]. Alternatives, such as tin, are being investigated, however solar cells fabricated using such materials currently exhibit much lower performance (<7% efficiency) than the lead based counterparts [27–29]. The scalability of perovskite solar cells also presents some issues. As with organic solar cells, most devices fabricated in laboratories have small active areas (<1cm^2), and attempts to increase this generally result in performance losses. Potentially the most important issue, however, is the stability of perovskite materials. Most studies of perovskites have shown them to be inherently unstable, decaying in a matter of hours [30].

In Table 1.1 the peak PCE and lifetimes of the current market leaders of inorganic solar cells alongside those for organic and perovskite solar cells. The performance of organic (12.2%) and perovskite (22.1%) solar cells are reaching the performances of amorphous silicon (13.6%) and cadmium telluride solar (22.1%) cells respectively. However, in both cases the lifetime of devices is severely reduced in comparison to the inorganic devices, with organic devices lasting only 1 year as a module (11 years have been achieved for much smaller devices), and perovskite devices lasting less than a year.

Solar Cell	Peak PCE (%)	Peak Lifetime	Processing Technique
Amorphous Silicon	13.6	20 years [31]	Chemical vapour deposition
Crystalline Silicon	25.0	30 years [32]	High-temperature annealing
Gallium Arsenide	28.8	30 years [32]	Vapour phase epitaxy
Cadmium Telluride	22.1	25 years [33]	Close space sublimation
Organic	12.2 [17]	11 years (lab) [21] 1 year (modules) [23]	Spin coating
Perovskite	22.1	0.57 years [34]	Spin coating

Table 1.1: Peak power conversion efficiency (acquired from the National Renewable Energy Laboratory Solar Cell Efficiency chart unless otherwise stated), lifetime, and primary processing techniques for several types of solar cell.

In order for organic and perovskite solar cells to reach commercial viability it has therefore become more important to optimise for stability, rather than chasing incrementally higher efficiencies. A more efficient device is not necessarily a more stable one, and there may be materials, device architectures, or processes that produce more stable devices at the expense of some efficiency which need to be investigated.

1.1: Thesis Summary and Motivation

The aim of this thesis is to investigate the lifetime and stability of both organic and perovskite PV devices, as well as the mechanisms at work and influencing factors. It is hoped that this will provide useful information to help improve the lifetime of such devices, and push them closer to commercialisation. The thesis is structured as follows. In Chapter 2, relevant background information and theory of the origin of semiconducting properties and the operational principles of both organic and perovskite solar cells is provided. For both materials, a brief literature review of lifetime experiments is included to highlight progress in this research field. The experimental methods used in this thesis are described in Chapter 3.

In Chapter 4, the effects of palladium (Pd), an impurity left over from the synthesis of most organic polymers used in PV, on the performance and stability of PCDTBT

and PFD2TBT-8 organic photovoltaic (OPV) devices are investigated. It is shown through laser beam induced current mapping and backscattered scanning electron microscopy (provides elemental contrast when imaging) that Pd is responsible for the formation of large aggregates in PCDTBT which act as current shunts between the contacts of the devices. When subjected to continuous illumination, it is found that efficiency losses during the initial rapid 'burn-in' are increased by the presence of Pd. It is speculated that such burn-in is due to the formation of new current shunts by Pd in the bulk of the active layer. In PFD2TBT-8 devices, Pd is shown to have a much smaller effect on the performance of devices, with no significant changes occurring below a certain concentration. It is speculated that this may be due to the improved solubility of PFD2TBT-8 over PCDTBT preventing the formation of large aggregates. This is also reflected in the lifetime measurements, where similar decay trends are seen for all Pd concentrations.

Chapter 5 characterises the operational stability of encapsulated 'inverted' architecture methylammonium lead iodide-chloride perovskite devices, over a period of one month. It is shown that such devices decay rapidly over the course of the test, having lifetimes (defined as the time taken for the power conversion efficiency to decrease by 20% during the linear decay period) shorter than 300 hours, with losses primarily occurring in the short circuit current density. Using external quantum efficiency, time resolved photoluminescence, and laser beam induced current, it is shown that the mechanisms behind the degradation most likely result from reactions with oxygen and water, causing the decomposition of the perovskite into lead iodide, hydroiodic acid, and methylamine.

Chapter 6 investigates the impact of adding 1 vol% hydroiodic acid to the precursor solution of spray coated methylammonium lead iodide-chloride perovskite devices on both initial performance and operational stability. The additive is shown to improve the initial performance of devices through an increase in the short circuit current density. This is a result of enhancement of the external quantum efficiency, removing a dip between 600 and 700 nm observed in devices fabricated without the additive. This is speculated to be due to greater control over precursor ratios due to the additive improving the solubility of the materials. When subjected to 1 month of continuous operation, the devices

utilising the additive also proved to have improved long term stability, an effect believed to be a result of improved chemical stability of the perovskite.

In Chapter 7, the effects of annealing methylammonium lead iodide-chloride perovskite at an elevated temperature after conversion of the precursor materials on the stability of devices is examined. It is shown that this additional anneal results in a loss of initial efficiency, but a significant increase in the stability of the devices. Initial losses are correlated with increased inhomogeneity of the spatially resolved photocurrent, most likely a caused by the extra anneal damaging the perovskite layer. The improved stability is believed to be due to the removal of water and oxygen absorbed into the hole transport and perovskite layer, reducing the rate at which decomposition reactions occur. In addition to this, the effects of substrate and solution temperature during the deposition of the perovskite layer on stability have been investigated. It is observed that the performance of devices improves as processing temperature increases, an effect correlated with increases in the short circuit current density. This is attributed to improved surface coverage, enabling improved absorption and better charge transport. However, the reverse effect was seen for the stability, with devices deposited at lower temperatures exhibiting the highest stability.

Finally, the results of this thesis are summarised in Chapter 8, along with suggestions about how the work can be built upon.

1.2: References

[1] J. Conti, P. Holtberg, J. Diefenderfer, A. LaRose, J.T. Turnure, L. Westfall, International Energy Outlook 2016, U.S Energy Information Administration, 2016.

[2] F. Birol, Key World Energy Statistics 2015, International Energy Agency, 2015.

[3] F. Birol, Energy and Air Pollution - World Energy Outlook 2016, International Energy Agency, 2016.

[4] M. van der Hoeven, World Energy Outlook 2012, International Energy

Agency, 2012.

[5] J. Goldemberg, World Energy Assessment, United Nations Developmental Programme, 2000.

[6] U.S.E.I. Administration, Levelized Cost and Levelized Avoided Cost of New Generation Resources in the Annual Energy Outlook 2015, (2015) 1–12.

[7] M.A. Green, K. Emery, Y. Hishikawa, W. Warta, E.D. Dunlop, Solar cell efficiency tables (version 47), Prog. Photovolt Res. Appl. 24 (2016) 3–11.

[8] M.A. Green, Third generation photovoltaics: Ultra-high conversion efficiency at low cost, Prog. Photovoltaics Res. Appl. 9 (2001) 123–135.

[9] P. Sinha, Life cycle materials and water management for CdTe photovoltaics, Sol. Energy Mater. Sol. Cells. 119 (2013) 271–275.

[10] K. Zweibel, The impact of tellurium supply on cadmium telluride photovoltaics., Science (80-.). 328 (2010) 699–701.

[11] F.C. Krebs, Fabrication and processing of polymer solar cells: A review of printing and coating techniques, Sol. Energy Mater. Sol. Cells. 93 (2009) 394–412.

[12] B. Kippelen, J.-L. Brédas, Organic photovoltaics, Energy Environ. Sci. 2 (2009) 251.

[13] G. Dennler, M.C. Scharber, C.J. Brabec, Polymer-Fullerene Bulk-Heterojunction Solar Cells, Adv. Mater. 21 (2009) 1323–1338.

[14] F.C. Krebs, All solution roll-to-roll processed polymer solar cells free from indium-tin-oxide and vacuum coating steps, Org. Electron. 10 (2009) 761–768.

[15] N. Espinosa, R. Garcia-Valverde, A. Urbina, F.C. Krebs, A life cycle analysis of polymer solar cell modules prepared using roll-to-roll methods under ambient conditions, Sol. Energy Mater. Sol. Cells. 95 (2011) 1293–1302.

[16] C.J.M. Emmott, A. Urbina, J. Nelson, Environmental and economic assessment

of ITO-free electrodes for organic solar cells, Sol. Energy Mater. Sol. Cells. 97 (2012) 14–21.

[17] W. Zhao, S. Li, S. Zhang, X. Liu, J. Hou, Ternary Polymer Solar Cells based on Two Acceptors and One Donor for Achieving 12.2% Efficiency, Adv. Mater. 29 (2017) 1604059. doi:10.1002/adma.201604059.

[18] S. Li, L. Ye, W. Zhao, S. Zhang, S. Mukherjee, H. Ade, J. Hou, Energy-Level Modulation of Small-Molecule Electron Acceptors to Achieve over 12% Efficiency in Polymer Solar Cells, Adv. Mater. 28 (2016) 9423–9429.

[19] Heliatek sets new Organic Photovoltaic world record efficiency of 13.2%., Heliatek Press Release. (2016). http://www.heliatek.com/en/press/press-releases/details/heliatek-sets-new-organic-photovoltaic-world-record-efficiency-of-13-2.

[20] S. Berny, N. Blouin, A. Distler, H.-J. Egelhaaf, M. Krompiec, A. Lohr, O.R. Lozman, G.E. Morse, L. Nanson, A. Pron, T. Sauermann, N. Seidler, S. Tierney, P. Tiwana, M. Wagner, H. Wilson, Solar Trees: First Large-Scale Demonstration of Fully Solution Coated, Semitransparent, Flexible Organic Photovoltaic Modules, Adv. Sci. 3 (2016) 1–7.

[21] C.H. Peters, I.T. Sachs-Quintana, J.P. Kastrop, S. Beaupré, M. Leclerc, M.D. McGehee, High efficiency polymer solar cells with long operating lifetimes, Adv. Energy Mater. 1 (2011) 491–494.

[22] E. Bovill, N. Scarratt, J. Griffin, H. Yi, A. Iraqi, a. R. Buckley, J.W. Kingsley, D.G. Lidzey, The role of the hole-extraction layer in determining the operational stability of a polycarbazole:fullerene bulk-heterojunction photovoltaic device, Appl. Phys. Lett. 106 (2015) 73301.

[23] S.A. Gevorgyan, M. V. Madsen, H.F. Dam, M. Jorgensen, C.J. Fell, K.F. Anderson, B.C. Duck, A. Mescheloff, E.A. Katz, A. Elschner, R. Roesch, H. Hoppe, M. Hermenau, M. Riede, F.C. Krebs, Interlaboratory outdoor stability studies of flexible roll-to-roll coated organic photovoltaic modules: Stability over 10,000 h, Sol. Energy Mater. Sol. Cells. 116 (2013) 187–196.

[24] M.A. Green, A. Ho-Baillie, H.J. Snaith, The emergence of perovskite solar cells, Nat. Photonics. 8 (2014) 506–514.

[25] Y. Zhou, K. Zhu, Perovskite Solar Cells Shine in the “Valley of the Sun,” ACS Energy Lett. (2016) 64–67.

[26] N.-G. Park, Perovskite solar cells: an emerging photovoltaic technology, Mater. Today. 18 (2015) 65–72.

[27] F. Hao, C.C. Stoumpos, D.H. Cao, R.P.H. Chang, M.G. Kanatzidis, Lead-free solid-state organic–inorganic halide perovskite solar cells, Nat. Photonics. 8 (2014) 489–494.

[28] N.K. Noel, S.D. Stranks, A. Abate, C. Wehrenfennig, S. Guarnera, A.-A. Haghighirad, A. Sadhanala, G.E. Eperon, S.K. Pathak, M.B. Johnston, A. Petrozza, L.M. Herz, H.J. Snaith, Lead-Free Organic-Inorganic Tin Halide Perovskites for Photovoltaic Applications, Energy Environ. Sci. 7 (2014) 3061–3068.

[29] B. Saparov, F. Hong, J.-P. Sun, H.-S. Duan, W. Meng, S. Cameron, I.G. Hill, Y. Yan, D.B. Mitzi, Thin-Film Preparation and Characterization of Cs3Sb2I9: A Lead-Free Layered Perovskite Semiconductor, Chem. Mater. 27 (2015) 5622–5632.

[30] D. Wang, M. Wright, N.K. Elumalai, A. Uddin, Stability of perovskite solar cells, Sol. Energy Mater. Sol. Cells. 147 (2016) 255–275.

[31] D.L. Staebler, R.S. Crandall, R. Williams, Stability of n-i-p amorphous silicon solar cells, Appl. Phys. Lett. 39 (1981) 733.

[32] N.J. Mohr, J.J. Schermer, M.A.J. Huijbregts, A. Meijer, L. Reijnders, Life Cycle Assessment of Thin- film GaAs and GaInP/GaAs Solar Modules, Prog. Photovoltaics Res. Appl. 15 (2007) 163–179.

[33] CdTe Technology | First Solar, (n.d.). http://firstsolar.com/en/Technologies-and-Capabilities/PV-Modules/First-Solar-Series-4-Modules/CdTe-Technology (accessed January 20, 2017).

[34] M. Saliba, T. Matsui, J.-Y. Seo, K. Domanski, J.-P. Correa-Baena, N. Mohammad K., S.M. Zakeeruddin, W. Tress, A. Abate, A. Hagfeldt, M. Gratzel, Cesium-containing Triple Cation Perovskite Solar Cells: Improved Stability, Reproducibility and High Efficiency, Energy Environ. Sci. 9 (2016) 1989–1997.

Chapter 2

Background Theory

2.0: Introduction

This chapter covers the physical and electrical properties behind organic semiconductor and perovskite materials used in photovoltaics. A brief introduction to photovoltaics is given in Section 2.1, with the characterisation of photovoltaic devices explained in Section 2.2. In Section 2.3 the origin of semiconducting properties in organic materials and the operational principles of organic photovoltaic devices are described. Section 2.4 covers the semiconducting properties and operational principles of perovskite solar cells. Towards the end of Sections 2.3 and 2.4 are brief reviews of the literature on the operational stability of organic photovoltaics and perovskite solar cells respectively.

2.1: Photovoltaics

The photovoltaic effect is the process of converting light into electricity that occurs in some semiconductors. In general, semiconductors have a band gap, E_g, the energy difference between the highest filled electron energy level (known as the valence band) and the lowest unoccupied electron energy level (known as the conduction band). If a photon incident on the semiconductor has energy, E_γ, greater than the band gap energy, then it will be absorbed, promoting an electron from the valence band to the conduction band and leaving a hole in the valence band. The electron-hole pair are coloumbically bound in a state known as an exciton and to collect the charge carriers this exciton must be dissociated. The binding energy of an exciton is dependent on the dielectric constant, ε_r, of the material, the level of screening between charges, and will therefore dictate how dissociation will occur. Materials with high ε_r have high charge screening, resulting in low exciton binding energy and high spatial separation. Excitons in these materials can dissociate thermally at ambient temperatures. Conversely, materials with a low ε_r have poor charge screening, resulting in an exciton with high binding energy and low spatial separation. In order to dissociate excitons an interface between materials with energy levels differing by more than the exciton binding energy must be used. Once the exciton is dissociated, the charges are swept to the electrodes by an electric field where they are collected and can then be used in an electronic circuit.

The choice of band gap for a photovoltaic device is very important, as this affects the available energy that can be harvested. For $E_\gamma > E_B$, the photon is absorbed, with excess photon energy used to promote the electron to energy levels above the conduction band. The electron then relaxes down to the conduction band minimum resulting in the loss of the excess energy. Conversely, if $E_\gamma < E_B$, then the photon will not be absorbed, again resulting in lost energy. Consequently, when considering a blackbody spectrum of 6000 K (approximately that of the Sun), it can be seen that with a band gap that is too large, a significant amount of photons will not be absorbed, whilst a too small band gap results in a large number of absorbed photons, but a significant loss of energy due to the relaxation of electrons to the conduction band minimum. This enables a theoretical maximum device efficiency

to be calculated by finding a balance between these two factors. Indeed, this was determined by Shockley and Queisser in 1961 to be approximately 33% [1].

The field of photovoltaics has been largely dominated by inorganic semiconductors since its discovery in 1839 by Edmond Bacquerel [2,3]. However, in the past few decades, the field of organic photovoltaics has been steadily growing, with efficiencies of champion devices now achieving over 11% [4]. More recently, a new field of photovoltaics has emerged, the perovskite solar cell, which has seen remarkable progress since its inception less than 10 years ago, with champion devices displaying efficiencies over 20% [5]. The progress of the entire field of photovoltaics, including organic and perovskite photovoltaics, can be seen in Figure 2.1, the solar cell efficiency chart by the National Renewable Energy Laboratory.

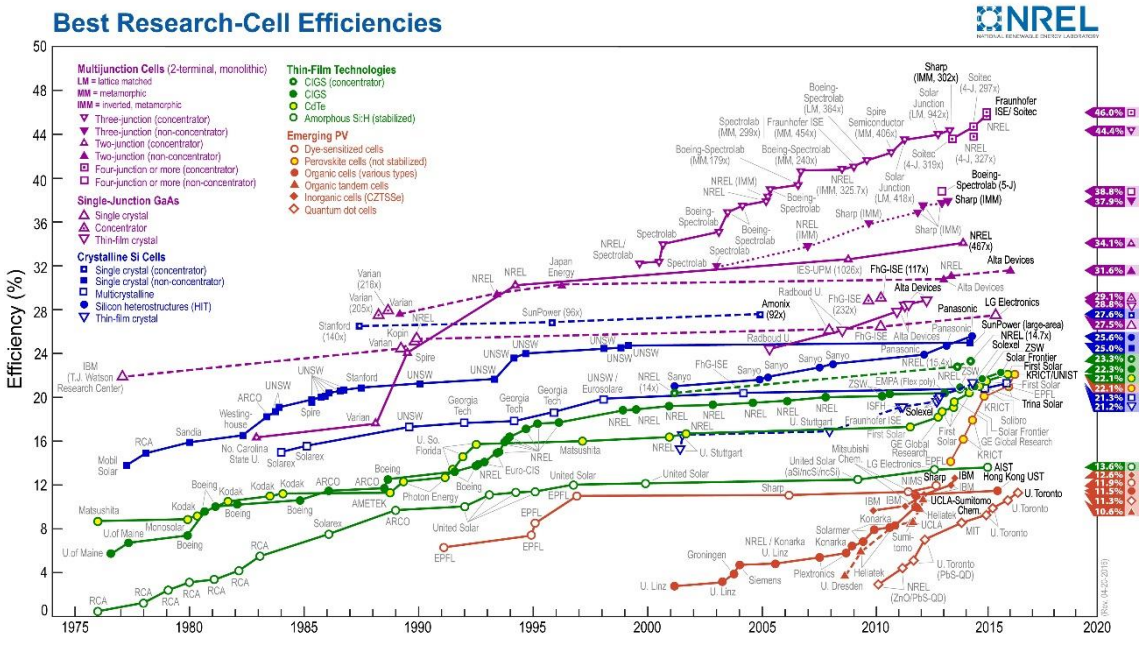

Figure 2.1: Peak solar cell efficiency since 1976 for all varieties of device. This plot is courtesy of the National Renewable Energy Laboratory, Golden, CO.

2.2: Characterising Photovoltaic Devices

To determine the performance of a solar cell, it must be measured whilst under solar illumination. The Sun emits a spectrum that is approximately a black body with a temperature of 5780 K. This spectrum has peak intensity in the visible

region and a large infra-red tail. However, in order to reach the surface of Earth it must first pass through the atmosphere, where a significant portion of the solar radiation is absorbed. Hence, when testing a solar cell, this spectrum is not used. Instead, the industry standard illumination is the AM1.5G (air mass 1.5 global) solar spectrum, shown in Figure 2.2, which has a power density of 100 mW/cm^2 [6]. This is the spectrum of solar irradiance after passing through 1.5 Earth atmospheres, equivalent to average solar irradiation at mid-latitudes, such as in Europe or the USA.

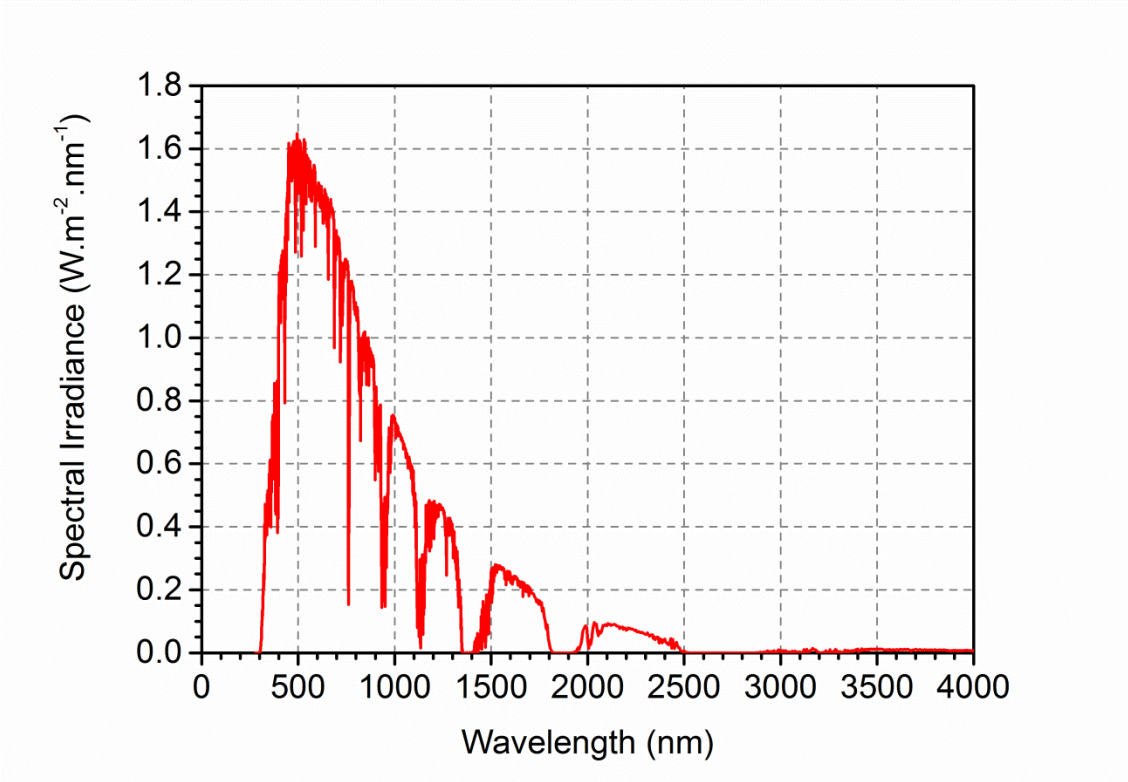

Figure 2.2: AM1.5G solar spectrum. Data courtesy of the National Renewable Energy Laboratory, Golden, CO [7].

The key parameter that is used to characterise a solar cell is its ability to convert solar radiation into electricity, known as the power conversion efficiency (PCE). This is the ratio of incident light power to output electrical power and can be determined by measuring the photocurrent density, *J*, whilst scanning across a range of voltages, *V*, under solar illumination. From the resultant *J-V* curve, several useful metrics of a device can be determined. An example *J-V* curve is shown in Figure 2.3, and is annotated with the various parameters which can be determined.

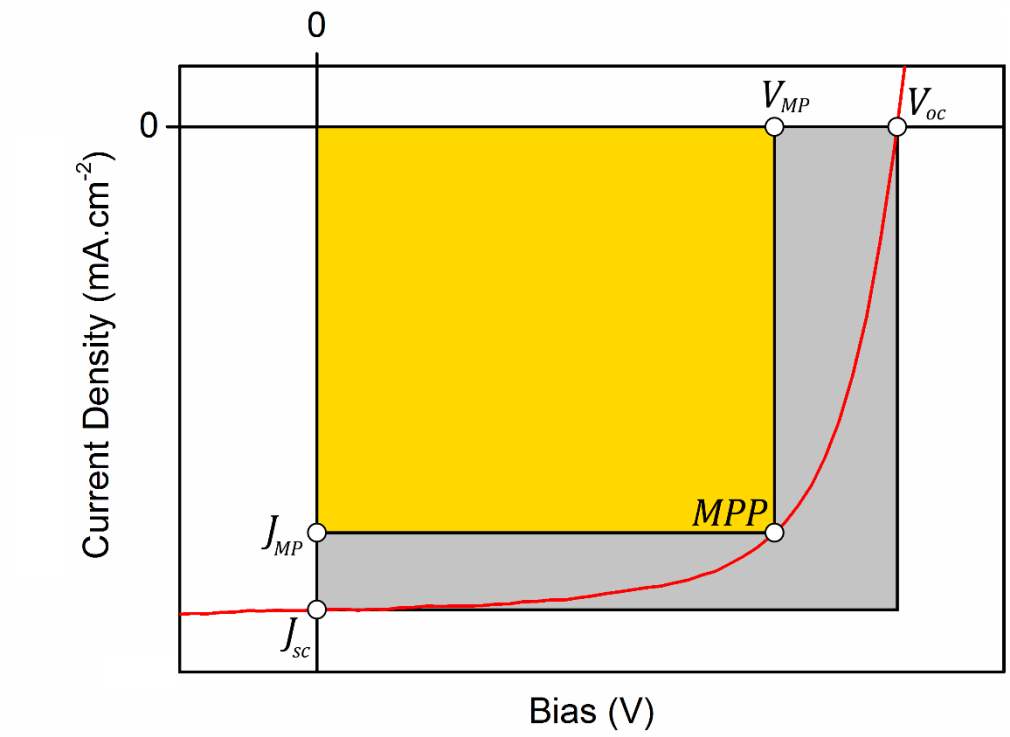

Figure 2.3: An example *J-V* curve showing the open circuit voltage (V_{oc}), short circuit current density (J_{sc}), maximum power point (*MPP*), and the voltage and current density at maximum power (V_{MP} and J_{MP} respectively). The area highlighted yellow shows the maximum power output of the solar cell, the ratio of this area to the area highlighted grey is the fill factor (*FF*) of the solar cell.

The PCE can be calculated using Equation 2.1:

$$PCE = \frac{P_{out}}{P_{in}} = \frac{J_{sc}V_{oc}FF}{P_{in}} \tag{2.1}$$

Here, P_{out} (P_{in}) is the output (input) power of the device, J_{sc} is the short circuit current density, V_{oc} is the open circuit voltage, and *FF* is the fill factor.

The J_{sc} is the current density generated by the cell with 0 V applied bias, using only the built-in field created by the difference in work functions of the electrodes to extract charges from the device. Therefore, this parameter is dependent on the absorption characteristics of the photoactive layer, and the charge generation, transport, and extraction efficiency of the device.

The V_{oc} is the voltage at which there is no generated photocurrent, and the maximum voltage output of a solar cell. This occurs when the applied electric field

cancels out the built-in field, removing all driving force for directed charge transport. The V_{oc} of a photovoltaic device is dependent upon the energy levels of the photoactive materials, the work functions of the electrode materials, and the charge carrier recombination rate within the device.

The *FF* can be calculated Equation 2.2:

$$FF = \frac{J_{MP}V_{MP}}{J_{sc}V_{oc}} \tag{2.2}$$

Here, J_{MP} and V_{MP} are the current density and voltage at the maximum power point respectively. This parameter is the ratio of the actual performance of a device to its performance with no series resistance and infinite shunt resistance, and is ideally as close to unity as possible.

A solar cell is a diode, and hence the current density-voltage characteristics can be described using the Shockley diode equation:

$$J(V) = J_{ph} - J_D = J_{ph} - J_0\left[\exp\left(\frac{eV}{k_BT}\right) - 1\right] \tag{2.3}$$

Here, J_{ph} is the generated photocurrent, J_D is the diode current density, J_0 is the dark saturation current density, and all other symbols have their usual meanings. However, this is for an ideal photodiode and does not account for potential losses in a solar cell. Therefore a modified version of the equation is used:

$$J(V) = J_{ph} - J_0\left[\exp\left(\frac{e(V + JR_s)}{nk_BT}\right) - 1\right] - \frac{V + JR_s}{R_{sh}} \tag{2.4}$$

Here, n is the diode ideality factor, and R_s and R_{sh} are the series and shunt resistances respectively. Using this equation, a solar cell can be modelled by the equivalent circuit diagram, shown in Figure 2.4.

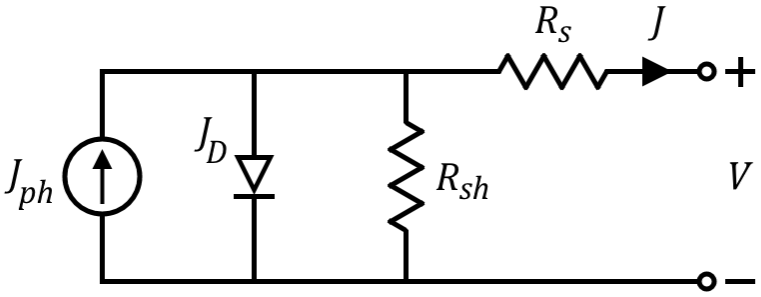

Figure 2.4: The equivalent circuit of a solar cell, all symbols have the meanings as described above.

The R_s accounts for bulk resistance within layers and interface resistance arising from energetic barriers. In an efficient solar cell this value should be minimised, as this resistance lowers charge collection efficiency. This can be minimised by the ensuring good energy level alignment of materials within the solar, thereby reducing the barriers to charge extraction, and charge carrier recombination rates. An approximate value of R_s can be calculated from the inverse of the gradient of a *J-V* curve at V_{oc}. The R_{sh} accounts for the resistance of alternate current pathways through a solar cell. This value is ideally as high as possible for an efficient device, unlike R_s, as this prevents current leakage. Maximising the R_{sh} can be achieved through the reduction of the recombination rate and current leakage pathways within the device. An approximate value of R_{sh} can be calculated from the inverse of the gradient of a *J-V* curve at J_{sc}.

The external quantum efficiency, EQE, is another parameter that can be used to characterise a device. It is the ratio of incident photons to charges extracted, and the wavelength dependant EQE can be calculated using Equation 2.5:

$$EQE(\lambda) = \frac{Jhc}{P(\lambda)\lambda e} \tag{2.5}$$

Here, $P(\lambda)$ is the incident power as a function of wavelength. The internal quantum efficiency, IQE, the ratio of absorbed photons to charges extracted can also be measured. The IQE is useful in providing information about the charge generation, transport and extraction efficiency of a device. However, this measurement only accounts for losses after photon absorption has occurred. The EQE quantifies the

efficiency of absorption and charge generation, transport and extraction, taking into account losses that can occur due to reflection at the front face, absorption by other layers within the device, and active layer thickness.

2.3: Organic Photovoltaics

2.3.1: Introduction

Organic photovoltaics (OPVs) use organic semiconducting polymers to produce the photovoltaic effect, converting light into electricity. They boast several advantages over inorganic materials, including lower weight, higher mechanical flexibility, and ability to be processed from solution, enabling the use of various printing and coating techniques, and the potential for roll-to-roll processing.

History of Organic Photovoltaics

The photovoltaic effect was first discovered in 1839 by Edmond Becquerel [2], and photoconductivity was first seen in an organic molecule, anthracene, 67 years later in 1906 by Pochettino [8]. It was not until 1982, however, until a polymer based photovoltaic device was fabricated, when Weinberger created a device using polyacetylene between aluminium and graphite. This device performed poorly, with PCE well below 1%, but showed that polymers could be used as the photoactive material in a solar cell. The low efficiency came from poor exciton dissociation in the organic layer, a consequence of the low dielectric constant of organic materials, which prevents thermal dissociation.

OPV devices continued to exhibit efficiencies below 1% until Tang reported a device containing two different organic layers in 1986, commonly thought of as the birth of the field of organic photovoltaics [9,10]. With this structure Tang was able to achieve PCE of ~1% due to improved exciton dissociation at the interface between the two organic materials. Despite this discovery, the efficiencies of devices did not rise significantly due to problems with exciton diffusion. In organic materials, excitons can generally travel approximately 10 nm before recombination of the electron and hole occurs [11]. This presented severe limitations on OPV devices, as the organic layers would have to be only 10 nm thick to ensure all excitons were able to reach the interface between the two materials,

resulting in very poor optical absorption in the active layer. If thicker organic layers were used to improve optical absorption, excitons not generated within 10 nm of the interface would be lost due to recombination.

This problem was solved independently in 1995 by Yu et al. [12] and Hall et al. [13], with the development of the 'bulk heterojunction' (BHJ). Here, two organic polymers were deposited from the same solution, resulting in the formation of an interpenetrating, bicontinuous network of the two materials. This enabled the creation of much thicker active layers whilst maintaining a short separation between the materials, enabling good optical absorption and efficient exciton dissociation. Further improvements were made by the adoption of the polymer:fullerene BHJ, with an organic polymer acting as an electron donor (hole transporting material) and a fullerene as an electron acceptor (electron transporting material), which is used in the most efficient devices to date [4,14].

Current State of Research

Since the development of the BHJ, the PCE of OPV devices has steadily risen through the synthesis of many new polymers. Some of the most studied donor polymers include derivatives of poly(p-phenylene vinylene) (PPV) and poly(alkyl-thiophenes) (in particular poly(3-hexylthiophene-2,5-diyl), P3HT) [15,16]. However, PPVs have relatively large band gaps, resulting in poor absorption and limiting the achievable PCE to <4% [16,17]. Similarly, despite good charge transport and light absorption properties, P3HT is limited by relatively poor energy level alignment with the most commonly used acceptor fullerenes are [6,6]-phenyl-C61-butyric acid methyl ester ($PC_{60}BM$), and [6,6]-phenyl-C71-butyric acid methyl ester ($PC_{70}BM$), resulting in V_{oc} reaching a peak value of < 0.7 V [18]. This has led to the synthesis of more polymer classes with a focus on smaller band gaps and better energy level alignment with fullerene materials.

One class of polymer that has attracted significant interest from the OPV community are poly carbazole derivatives, with the most studied being poly[N-90-heptadecanyl-2,7-carbazole-alt-5,5-(40,70-di-2-thenyl-20,10,30-benzothiadiazole)] (PCDTBT). In optimised devices PCDTBT has displayed PCEs of 7.5% [19], with IQE approaching 100% [20], and in operational stability studies

lifetimes exceed 7 years have been exhibited [21]. PCDTBT has also been shown to have a good degree of ambient stability, with comparable performance for devices fabricated both in inert and ambient conditions [22]. Structural variations of PCDTBT have also been investigated, such as the addition of alkyl chains to the benzothiadiazole, improving the solubility of the polymer whilst maintaining its performance. The addition of extra thiophene moieties to the polymer backbone has been shown to reduce the band gap energy of PCDTBT, as well as improving the intramolecular charge transport [23].

The peak certified PCE for single junction OPV devices is currently 11.5% (see Figure 2.1) for a poly[(5,6-difluoro-2,1,3-benzothiadiazole-4,7-diyl)-alt-(3,3'''-di(2-nonyltridecyl)-2,2';5',2'';5'',2'''-quaterthiophen-5,5'''-diyl)] (PffBT4T-C_9C_{13}) based device using $PC_{70}BM$ as the acceptor fullerene in the structure ITO/ZnO/active layer/V_2O_5/Al [4]. The authors used 1,2,4-trimethylbenzene as the solvent for the polymer:fullerene solution, with an additive 1-phenylnaphthalene, to achieve improved active layer morphology. For multi-junction devices, the peak certified performance is currently held by Heliatek, who have achieved 13.2% with thermally evaporated small molecules [24].

OPV devices have also been processed using scalable techniques such as spray coating [25] and doctor blading [26], showing comparable performance to devices fabricated using spin coating, the most common fabrication technique. Indeed, devices based on P3HT, fabricated entirely using inkjet printing have been shown to achieve over 75% of the performance of reference devices [27]. There have also been reports of large area OPV devices fabricated entirely via roll-to-roll processing being employed in a small scale solar farm, exhibiting over 2% PCE from P3HT:PCBM devices with an active area of 14.7 m^2 [28] (typical laboratory solar cells have an active area <1 cm^2). More recently, OPV modules using PBTZT-stat-BDTT-8 (full name not provided) have achieved PCE of 4.5% for an active area of 114.5 cm^2 [29].

Device Architecture

OPV device architectures can be in one of two forms, 'standard' or 'inverted', and are shown in Figure 2.5. In standard architecture devices, the active layer is

situated between a transparent hole extracting anode and reflective electron extracting cathode. In the inverted architecture, this is reversed, with the anode being reflective and the cathode being transparent [30]. In both of these architectures the non-transparent electrode is reflective to improve the light absorption of the active layer, and thus increase the number of photogenerated charge carriers in a device.

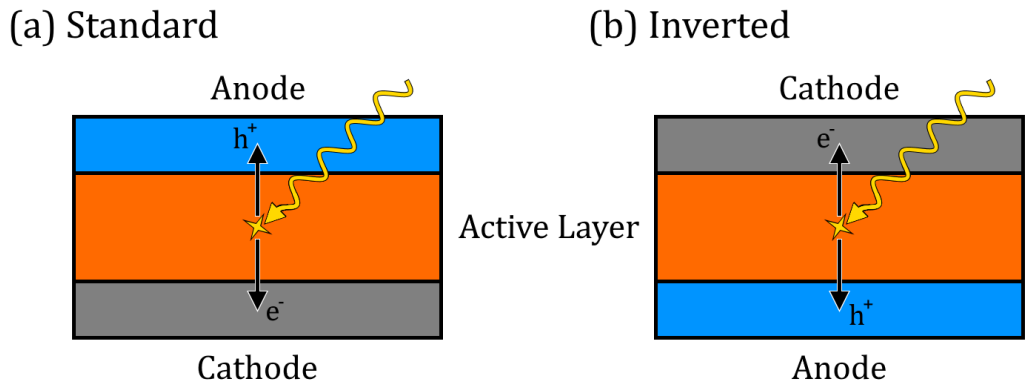

Figure 2.5: Schematic diagram of incident light, and electron and hole extraction for (a) standard and (b) inverted architecture OPV devices.

In addition to these layers, an electron transport layer (ETL) and hole transport layer (HTL) are often included in a device. These facilitate the extraction of charge carries from the active layer by providing an intermediate energy level between those of the active materials and the electrodes. They can also be used to determine the polarity of the device, i.e., whether it is standard or inverted architecture, by choice of position within the device stack and materials used. Here, they act as 'blocking layers', preventing undesired charge carriers from reaching an electrode. This can enable the use of the same electrode materials in both architectures, such as the commonly used indium tin oxide (ITO) which can be used as a transparent anode or cathode [31], with the direction of charge extraction dictated by the ETL and HTL positions. An energy level diagram of a typical standard architecture PCDTBT:$PC_{70}BM$ OPV device employing both a HTL and an ETL is shown in Figure 2.6. Here, it can be seen that PEDOT:PSS provides an intermediate energy level between the ITO and the highest occupied molecular orbital (section 2.3.4) of the PCDTBT, which will assist in the collection of holes.

Meanwhile, the calcium ETL provides a blocking layer, preventing holes from reaching the aluminium cathode.

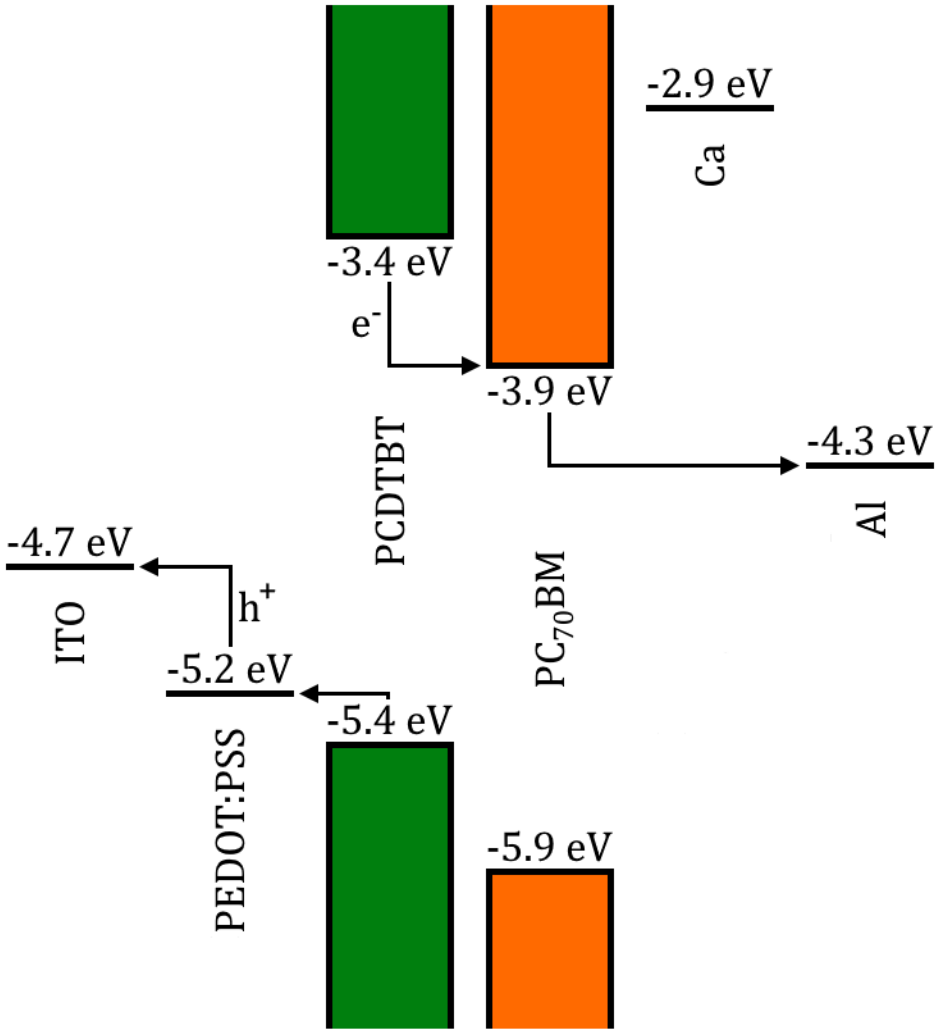

Figure 2.6: Energy level diagram of a typical PCDTBT:$PC_{70}BM$ OPV device, with an indium tin oxide (ITO) anode and aluminium (Al) cathode. A PEDOT:PSS hole transport layer and calcium (Ca) electron transport layer are also employed. The path of electrons and holes through the device is highlighted.

The inverted architecture has gained interest due to the potential for increased device stability over those using the standard architecture. Standard architecture devices make use of low work function metals, such as Ca and Al, which are susceptible to reactions with water and oxygen. In the inverted architecture, higher work function metals such as Ag and Au are used instead, providing devices with much greater ambient stability [32].

2.3.2: Atomic and Molecular Orbitals

Electrons that exist within atoms are said to occupy orbitals. These orbitals are quantum mechanical in nature and, unlike classical orbitals with well-defined positions, can be thought of as the probability of an electron existing in a certain location due to the uncertainty principle [33]. The properties of atomic orbitals, including occupancy and shape, are defined by four quantum numbers, given in Table 2.1 along with their possible values.

Quantum Number	Symbol	Electron Property	Values
Principle	n	Potential energy	$n \geq 1$
Azimuthal	l	Magnitude of angular momentum	$0 \leq l \leq n-1$
Magnetic	m_l	Direction of angular momentum	$-l \leq m_l \leq l$
Spin	m_s	Direction of spin	$m_s = \pm {}^1/_2$

Table 2.1: Quantum numbers defining atomic orbitals. The values for n, l and m_l may only be integers.

The shell an electron occupies is determined by n, the principle quantum number, with the particular orbital defined by l, the azimuthal quantum number. Due to the Pauli Exclusion Principle, only one electron can have each combination of values for the four quantum numbers, dictating the maximum electron occupancy of each orbital. Table 2.2 shows each combination of the quantum numbers and the maximum occupancy of the orbitals in the first two shells of an atom. The first orbital is the 1s orbital; 's' orbitals exist where $l = 0$, and can contain a maximum of two electrons. This occurs at each value of n, meaning that the first orbital of each shell, i.e. 1s, 2s, 3s, can only contain two electrons. In the second shell, $l = 0$ or 1, meaning a second orbital exists in addition to the 2s orbital. This extra orbital is a 'p' orbital and can contain up to six electrons. As $m_l = -1$, 0, or 1 for 'p' orbitals, they are split into sub-orbitals p_x, p_y, and p_z. These orbitals have equal energy, but are orientated along the x, y, and z axes of the atom respectively, as shown in Figure 2.6(b). At higher energies the angular momentum can take higher values, forming

'd' (l = 2) and 'f' (l = 3) orbitals. These orbitals have complex shapes and are rarely encountered in organic semiconductors, and will therefore not be covered in this thesis.

n	l	m_l	m_s	Orbital Name	Total Electrons
1	0	0	½	1s	2
			-½		
2	0	0	½	2s	8
			-½		
	1	-1	½	2p	
			-½		
		0	½		
			-½		
		1	½		
			-½		

Table 2.2: Quantum numbers, orbital names and electron occupancy for the orbitals of the first two shells of an atom.

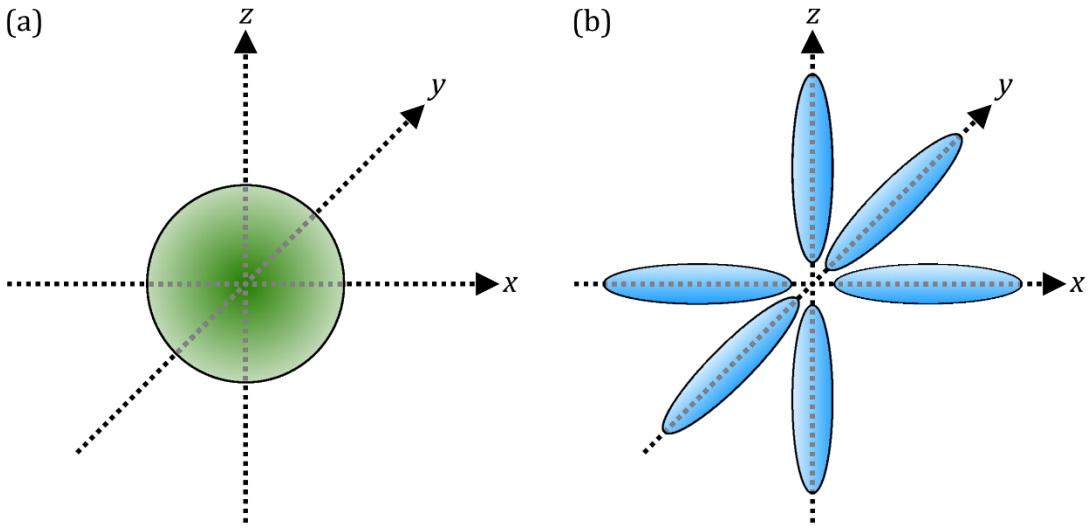

Figure 2.6: Schematic diagram of (a) an s orbital and (b) p orbitals of electrons.

In order to create organic semiconducting polymers, atoms need to be bound together into molecules using covalent bonds. By bringing two atoms close enough

together, the orbitals will overlap and combine, creating a single probability cloud for both electrons, known as a bonding orbital. More specifically, a bonding orbital occurs when the electron wavefunctions combine in-phase. This results in a lowering of the energy of the orbital as the increased electron density between the two atoms increases the shielding from Coulombic repulsion. However, if there are additional electrons, such as in a full orbital, they will be unable to occupy the bonding orbital due to the Pauli Exclusion Principle [34] and will instead occupy an antibonding orbital, combing wavefunctions out-of-phase. This orbital does not occupy the region between the atoms and is higher energy, due to reduced electron density and therefore Coulombic shielding, resulting in an unstable bond. The bonding and anti-bonding orbitals are shown in Figure 2.8(a), along with the energy level splitting in Figure 2.8(b).

Both bonding orbitals and antibonding orbitals can exist as σ bonds or π bonds, depending on the symmetry of the orbital. If the orbital is symmetric around the axis between the two atoms, the bond is a σ bond. If the orbital is asymmetric around the axis between the two atoms, it is a π bond. As a π bond exists away from the axis connecting the two atoms, the electron density is reduced, leading to the π bond being weaker than the σ bond [35].

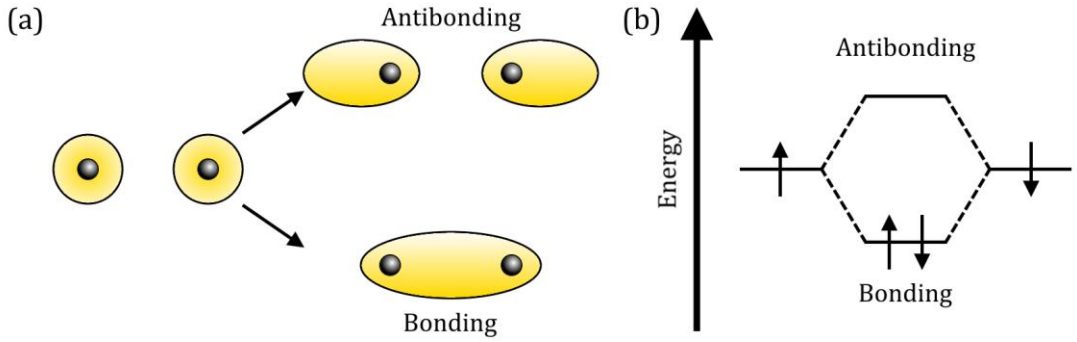

Figure 2.8: (a) Schematic of electron orbitals and (b) energy level splitting for bonding and antibonding.

2.3.3: Atomic Orbital Hybridisation

The main and most important component of organic polymers is the carbon atom. Carbon (^{12}C) has 6 electrons with the configuration $1s^2$, $2s^2$, $2p_x^1$, $2p_y^1$ in the ground state. Normally, the filled 2s orbital would mean that the atom could only

form a maximum of two bonds using the electrons in the 2p orbital. However, when forming bonds carbon undergoes a process known as atomic orbital hybridisation which enables the atom to form up to four bonds. This is a two-step process with the first step being the promotion of a 2s electron to the 2p orbital, resulting in the configuration $1s^2$, $2s^1$, $2p_x^1$, $2p_y^1$, $2p_z^1$. The energy for this promotion originates from electromagnetic attraction of the other atom involved in the bonding process. The remaining 2s orbital is then combined with one, two or all three of the 2p orbitals to create sp, sp^2 or sp^3 hybrid orbitals respectively.

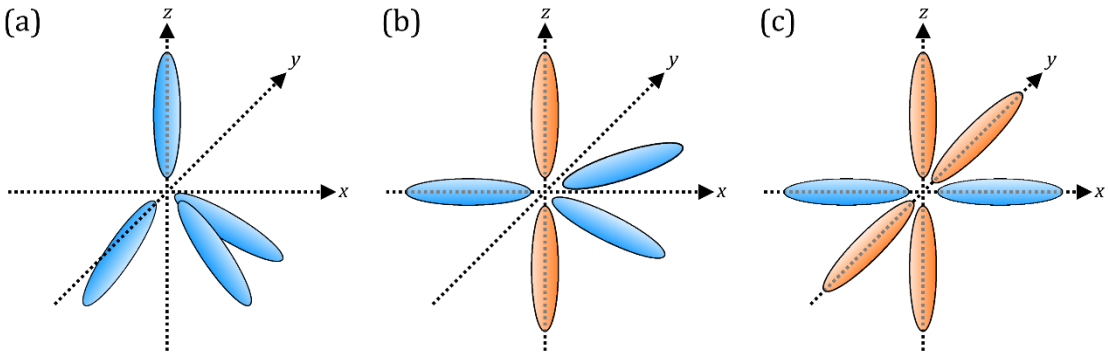

Figure 2.9: Schematic diagram of (a) sp^3, (b) sp^2, and (c) sp hybridised s and p electron orbitals. Blue orbitals represent hybridised orbitals, whilst orange orbitals represent unhybridised p orbitals.

The sp^3 hybrid orbital results in 4 available hybrid bonds, which are equally spaced in a tetragonal structure with 109.5° between each bond, as shown in Figure 2.9(a). Covalent bonds created with these hybrid orbitals are σ bonds, and are very strong and highly localised. Therefore, structures created using sp^3 hybridised carbon are usually chemically inert and electrical insulators. The sp^2 hybrid orbital creates 3 available hybrid bonds, as shown in Figure 2.9(b), spaced 120° apart in-plane, with the remaining non-hybridised p orbital existing perpendicular to this plane. When a σ bond is formed, the p orbitals of the two atoms overlap and combine, forming a π bond existing parallel to the σ bonds, as shown in Figure 2.10.

It is important to note that atomic orbital hybridisation is not limited to just carbon, and can occur for many atoms.

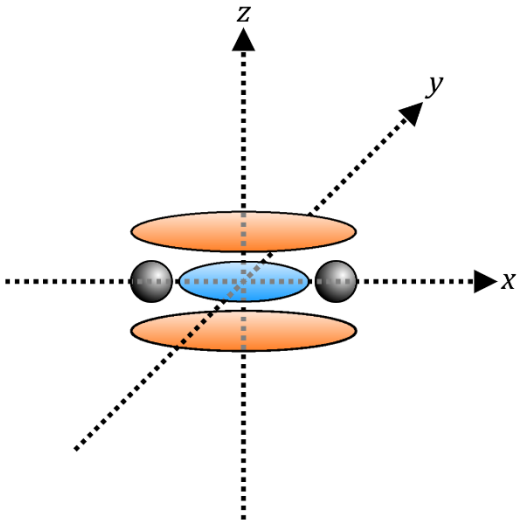

Figure 2.10: Schematic diagram of a σ and π bonds. The blue orbital represents a σ bond, and the orange orbitals represent π bonds.

2.3.4: Conjugation and Band Formation

The σ bond is often referred to as a single bond, whilst a combination of a σ and a π bond is referred to as a double bond. When a molecule or polymer contains alternating single and double bonds it is said to be conjugated. To demonstrate how this leads to semiconducting properties, the benzene molecule is commonly used. Benzene is a ring of six sp^2 hybridised carbon atoms with alternating single and double bonds. There are two possibilities for the relative position of these bonds within the molecule as shown in Figure 2.11. In both cases, the π electron orbitals exist as rings above and below the plane of the molecule, making the two configurations effectively identical as the bond position does not affect the properties of the molecule. This makes the configurations indistinguishable, resulting in the π bonds being able to exist in both positions simultaneously. The π electrons therefore become delocalised around the entire ring, being unable to be associated with a specific bond between carbon atoms [35]. This delocalisation of the π electrons gives conjugated systems their semiconducting properties.

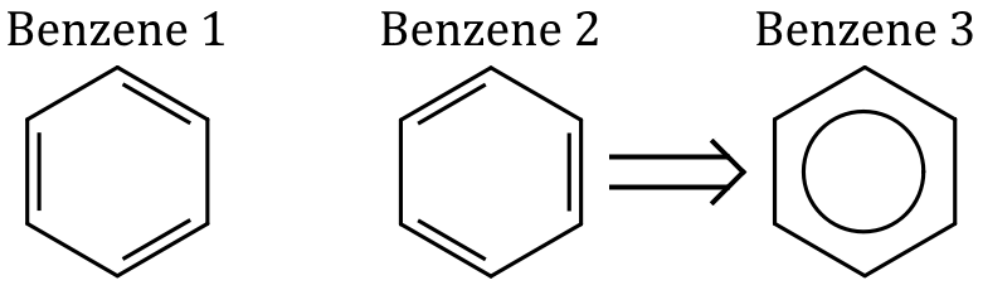

Figure 2.11: Benzene 1 and 2 show the two possible relative positions on π bonds. As these are indistinguishable the π are delocalised around the entire ring of carbon atoms, as shown in benzene 3.

Due to the relative weakness of the π bonding orbital, it is the highest energy state in the system occupied by electrons. This state is known as the highest occupied molecular orbital (HOMO) and is analogous to the valence band in an inorganic semiconductor. As this state is fully occupied, any additional electrons added to the system will occupy the next highest energy state. This is the π* antibonding orbital and is known as the lowest unoccupied molecular orbital (LUMO). Like the HOMO, this state has a parallel in inorganic semiconductors, in this case the conduction band. The relative energies of the σ and π bonding and antibonding orbitals are shown in Figure 2.12. The HOMO and LUMO of a molecule correspond to the ionisation potential (I_P) and electron affinity (E_A) respectively, and the difference between them is the defined as energy band gap of the system.

The HOMO and LUMO energies of a system are also affected by the environment surrounding them. Inorganic semiconductors are generally ordered systems, with a structure of repeating units, giving well-defined energies for the valence and conduction bands. Conjugated systems, however, are generally disordered. This can lead to an increase in the localisation of electrons in the system, altering the energy of the HOMO and LUMO. Furthermore, this makes the bands 'broader' increasing available transitions within the system.

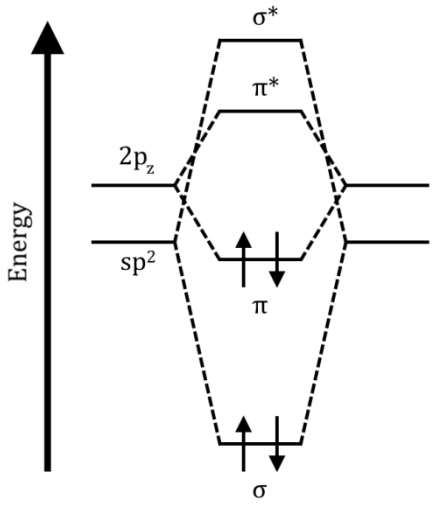

Figure 2.12: Relative energy levels of the σ and π bonding and antibonding orbitals.

Polyacetylene is the simplest conjugated polymer, a chain of carbon atoms with alternating single and double bonds, as shown in Figure 2.13(a). It is apparent that if the single and double bonds are equal in length, then the π electrons would be delocalised along the entire chain of the polymer, effectively making it a one-dimensional metal. Empirically, however, it has been shown that polyacetylene exhibits semiconducting behaviour, not metallic behaviour. This is due to Peierls instability, whereby one dimensional metals are unstable and undergo lattice distortions resulting in differences between the lengths of single and double bonds, as shown in Figure 2.13(b) and (c). To explain this, a system with equally spaced identical atoms is considered. Here, the electrons half fill the energy band of the system. To change the atom spacing costs elastic energy as being equally spaced is the most energetically favourable state. This changes the period of the atomic lattice, opening a band gap in the system and lowering the energy of the occupied electron states. If this decrease is greater than the elastic energy cost to move the atoms, it creates a more energetically favourable state for the system, resulting in semiconducting behaviour instead of conducting behaviour [36]. The extent of the delocalisation of π electrons is therefore reduced to several repeat units rather than the whole polymer chain, reducing the energy of the bonding orbital and creating an energy gap. For example, in polyacetylene the bond lengths have been found to be 1.44 and 1.36 Å for single and double bonds respectively [37], giving an energy gap of 1.4 eV [38].

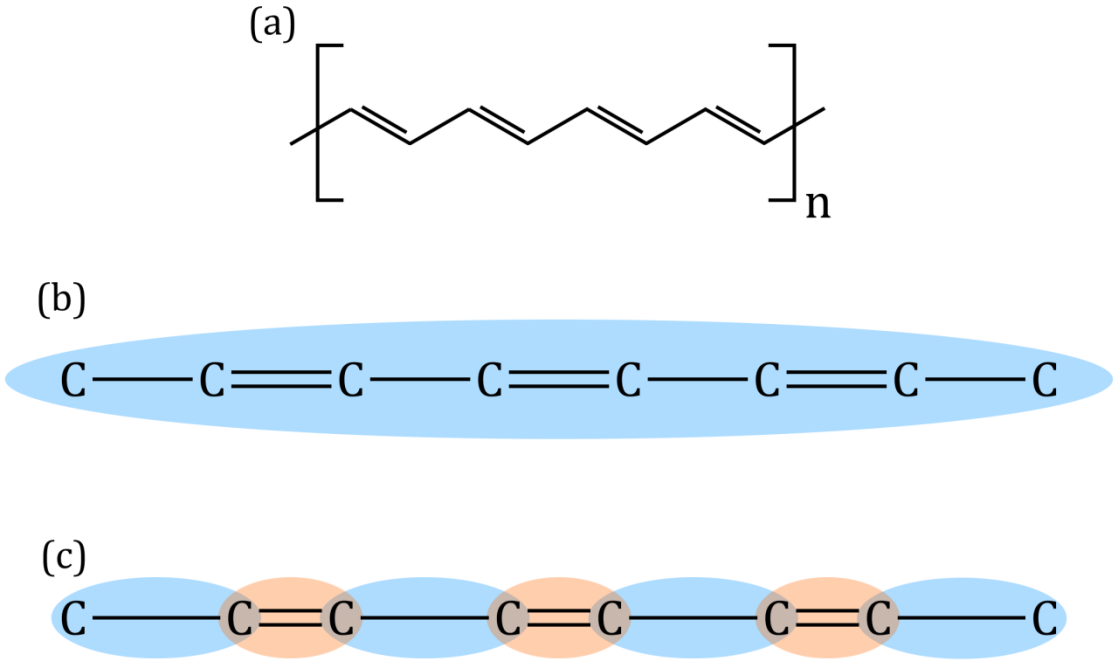

Figure 2.13: (a) Polyacetylene, (b) π electron cloud for equal single and double bond lengths, (c) electron clouds due to Peirels instability, with electron density increased around double bonds.

2.3.5: Photocurrent Generation in Organic Photovoltaic Devices

Exciton Formation

An energy level diagram of an idealised system is shown in Figure 2.14. Here, the curves represent the HOMO and LUMO of a conjugated system, with each of these states containing additional vibrational energy levels.

If a photon incident on a conjugated system is equal to, or greater than, the energy band gap, it will be absorbed and an electron will be excited from the LUMO, leaving a hole in the HOMO. As nuclear motion occurs over much longer time scales than electronic transitions, the excitation is represented using a vertical line. This is known as the Franck-Condon principle: an electronic transition is most likely to occur without changes in the position of the nuclei [39]. If the photon energy is greater than the band gap, then the electron will be excited into one of the higher vibrational levels of the LUMO, before undergoing non-radiative relaxation to the lowest vibrational level over a timescale of 0.1 ps [40].

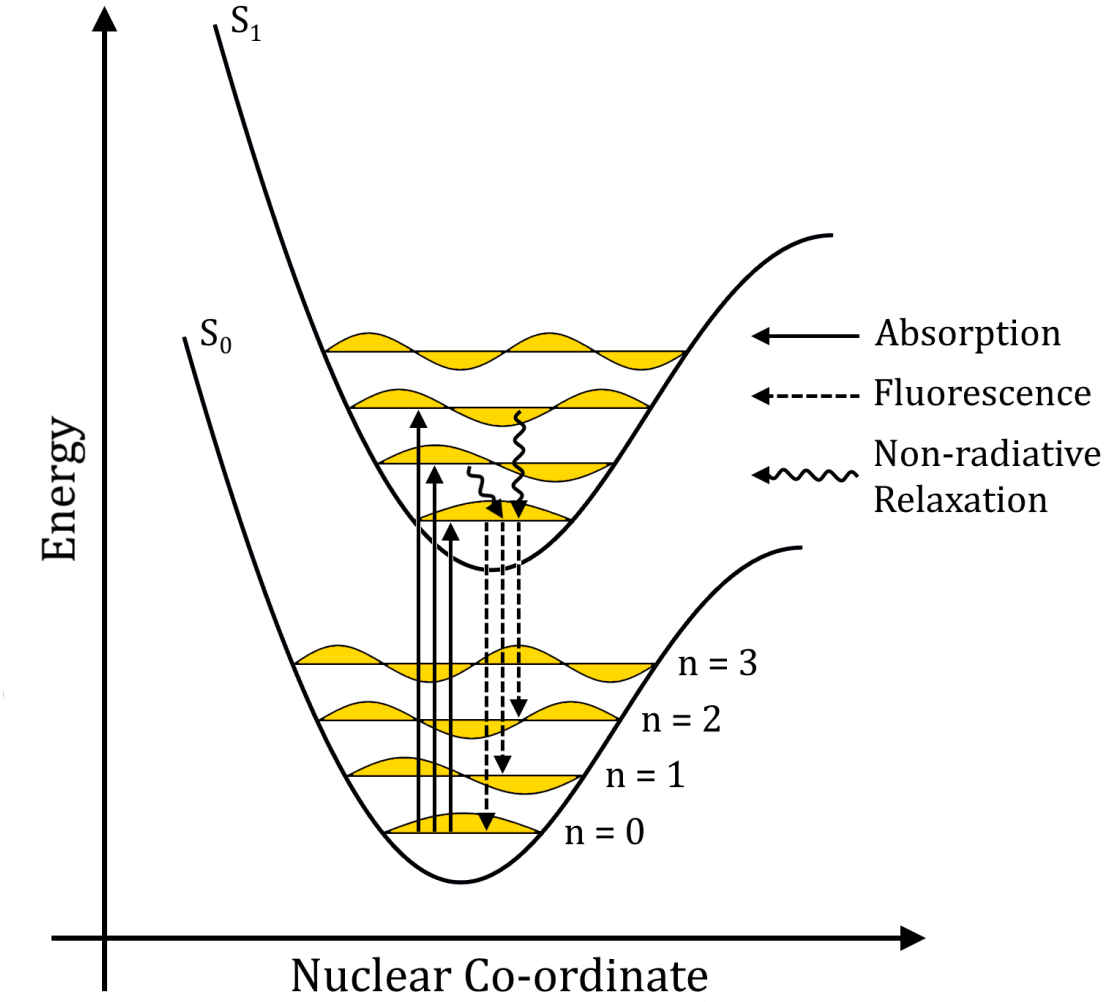

Figure 2.14: Franck-Condon energy level diagram showing the ground state, S_0, and first excited state, S_1, and vibrational energy levels within each state. Electron transitions are highlighted for absorption, fluorescence, and non-radiative relaxation. The offset of the energy states is due to electron transition rules.

Unlike inorganic semiconductors, organic semiconductors generally have low dielectric constants (ε_r), typically 3-4 [30,41]. This means that the electron and hole generated in photoexcitation are Coulombically bound in an electrically neutral quasiparticle known as an exciton. These excitons have a lifetime on the order of 1 ns, after which the electron and hole will recombine (known as geminate recombination as the charge carriers originate from the same initial state). This occurs through the emission a photon with energy equal to or less than, the band

gap of the system, allowing the electron to relax back to one of the vibrational levels of the HOMO, in a process known as fluorescence.

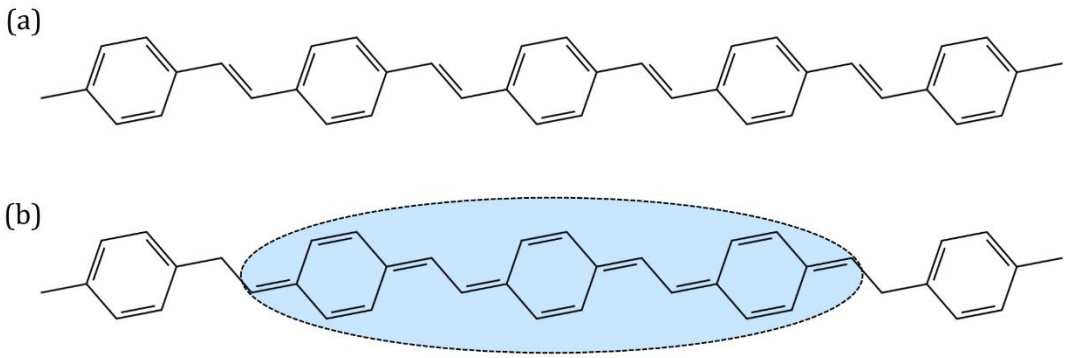

Figure 2.15: The chemical structure of poly(p-phenylene vinylene) in (a) the ground state, and (b) the photoexcited state. The presence of an exciton is illustrated by the blue ellipse.

When an exciton is generated it causes distortions to the atomic lattice of the material, shifting the structure from aromatic to quinoidal in the region near the exciton, as shown in Figure 2.15. The electron and hole in the exciton are therefore quasiparticles known as polarons, a combination of charge carrier and deformation. As mentioned in the previous section, the HOMO and LUMO energies of a material are affected by their environment, therefore the generation of an exciton polaron results in changes to the energy levels of the system [42]. An electron in the LUMO is an electron polaron and causes a decrease in the energy of the orbital due to the relaxation of surrounding bonds. Similarly, a hole in the HOMO is a hole polaron and causes an increase in the energy of the orbital due to changes in the surrounding bonds [43].

Exciton Diffusion

Photogenerated excitons in organic semiconductors are typically Frenkel excitons, characterised by a relatively high degree of localisation (from polaronic interactions with the atomic lattice), low exciton radius, and high binding energies (E_B). In contrast, excitons in inorganic semiconductors generally display Wannier-Mott exciton characteristics, i.e. delocalised, high exciton radius, and low binding energies, owing to the high dielectric constants (silicon has ε_r = 12.3 [44]). The low dielectric constant typical of many organic systems means that photogenerated

excitons have E_B of ~0.3 eV [10,45], which is greater than thermal energy at ambient temperatures ($k_BT \sim 0.026$ eV). Therefore, the exciton will not dissociate spontaneously, as occurs in inorganic semiconductors. As is discussed in the next section, this high binding energy has consequences for the operation of an organic photovoltaic device as charge separation can only occur at an interface between two materials with an energy offset greater than E_B. In organic photovoltaic devices this interface is typically formed between a donor polymer and a fullerene acceptor.

Excitons travel through organic semiconductors by a process called diffusion where a random 'hopping' process occurs from site to site. This 'hopping' can occur either within a molecule or polymer chain (intramolecular hopping), or between different molecules or polymer chains (intermolecular hopping). The average distance over which exciton can diffuse (L_D) before recombining is given by [46]:

$$L_D = \sqrt{D\tau} \tag{2.6}$$

Here, D is the diffusion coefficient and τ is the photoluminescence decay lifetime. In conjugated polymer systems the exciton diffusion length is typically 5 – 10 nm [11]. There are two main mechanisms by which excitons diffuse: Förster resonant energy transfer (FRET) and Dexter electron transfer. FRET occurs when the emission spectrum of the donor and the absorption spectrum of the acceptor overlap, enabling the energy of the exciton in the donor to be transferred to the acceptor via a dipole-dipole electromagnetic interaction. Here, the electron in the donor relaxes back to the ground state and the energy is used to promote the electron in the acceptor. This energy transfer process occurs over donor-acceptor separations (r) of 1 – 5 nm, with efficiency decreasing as r^{-6}. In Dexter electron transfer the donor and acceptor exchange electrons, moving the excited state to the acceptor. This occurs over shorter separations than FRET, typically less than 1 nm, with the probability decreasing exponentially with r [11]. Both FRET and Dexter electron transfer are illustrated in Figure 2.16.

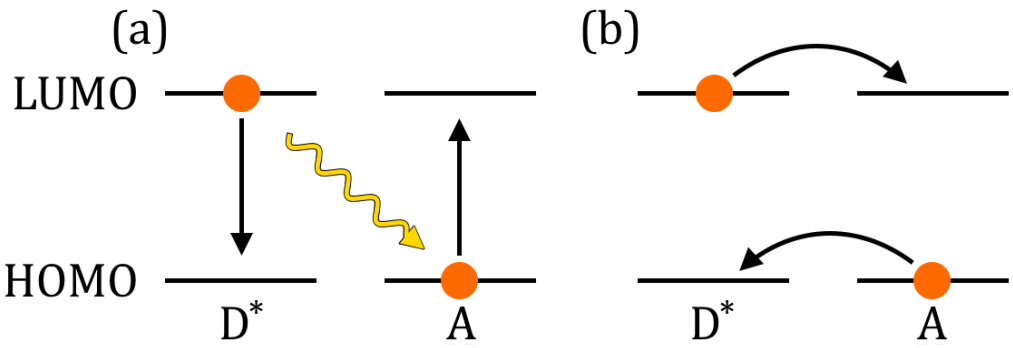

Figure 2.16: Schematic diagrams of (a) Förster resonant energy transfer, and (b) Dexter electron transfer.

Exciton Dissociation

In a photovoltaic device, a key initial step in the creation of a charge-separated state is exciton dissociation. In OPVs this occurs at an interface formed from dissimilar materials and will only occur providing it is energetically favourable. This requires that the LUMO energy of the acceptor is lower relative to LUMO energy of the donor, allowing the electron to transfer from the donor to the acceptor. Similarly, for hole transfer the HOMO energy of the donor must be higher relative to the HOMO energy of the acceptor. This is shown in Figure 2.6 for for the donor polymer PCDTBT and the acceptor fullerene $PC_{70}BM$. Whilst the two charge carriers now reside in separate materials (the electron in the acceptor and the hole in the donor), they remain bound by mutual Coulombic attraction, as shown in Figure 2.17(c). At this point they are said to reside in a charge-transfer (CT) state. The next step in dissociation requires breaking the CT state, which can be described by Onsager's theory, whereby the thermal energy of the electron and hole must surpass their Coulombic attraction to be considered separated. The separation distance at which this condition arises, r_c, is given by [40]:

$$r_c = \frac{e^2}{4\pi\varepsilon_r\varepsilon_0 k_B T} \tag{2.7}$$

Here, e is the elementary charge, ε_r is the dielectric constant of the materials, ε_0 is permittivity of vacuum, k_B is the Boltzmann constant and T is the temperature of the system. For organic semiconductors r_c is approximately 15 – 20 nm in ambient

conditions. However, dissociation of the CT state can also be assisted by an external electric field, and will effectively reduce the required separation [47].

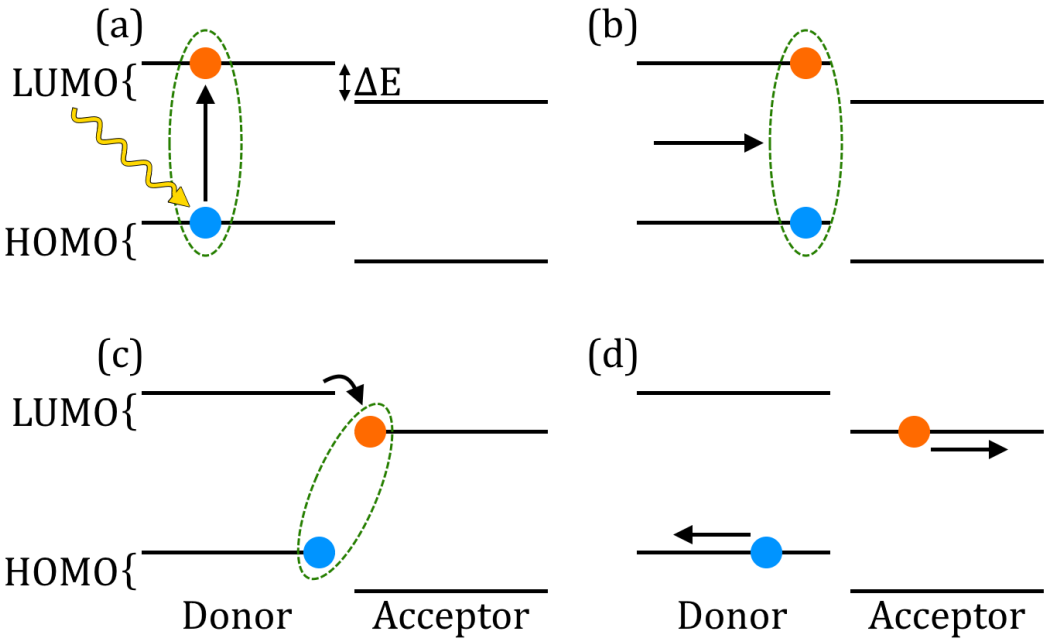

Figure 2.17: Schematic diagram of photocurrent generation in an OPV, illustrating (a) exciton formation, (b) exciton diffusion, (c) the charge-transfer state, and (d) free charge transport.

If the conditions required for the dissociation of the exciton are not met, there are several recombination mechanisms that can occur, as shown in Figure 2.18 [48]. Firstly, if the distance to the interface between the donor and acceptor is greater than the exciton diffusion length, then the exciton will undergo excited state geminate recombination (Figure 2.18(a)). Secondly, if there is insufficient thermal energy, or the external electric field is too weak, then the CT state will not be broken, and the electron and hole will geminately recombine (Figure 2.18(b)). Finally, if the HOMO of the acceptor is too high or the LUMO of the donor too low, then exciton transfer may occur instead of charge transfer, followed by recombination in the acceptor (Figure 2.18(c)). Additionally, after the charges have been separated, non-geminate recombination (in which electrons and holes from different initial states recombine) may occur as a result of electronic traps. This process is known as Shockley-Read-Hall recombination (Figure 2.18(d)).

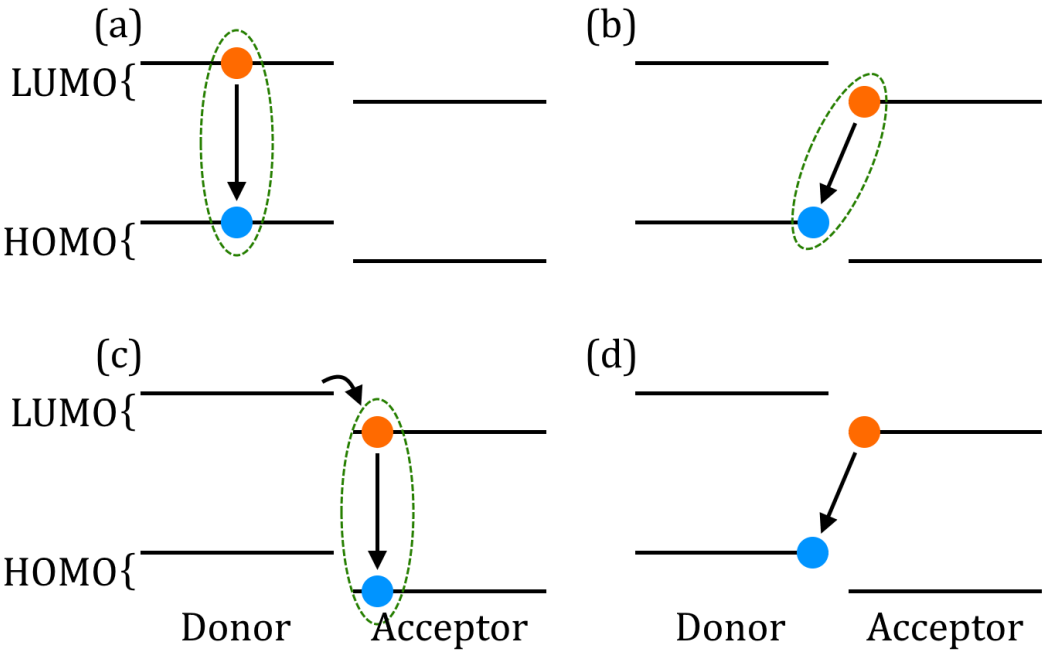

Figure 2.18: Schematic diagrams of (a) excited state geminate recombination, (b) CT state geminate recombination, (c) recombination after energy transfer, and (d) non-geminate recombination.

It should be noted that whilst charge transfer requires an energy offset between the donor and acceptor, the rate of transfer does not increase continually with the magnitude of the offset. Indeed, with an offset much greater than E_B, energy is lost in the process, leading a reduction in photovoltaic device efficiency.

Charge Transport

In order to extract the newly dissociated charge carriers, they must be transported through the donor and acceptor materials to the electrodes. Charge carriers are localised to single molecules due the energetic and spatial disorder of the system, as well as weak intermolecular coupling. The process of charge transport can therefore be described as phonon-assisted 'hopping', rather than the band transport that occurs in inorganic semiconductors. A Gaussian disorder model, in which charge transport is assumed to occur within a Gaussian distribution of disordered states, provides the simplest description of charge transport. The distribution of energetic states, $g(E)$, is given by [49]:

$$g(E) = \frac{1}{\sqrt{2\pi\sigma}} \exp\left(-\frac{E^2}{2\sigma^2}\right) \tag{2.8}$$

Here, σ is the disorder parameter, which represents the width of the density of states (DOS), and E is the energy of the site. This distribution of energy states allows transport to occur without the presence of an electric field via diffusion to lower energy states. However, the direction in which this occurs will be random, limiting the usefulness of this process. At elevated temperatures, T, diffusion to higher energy states is activated, and the hopping rate, ν_{ij}, between sites i and j for both conditions is given by the Miller-Abrahams equation [50]:

$$\nu_{ij} = \nu_0 \exp(-2\gamma \Delta r_{ij}) \begin{cases} \exp\left(-\frac{E_j - E_i}{k_B T}\right) & E_i < E_j \\ 1 & E_i \geq E_j \end{cases} \tag{2.9}$$

Here, ν_0 is the attempt-to-escape frequency, Δr_{ij} is distance between sites i and j, γ is coupling matrix element between sites, and E_i and E_j are the energies of sites i and j respectively. It is therefore only energetically favourable for the charge to hop from site i to site j when $E_i \geq E_j$ in the absence of temperature activation. In the case of Figure 2.6, it can be seen that holes should transfer from PCDTBT to PEDOT:PSS, and finally to ITO, due to the relative position of the energy levels. Here, it should be noted that Ca is implemented as a hole blocking layer, made thin enough to allow electrons to pass through to the cathode. Consequently, if a charge carrier hops to site with significantly lower energy than those surrounding it, it may become trapped and eventually recombine.

The presence of an electric field, F, also affects the charge transport by tilting the DOS, reducing the energy required for charge transport [51]. Whilst under the influence of an electric field, charge carrier mobility, μ, is typically used to describe the charge transport. The electric field and temperature dependant mobility, as determined by Monte-Carlo simulations, is given by [49,52]:

$$\mu(T,F) = \mu_0 \exp\left[-\left(\frac{2\sigma}{3k_B T}\right)^2\right] \begin{cases} \exp\left[C(\sigma^2 - \Sigma^2)E^{1/2}\right] & \Sigma \geq 1.5 \\ \exp\left[C(\sigma^2 - 2.25)E^{1/2}\right] & \Sigma < 1.5 \end{cases} \tag{2.10}$$

Here, μ_0 is the zero-field mobility at infinite temperature, Σ is the spatial disorder of the system, and C is an empirical constant related to intermolecular distance.

Note that charge carrier mobility can be increased by reducing either the energetic (σ) or spatial (Σ) disorder of the system. Organic semiconductors typically demonstrate mobilities on the order of 10^{-3} cm^2/Vs [51], several orders of magnitude lower than inorganic semiconductors.

Finally, it is important to note that charge carriers can still recombine whilst being transported to the electrodes for extraction. Whilst under an electric field, the average distance that the charge can travel before this occurs, L_{drift}, is given by [53]:

$$L_{drift} = \mu\tau F \tag{2.11}$$

Here, τ is the average time before a carrier recombines and F is the applied electric field. As organic semiconductors exhibit low carrier mobilities, L_{drift} is a relatively short distance, limiting the thickness of the light-harvesting layer of an organic photovoltaic device. Indeed, typically the optimised thickness of this layer is <100 nm, despite poor light absorption at these thicknesses.

Charge Extraction

Once the charge carrier reaches the interface with the electrode, appropriate energy level alignment is required to efficiently extract it. For ideal charge extraction, the work function of the anode, Φ_{anode}, should be equal to the HOMO energy of the donor, and the work function of the cathode, $\Phi_{cathode}$, should be equal to the LUMO energy of the acceptor. This results in ohmic contact between the two materials, where free flow of charges across the interface occurs. Here, the Fermi levels of the two materials align through the transfer of electrons from the material with the higher Fermi level to that with the lower Fermi level. If these energy levels are not well aligned, which could result from poor active layer morphology or electrode material choice, then the materials are in non-ohmic contact. Here, the resistance is high, leading to reduced extraction efficiency and a build-up of charges at the interface, increasing non-geminate recombination rates. The morphology of a BHJ active layer can also impact the extraction efficiency, as an abundance of acceptor material at the anode interface, or donor material at the cathode interface, may increase recombination rates near the interface, reducing charge extraction [54].

The difference in work functions of the electrodes creates a built-in potential, V_{BI}, which dictates the direction of charge transport within the device. In an OPV device with non-ohmic contact, the open-circuit voltage, V_{oc}, (the maximum voltage output of a solar cell) is equal to the V_{BI} [55]. However, in a device with ohmic contact, the V_{oc} is determined by the energy levels of the donor and acceptor materials, rather than the V_{BI}, and can be estimated using the following equation [56]:

$$V_{oc} = \frac{1}{e}\left(E_{HOMO}^{Donor} - E_{LUMO}^{Acceptor}\right) - 0.3\ \text{V} \tag{2.12}$$

Here, e is the elementary charge, and the -0.3 V is an empirically determined constant to account for the difference between the V_{oc} and the V_{BI}. However, there are other factors that affect the V_{oc} of an OPV. It has been observed that the formation of CT states [57], charge carrier recombination rates [58], and illumination intensity [59,60] can all influence the V_{oc}, causing further deviations from the V_{BI}.

As mentioned in Section 2.3.1, it has become common practise in OPV devices to utilise hole and electron transport layers. These layers have intermediate work functions between the active layer and electrode materials, thus reducing energy barriers to charge extraction. Furthermore, they can act as charge blocking layers, improving device performance by preventing current leakage [61].

The efficiency of each of the mechanisms described, exciton formation, exciton diffusion, exciton dissociation, and charge transport and extraction, contributes to the external quantum efficiency, η_{EQE}, of an OPV device. This can be expressed as shown in Equation 2.13 [62,63]:

$$\eta_{EQE} = \eta_A \eta_{ED} \eta_{CT} \eta_{CC} \tag{2.13}$$

Here η_A is the absorption efficiency of the active layer, representing exciton formation, η_{ED} is the exciton diffusion efficiency, η_{CT} is the charge transfer efficiency, representing the efficiency of exciton dissociation, and η_{CC} is the charge collection efficiency, representing the efficiency of charge transport and extraction from the device. By looking at Equation 2.31, it is apparent that to achieve a high

performance OPV device each of these processes must be made as efficient as possible.

Space Charge Limited Current

Space charge occurs when there is a build-up of charge carriers within a material, resulting in a spatially distributed continuum of electrical charge. In semiconductors this can occur when there is ohmic contact with an electrode injecting one type of charge carriers. With no space charge, carriers will diffuse from the electrode into the electrically neutral semiconductor, resulting in a charge density dependent current. However, when there is space charge, the current is no longer charge density dependant as the semiconductor is no longer electrically neutral. Instead, the current flow is dependent on the charge mobility of the material and the applied electric field. This is known as the space charge limited current (SCLC) regime, and can be used to determine the charge carrier mobility of a semiconductor [64].

Here, the semiconductor is sandwiched between electrodes both having work functions matching either its HOMO or LUMO so that only one species of charge carrier can be injected or extracted. The SCLC can then be observed from a dark current-voltage measurement, as shown in Figure 2.19.

The dark current-voltage curve consists of three regions of differing current dependence on applied bias. The first region is the ohmic regime occurring at low bias, where the current is created by charges that are free to move throughout the device. The second region, occurring at higher bias, is the trap-filling regime. Here, the rapid increase in current results from the filling of trap states, consequently increasing the Fermi level until it resides above the trap energy [65]. Charge carriers in trap sites are immobile, and serve to reduce the electric field within the device through 'screening' of the applied field. Once the Fermi level reaches this energy, most of the traps are filled and the device enters the SCLC region.

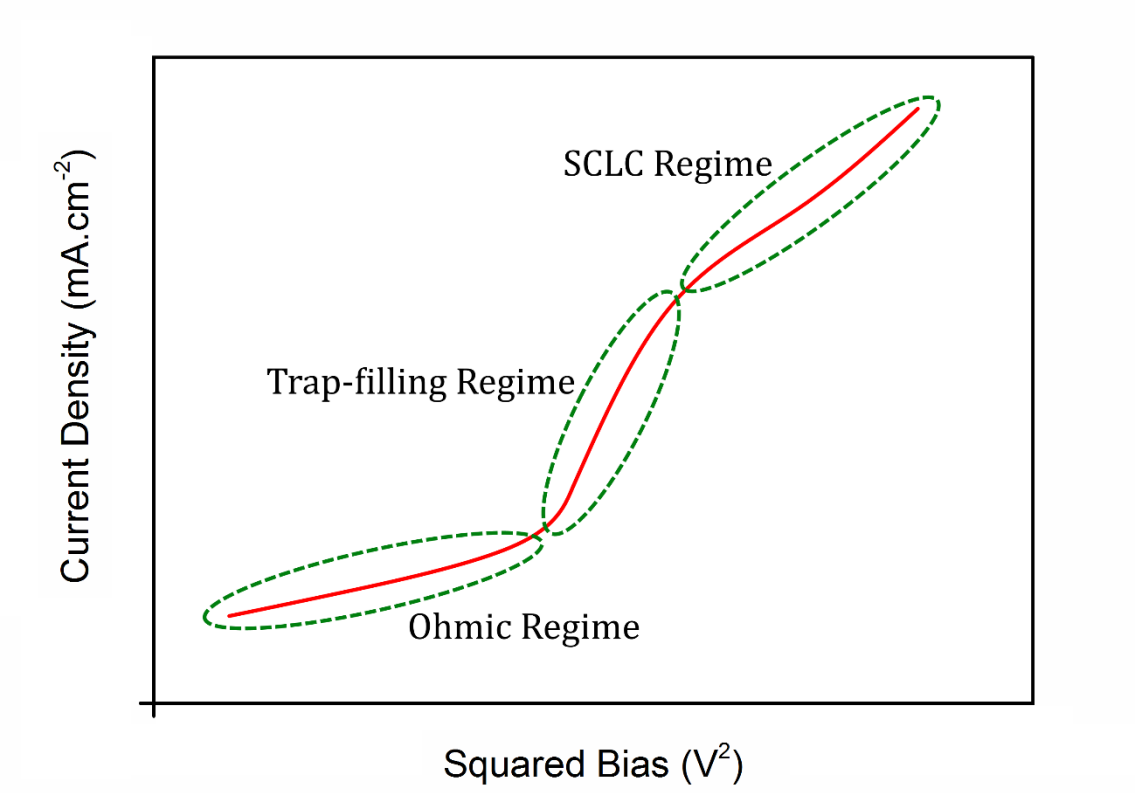

Figure 2.19: An example SCLC current density-voltage measurement with the current dependence regimes highlighted. The axes of the plot are logarithmic.

In the SCLC region the current density, *J*, can be calculated using the Mott-Gurney law [66]:

$$J = \frac{9}{8}\varepsilon_r \varepsilon_0 \mu \frac{E^2}{L} \qquad (2.14)$$

Here, ε_r is the dielectric constant of the organic semiconductor, ε_0 is the permittivity of free space, *E* is the electric field across the device, *L* is the thickness of the organic semiconductor layer, and μ is the steady state charge carrier mobility. Equation 2.14 enables the mobility of a charge carrier to be easily determined from the gradient of the SCLC regime, as ε_r, ε_0, and *L* are known constants.

2.3.6: Organic Photovoltaic Device Degradation

There have been a number of long term stability experiments on organic photovoltaic devices, primarily conducted on devices using P3HT:PCBM as the active layer. A useful measure of the lifetime of a solar cell is T_{80} lifetime, the time

taken for the PCE of a device to reach 80% of the initial PCE. This is not given in all studies, but will be mentioned if it is reported.

In 2006, De Bettignies et al. [67], subjected unencapsulated standard architecture P3HT devices with Ca/Ag and LiF/Al cathodes to 200 hours of continuous illumination. The devices with Ca/Ag were found to be more stable than those with LiF/Al, with PCE decreasing by 40% over 200 hours and 90% over 100 hours respectively.

Hayakawa et al. [68] examined the effect of an additional TiO_x hole blocking layer between the Al cathode and the P3HT:PCBM active layer of standard architecture OPV devices on the stability of the short circuit current over 100 hours of continuous illumination. Solar cells without the hole blocking layer degraded completely over this period, whereas the short circuit current of devices with the TiO_x layer decreased by only 6%. This difference in stability was attributed to the TiO_x blocking the invasion of oxygen into the active layer, preventing detrimental photo-oxidation reactions.

To determine the influence of oxygen and moisture on inverted architecture P3HT:PCBM OPV devices, Norrman et al. [69] subjected encapsulated and unencapsulated devices to continuous illumination in an oxygen free, humid atmosphere and in dry air. For the oxygen free atmosphere, the devices were illuminated for 470 hours, during which time the unencapsulated devices completely degraded. The PCE of the encapsulated devices, however, decreased by only 30%. In dry air, the devices were only illuminated for 70 hours, however, within this time the unencapsulated devices completely degraded and the PCE of encapsulated devices decreased to 20%. In both cases, the major loss mechanism was ascribed to reactions with oxygen or water resulting in phase separation of the HTL and active layer interface.

Zimmermann et al. [70] investigated the effects of two different ETLs, as well as active layer thickness, on the stability of inverted P3HT:PCBM devices. Encapsulated devices using either a Cr or Ti ETL, and either 80 or 170 nm thick active layers, were illuminated for 1,500 hours. Cr was found to be the most stable ETL for both 80 and 170 nm thick active layers, with PCE degrading by 10% and

20% respectively. The thinner active layer was also found to be more stable for the Ti ETL, with PCE decreasing by 30%, whilst devices with the thicker active layer degraded by 40%.

Peters et al. [21] used a custom built system to monitor the performance of P3HT:PCBM and PCDTBT:$PC_{70}BM$ OPV devices over 4,400 hours of continuous illumination. The devices were encapsulated using a glass slide with a recess containing a desiccant, sealed at the edges. During the illumination, the PCE of both types of device degraded by ~25%. However, the rate of degradation differs between the two devices resulting in different T_{80} lifetimes. For the P3HT devices, a T_{80} lifetime of 3.1 years was achieved, whereas the PCDTBT devices gave twice the T_{80} lifetime of 6.2 years. Both of these values were estimated assuming 5.5 hours of sunlight per day, 365 days per year.

Further stability measurements on PCDTBT:$PC_{70}BM$ solar cells were performed by Bovill et al. [71]. Here, poly(3,4-ethylenedioxythiophene) polystyrene sulfonate (PEDOT:PSS), molybdenum oxide (MoO_x), and vanadium oxide (V_2O_5) HTLs were used to determine the role of the HTL on the stability of standard architecture OPV devices over a 620 hour period of continuous illumination. It was found that PEDOT:PSS provided the greatest stability, with PCE decreasing by ~25% over the period, resulting in a T_{80} lifetime of 14,500 hours. Losses for this layer were ascribed to the anode being damaged by the acidic PEDOT:PSS. V_2O_5 proved to be the least stable, with PCE decreasing by ~80% over the period, exhibiting a T_{80} lifetime of only 350 hours. This was speculated to be due to precursor solvent for the V_2O_5 being trapped within the device and damaging the active layer. MoO_x provided slightly greater stability than the V_2O_5, but was worse than PEDOT:PSS, with PCE decreasing by 60%, giving a T_{80} lifetime of 1,000 hours. The losses were ascribed to the breakdown of the MoO_x resulting in the formation of charge trapping states.

There have been long term studies on the lifetime of flexible OPV devices based on P3HT. Hauch et al. [72] placed P3HT:PCBM OPV modules outside for 14 months, with maximum power output measured every 60 seconds. Over the first few months the maximum power output increased by 40%, and after approximately 8

months the power output decayed linearly down to 80% of the starting power. Interestingly, despite the overall loss in power output the PCE of the modules increased by ~3%, due to a 10% increase in the FF. The decrease in power output is explained by the 7% decrease of the V_{oc} changing the maximum power point.

This was taken further by Gevorgyan et al. [73], who distributed flexible inverted architecture P3HT:PCBM OPV modules to various geographic locations to measure the stability in real world conditions. The modules were split into three groups based upon the stability they exhibited. Group 1 and 2 modules were tested for 3,500 hours, with group 1 being the least stable, giving T_{80} lifetimes less than 500 hours. The modules in group 2 fared better, exhibiting T_{80} lifetimes between 500 and 1,000 hours. The most stable devices were in group 3. These modules were tested for 10,000 hours, with only a 10% reduction in PCE over this period, resulting in a T_{80} lifetime greater than 8,000 hours. The losses observed in all of the modules were ascribed to deterioration of the encapsulation due to the metal contact, allowing the ingress of oxygen and water into the device.

Shelf-life studies have also been conducted on P3HT. Here, devices are tested over an extended period, but are not illuminated between measurements. Lloyd et al. [74] performed a comparison of the shelf-life of several different device structures, both for standard and inverted architectures, stored in ambient conditions for 960 hours. All standard architecture devices were observed to degrade over this time. Both device structures using a Ag cathode degraded completely in this time, whilst those using Ca/Al with no HTL proved the most stable, with 60% loss of PCE. Interestingly the PCE of devices using the inverted architecture actually increased during the study, reaching 140% of the initial PCE in devices utilising a BHJ. The effect of a ZnO ETL on the shelf-life of standard architecture P3HT devices in air was investigated by Ferreira et al. [75]. Without the ZnO layer, devices completely degraded within 24 hours, due to reactions between the Al cathode and the active layer compromising the interface. With ZnO nanoparticles (NP) between the two layers, the stability was significantly improved by reducing these reactions, resulting in 90% decrease over 1,870 hours. This was further improved through the addition of a ZnO NP layer deposited via the sol-gel method, resulting in only 40% losses over 1,870 hours of storage. This is ascribed to improved adhesion of

the ETL to the active layer. Kang et al. [76] investigated the effect of the deposition method for a ZnO ETL on the stability of inverted architecture devices. Spin coating, spray coating, and sputtering were used to deposit the layer, and the devices were stored for 720 hours in air. The PCE for all of the devices degraded by 20%, indicating that these deposition methods had no impact on the air-stability of devices.

In Chapter 4 the operational stability of OPV devices with varying impurity concentrations is compared. It is therefore important to understand the possible degradation pathways that can occur in an OPV device. There are four main mechanisms: photobleaching, trap formation, phase separation, and delamination, which are covered in greater detail in the following sections. The degradation of OPV devices is not necessarily influenced by all of these mechanisms simultaneously, and each will affect the device to differing degrees.

Author	Architecture	Test Type	Encapsulation	Study	Study Length (hours)	PCE Loss/T_{80} lifetime
De Bettignies [63]	Standard	Operational	Not mentioned	Cathode – Ca/Ag	200	40%
				Cathode – LiF/Al	100	90%
Hayakawa [64]	Standard	Operational	Not mentioned	ETL – None (control)	100	I_{sc} – 100%
				ETL – TiO_x		I_{sc} – 6%
Norrman [65]	Inverted	Operational	Yes	Atmosphere – RH 65%, No O_2	470	30%
				Atmosphere – dry air	70	20%
			No	Atmosphere – RH 65%, No O_2	470	100%
				Atmosphere – dry air	70	100%
Zimmermann [66]	Inverted	Operational	Glass + UV epoxy	ETL – Cr, thin active layer	1,500	10%
				ETL – Cr, thick active layer		20%
				ETL – Ti, thin active layer		30%
				ETL – Ti, thick active layer		40%
Peters [20]	Standard	Operational	Glass + desiccant + UV epoxy edge seal	Polymer – P3HT	4,400	T_{80} = 3.1 yr
				Polymer – PCDTBT		T_{80} = 6.2 yr
Bovill [67]	Standard	Operational	Glass + UV epoxy	HTL – PEDOT:PSS	620	T_{80} = 14,500 hr
				HTL – MoO_x		T_{80} = 1,000 hr
				HTL – V_2O_5		T_{80} = 350 hr
Hauch [68]	Standard	Operational	Yes – Flexible	Outdoors	9,912	-3%
Gevorgyan [69]	Inverted	Operational – Outdoors	Yes – Flexible	Group 1	3,500	T_{80} < 500 hr
				Group 2		T_{80} < 1,000 hr
				Group 3	10,000	T_{80} > 8,000 hr

Table 2.3: Summary of organic photovoltaic device operational lifetime studies covered in Section 2.3.6.

Author	Architecture	Test Type	Encapsulation	Study	Study Length (hours)	PCE Loss/T_{80} lifetime
Lloyd [70]	Standard	Shelf-life	No	ITO/BHJ/Ca/Al	960	60%
				ITO/PEDOT:PSS/BHJ/Ca/Al		80%
				ITO/BHJ/Ag		100%
				ITO/PEDOT:PSS/BHJ/Ag		100%
	Inverted			ITO/ZnO/BHJ/Ag		-40%
				ITO/ZnO/P3HT/Ag		-15%
Ferreira [71]	Standard	Shelf-life	No	No ETL (control)	24	100%
				ETL – ZnO NP	1,870	90%
				ETL – ZnO NP/ZnO sol-gel		40%
Kang [72]	Inverted	Shelf-life	No	Spin cast ETL	720	30%
				Spray cast ETL		30%
				Sputtered ETL		30%

Table 2.4: Summary of organic photovoltaic device shelf-life studies covered in Section 2.3.6.

Photobleaching

Photobleaching of polymers occurs when a polymer undergoes a photochemical reaction that reduces its ability to absorb light. This reaction is typically photo-oxidative, causing chain scission of the polymer backbone, resulting in the breaking of conjugation of the polymer. As this is a photochemical reaction, it will occur whenever the device is in operation, making it important to limit the exposure of the active layer to oxygen [77].

Trap Formation

The formation of traps in a device leads to the degradation of device performance. Deep traps can form as a result of photochemical reactions or the diffusion of metal ions from the electrodes. Charges that enter deep traps are unlikely to escape and will recombine through non-geminate recombination. This leads to a loss of charge carriers and will reduce the FF, J_{sc}, and V_{oc} of a device. Additionally, shallow traps can form through photochemical reactions or molecular reorganisation increasing energetic disorder within the system. Charges situated within shallow traps create space-charge build-up at the interfaces, resulting in band bending and reduced charge extraction efficiency [78].

Phase Separation

If the temperature of an OPV device exceeds the glass transition temperature of the active materials then phase separation will occur. During this process larger donor and acceptor regions form, potentially resulting in the distance to an interface exceeding the exciton diffusion length. This leads to a reduction in the internal quantum efficiency of a device due to losing photogenerated excitons through excited state geminate recombination [79].

Delamination

Delamination is the breaking of contact between layers of a device, and is caused by thermo-mechanical stresses [80]. This can result in an energetic barrier against charge extraction, usually leading to complete loss of performance in the regions affected.

Decay Behaviour

Most OPV device decay curves, which measure PCE as a function of time, have the same general behaviour, as shown in Figure 2.20. There is an initial decay period, known as the 'burn-in' period, in which device performance undergoes rapid, exponential decay. The magnitude and duration of this period varies with material systems and device architectures. After the burn-in period the degradation stabilises, becoming linear and usually lasting for significantly longer than the burn-in period.

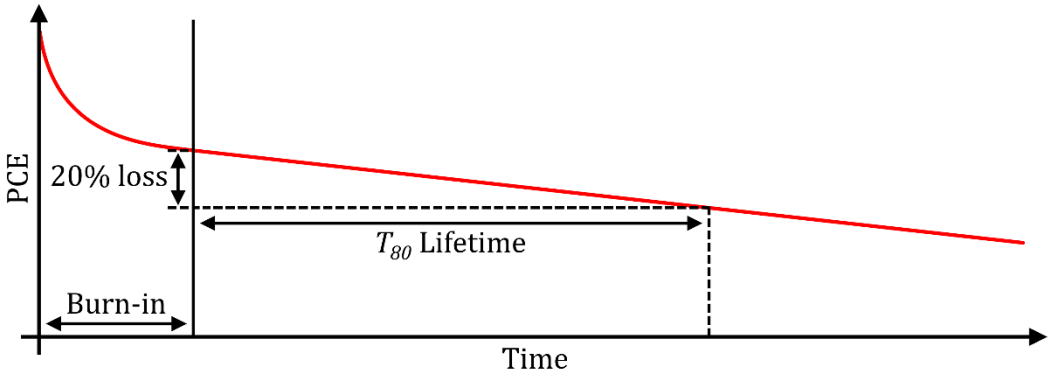

Figure 2.20: Typical decay profile for the PCE of an OPV device. An initial rapid decay, known as the burn-in, occurs followed by linear degradation.

The lifetime of a device is determined after the end of the burn-in period and is defined by the T_{80} lifetime. This is the time taken for the PCE of the device to reach 80% of its value immediately after the end of the burn-in period.

2.4: Perovskite Solar Cells

2.4.1: Introduction

A perovskite is a material with the structure ABX_3, first discovered in 1839 by Gustav Rose, and named after the Russian mineralogist, L.A. Perovski [81]. Perovskite solar cells (PSCs) use these materials to convert solar radiation into electricity, and are the most rapidly improving photovoltaic device, having reached PCEs in excess of 20% in the 4 years since birth of the field [5,82] (see Figure 2.1). This is due to the remarkable properties exhibited by perovskites, such as

ambipolar charge transport [83], tunable band gap [84], and being processed from scalable processes [85–87].

History of Perovskite Solar Cells

The first use of a perovskite material in a solar cell was reported in 2006 by Miyasaka et al., using the perovskite $CH_3NH_3PbBr_3$, as a visible light sensitiser in a dye-sensitised solar cell (DSSC), achieving a PCE of 2.2% [88]. DSSCs typically use a TiO_2 scaffold coated in a light absorbing dye, known as the sensitiser, to produce photocurrent. The same group improved this to 3.8% in 2009 by replacing the Br in the perovskite with iodine [89]. By using the $CH_3NH_3PbI_3$ in the form of quantum dots as the sensitiser, Im et al. were able to push the PCE to 6.5% in 2011 [90]. However, DSSCs use electrolytes as a hole transport layer (HTL), and perovskites were typically found to be soluble in these electrolytes, resulting in rapid degradation of the devices. This problem was solved by Kim et al. in 2012, a major turning point for the material, by replacing the electrolytic HTL with spiro-OMeTAD (2,2',7,7'-tetrakis(N,N-di-p-methoxyphenylamine)-9,9'-spirobifluorene), a solid state material used for hole injection in organic LEDs, not only improving the stability, but also boosting the PCE to 9.7% [91].

In the same year, another major turning point for perovskites, and the birth of the PSC field, was reported by Lee et al. [92]. Here, several key developments were reported. Firstly, the use of the mixed halide perovskite $CH_3NH_3PbI_{3-x}Cl_x$, which was found to have better stability and charge transport properties than $CH_3NH_3PbI_3$. Secondly, the nanocrystal perovskite used up to this point was replaced with a 50 – 100 nm thin film over the scaffold. Thirdly, by replacing the TiO_2 scaffold typically used with insulating Al_2O_3, the V_{oc} was improved resulting in a PCE of 10.9%, showing that the perovskite could transport both electrons and holes. Finally, this was further exemplified by the fabrication of a planar device without any scaffold, exhibiting 1.8% PCE.

Current State of Research

Since the work of Lee et al. in 2012 PSCs have seen a remarkably rapid rise in device performance, with the champion certified PCE currently at 22.1% (see Figure 2.1) [93]. The most studied perovskite is methylammonium lead triiodide,

$CH_3NH_3PbI_3$ [5,94], with other important perovskites including the mixed halide variations, $CH_3NH_3PbI_{3-x}Cl_x$ and $CH_3NH_3PbI_{3-x}Br_x$, both having improved environmental stability over $CH_3NH_3PbI_3$, and achieving 18.9% and 12.3% PCE respectively [84,92,95]. Replacements for the methyammonium (CH_3NH_3), termed MA have been investigated, with formamidinium ($HC(NH_2)_2^+$), termed FA, and caesium being among the most common, achieving PCE of 14.2% and 6.8% for $FAPbI_3$ and $CsPbI_3$ respectively [96–100]. The reduced performance of $CsPbI_3$ is primarily a result of an increase in the band gap from 1.57 eV to 1.73 eV when MA is substituted by Cs [99,101]. Through partial substitution of I with Br, creating $CsPbBrI_2$, the PCE of Cs based perovskites has been improved to 6.5% through improved optical and structural stability [100]. Conversely to $CsPbI_3$, $FAPbI_3$ has a smaller bad gap than $MAPbI_3$, at 1.48 eV, suggesting greater potential for these materials than $MAPbI_3$. However, PCEs of only 14.2% have been achieved so far, suggesting further work is required for these materials to reach the performances of $MAPbI_3$ [96]. Mixtures of these cations have also been investigated, for example, $FA_{0.9}Cs_{0.1}PbI_3$ has been shown to achieve a PCE of 16.5%, an improvement over $FAPbI_3$ due to a reduction of trapping states within the active layer [98].

In an attempt to move away from lead, alternate anion materials are being examined, with work primarily focussed on tin. So far, performance of these materials, such as $MASnI_3$ and $FASnI_3$, has been relatively poor, achieving peak PCEs of ~6% in both cases [102–104]. This relatively poor performance is attributed to several factors: the formation of electrical shorts through the oxidation of Sn, poor film uniformity due to rapid crystallisation, and reactions with other layers damaging the perovskite, particularly in standard architecture devices [103].

As with OPVs, perovskite solar cells have been fabricated using a variety of scalable techniques, such as spray casting [85,86,105] and blade coating [87]. For both of these techniques performances comparable to those of spin cast devices were achieved. In the case of blade coating, improved ambient stability of the perovskite was also achieved due to the formation of a more densely packed perovskite layer, with larger domains, preventing the infiltration of degradation catalysts oxygen

and water into the perovskite. This highlights potential for perovskites to be fabricated via cheap and rapid roll-to-roll processes, similar to OPVs.

There is increasing interest in the stability of perovskites as the performance of such devices are now comparable to those of commercial silicon solar cells. This will be covered in more detail in Section 2.4.7, but a general overview will be given now. Typically, $CH_3NH_3PbI_3$ and its derivatives have been found to be unstable, with decomposition occurring in the presence of water and oxygen [106–108], making it necessary to either improve the stability of this perovskite, find a more stable perovskite, or improve device encapsulation to produce PSCs with long lifetimes. Recently, a perovskite with the composition $Cs_5(MA_{0.17}FA_{0.83})_{95}Pb(I_{0.83}Br_{0.17})_3$ has been found to achieve a lifetime of ~5,000 (~30 weeks) hours, making it the most stable perovskite to date [109].

Device Architecture

As PSCs originally started as DSSCs, the most common architecture for PSCs is with light incident through the electron extracting cathode. This is referred to as the standard architecture. If the light is incident through the hole extracting anode, it is known as the inverted architecture (note that this nomenclature is the opposite way round to that used for OPVs). Standard architecture devices can be split into two main structures: planar and mesoporous, whilst inverted architecture devices only use the planar structure. Planar devices employ a structure similar to OPVs, with the active layer perovskite sandwiched between a pair of electrodes. Electron and hole transport layers (ETLs and HTLs) are commonly included for the same reasons described in Section 2.3.1, and an energy level diagram of a typical inverted architecture $CH_3NH_3PbI_{3-x}Cl_x$ PSC is shown in Figure 2.21. Mesoporous devices utilise a mesoporous scaffold onto which the active layer is deposited, and can exist either in a 'sensitised' or 'meso-superstructured' form. In the 'sensitised' form, the scaffold acts as an ETL, transporting electrons generated in the perovskite to the cathode. In the 'meso-superstructured' form, the scaffold is purely structural, with electron transport occurring through the perovskite [83,110]. All of these architectures are illustrated schematically in Figure 2.22.

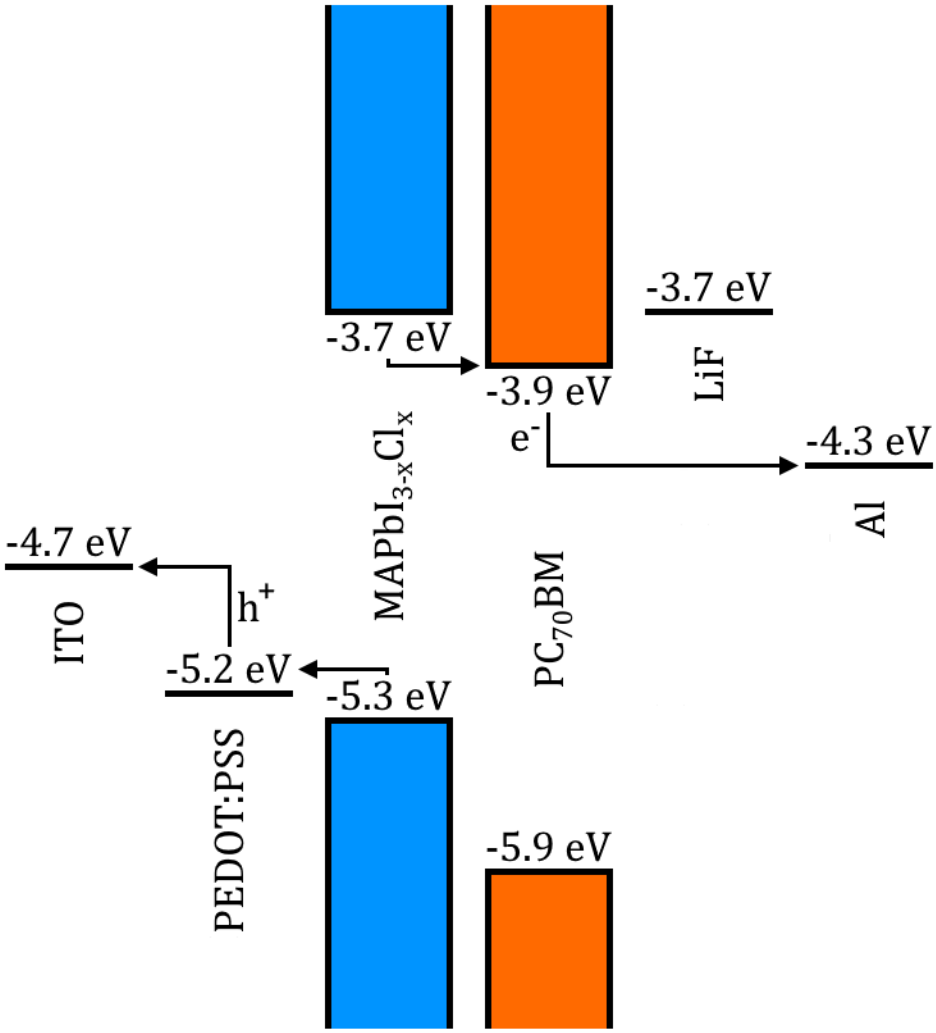

Figure 2.21: Energy level diagram of a typical inverted architecture $CH_3NH_3PbI_{3-x}Cl_x$ ($MAPbI_{3-x}Cl_x$) with an indium tin oxide (ITO) anode and aluminium (Al) cathode. A PEDOT:PSS hole transport layer and lithium fluoride (LiF) electron transport layer are also employed. The path of electrons and holes through the device is highlighted.

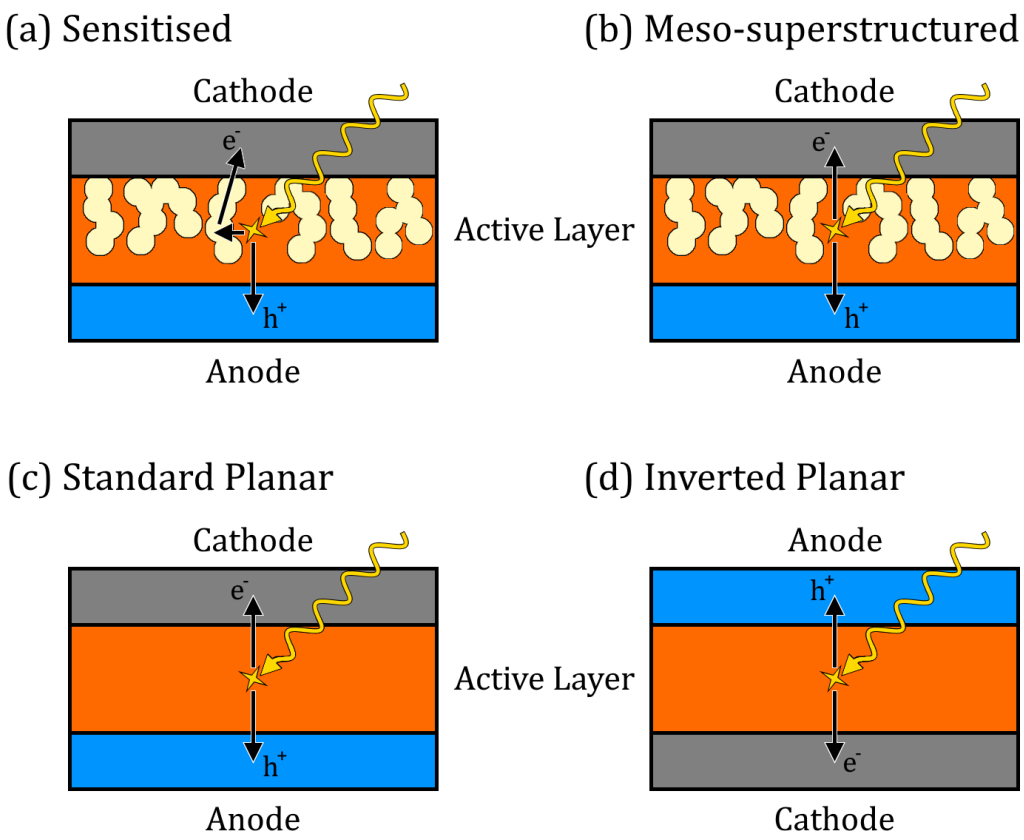

Figure 2.22: Schematic diagram of incident light, and electron and hole extraction for (a) sensitised and (b) meso-superstructured mesoporous architecture PSCs, and (c) standard and (d) inverted planar architecture PSCs.

2.4.2: Perovskite Crystal Structure

Within the ABX_3 structure of a perovskite, A and B are cations and X is an anion. Here, six X anions form an octahedron, with the B situated at the centre, and each X is a vertex of two octahedra, forming a 3D structure of connected octahedra. The A cation, which is larger than the B cation, resides in the space between the octahedra. This is shown in Figure 2.23(a). Due to this structure, the size of each ion is critical in the formation of a perovskite crystal, and will affect the optoelectronic properties of the material [81]. The perovskite crystal generally exists in one of three structures, cubic, tetragonal, or orthorhombic, dependant on the geometry of the unit cell. Figure 2.23(b) shows the unit cell of a perovskite crystal with side lengths *a*, *b*, and *c*. The cubic structure unit cell has sides of equal length, i.e. $a = b = c$. Tetragonal and orthorhombic structures are stretched along

one and two sides respectively, such that for a tetragonal unit cell $a = b \neq c$, and for an orthorhombic unit cell $a \neq b \neq c$.

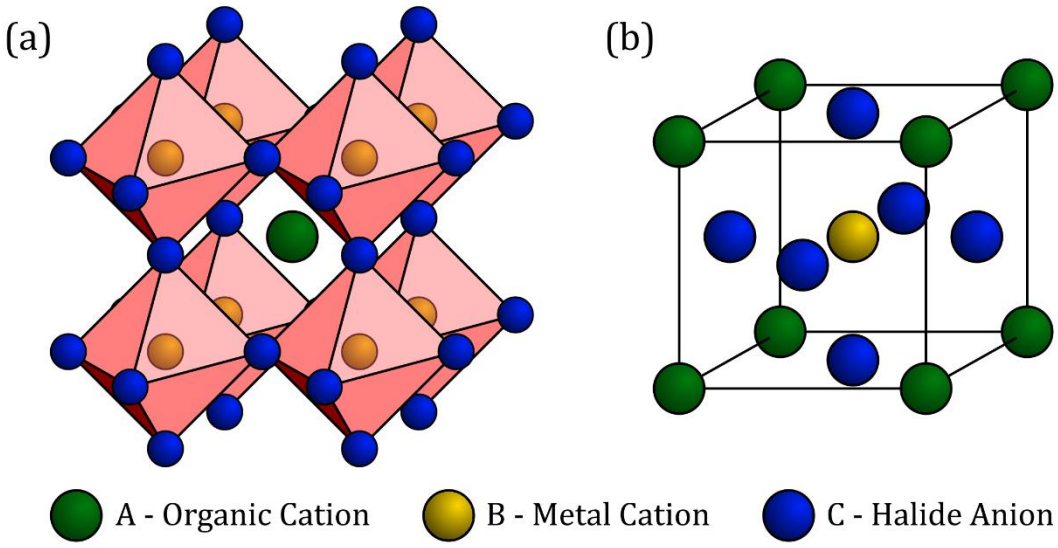

Figure 2.23: (a) Perovskite crystal structure, and (b) the unit cell for the perovskite crystal.

The stability of a perovskite crystal, as well as the probable structure it will form can be determined from a tolerance factor, *t*, given by [111]:

$$t = \frac{R_A + R_X}{\sqrt{2}(R_B + R_X)} \tag{2.15}$$

Here, R_A, R_B, and R_X are the ionic radii of ions A, B, and X respectively. In order to form a perovskite crystal, the tolerance factor must be $0.76 < t < 1.13$, for values outside of this range the formation of a perovskite crystal is energetically unfavourable. For $0.89 < t < 1.0$, the resultant perovskite will have a cubic crystal structure, with lower values of t resulting in tetragonal or orthorhombic structures [5].

In a typical organometal halide perovskite, A is an organic cation, B is a metal cation, and X is a halide anion. In the most commonly reported organometal halide perovskites methylammoium lead triiodide ($CH_3NH_3PbI_3$), termed $MAPbI_3$, and mixed-halide $CH_3NH_3PbI_{3-x}Cl_x$, the organic cation A is methylammonium ($CH_3NH_3^+$, MA^+), with R_A = 0.18 nm [112], the metal cation B is lead (Pb^{2+}), with R_B = 0.119 nm, and the halide anion X is iodine (I^-), with R_X = 0.22 nm, or chlorine (Cl^-), with R_X

= 0.181. By using Equation 2.15 with these ionic radii, $MAPbI_3$ perovskite gives t = 0.83 [5,113], indicating that it will not form a cubic structure. However, transitions between orthorhombic, tetragonal and cubic structures have been observed to occur on heating of the perovskite. For example, $MAPbI_3$ transitions from orthorhombic to tetragonal at ~160 K, and from tetragonal to cubic at ~330 K [90,114]. Note that this is below the expected operating temperature of a solar cell, ~350 K.

2.4.3: Band Formation in Crystals

As described in Section 2.3.2, when atoms are brought close enough together they form bonding and antibonding orbitals. However, when increasing numbers of atoms are brought together, the overlapping orbitals cannot exist with the same energy due to the Pauli Exclusion Principle. Therefore, small shifts in the energy of the orbitals occur. When the density of these states becomes great enough, such as exists in a crystal, the energy levels can be thought of as a continuous band of allowed energy states, rather than individual levels [115].

2.4.4: Semiconducting Properties of Perovskites

In order to describe the origin of semiconducting properties in perovskites, $MAPbI_3$ will be used as an example. Perovskites are crystals and therefore have a conduction and valence band, as with inorganic semiconductors. The energies of these bands are determined primarily by the electronic structure of the metal cation and halide anion in the material. In $MAPbI_3$, these are Pb and I. The outer electron shells of Pb has the structure $5d^{10}$, $6s^2$, $6p^2$, and the outer shells of I has the structure $4d^{10}$, $5s^2$, $5p^5$. However, these atoms exist as ions in the perovskite, Pb^{2+} and I^-, altering the electronic structures to $5d^{10}$, $6s^2$, $6p^0$, and $4d^{10}$, $5s^2$, $5p^6$ respectively. The empty 6p orbital in the Pb ion forms the conduction band of the perovskite, whilst the valence band is an antibonding orbital resulting from the hybridisation of the Pb 6s and I 5p states, giving the perovskite its semiconducting properties [106,116,117].

The organic cation, MA^+, has been found to not significantly affect the energies of the conduction and valence band as the HOMO lies deeper than the valence band and the LUMO lies significantly above the conduction band, instead it acts

primarily as a charge compensator [106]. However, interactions between the MA^+ and PbI_6 octahedra can significantly affect the nature of the band gap. The size and shape of MA^+ mean that in certain orientations it exerts strain on the PbI_6 octahedra. This strain changes the band gap from direct to indirect by the creation of a state ~25 meV lower than the direct transition, as shown in Figure 2.24 [118]. At room temperature the organic cation rotates rapidly [119], meaning that the band gap is constantly switching between direct and indirect transitions and vice versa. It is this switching of band gap from direct to indirect which provides organic-inorganic halide perovskites with their remarkable properties; the direct band gap giving the perovskite strong absorption characteristics, while the indirect band gap results in long charge carrier lifetimes.

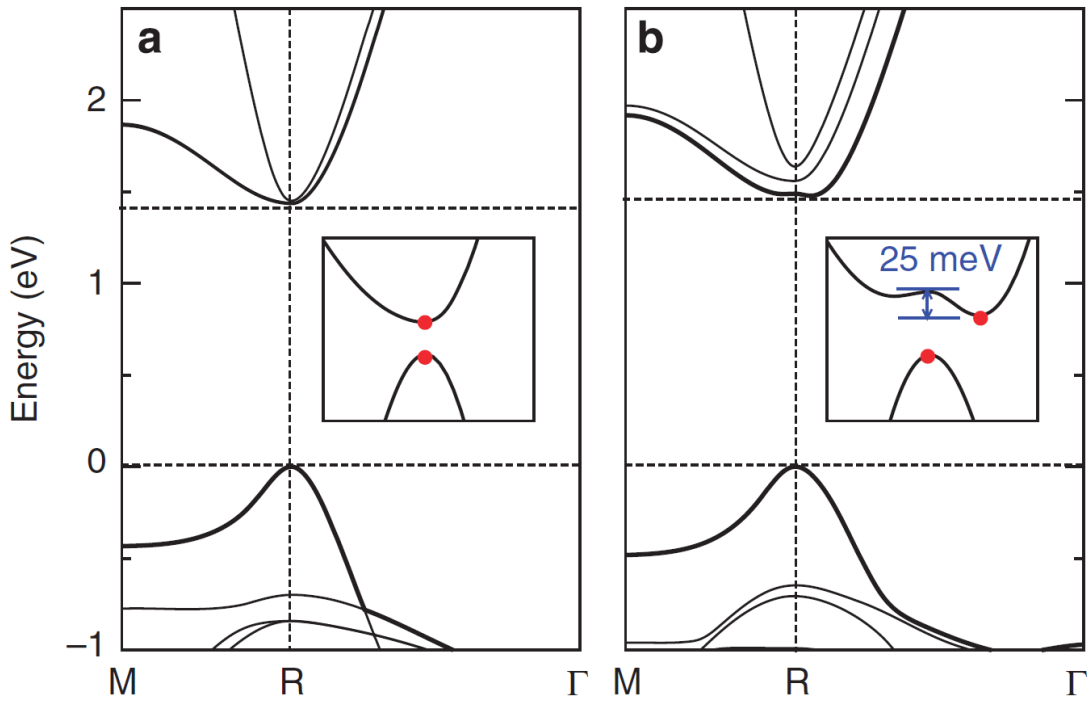

Figure 2.24: $CH_3NH_3PbI_3$ band structure for two different orientations of the organic cation, predicted by density functional theory calculations. Taken from Motta et al. [118]

2.4.5: Photocurrent Generation in Perovskite Solar Cells

The generation of photocurrent in a $MAPbI_3$ perovskite solar cell (PSC) is much simpler than occurs in OPVs. When a photon is absorbed by the perovskite, an exciton is formed, however, unlike in OPVs, this is a Wannier-Mott exciton. Initially,

these excitons were thought to have E_B in the region of ~35 – 50 meV [120,121], which, whilst lower than that of organic semiconductors (~300 meV), is still higher than ambient thermal energy (~27 meV). However, more recently it has been found that E_B is in the region of ~2 – 16 meV [122,123], allowing for thermal dissociation into free charge carriers on the order of picoseconds [124], without the need for interfaces to facilitate the process.

As with OPVs, once the exciton is dissociated, the charge carriers must be transported to the electrodes for extraction. In perovskites, charges are transported via energy bands as with inorganic semiconductors, rather than through the hopping process that occurs in organic semiconductors [125]. Here, the built-in or applied electric field cause the conduction band minimum and valence band maximum to tilt, creating a gradient of energy levels. This gradient reduces the energy of the bands at the cathode, and increased energy at the anode, making it energetically favourable for charge carriers to be transported to the appropriate electrode. This leads to charge mobilities on the order of 10 cm^2/Vs [124,126], significantly greater than seen in organics (10^{-3} cm^2/Vs). Due to this high mobility, and rapid exciton dissociation, perovskites have low geminate recombination rates. These high mobilities, along with the long carrier lifetimes resulting from the indirect band gap, also lead to large values of L_{drift}, reaching over 1000 nm in $CH_3NH_3PbI_{3-x}Cl_x$ perovskites [127], allowing the fabrication of significantly thicker photoactive layers than are practical in OPVs. $MAPbI_3$ perovskites have also been observed to have ambipolar charge transport properties, exhibiting similar mobilities for both electrons and holes [127,128]. This prevents the build-up of space charge within the layer, which would otherwise increase non-geminate recombination rates, reducing device performance.

2.4.6: Hysteresis in Perovskite Solar Cells

During *J-V* measurements, PSCs have been observed to display hysteresis. Hysteresis is observed when a device displays different performances depending on the direction of the voltage scan (i.e. short circuit to forward bias, 'forward' scan, or forward bias to short circuit, 'reverse' scan). The magnitude of the hysteresis is affected by the scan rate, with moderate scan rates exhibiting the

highest levels of hysteresis [129]. This difference primarily affects the *FF* of a device, with reverse scans typically showing improved *FF* over forward scans when hysteresis is present. There is currently no consensus on the mechanism behind the hysteresis, but there are three mechanisms that have been proposed that could be the cause, either independently or concurrently.

Firstly, trap states near the interface could be responsible. These are expected to fill under forward bias, improving contact with the charge extraction layers and boosting performance by improving extraction efficiency. Under short circuit conditions the traps would empty by transferring directly to the extraction layers, reducing the performance of the device until they were filled again [129,130].

Secondly, organometallic halide perovskites have displayed ferroelectric properties. Therefore, the organic cation may align with the applied electric field, causing distortions to the inorganic octahedra and altering the band structure of the perovskite [131,132].

Thirdly, free ions within the perovskite layer may accumulate at the interfaces when an electric field is applied. This would cause band bending at the interfaces, changing the energetic barriers between the layers and improving or hindering charge extraction [133–135].

Recently, it has been shown that a combination of ion migration and interfacial recombination are required for hysteresis to occur [136]. The authors report that the electric field across the device during a forward scan drives charge carriers away from their electrodes, causing a build-up of minority charge carriers at the contact interfaces. The recombination rate at the contact interfaces then affects the charge collection efficiency of the device. With a high recombination rate, the efficiency of charge collection is reduced, and with a low recombination rate, the collection efficiency is improved by the build-up of charge carriers.

Regardless of the mechanism, it is agreed that it is slow, occurring over time scales of seconds [135,137]. This explains the scan rate-dependence of the hysteresis displaying the highest levels at moderate scan rates. At very low scan rates the system is able to enter a quasi-stable state before the current is measured and the applied field is changed, and at high scan rates the scan is able to complete before

the mechanism influences the device. At the intermediate scan rates, however, the mechanism is active with the measurement being taken before a stable state is reached, therefore the previous applied bias will affect subsequent measurements.

In order to determine the real PCE of a PSC that exhibits a large degree of hysteresis, measuring the stabilised power output measurements has been suggested [129,138]. Here the device is held at the maximum power point under AM1.5 illumination for an extended period, usually 10s to 100s of seconds, whilst the current is measured. This enables measurement of the photocurrent and PCE free from the influence of *J-V* curve scan rate and direction, as dynamic processes are allowed to reach equilibrium.

2.4.7: Perovskite Lifetime and Degradation

As mentioned in Section 2.4.1, perovskite solar cells now boast PCEs of over 20%. This is comparable to commercial silicon solar cells, making it important to investigate the stability of such devices whilst under operation and to understand possible degradation mechanics. This section reviews the current work that has been done in this area and discusses the sources and mechanisms of the degradation seen.

The best test for the stability of a perovskite solar cell is that of operational lifetime. This involves subjecting the completed device to continuous AM1.5 illumination in ambient conditions, performing J-V sweeps regularly and holding the device at either the maximum power point (MP) or open circuit (OC) between measurements.

Standard Architecture

The most frequently used architecture for stability studies of perovskite solar cells is the standard architecture given in Section 2.4.1, and the devices in the studies referenced in this section use the structure: FTO/compact TiO_2 (C-TiO_2)/mesoporous TiO_2 (MP-TiO_2)/Perovskite/Spiro-OMeTAD/Au unless otherwise specified.

Leijtens et al. [110] performed 2 different stability tests, with each test using a different structure. Firstly, a short test with 5 hours of continuous illumination to

determine the effects of encapsulation and UV light on $CH_3NH_3PbI_{3-x}Cl_x$ perovskite devices. The devices were encapsulated using a glass coverslip attached with a UV-cured epoxy. Interestingly, encapsulated devices suffered near complete failure within this time, whilst unencapsulated device efficiencies were only reduced by 50%. In both cases this was due to losses in the J_{sc} of the devices. A third set of devices contained encapsulated devices which also had a UV filter; these were found to only lose 15% of their PCE, this time as a result of J_{sc} and *FF* losses. Due to similar losses in photocurrent seen by the authors in DSSCs, and there being no change in UV-vis spectra, the losses were not ascribed to degradation of the perovskite. The second investigation studied 1,000 hours of continuous illumination of FTO/C-TiO_2/MP-Al_2O_3/$CH_3NH_3PbI_{3-x}Cl_x$/Spiro-OMeTAD/Au devices which were encapsulated in a N_2 glove box. These devices were tested every 15 minutes and held at OC between measurements. Here it was observed that the devices lost approximately 45% of their initial PCE (11% down to 6%) in the first 200 hours of the test, caused by reductions in the *FF* and V_{oc}, after which no more losses were observed. The authors speculate that the perovskite itself was not the primary source of degradation as only small changes in the J_{sc} were observed.

Building on this, Guarnera et al. [139] used the same FTO/C-TiO_2/MP-Al_2O_3/$CH_3NH_3PbI_{3-x}Cl_x$/Spiro-OMeTAD/Au structure but with a buffer layer of Al_2O_3 nanoparticles between the perovskite and the Spiro-OMeTAD layer. Devices both with and without the buffer layer were subjected to 350 hours of continuous 100 $mW.cm^{-2}$ illumination, whilst being held at OC. As with the previous study, the devices without the buffer layer degraded over the first 200 hours to approximately 50% of the initial PCE. However, the devices with the buffer layer were reduced to 95% of the initial PCE after 350 hours. The improved stability was attributed to the buffer layer preventing the migration of metal atoms into the perovskite layer so that current shunts cannot form.

Burschka et al. [140] conducted a similar study, using $MAPbI_3$ perovskite solar cells in the standard architecture. Here they subjected a device, which had been encapsulated whilst under argon, to 500 hours of continuous illumination with an intensity of ~100 $mW.cm^{-2}$. The authors did not discuss the method of encapsulation. White light LEDs were used as the light source, with devices not

exposed to UV light during the test. The device was tested every 2 hours and was held at MP between measurements. Over the 500 hour period the device decayed linearly to approximately 80% of the initial PCE, due to a decrease in the *FF* and V_{oc}.

To determine the effects of encapsulation on standard architecture $MAPbI_3$ perovskite solar cells (using Ag instead of Au for the anode), Han et al. [141] sealed devices using two different methods. The first method involved covering the device in a UV-curable epoxy to which a glass cover slip was attached. The second method used a glass cover slip that was attached with a UV-curable epoxy at the edges of the device, with the encapsulation not in contact with the active area of the device. The glass cover slip also contained a recess containing a desiccant, intended to absorb moisture that leaked through the epoxy. Devices were subjected to continuous illumination of approximately 1 sun at 85°C and 80% RH for 80 hours. It was found that devices encapsulated using the first method decayed faster (within 20 hours) than those sealed using the second method, which were still working after the test (albeit at 10% of the original PCE, reached after 50 hours). The authors also conducted a study on the effect of temperature and humidity on the stability of PSCs encapsulated using the encapsulation utilising epoxy over the whole device area. As temperature and humidity were reduced, the devices became more stable, with devices tested at low temperature and humidity maintaining >90% of the initial PCE. In order to determine the mechanisms behind the degradation, the authors used cross-sectional FIB-SEM and XRD. These techniques showed that moisture caused the perovskite to decompose, resulting in the creation of PbI_2, visibly changing the film from brown to yellow. The gaseous products of this decomposition caused corrosion of the Ag and the formation of voids in the Spiro-OMeTAD and perovskite layers. Furthermore the perovskite layer was found to delaminate from the TiO_2 layer.

Ito et al. [142] subjected unencapsulated standard architecture $MAPbI_3$ devices to 12 hours of continuous AM1.5 illumination. After 5 hours the devices had almost completely degraded, with absorbance and XRD measurements showing that the perovskite had decomposed into PbI_2. The authors propose that the degradation is driven by the electron extraction of the TiO_2. Due to the anionic nature of the

iodide (I^-) in the perovskite crystal, it is possible for the TiO_2 to extract the electrons from the iodide creating I_2. This results in the perovskite crystal being deconstructed, and the remaining $CH_3NH_3^+$ in the film degrading into CH_3NH_2 and H^+. The I_2 can then react with the H^+ to form HI, which is emitted, along with the CH_3NH_2 to leave a PbI_2 film. In order to counter this problem, the authors added a layer of Sb_2S_3 between the two layers, which prevented the reaction of the iodide with TiO_2 and significantly increased the lifetime of the devices

Other groups have performed 'shelf-life' stability experiments, where the devices have been tested over a period of time, but not exposed to continuous illumination between the measurements. Whilst this is not as useful as operational lifetime tests, it can be used to determine other factors that can affect the stability of a device, such as temperature or humidity, or to determine relative stabilities of different material systems. Noh et al. [84] used this type of study to compare the effect of humidity on unencapsulated $MAPb(I_{1-x}Br_x)_3$ devices (standard architecture) with varying quantities of Br. Devices were stored in air at room temperature with the humidity controlled and maintained at 35%. The humidity was increased to 55% for one day, resulting in significant PCE losses in the devices with very little or no Br (x = 0, 0.06), but no change devices with higher quantities (x = 0.20, 0.29, approximately 2:1 ratio of I:Br). The authors speculate that the improved stability is a result of reduced lattice constants brought about by the smaller size of Br atoms than I atoms. Another study also investigated using $MAPbI_xBr_{3-x}$ with varying x, however, this time the intention was to remove the hole transport layer (HTL) from the device [143]. Unencapsulated devices were stored in ambient conditions for 80 days (1,920 hours) to compare the stability of different ratios of I to Br. Again, it was found that having approximate 2:1 ratio of I:Br provides greater stability, with these devices showing no degradation of PCE over the test.

Several reports have investigated various replacements for the commonly used Spiro-OMeTAD HTL in unencapsulated standard architecture $MAPbI_3/CH_3NH_3PbI_{3-x}Cl_x$ devices. The replacements include tetrathiafulvalene (TTF-1) [144], poly [N-9-hepta-decanyl-2,7-carbazole-alt-3,6-bis-(thiophene-5-yl)-2,5-dioctyl-2,5-di-hydropyrrolo[3,4-]pyrrole-1,4-dione] (PCBTDPP) [145] and DR3TBDTT [146] (full

name not provided). The tests lasted for 500, 900 and 312 hours respectively, with the TTF-1 devices stored in ambient conditions between measurements and the other kept in the dark. In all cases, the alternative ETL improved the stability of the devices over Spiro-OMeTAD tested using the same conditions. Another group replaced the TiO_2 electron transport layer (ETL) with a ZnO nanorod array [147]. The devices were stored in ambient conditions without encapsulation and tested several times over 500 hours. Over this period, the PCE of devices increased from ~4% to 5% over the first 30 hours, before decreasing linearly to 4.35% by the end of the study.

Alternatives to the commonly used $MAPbI_3$ perovskite have also been investigated. Lee et al. [98] investigated the stability of $HC(NH2)_2PbI_3$ (FAPbI) and $FA_{0.9}Cs_{0.1}PbI_3$ based solar cells using the standard architecture, without the mesoporous TiO_2 layer. Devices encapsulated with UV-cured epoxy were subjected to 220 hours of continuous 100 $mW.cm^{-2}$ illumination, with relative humidity <50% and <65°C. At the end of the test the PCE of both devices retained 70% of the initial PCE. However, when unencapsulated devices were subjected to a similar test, this time for only 1 hour, the $FA_{0.9}Cs_{0.1}PbI_3$ devices were found to be more stable than the FAPbI devices. The improved stability was thought to result from a reduction of HI generation by the CsI, preventing the decomposition of the perovskite into PbI_2. Recently, Saliba et al. [109] demonstrated perovskite devices based on the composition $Cs_5(MA_{0.17}FA_{0.83})_{95}Pb(I_{0.83}Br_{0.17})_3$ having remarkably improved stability when held in a nitrogen atmosphere. On illumination, it was found that the *PCE* decreased by approximately 10% over an initial 250 hour period, before then decaying with a half-life of ~5,000 hours.

Inverted Architecture

Fewer studies have been performed on devices that employ the inverted architecture. Xie et al. [148] investigated the stability of devices with a structure of ITO/PEDOT:PSS/$MAPbI_3$ Perovskite/PCBM/PFN-Br/Ag, both with and without $2CH_3NH_3Cl$ (MACl) residue, a by-product of the conversion of the precursor into perovskite. The devices were illuminated over 10 hours with PCE measurements taken every hour. After 2 hours of illumination the devices with the MACl residue had completely degraded, whereas those without the residue remained consistent

throughout the test. The authors attribute this difference to the MACl absorbing water from the air, facilitating the decomposition of the perovskite. Indeed they observed the film changing from brown to yellow, indicative of the formation of PbI_2.

Interestingly, stability of $MAPbI_3$ perovskite has shown to be increased by changing the method with which it is deposited. Kim et al. [87] fabricated inverted architecture devices using both spin coating and blade coating before storing them in air without encapsulation for 268 hours. Spin coated devices degraded completely within 125 hours, with XRD measurements showing complete conversion of the perovskite into PbI_2. Blade-coated devices showed much greater stability, with PCE reducing by approximately 5% over the entire testing period. This improved stability originated from improved surface coverage, a denser film and the formation of large crystalline domains resulting from slower film drying times. These factors serve to reduce the diffusion of moisture and oxygen into the film, significantly slowing down the decomposition of the perovskite. This result also serves to illustrate that the final structure of the perovskite film very important to the stability of a PSC.

As with the standard architecture devices, attempts to improve stability through the replacement of the ETL, in this case replacing PEDOT:PSS with copper doped nickel oxide ($Cu:NiO_x$) [149]. $MAPbI_3$ perovskite devices, using the structure ITO/ETL/$MAPbI_3$ Perovskite/PCBM/C_{60}-bis/Ag were stored in air without encapsulation for 240 hours and tested periodically. Devices utilising the $Cu:NiO_x$ layer were observed to lose less than 10% of the initial PCE over this time, whereas the PCE of those using PEDOT:PSS were reduced by approximately 70%. These losses originated from a reduction of the FF and, to a less extent, the J_{sc}. The acidic and hygroscopic nature of PEDOT:PSS was speculated to be the cause of this instability, providing a source of moisture for the perovskite to react with.

Author	Architecture	Test Type	Encapsulation	Study	Study Length (hours)	PCE Loss
Leijtens [106]	Standard	Operational	Glass + UV epoxy	MP-Al_2O_3/$CH_3NH_3PbI_{3-x}Cl_x$	1,000	45%
Guarnera [134]	Standard	Operational	Glass + UV epoxy	$CH_3NH_3PbI_{3-x}Cl_x$ (control)	350	60%
				Al_2O_3 nanoparticle buffer layer	350	5%
Burschka [135]	Standard	Operational	Yes	$CH_3NH_3PbI_3$	500	20%
Han [136]	Standard	Operational	Glass + UV epoxy	RH 0%, -20°C	120	0%
				RH 10%, 55°C	120	60%
				RH 80%, 55°C	20	100%
			Yes	Glass + UV epoxy encapsulation (control)	20	100%
				Glass + desiccant encapsulation	80	90%
Ito [137]	Standard	Operational	No	Control	10	90%
				Sb_2S_3 layer between ETL and active layer	10	35%
Noh [80]	Standard	Shelf-life	No	$CH_3NH_3PbI_3$ (control)	480	65%
				$CH_3NH_3PbI_{2.4}Br_{0.6}$	480	0%
Aharon [138]	Standard	Shelf-life	No	$CH_3NH_3PbI_2Br_1$	1,920	0%
Liu [139]	Standard	Shelf-life	No	HTL – Spiro-OMeTAD (control)	500	100%
				HTL – TTF1	500	20%
Cai [140]	Standard	Shelf-life	No	HTL – PCBTDPP	900	-11%
Zheng [141]	Standard	Shelf-life	No	HTL – DR3TBDTT	312	0%
Bi [142]	Standard	Shelf-life	No	ETL – ZnO nanorod array	500	0%
Lee [94]	Standard	Operational	Glass + UV epoxy	$HC(NH_2)_2PbI_3$	220	30%
				$(HC(NH_2)_2)_{0.9}Cs_{0.1}PbI_3$	220	30%
Saliba [105]	Standard	Operational	No	$Cs_5(MA_{0.17}FA_{0.83})_{95}Pb(I_{0.83}Br_{0.17})_3$	250	10%
Xie [143]	Inverted	Operational	No	With $2CH_3NH_3Cl$	2	100%
				Without $2CH_3NH_3Cl$	10	0%
Kim [83]	Inverted	Shelf-life	No	Spin cast perovskite (control)	125	100%
				Spray cast perovskite	275	5%
Kim [144]	Inverted	Shelf-life	No	HTL – PEDOT:PSS	240	70%
				HTL – Cu:NiO_x	240	10%

Table 2.5: Summary of perovskite solar cell lifetime studies covered in Section 2.4.7.

Perovskite Degradation Mechanisms

The most commonly claimed mechanism behind $MAPbI_3$ perovskite device degradation is moisture induced decomposition of the perovskite [84,87,141,142,146,150]. Frost et al. [106] propose the following decomposition pathway for $MAPbI_3$ perovskite:

$$\left[\left(CH_3NH_3^+\right)PbI_3\right]_n + H_2O \leftrightharpoons \left[\left(CH_3NH_3^+\right)_{n-1}(CH_3NH_2)_n(PbI_3)_n\right][H_3O^+] + CH_3NH_2$$

$$\left[\left(CH_3NH_3^+\right)_{n-1}(PbI_3)_n\right][H_3O^+] \leftrightharpoons HI + PbI_2 + \left[\left(CH_3NH_3^+\right)PbI_3\right]_{n-1} + H_2O$$

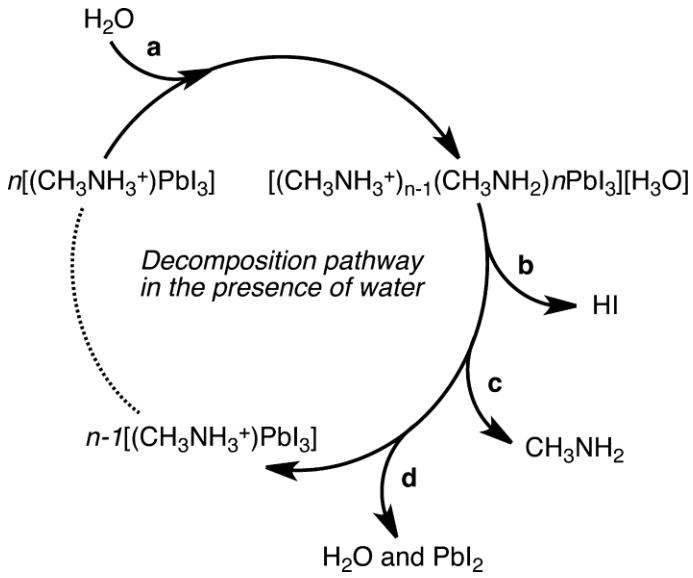

Figure 2.25: Decomposition pathway of $MAPbI_3$ perovskite proposed by Frost et al. [106]

The products of this decomposition are HI, CH_3NH_2 and PbI_2. As the HI is soluble in water, and the CH_3NH_2 is volatile, the perovskite film will fully convert into a PbI_2 film in the presence of sufficient water. This film is readily identified by its characteristic yellow colour, and has been observed experimentally in several reports [84,87,141,142,146,148]. Furthermore, interactions between the degradation products and other layers in the device can lead to additional degradation, such as corrosion of the metal electrode and the formation of voids, leading to delamination [141].

Oxygen has also been found to cause decomposition of perovskites when under illumination. Pearson *et al.* [151] and Bryant *et al.* [152] have both investigated the

effects of oxygen on $CH_3NH_3PbI_{3-x}Cl_x$ and $CH_3NH_3PbI_3$ respectively, in both cases using standard architecture devices with a mesoporous TiO_2 ETL. As with the moisture induced degradation, oxygen is found to cause the perovskite to decompose into PbI_2. However, this occurs more rapidly than with moisture, making it the dominant degradation mechanism in unencapsulated devices under illumination. The proposed decay pathway has been reported by Aristidou *et al.* [108]:

$$CH_3NH_3PbI_3 + O_2^{\bullet -} \longrightarrow CH_3NH_2 + PbI_2 + I_2 + H_2O$$

Here, the superoxide ($O_2^{\bullet -}$) is generated by electron transfer from the photoexcited perovskite, which then attacks the perovskite leading to its decomposition. It is important to note that only one of the decay products differs between water and oxygen induced decomposition, being hydroiodic acid and iodine respectively.

2.5: Summary

In this section, the background and theory of both organic and perovskite solar cells has been covered. Section 2.1 gave a brief introduction to photovoltaics and Section 2.2 covered the characterisation of photovoltaic devices. The information in these two Sections is relevant to all the following chapters in this thesis.

In Section 2.3, a brief history and overview of research of organic photovoltaics was given. This was followed by the origin of semiconducting properties in organic materials, the operational principles of organic solar cells, and an overview of degradation mechanisms. This information is relevant to Chapter 4, where organic photovoltaic devices containing differing levels of impurities are compared.

In Section 2.4, a brief history and overview of research of perovskite solar cells was given. This was followed by the crystal structure and the origin of semiconducting properties in perovskites. Finally, the operational principles of perovskite solar cells, the origin of hysteresis when testing devices, and an overview of degradation mechanisms were explored. This information is relevant to Chapters 5, 6, and 7, where various lifetime studies of perovskite solar cells are presented.

2.6: References

[1] W. Shockley, H.J. Queisser, Detailed balance limit of efficiency of p-n junction solar cells, J. Appl. Phys. 32 (1961) 510–519.

[2] A.E. Becquerel, Recherches sur les effets de la radiation chimique de la lumiere solaire au moyen des courants electriques, Comptes Rendus L'Academie Des Sci. 9 (1839) 145–149.

[3] M.A. Green, Photovoltaics: Coming of Age, Photovolt. Spec. Conf. 1990., Conf. Rec. Twenty First IEEE. 1 (1990) 1–8 vol.1.

[4] J. Zhao, Y. Li, G. Yang, K. Jiang, H. Lin, H. Ade, W. Ma, H. Yan, Efficient organic solar cells processed from hydrocarbon solvents, Nat. Energy. 1 (2016) 15027.

[5] M.A. Green, A. Ho-Baillie, H.J. Snaith, The emergence of perovskite solar cells, Nat. Photonics. 8 (2014) 506–514.

[6] C.A. Gueymard, D. Myers, K. Emery, Proposed Reference Irrandiance Spectra for Solar Energy Systems Testing, Sol. Energy. 73 (2003) 443–467.

[7] NREL, Solar Spectral Irradiance: Air Mass 1.5, (n.d.). http://rredc.nrel.gov/solar/spectra/am1.5/ (accessed September 2, 2016).

[8] H. Spanggaard, F.C. Krebs, A brief history of the development of organic and polymeric photovoltaics, Sol. Energy Mater. Sol. Cells. 83 (2004) 125–146.

[9] C.W. Tang, Two-layer organic photovoltaic cell, Appl. Phys. Lett. 48 (1986) 183–185.

[10] B.C. Thompson, J.M.J. Frechet, Polymer-fullerene composite solar cells, Angew. Chemie - Int. Ed. 47 (2008) 58–77.

[11] O. V Mikhnenko, P.W.M. Blom, T.-Q. Nguyen, Exciton diffusion in organic semiconductors, Energy Environ. Sci. 8 (2015) 1867–1888.

[12] G. Yu, A.J. Heeger, Charge separation and photovoltaic conversion in polymer composites with internal donor/acceptor heterojunctions, J. Appl. Phys. 78 (1995) 4510–4515.

[13] J.J.M. Halls, C.A. Walsh, N.C. Greenham, E.A. Marseglia, R.H. Friend, S.C. Moratti, A.B. Holmes, Efficient photodiodes from interpenetrating polymer networks, Nature. 376 (1995) 498–500.

[14] N.S. Sariciftci, L. Smilowitz, A.J. Heeger, F. Wuld, Photoinduced Electron Transfer from a Conducting Polymer to Buckminsterfullerene, Science (80-.). 258 (1992) 1474–1476.

[15] F.G. Brunetti, R. Kumar, F. Wudl, Organic electronics from perylene to organic photovoltaics: painting a brief history with a broad brush, J. Mater. Chem. 20 (2010) 2934.

[16] A.C. Mayer, S.R. Scully, B.E. Hardin, M.W. Rowell, M.D. McGehee, Polymer-based solar cells, Mater. Today. 10 (2007) 28–33.

[17] C.J. Brabec, S.E. Shaheen, C. Winder, N.S. Sariciftci, P. Denk, Effect of LiF/metal electrodes on the performance of plastic solar cells, Appl. Phys. Lett. 80 (2002) 1288–1290. doi:10.1063/1.1446988.

[18] A.J. Moulé, K. Meerholz, Controlling morphology in polymer-fullerene mixtures, Adv. Mater. 20 (2008) 240–245.

[19] D.H. Wang, J.K. Kim, J.H. Seo, I. Park, B.H. Hong, J.H. Park, A.J. Heeger, Transferable graphene oxide by stamping nanotechnology: electron-transport layer for efficient bulk-heterojunction solar cells., Angew. Chem. Int. Ed. Engl. 52 (2013) 2874–80.

[20] S.H. Park, A. Roy, S. Beaupré, S. Cho, N.E. Coates, J.S. Moon, D. Moses, M. Leclerc, K. Lee, A.J. Heeger, Bulk Heterojunction solar cells with internal quantum efficiency approaching 100%, Nat. Photonics. 3 (2009) 297–302.

[21] C.H. Peters, I.T. Sachs-Quintana, J.P. Kastrop, S. Beaupré, M. Leclerc, M.D. McGehee, High efficiency polymer solar cells with long operating lifetimes, Adv. Energy Mater. 1 (2011) 491–494.

[22] E. Bovill, H. Yi, A. Iraqi, D.G. Lidzey, E. Bovill, H. Yi, A. Iraqi, D.G. Lidzey, The fabrication of polyfluorene and polycarbazole-based photovoltaic devices using an air-stable process route The fabrication of polyfluorene and

polycarbazole-based photovoltaic devices using an air-stable process route, Appl. Phys. Lett. 105 (2014) 223302.

[23] H. Yi, S. Al-Faifi, A. Iraqi, D.C. Watters, J. Kingsley, D.G. Lidzey, Carbazole and thienyl benzo[1,2,5]thiadiazole based polymers with improved open circuit voltages and processability for application in solar cells, J. Mater. Chem. 21 (2011) 13649–13656.

[24] Heliatek sets new Organic Photovoltaic world record efficiency of 13.2%., Heliatek Press Release. (2016). http://www.heliatek.com/en/press/press-releases/details/heliatek-sets-new-organic-photovoltaic-world-record-efficiency-of-13-2.

[25] T. Wang, N.W. Scarratt, H. Yi, A.D.F. Dunbar, A.J. Pearson, D.C. Watters, T.S. Glen, A.C. Brook, J. Kingsley, A.R. Buckley, M.W.A. Skoda, A.M. Donald, R.A.L. Jones, A. Iraqi, D.G. Lidzey, Fabricating high performance, donor-acceptor copolymer solar cells by spray-coating in air, Adv. Energy Mater. 3 (2013) 505–512.

[26] P. Schilinsky, C. Waldauf, C.J. Brabec, Performance analysis of printed bulk heterojunction solar cells, Adv. Funct. Mater. 16 (2006) 1669–1672.

[27] T.M. Eggenhuisen, Y. Galagan, A. Biezemans, M. Coenen, J. Gilot, P. Groen, R. Andriessen, Organic photovoltaic cells with all inkjet printed layers and freedom of form, 2014 IEEE 40th Photovolt. Spec. Conf. PVSC 2014. 2 (2014) 2842–2845.

[28] F.C. Krebs, N. Espinosa, M. Hosel, R.R. Sondergaard, M. Jorgensen, 25th anniversary article: Rise to power - OPV-based solar parks, Adv. Mater. 26 (2014) 29–39.

[29] S. Berny, N. Blouin, A. Distler, H.-J. Egelhaaf, M. Krompiec, A. Lohr, O.R. Lozman, G.E. Morse, L. Nanson, A. Pron, T. Sauermann, N. Seidler, S. Tierney, P. Tiwana, M. Wagner, H. Wilson, Solar Trees: First Large-Scale Demonstration of Fully Solution Coated, Semitransparent, Flexible Organic Photovoltaic Modules, Adv. Sci. 3 (2016) 1–7.

[30] Y. Su, S. Lan, K. Wei, Organic photovoltaics, Mater. Today. 15 (2012) 554–562.

[31] G. Li, C.W. Chu, V. Shrotriya, J. Huang, Y. Yang, Efficient inverted polymer solar cells, Appl. Phys. Lett. 88 (2006) 3–6.

[32] M.D. Archer, M.A. Green, Clean electricity from photovoltaics, Imperial College Press, London, 2015.

[33] W. Heisenberg, Uber den anschaulichen Inhalt der quantentheoretischen Kinematik und Mechanik, Zeitschrift Fur Phys. 43 (1927) 172–198.

[34] W. Pauli, Uber den Zusammenhang des Abschlusses der Elektronengruppen im Atom mit der Komplexstruktur der Spektren, Zeitschrift Fur Phys. 31 (1925) 765–783.

[35] J. Clayden, N. Greeves, S. Warren, P. Wothers, Organic Chemistry, Oxford University Press, Oxford, 2001.

[36] R.E. Peierls, Quantum Theory of Solids, Oxford University Press, Oxford, 1955.

[37] C.S. Yannoni, T.C. Clarke, Molecular geometry of cis- and trans-polyacetylene by nutation NMR spectroscopy, Phys. Rev. Lett. 51 (1983) 1191–1193.

[38] A.O. Patil, A.J. Heeger, F. Wudl, Optical properties of conducting polymers, Chem. Rev. 88 (1988) 183–200.

[39] C.G. Wermuth, C.R. Ganellin, P. Lindberg, L. a. Mitscher, Glossary of Terms Used in Photochemistry, Pure Appl. Chem. 70 (1998) 1129–1143.

[40] T.M. Clarke, J.R. Durrant, Charge photogeneration in organic solar cells, Chem. Rev. 110 (2010) 6736–6767.

[41] J. Nelson, Polymer:fullerene bulk heterojunction solar cells, Mater. Today. 14 (2011) 462–470.

[42] V. Coropceanu, J. Cornil, D.A. da Silva Filho, Y. Olivier, R. Silbey, J.-L. Brédas, Charge transport in organic semiconductors, Chem. Rev. 107 (2007) 926–

952.

[43] B. Kippelen, J.-L. Brédas, Organic photovoltaics, Energy Environ. Sci. 2 (2009) 251.

[44] D.R. Lide, ed., Handbook of Chemistry and Physics, 79th ed., CRC Press, 1998.

[45] S.F. Alvarado, P.F. Seidler, D.G. Lidzey, D.D.C. Bradley, Direct determination of the exciton binding energy of conjugated polymers using a scanning tunneling microscope, Phys. Rev. Lett. 81 (1998) 1082–1085.

[46] L.A.A. Pettersson, L.S. Roman, O. Inganas, Modeling photocurrent action spectra of photovoltaic devices based on organic thin films, J. Appl. Phys. 86 (1999) 487–496.

[47] V. Mihailetchi, L. Koster, J. Hummelen, P. Blom, Photocurrent Generation in Polymer-Fullerene Bulk Heterojunctions, Phys. Rev. Lett. 93 (2004) 216601.

[48] C.M. Proctor, M. Kuik, T.-Q. Nguyen, Charge carrier recombination in organic solar cells, Prog. Polym. Sci. 38 (2013) 1941–1960.

[49] D. Hertel, H. Bassler, Photoconduction in amorphous organic solids, ChemPhysChem. 9 (2008) 666–688.

[50] A. Miller, E. Abrahams, Impurity conduction at low concentrations, Phys. Rev. 120 (1960) 745–755.

[51] M. Van Der Auweraer, F.C. De Schryver, P.M. Borsenberger, H. Bässler, Disorder in Charge Transport in doped polymers, Adv. Mater. 6 (1994) 199–213.

[52] H. Bässler, Charge Transport in Disordered Organic Photoconductors a Monte Carlo Simulation Study, Phys. Status Solidi B. 175 (1993) 15–56.

[53] P.W.M. Blom, V.D. Mihailetchi, L.J. a. Koster, D.E. Markov, Device Physics of Polymer:Fullerene Bulk Heterojunction Solar Cells, Adv. Mater. 19 (2007) 1551–1566.

[54] T. Lai, S. Tsang, J.R. Manders, S. Chen, F. So, Properties of interlayer for

organic photovoltaics, Mater. Today. 16 (2013) 424–432. doi:10.1016/j.mattod.2013.10.001.

[55] V.D. Mihailetchi, P.W.M. Blom, J.C. Hummelen, M.T. Rispens, Cathode dependence of the open-circuit voltage of polymer:fullerene bulk heterojunction solar cells, J. Appl. Phys. 94 (2003) 6849–6854.

[56] M.C. Scharber, D. Mühlbacher, M. Koppe, P. Denk, C. Waldauf, a. J. Heeger, C.J. Brabec, Design Rules for Donors in Bulk-Heterojunction Solar Cells—Towards 10 % Energy-Conversion Efficiency, Adv. Mater. 18 (2006) 789–794.

[57] K. Vandewal, K. Tvingstedt, A. Gadisa, O. Inganäs, J. V Manca, On the origin of the open-circuit voltage of polymer–fullerene solar cells, Nat. Mater. 8 (2009) 904–909.

[58] A. Maurano, R. Hamilton, C.G. Shuttle, A.M. Ballantyne, J. Nelson, B. O'Regan, W. Zhang, I. McCulloch, H. Azimi, M. Morana, C.J. Brabec, J.R. Durrant, Recombination dynamics as a key determinant of open circuit voltage in organic bulk heterojunction solar cells: A comparison of four different donor polymers, Adv. Mater. 22 (2010) 4987–4992.

[59] P. Schilinsky, C. Waldauf, J. Hauch, C.J. Brabec, Simulation of light intensity dependent current characteristics of polymer solar cells, J. Appl. Phys. 95 (2004) 2816–2819. doi:10.1063/1.1646435.

[60] L.J.A. Koster, V.D. Mihailetchi, R. Ramaker, P.W.M. Blom, Light intensity dependence of open-circuit voltage of polymer:fullerene solar cells, Appl. Phys. Lett. 86 (2005) 1–3.

[61] Z. He, C. Zhong, X. Huang, W.-Y. Wong, H. Wu, L. Chen, S. Su, Y. Cao, Simultaneous enhancement of open-circuit voltage, short-circuit current density, and fill factor in polymer solar cells., Adv. Mater. 23 (2011) 4636–43.

[62] S.R. Forrest, The Limits to Organic Photovoltaic Cell Efficiency, MRS Bull. 30 (2005) 28–32.

[63] P. Peumans, A. Yakimov, S.R. Forrest, P. Peumans, A. Yakimov, S.R. Forrest, Small molecular weight organic thin-film photodetectors and solar cells, J. Appl. Phys. 93 (2003) 3693–3723.

[64] G.T. Wright, Mechanisms of space-charge-limited current in solids, Solid. State. Electron. 2 (1961) 165–189.

[65] A. Carbone, B.K. Kotowska, D. Kotowski, Space-charge-limited current fluctuations in organic semiconductors, Phys. Rev. Lett. 95 (2005) 2–5.

[66] T. Yasuda, Y. Yamaguchi, D.C. Zou, T. Tsutsui, Carrier mobilities in organic electron transport materials determined from space charge limited current, Japanese J. Appl. Physics, Part 1 Regul. Pap. Short Notes Rev. Pap. 41 (2002) 5626–5629.

[67] R. De Bettignies, J. Leroy, M. Firon, C. Sentein, Accelerated lifetime measurements of P3HT:PCBM solar cells, Synth. Met. 156 (2006) 510–513.

[68] A. Hayakawa, O. Yoshikawa, T. Fujieda, K. Uehara, S. Yoshikawa, High performance polythiophene/fullerene bulk-heterojunction solar cell with a TiOX hole blocking layer, Appl. Phys. Lett. 90 (2007) 1–4.

[69] K. Norrman, M. V. Madsen, S.A. Gevorgyan, F.C. Krebs, Degradation patterns in water and oxygen of an inverted polymer solar cell, J. Am. Chem. Soc. 132 (2010) 16883–16892.

[70] B. Zimmermann, U. Würfel, M. Niggemann, Longterm stability of efficient inverted P3HT:PCBM solar cells, Sol. Energy Mater. Sol. Cells. 93 (2009) 491–496.

[71] E. Bovill, N. Scarratt, J. Griffin, H. Yi, A. Iraqi, a. R. Buckley, J.W. Kingsley, D.G. Lidzey, The role of the hole-extraction layer in determining the operational stability of a polycarbazole:fullerene bulk-heterojunction photovoltaic device, Appl. Phys. Lett. 106 (2015) 73301.

[72] J.A. Hauch, P. Schilinsky, S.A. Choulis, R. Childers, M. Biele, C.J. Brabec, Flexible organic P3HT:PCBM bulk-heterojunction modules with more than 1 year outdoor lifetime, Sol. Energy Mater. Sol. Cells. 92 (2008) 727–731.

[73] S.A. Gevorgyan, M. V. Madsen, H.F. Dam, M. Jorgensen, C.J. Fell, K.F. Anderson, B.C. Duck, A. Mescheloff, E.A. Katz, A. Elschner, R. Roesch, H. Hoppe, M. Hermenau, M. Riede, F.C. Krebs, Interlaboratory outdoor stability studies of flexible roll-to-roll coated organic photovoltaic modules: Stability over 10,000 h, Sol. Energy Mater. Sol. Cells. 116 (2013) 187–196.

[74] M.T. Lloyd, D.C. Olson, P. Lu, E. Fang, D.L. Moore, M.S. White, M.O. Reese, D.S. Ginley, J.W.P. Hsu, Impact of contact evolution on the shelf life of organic solar cells, J. Mater. Chem. 19 (2009) 7638.

[75] S.R. Ferreira, P. Lu, Y.J. Lee, R.J. Davis, J.W.P. Hsu, Effect of zinc oxide electron transport layers on performance and shelf life of organic bulk heterojunction devices, J. Phys. Chem. C. 115 (2011) 13471–13475.

[76] Y.-J. Kang, K. Lim, S. Jung, D.-G. Kim, J.-K. Kim, C.-S. Kim, S.H. Kim, J.-W. Kang, Spray-coated ZnO electron transport layer for air-stable inverted organic solar cells, Sol. Energy Mater. Sol. Cells. 96 (2012) 137–140.

[77] M. Jørgensen, K. Norrman, F.C. Krebs, Stability/degradation of polymer solar cells, Sol. Energy Mater. Sol. Cells. 92 (2008) 686–714.

[78] X. Tong, N. Wang, M. Slootsky, J. Yu, S.R. Forrest, Intrinsic burn-in efficiency loss of small-molecule organic photovoltaic cells due to exciton-induced trap formation, Sol. Energy Mater. Sol. Cells. 118 (2013) 116–123.

[79] X. Yang, J.K.J. Van Duren, R.A.J. Janssen, M.A.J. Michels, J. Loos, Morphology and thermal stability of the active layer in poly(p-phenylenevinylene)/methanofullerene plastic photovoltaic devices, Macromolecules. 37 (2004) 2151–2158.

[80] S.R. Dupont, M. Oliver, F.C. Krebs, R.H. Dauskardt, Interlayer adhesion in roll-to-roll processed flexible inverted polymer solar cells, Sol. Energy Mater. Sol. Cells. 97 (2012) 171–175.

[81] S. Kazim, M.K. Nazeeruddin, M. Gratzel, S. Ahmad, Perovskite as light harvester: A game changer in photovoltaics, Angew. Chemie - Int. Ed. 53 (2014) 2812–2824.

[82] M.A. Green, K. Emery, Y. Hishikawa, W. Warta, E.D. Dunlop, Solar cell efficiency tables (version 47), Prog. Photovolt Res. Appl. 24 (2016) 3–11.

[83] H.J. Snaith, Perovskites : The Emergence of a New Era for Low-Cost , High-Efficiency Solar Cells, J. Phys. Chem. Lett. 4 (2013) 3623−3630.

[84] J.H. Noh, S.H. Im, J.H. Heo, T.N. Mandal, S. Il Seok, Chemical management for colorful, efficient, and stable inorganic-organic hybrid nanostructured solar cells, Nano Lett. 13 (2013) 1764–1769.

[85] A.T. Barrows, A. Pearson, C. Kwak, A. Dunbar, A. Buckley, D.G. Lidzey, Efficient planar heterojunction mixed-halide perovskite solar cells deposited via spray-deposition, Energy Environ. Sci. 7 (2014) 1–7.

[86] D.K. Mohamad, J. Griffin, C. Bracher, A.T. Barrows, D.G. Lidzey, Spray-Cast Multilayer Organometal Perovskite Solar Cells Fabricated in Air, Adv. Energy Mater. (2016) 1600994.

[87] J.H. Kim, S.T. Williams, N. Cho, C.C. Chueh, A.K.Y. Jen, Enhanced Environmental Stability of Planar Heterojunction Perovskite Solar Cells Based on Blade-Coating, Adv. Energy Mater. 5 (2015) 2–7.

[88] A. Kojima, K. Teshima, Y. Shirai, T. Miyasaka, Novel Photoelectrochemical Cell with Mesoscopic Electrodes Sensitized by Lead-halide Compounds (2), in: Proc. 210th ECS Meet., 2006.

[89] A. Kojima, K. Teshima, Y. Shirai, T. Miyasaka, Organometal halide perovskites as visible-light sensitizers for photovoltaic cells, J. Am. Chem. Soc. 131 (2009) 6050–6051.

[90] T. Baikie, Y. Fang, J.M. Kadro, M. Schreyer, F. Wei, S.G. Mhaisalkar, M. Gratzel, T.J. White, Synthesis and crystal chemistry of the hybrid perovskite (CH3NH3)PbI3 for solid-state sensitised solar cell applications, J. Mater. Chem. A. 1 (2013) 5628.

[91] H.-S. Kim, C.-R. Lee, J.-H. Im, K.-B. Lee, T. Moehl, A. Marchioro, S.-J. Moon, R. Humphry-Baker, J.-H. Yum, J.E. Moser, M. Grätzel, N.-G. Park, Lead iodide perovskite sensitized all-solid-state submicron thin film mesoscopic solar

cell with efficiency exceeding 9%., Sci. Rep. 2 (2012) 591.

[92] M.M. Lee, J. Teuscher, T. Miyasaka, T.N. Murakami, H.J. Snaith, Efficient Hybrid Solar Cells Based on Meso-Superstructured Organometal Halide Perovskites, Science (80-.). 338 (2012) 643–647.

[93] Y. Zhou, K. Zhu, Perovskite Solar Cells Shine in the "Valley of the Sun," ACS Energy Lett. (2016) 64–67.

[94] H.S. Jung, N.-G. Park, Perovskite solar cells: From materials to devices, Small. (2014) 10–25.

[95] Q. Dong, Y. Yuan, Y. Shao, Y. Fang, Q. Wang, J. Huang, Abnormal Crystal Growth in CH3NH3PbI3-xClx Using a Multi-cycle Solution Coating Process, Energy Environ. Sci. 8 (2015) 2464–2470. doi:10.1039/C5EE01179E.

[96] G.E. Eperon, S.D. Stranks, C. Menelaou, M.B. Johnston, L.M. Herz, H.J. Snaith, Formamidinium lead trihalide: a broadly tunable perovskite for efficient planar heterojunction solar cells, Energy Environ. Sci. 7 (2014) 982.

[97] S. Pang, H. Hu, J. Zhang, S. Lv, Y. Yu, F. Wei, T. Qin, H. Xu, Z. Liu, G. Cui, NH2CH=NH2PbI3: An alternative organolead iodide perovskite sensitizer for mesoscopic solar cells, Chem. Mater. 26 (2014) 1485–1491.

[98] J.W. Lee, D.H. Kim, H.S. Kim, S.W. Seo, S.M. Cho, N.G. Park, Formamidinium and cesium hybridization for photo- and moisture-stable perovskite solar cell, Adv. Energy Mater. 5 (2015).

[99] G.E. Eperon, G.M. Paterno, R.J. Sutton, A. Zampetti, A.A. Haghighirad, F. Cacialli, H.J. Snaith, Inorganic caesium lead iodide perovskite solar cells, J. Mater. Chem. A. 3 (2015) 19688–19695.

[100] R.E. Beal, D.J. Slotcavage, T. Leijtens, A.R. Bowring, R.A. Belisle, W.H. Nguyen, G.F. Burkhard, E.T. Hoke, M.D. McGehee, Cesium Lead Halide Perovskites with Improved Stability for Tandem Solar Cells, J. Phys. Chem. Lett. 7 (2016) 746–751.

[101] G.E. Eperon, S.D. Stranks, C. Menelaou, M.B. Johnston, L.M. Herz, H.J. Snaith,

Formamidinium lead trihalide: a broadly tunable perovskite for efficient planar heterojunction solar cells, Energy Environ. Sci. 7 (2014) 982.

[102] N.K. Noel, S.D. Stranks, A. Abate, C. Wehrenfennig, S. Guarnera, A.-A. Haghighirad, A. Sadhanala, G.E. Eperon, S.K. Pathak, M.B. Johnston, A. Petrozza, L.M. Herz, H.J. Snaith, Lead-Free Organic-Inorganic Tin Halide Perovskites for Photovoltaic Applications, Energy Environ. Sci. 7 (2014) 3061–3068.

[103] W. Liao, D. Zhao, Y. Yu, C.R. Grice, C. Wang, A.J. Cimaroli, P. Schulz, W. Meng, K. Zhu, R.G. Xiong, Y. Yan, Lead-Free Inverted Planar Formamidinium Tin Triiodide Perovskite Solar Cells Achieving Power Conversion Efficiencies up to 6.22%, Adv. Mater. (2016) 1–8.

[104] S.J. Lee, S.S. Shin, Y.C. Kim, D. Kim, T.K. Ahn, J.H. Noh, J. Seo, S. Il Seok, Fabrication of Efficient Formamidinium Tin Iodide Perovskite Solar Cells through SnF2-Pyrazine Complex, J. Am. Chem. Soc. 138 (2016) 3974–3977. doi:10.1021/jacs.6b00142.

[105] J.H. Heo, M. Lee, M.H. Jang, S.H. Im, Highly efficient CH3NH3PbI3-xClx mixed halide perovskite solar cells prepared by re-dissolution and crystal grain growth via spray coating, J. Mater. Chem. A. (2016).

[106] J.M. Frost, K.T. Butler, F. Brivio, C.H. Hendon, M. Van Schilfgaarde, A. Walsh, Atomistic origins of high-performance in hybrid halide perovskite solar cells, Nano Lett. 14 (2014) 2584–2590.

[107] A.J. Pearson, G.E. Eperon, P.E. Hopkinson, S.N. Habisreutinger, J.T.W. Wang, H.J. Snaith, N.C. Greenham, Oxygen Degradation in Mesoporous Al2O3/CH3NH3PbI3-xClx Perovskite Solar Cells: Kinetics and Mechanisms, Adv. Energy Mater. 6 (2016) 1–10.

[108] N. Aristidou, I. Sanchez-Molina, T. Chotchuangchutchaval, M. Brown, L. Martinez, T. Rath, S.A. Haque, The Role of Oxygen in the Degradation of Methylammonium Lead Trihalide Perovskite Photoactive Layers, Angew. Chemie - Int. Ed. 54 (2015) 8208–8212.

[109] M. Saliba, T. Matsui, J.-Y. Seo, K. Domanski, J.-P. Correa-Baena, N. Mohammad K., S.M. Zakeeruddin, W. Tress, A. Abate, A. Hagfeldt, M. Gratzel, Cesium-containing Triple Cation Perovskite Solar Cells: Improved Stability, Reproducibility and High Efficiency, Energy Environ. Sci. 9 (2016) 1989–1997.

[110] T. Leijtens, G.E. Eperon, S. Pathak, A. Abate, M.M. Lee, H.J. Snaith, Overcoming ultraviolet light instability of sensitized TiO2 with meso-superstructured organometal tri-halide perovskite solar cells., Nat. Commun. 4 (2013) 2885.

[111] C. Li, X. Lu, W. Ding, L. Feng, Y. Gao, Z. Guo, Formability of ABX(3) (X = F, Cl, Br, I) halide perovskites, Acta Crystallogr. Sect. B Struct. Sci. 64 (2008) 702–707.

[112] N.K. McKinnon, D.C. Reeves, M.H. Akabas, 5-HT3 receptor ion size selectivity is a property of the transmembrane channel, not the cytoplasmic vestibule portals, J. Gen. Physiol. 138 (2011) 453–466.

[113] N.-G. Park, Perovskite solar cells: an emerging photovoltaic technology, Mater. Today. 18 (2015) 65–72.

[114] A. Poglitsch, D. Weber, Dynamic disorder in methylammoniumtrihalogenoplumbates (II) observed by millimeter-wave spectroscopy, J. Chem. Phys. 87 (1987) 6373.

[115] C. Kittel, Introduction to Solid State Physics, 8th ed., John Wiley and Sons, 2005.

[116] F. Brivio, A.B. Walker, A. Walsh, Structural and electronic properties of hybrid perovskites for high-efficiency thin-film photovoltaics from first-principles, APL Mater. 1 (2013) 12–17.

[117] F. Brivio, K.T. Butler, A. Walsh, M. Van Schilfgaarde, Relativistic quasiparticle self-consistent electronic structure of hybrid halide perovskite photovoltaic absorbers, Phys. Rev. B - Condens. Matter Mater. Phys. 89 (2014) 1–6.

[118] C. Motta, F. El-Mellouhi, S. Kais, N. Tabet, F. Alharbi, S. Sanvito, Revealing the role of organic cations in hybrid halide perovskite CH3NH3PbI3., Nat.

Commun. 6 (2015) 7026.

[119] R.E. Wasylishen, O. Knop, J.B. Macdonald, Cation rotation in methylammonium lead halides, Solid State Commun. 56 (1985) 581–582.

[120] M. Hirasawa, T. Ishihara, T. Goto, K. Uchida, N. Miura, Magnetoabsorption of the lowest exciton in perovskite-type compound (CH3NH3)PbI3, Phys. B Phys. Condens. Matter. 201 (1994) 427–430.

[121] V. D'Innocenzo, G. Grancini, M.J.P. Alcocer, A.R.S. Kandada, S.D. Stranks, M.M. Lee, G. Lanzani, H.J. Snaith, A. Petrozza, Excitons versus free charges in organo-lead tri-halide perovskites., Nat. Commun. 5 (2014) 3586.

[122] Q. Lin, A. Armin, R. Chandra, R. Nagiri, P.L. Burn, P. Meredith, Electro-optics of perovskite solar cells, Nat. Photonics. 9 (2014) 106–112.

[123] A. Miyata, A. Mitioglu, P. Plochocka, O. Portugall, J.T.-W. Wang, S.D. Stranks, H.J. Snaith, R.J. Nicholas, Direct measurement of the exciton binding energy and effective masses for charge carriers in organic-inorganic tri-halide perovskites, Nat. Phys. 11 (2015) 582–587.

[124] C.S. Ponseca, T.J. Savenije, M. Abdellah, K. Zheng, A. Yartsev, T. Pascher, T. Harlang, P. Chabera, T. Pullerits, A. Stepanov, J.P. Wolf, V. Sundstr??m, Organometal halide perovskite solar cell materials rationalized: Ultrafast charge generation, high and microsecond-long balanced mobilities, and slow recombination, J. Am. Chem. Soc. 136 (2014) 5189–5192.

[125] T. Zhao, W. Shi, J. Xi, D. Wang, Z. Shuai, Intrinsic and Extrinsic Charge Transport in CH3NH3PbI3 Perovskites Predicted from First-Principles, Sci. Rep. 6 (2016) 19968.

[126] T.J. Savenije, C.S. Ponseca, L. Kunneman, M. Abdellah, K. Zheng, Y. Tian, Q. Zhu, S.E. Canton, I.G. Scheblykin, T. Pullerits, A. Yartsev, V. Sundström, Thermally activated exciton dissociation and recombination control the carrier dynamics in organometal halide perovskite, J. Phys. Chem. Lett. 5 (2014) 2189–2194.

[127] S.D. Stranks, G.E. Eperon, G. Grancini, C. Menelaou, M.J.P. Alcocer, T. Leijtens,

L.M. Herz, A. Petrozza, H.J. Snaith, Electron-Hole Diffusion Lengths Exceeding 1 Micrometer in an Organometal Trihalide Perovskite Absorber, Science. 342 (2014) 341–344.

[128] G. Xing, N. Mathews, S.S. Lim, Y.M. Lam, S. Mhaisalkar, T.C. Sum, Long-Range Balanced Electron- and Hole-Transport Lengths in Organic-Inorganic CH3NH3PbI3, Science (80-.). 342 (2013) 344–347.

[129] H.J. Snaith, A. Abate, J.M. Ball, G.E. Eperon, T. Leijtens, N.K. Noel, S.D. Stranks, J.T.-W. Wang, K. Wojciechowski, W. Zhang, Anomalous Hysteresis in Perovskite Solar Cells, J. Phys. Chem. Lett. 5 (2014) 1511–1515.

[130] Y. Shao, Z. Xiao, C. Bi, Y. Yuan, J. Huang, Origin and elimination of photocurrent hysteresis by fullerene passivation in CH3NH3PbI3 planar heterojunction solar cells, Nat. Commun. 5 (2014) 1–7.

[131] R. Gottesman, E. Haltzi, L. Gouda, S. Tirosh, Y. Bouhadana, A. Zaban, E. Mosconi, F. De Angelis, Extremely slow photoconductivity response of CH3NH 3PbI3 perovskites suggesting structural changes under working conditions, J. Phys. Chem. Lett. 5 (2014) 2662–2669.

[132] R.S. Sánchez, V. Gonzalez-pedro, J. Lee, N. Park, Y.S. Kang, I. Mora-sero, J. Bisquert, Slow Dynamic Processes in Lead Halide Perovskite Solar Cells. Characteristic Times and Hysteresis, J. Phys. Chem. Lett. 5 (2014) 2357–2363.

[133] Y. Zhao, C. Liang, H. min Zhang, D. Li, D. Tian, G. Li, X. Jing, W. Zhang, W. Xiao, Q. Liu, F. Zhang, Z. He, Anomalously large interface charge in polarity-switchable photovoltaic devices: an indication of mobile ions in organic-inorganic halide perovskites, Energy Environ. Sci. 0 (2015) Advance.

[134] W. Tress, N. Marinova, T. Moehl, S.M. Zakeeruddin, N. Mohammad K., M. Grätzel, M.K. Nazeeruddin, M. Grätzel, Understanding the rate-dependent J–V hysteresis, slow time component, and aging in CH3NH3PbI3 perovskite solar cells: the role of a compensated electric field, Energy Environ. Sci. 8 (2015) 995–1004.

[135] H. Zhang, C. Liang, Y. Zhao, M. Sun, H. Liu, J. Liang, D. Li, F. Zhang, Z. He, Dynamic interface charge governing the current-voltage hysteresis in perovskite solar cells, Phys. Chem. Chem. Phys. 17 (2015) 9613.

[136] P. Calado, A.M. Telford, D. Bryant, X. Li, J. Nelson, B.C. O'Regan, P.R.F. Barnes, Evidence for ion migration in hybrid perovskite solar cells with minimal hysteresis, Nat. Commun. 7 (2016) 13831.

[137] H.S. Kim, N.-G. Park, Parameters Affecting I-V Hysteresis of CH3NH3PbI3 Perovskite Solar Cells: Effects of Perovskite Crystal Size and Mesoporous TiO2 Layer, J. Phys. Chem. Lett. 5 (2014) 2927–2934.

[138] Y. Zhang, M. Liu, G.E. Eperon, T.C. Leijtens, D. McMeekin, M. Saliba, W. Zhang, M. de Bastiani, A. Petrozza, L.M. Herz, M.B. Johnston, H. Lin, H.J. Snaith, Charge selective contacts, mobile ions and anomalous hysteresis in organic–inorganic perovskite solar cells, Mater. Horiz. 1 (2015) 96.

[139] S. Guarnera, A. Abate, W. Zhang, J.M. Foster, G. Richardson, A. Petrozza, H.J. Snaith, Improving the long-term stability of perovskite solar cells with a porous Al2O3 buffer layer, J. Phys. Chem. Lett. 6 (2015) 432–437.

[140] J. Burschka, N. Pellet, S.-J. Moon, R. Humphry-Baker, P. Gao, M.K. Nazeeruddin, M. Grätzel, Sequential deposition as a route to high-performance perovskite-sensitized solar cells., Nature. 499 (2013) 316–9.

[141] Y. Han, S. Meyer, Y. Dkhissi, K. Weber, J.M. Pringle, U. Bach, L. Spiccia, Y.-B. Cheng, Degradation observations of encapsulated planar CH3NH3PbI3 perovskite solar cells at high temperatures and humidity, J. Mater. Chem. A. 3 (2015) 8139–8147.

[142] S. Ito, S. Tanaka, K. Manabe, H. Nishino, Effects of Surface Blocking Layer of Sb2S3 on Nanocrystalline TiO 2 for CH3NH3PbI3 Perovskite Solar Cells, J. Phys. Chem. C. 118 (2014) 16995–17000.

[143] S. Aharon, B. El Cohen, L. Etgar, Hybrid lead halide iodide and lead halide bromide in efficient hole conductor free perovskite solar cell, J. Phys. Chem. C. 118 (2014) 17160–17165.

[144] J. Liu, Y. Wu, C. Qin, X. Yang, T. Yasuda, A. Islam, K. Zhang, W. Peng, W. Chen, L. Han, A dopant-free hole-transporting material for efficient and stable perovskite solar cells, Energy Environ. Sci. 7 (2014) 2963–2967.

[145] B. Cai, Y.D. Xing, Z. Yang, W.H. Zhang, J.S. Qiu, High performance hybrid solar cells sensitized by organolead halide perovskites, Energy Environ. Sci. 6 (2013) 1480–1485.

[146] L. Zheng, Y.S. Chung, Y. Ma, L. Zhang, L. Xiao, Z. Chen, S. Wang, B. Qu, Q. Gong, A Hydrophobic Hole Transporting Oligothiophene for Planar Perovskite Solar Cells with Improved Stability., Chem. Commun. 50 (2014) 11196–11199.

[147] D. Bi, G. Boschloo, S. Schwarzmüller, L. Yang, E.M.J. Johansson, A. Hagfeldt, Efficient and stable CH3NH3PbI3-sensitized ZnO nanorod array solid-state solar cells., Nanoscale. 5 (2013) 11686–11691.

[148] F.X. Xie, D. Zhang, H. Su, X. Ren, K.S. Wong, M. Grätzel, W.C.H. Choy, Vacuum-Assisted Thermal Annealing of CH3NH3PbI3 for Highly Stable and Efficient Perovskite Solar Cells, ACS Nano. 9 (2015) 639–646.

[149] J.H. Kim, P.W. Liang, S.T. Williams, N. Cho, C.C. Chueh, M.S. Glaz, D.S. Ginger, A.K.Y. Jen, High-performance and environmentally stable planar heterojunction perovskite solar cells based on a solution-processed copper-doped nickel oxide hole-transporting layer, Adv. Mater. 27 (2015) 695–701.

[150] H. Li, K. Fu, A. Hagfeldt, M. Grätzel, S.G. Mhaisalkar, A.C. Grimsdale, A simple 3,4-ethylenedioxythiophene based hole-transporting material for perovskite solar cells, Angew. Chemie - Int. Ed. 53 (2014) 4085–4088.

[151] A.J. Pearson, G.E. Eperon, P.E. Hopkinson, S.N. Habisreutinger, J.T.W. Wang, H.J. Snaith, N.C. Greenham, Oxygen Degradation in Mesoporous Al2O3/CH3NH3PbI3-xClx Perovskite Solar Cells: Kinetics and Mechanisms, Adv. Energy Mater. 6 (2016) 1600014.

[152] D. Bryant, N. Aristidou, S. Pont, I. Sanchez-Molina, T. Chotchunangatchaval, S. Wheeler, J.R. Durrant, S.A. Haque, Light and oxygen induced degradation

limits the operational stability of methylammonium lead triiodide perovskite solar cells, Energy Environ. Sci. 9 (2016) 1655–1660.

Chapter 3

Experimental Methods

3.0: Introduction

This chapter describes the various experimental procedures used in this thesis to prepare and characterise polymers, organic photovoltaic (OPV) devices and perovskite solar cells (PSCs). The fabrication techniques used for devices are described in Section 3.1, with solution preparation and device fabrication described in Section 3.2 and 3.3 for OPVs and PSCs respectively. Device and polymer characterisation are described in Section 3.4 and 3.5 respectively. The various experimental techniques used are covered in Sections 3.6 and 3.7. The development of a laser beam induced current (LBIC) mapping system is given in Section 3.8. Finally, Section 3.9 discusses where these techniques have been used in this thesis.

3.1: Device Fabrication Techniques

3.1.1: Spin Coating

Spin coating was used to form the majority of the thin films explored in this thesis. Spin coating is the process of creating a film by depositing a droplet (25-50 µl) of solution on a rapidly rotating substrate. The centrifugal forces spread the droplet uniformly over the substrate and removes any excess solution. The solvent then evaporates whilst the substrate is still rotating, leaving the solute as a relatively smooth and uniform film. The resultant thickness of a spin coated film is proportional to the inverse of the spin speed as show in Equation 3.1 [1,2]:

$$t \propto \frac{1}{\sqrt{\omega}} \tag{3.1}$$

Here, t is the final film thickness, and ω is the spin speed. This relationship can be used to calculate the spin speed required for a desired thickness from a known spin speed and thickness if the same solution is used in both cases, as other factors that influence the film thickness, such as the material concentration, solvent evaporation rate, and solvent viscosity, should remain constant. This new relationship is given in Equation 3.2:

$$\omega_D = \omega_R \left(\frac{t_R}{t_D}\right)^2 \tag{3.2}$$

Here, t_R and t_D are the reference and desired film thickness respectively, and ω_R and ω_D are the reference and desired spin speed. By spin casting test films at known spin speeds and measuring their thickness, Equation 3.2 allows for ease of achieving a desired film thickness by using these values to calculate the spin speed required.

Spin coating has a major disadvantage in its scalability, being able to only cast onto a single substrate at a time limits the throughput of the method. Furthermore, it is a particularly wasteful technique, as most of the deposited solution is removed during spin coating [2].

3.1.2: Ultrasonic Spray Coating

Spray coating is an alternative technique to spin coating for depositing solution processable materials. The advantages of using spray coating over spin coating include compatibility with roll-to-roll processing and ease of scaling up to large area deposition. Ultrasonic spray coating is a variety of spray coating that utilises a tip vibrating at ultrasonic frequency (35 kHz) to dispense solution. This atomises the solution that is fed onto it and creating a fine mist. A flow of air is used to planarise the mist into a sheet which is passed over the substrate to deposit a film. The thickness of this film is controlled by changing the height and speed at which the spray is deposited. If the solution wets to the substrate, it spreads across the surface before the solvent evaporates and leaves behind a film with good surface coverage. However, if the solution has poor wettability then it will form into separate droplets across the substrate, resulting in poor surface coverage. This can be controlled in several ways. Firstly, solvent choice is very important; if the boiling point of the solvent being used is too low, it can evaporate before reaching the substrate, if the surface tension is too high, then it may not completely wet the substrate [3–5]. Secondly, additives can be used, which can change the wettability of a solution by altering its properties, such as viscosity or boiling point [6,7]. Thirdly, the choice of surface being sprayed onto will affect the wettability, due to roughness and surface energy. The thickness of a spray cast film is determined by the solution concentration, wettability, and evaporation rate.

3.2: Organic Photovoltaic Device Fabrication

3.2.1: Materials and Solution Preparation

Both donor polymers used in this thesis were synthesised by Hunan Yi in the Department of Chemistry, University of Sheffield. The fullerene $PC_{70}BM$ (dry powder, 95% pure) was used as supplied by Ossila Ltd. The chemical structures and full names for the polymers used, PCDTBT and PFD2TBT-8, are shown in Figure 3.1, along with $PC_{70}BM$. PEDOT:PSS (poly(3,4-ethylenedioxythiophene) polystyrene sulfonate) used as a hole transport layer was supplied by Ossila Ltd. as a 1.3 – 1.7 wt% suspension in water.

To prepare polymer solutions, the materials were added as dry powder to a 4 ml vial at a concentration of 5 mg/ml and dissolved in the appropriate solvent. Here chlorobenzene (CB) was used for PCDTBT and chloroform (CF) for PFD2TBT-8. The solutions were placed on a hotplate at 70°C overnight to aid dissolution. The solution was then added to another vial containing $PC_{70}BM$ at a concentration of 20 mg/ml to create a polymer:fullerene blend solution with a total concentration of 25 mg/ml. As before, the solution was placed on a hotplate at 70°C overnight. This blend ratio of 1:4 polymer to fullerene was used as it was determined to the optimum, enabling the formation of an efficient bulk heterojunction with pathways of polymer and fullerene leading to the appropriate transport layers. The materials were all measured in ambient condition using a calibrated microbalance before being transferred to a glove box to add the solvent. CB and CF were supplied by Sigma-Aldrich, were anhydrous and were greater than 99% pure. All vials used were borosilicate amber glass to minimise photodegradation of the solvents. For single carrier devices, solutions at twice the concentration were prepared in order to achieve a thicker film.

In Chapter 4, the effects of palladium content of the polymers on device performance and lifetime is studied. To achieve this each polymer was split into 3 batches after synthesis. The first batch was put through a cleaning procedure to remove Pd and produce a 'clean' polymer. The second batch had the Pd content increased through a pollution procedure to produce a 'dirty' polymer. The final batch was not subjected to any additional procedure to provide a polymer with intermediate Pd content. The specifics of the cleaning and pollution procedures are covered in detail in Chapter 4.

PCDTBT

Poly[N-9'-heptadcanyl-2,7-carbozole-alt-5,5-(4',7'-di-2-thenyl-2',1',3'-benzothiadiazole)]

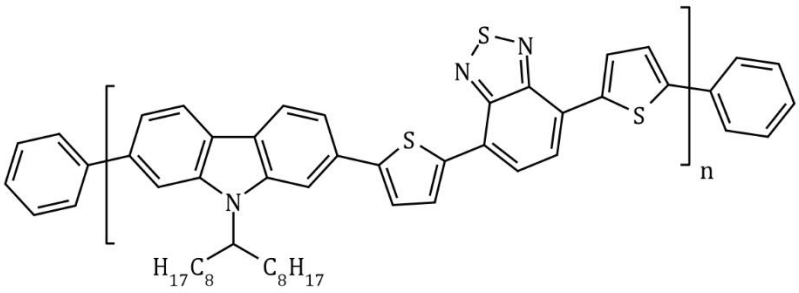

PFD2TBT-8

poly[9,9-dioctylfluorene-4,7-alt-(5,6-bis(octyloxy)-4,7-di(2,2′-bithiophen-5-yl)benzo[c][1,2,5]thiadiazole)-5,5-diyl]

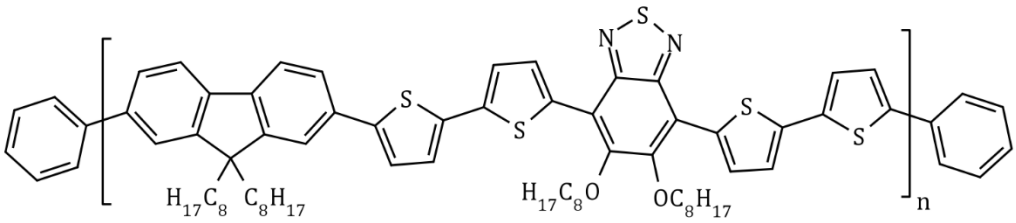

$PC_{70}BM$

[6,6]-phenyl-C71-butyric acid methyl ester

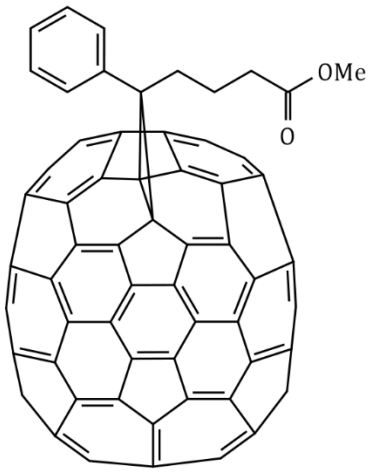

Figure 3.1: Chemical structures of PCDTBT, PFD2TBT-8 and $PC_{70}BM$.

3.2.2: Device Architecture

For all organic photovoltaic (OPV) devices used in this thesis, the standard architecture was used, as described in Chapter 2 and shown in Figure 3.2. This architecture utilises the transparent front contacts the anode and a reflective rear contact as the cathode, positioned either side of the active layer. Additionally, charge transport layers were situated between the electrodes and the active layer to facilitate charge extraction by improving energy level alignment within the device. The active polymer-fullerene layer formed a bulk heterojunction (BHJ). Here, the polymer and fullerene were deposited from the same solution, creating an interpenetrating network of polymer-rich and fullerene-rich regions. This greatly increased the interface area between the two materials, significantly increasing the likelihood that an exciton was generated within 10 nm (the exciton diffusion length) of the interface. Consequently, OPV devices that employ the BHJ often have internal quantum efficiencies approaching unity [8]. The materials and thicknesses for each layer of the OPV devices used in this thesis are given in Table 3.1.

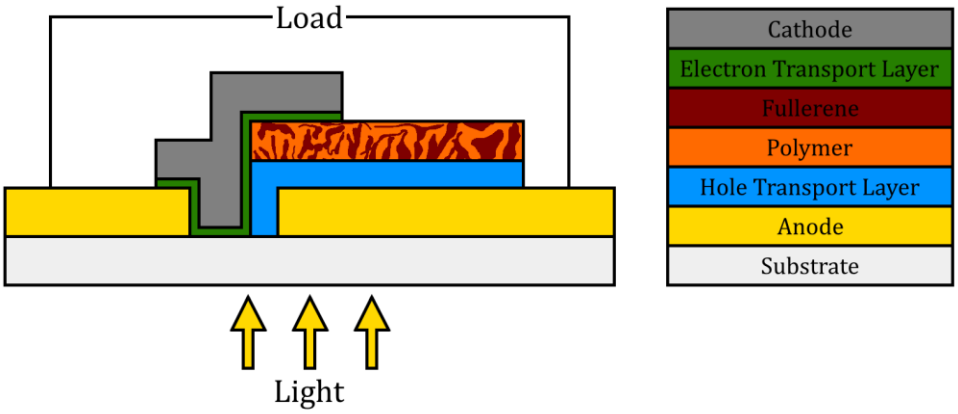

Figure 3.2: Schematic diagram of the OPV device architecture used in this thesis.

Layer	Material	Thickness (nm)
Anode	Indium tin oxide (ITO)	100
HTL	PEDOT:PSS	30 – 40
HTL	Molybdenum Oxide (MoO_3)	9.5 – 10.5
Active	PCDTBT:$PC_{70}BM$ BHJ	70 – 75
Active	PFD2TBT-8:$PC_{70}BM$ BHJ	70 – 75
ETL	Calcium	4.5 – 5.5
Cathode	Aluminium	95 – 105

Table 3.1: Materials used and thickness for each layer of the OPV devices in this thesis.

3.2.3: Device Fabrication

OPV devices were fabricated on 15x20 mm glass substrates with a 100 nm pre-patterned layer of ITO as shown in Figure 3.3(a). Before use, the substrates were cleaned to remove dust or contaminations from the surface. To do this, the substrates were loaded in a rack and sonicated in hot 5% Hellmanex solution, hot deionised (DI) water and finally in iso-propan-2-ol (IPA) for 5 minutes each. Between each sonication the substrates were dump rinsed in hot DI water, and after the final sonication substrates were rinsed with IPA and dried with a nitrogen gun.

Once cleaned and dried, a hole transport layer (HTL) was deposited onto the substrate. This layer was either a thermally evaporated 10 nm layer of molybdenum oxide (MoO_3) or a 30 – 40 nm spin cast layer of PEDOT:PSS (Ossila M124). To deposit MoO_3, the substrates were transferred into a nitrogen filled glove box, loaded into a shadow mask and placed in vacuum chamber. The vacuum chamber was pumped down to a pressure of $\sim 10^{-7}$ mbar before the evaporation was performed. The MoO_3 was thermally evaporated at a rate of ~0.3 Å/s, during which the substrates were rotated to achieve more uniform surface coverage. After 10 nm of MoO_3 had been deposited, the system was left to cool for short time before the substrates were removed. To deposit PEDOT:PSS, it was added to a syringe with a PVDF filter before being spin coated at 5000 rpm for 30 seconds. The layer was removed from the edges of the substrate using DI water, as shown in

Figure 3.3(b) and placed on a hotplate at 125°C for 10 minutes to remove moisture from the film.

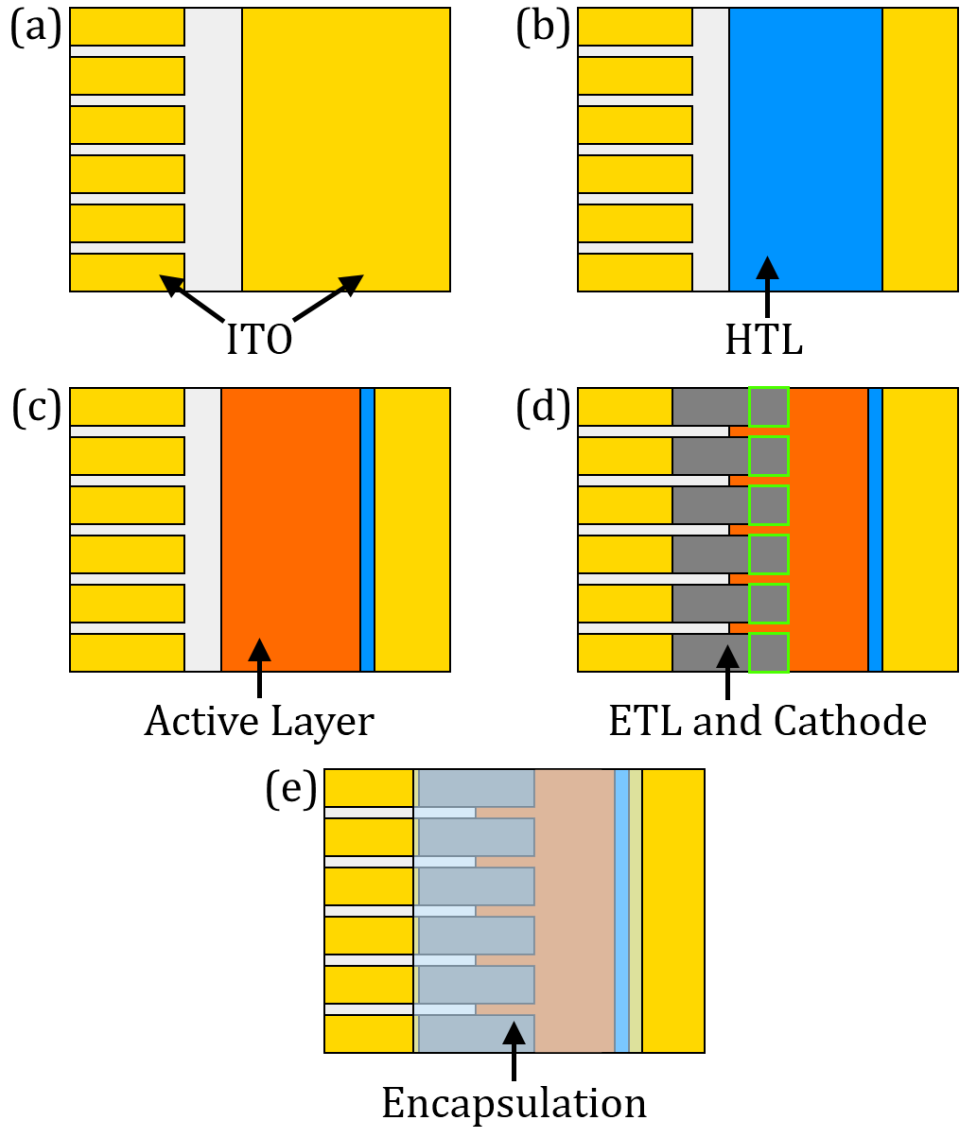

Figure 3.3: OPV device structure used and areas covered by each layer. The area highlighted in green in part (d) shows the active area of each device (2 x 2 mm).

The next layer to be deposited was the active layer of the solar cell. This was performed in a nitrogen filled glove box. Both PCDTBT and PFD2TBT-8 devices were spin cast to give a 70 nm layer, using spin speeds of 1200 rpm and 2500 rpm respectively (checked using a surface profilometer). The films were removed from

the edges of the substrate using CB, in the same manner as the PEDOT:PSS, as shown in Figure 3.3(c).

The electron transport layer (ETL) and cathode were deposited using thermal evaporation. This was performed in a vacuum chamber at a pressure of $\sim 10^{-7}$ mbar. The ETL was a 5 nm layer of Ca and the cathode was a 100 nm layer of Al, deposited at rates of ~0.2 Å/s and 1.0 – 1.5 Å/s respectively. A cooling period of 5 – 10 mins was included after each evaporation. A shadow mask was used to define the areas on which the layers were deposited and the substrates were rotated for the duration of the deposition.

Finally, the devices were removed from the vacuum chamber and encapsulated. This was done by applying a drop of UV-curable epoxy to the device and placing a 12x15 mm glass coverslip as shown in Figure 3.3(e). The device was placed in a UV box for 30 minutes to cure the epoxy.

Hole-only devices were fabricated using the same procedure as the photovoltaic devices, however the Ca/Al cathode was replaced with a 70 nm layer of Au. This was deposited via thermal evaporation at a pressure of $\sim 10^{-7}$ mbar, at a rate of 1.2 Å/s. Electron-only devices utilised a Ca/Al cathode, together with a 10 nm layer of caesium carbonate instead of PEDOT:PSS, deposited by spin-coating. For both of these a 150 – 200 nm thick active layer was used to ensure that sufficient space charge could build up to limit current flow. If the layer is too thin, then carriers can escape through the collection electrode before space charge can accumulate, preventing the current from becoming dependant on charge carrier mobility.

3.3: Perovskite Solar Cell Fabrication

3.3.1: Materials and Solution Preparation

The perovskite precursor ink used in this thesis was a mixture of $PbCl_2$ (99.999% pure), and methylammonium iodide (MAI, >99% pure) with a molar ratio of 1:3, dissolved in anhydrous dimethylformamide (DMF, 99.8% pure). This precursor was formulated to be spin-cast and annealed in air. $PC_{70}BM$ solutions, used as an electron extracting material, were prepared at a concentration of 50 mg/ml, dissolved in CB, and heated at 70°C overnight.

3.3.2: Device Architecture

The architecture used for perovskite solar cells (PSCs) was similar to that of the OPVs. The perovskite active layer was deposited between a transparent anode and reflective cathode. This is the inverted architecture as described in Chapter 2 and shown in Figure 3.4. As with OPVs, charge transport layers were employed between the electrodes and the perovskite to improve the energy level alignment of the system. Additionally, a layer of $PC_{70}BM$ was employed between the ETL and perovskite layer to further improve energy level alignment (i.e. an additional ETL, see Figure 2.21) and also planarise the surface due to the roughness of the perovskite. The materials and thicknesses for each layer of the PSCs used in this thesis are given in Table 3.2.

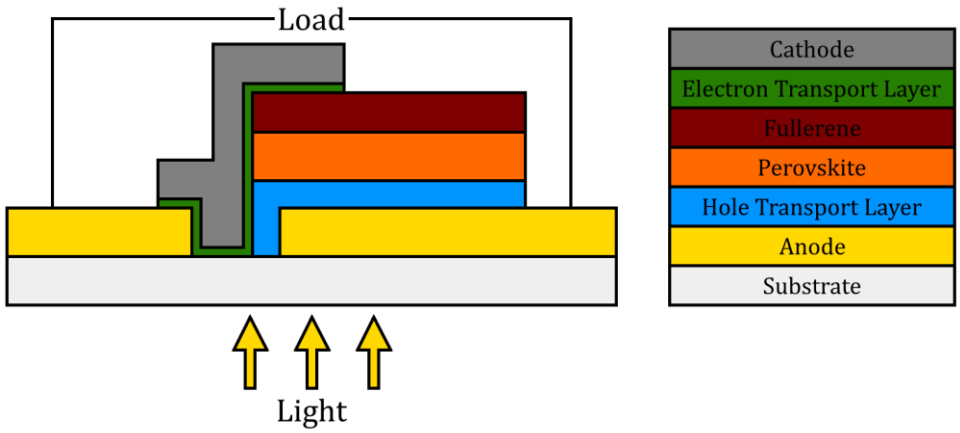

Figure 3.4: Schematic diagram of the PSC device architecture used in this thesis.

Layer	Material	Thickness (nm)
Anode	Indium tin oxide (ITO)	100
HTL	PEDOT:PSS	30 – 40
Active	$CH_3NH_3PbI_{3-x}Cl_x$ Perovskite	350 – 500
ETL 1	$PC_{70}BM$	130 – 150
ETL 2	Lithium Fluoride	1.9 – 2.1
ETL 2	Calcium	4.5 – 5.5
Cathode	Aluminium	95 – 105

Table 3.2: Materials used and thickness for each layer of the PSCs in this thesis.

3.3.3: Device Fabrication

PSCs were fabricated on the same substrates and used the same cleaning procedure as OPV devices. A 30 – 40 nm layer of PEDOT:PSS was used as the HTL, which was deposited in the same manner as with OPV devices, except without being removed from the substrate edges at this stage.

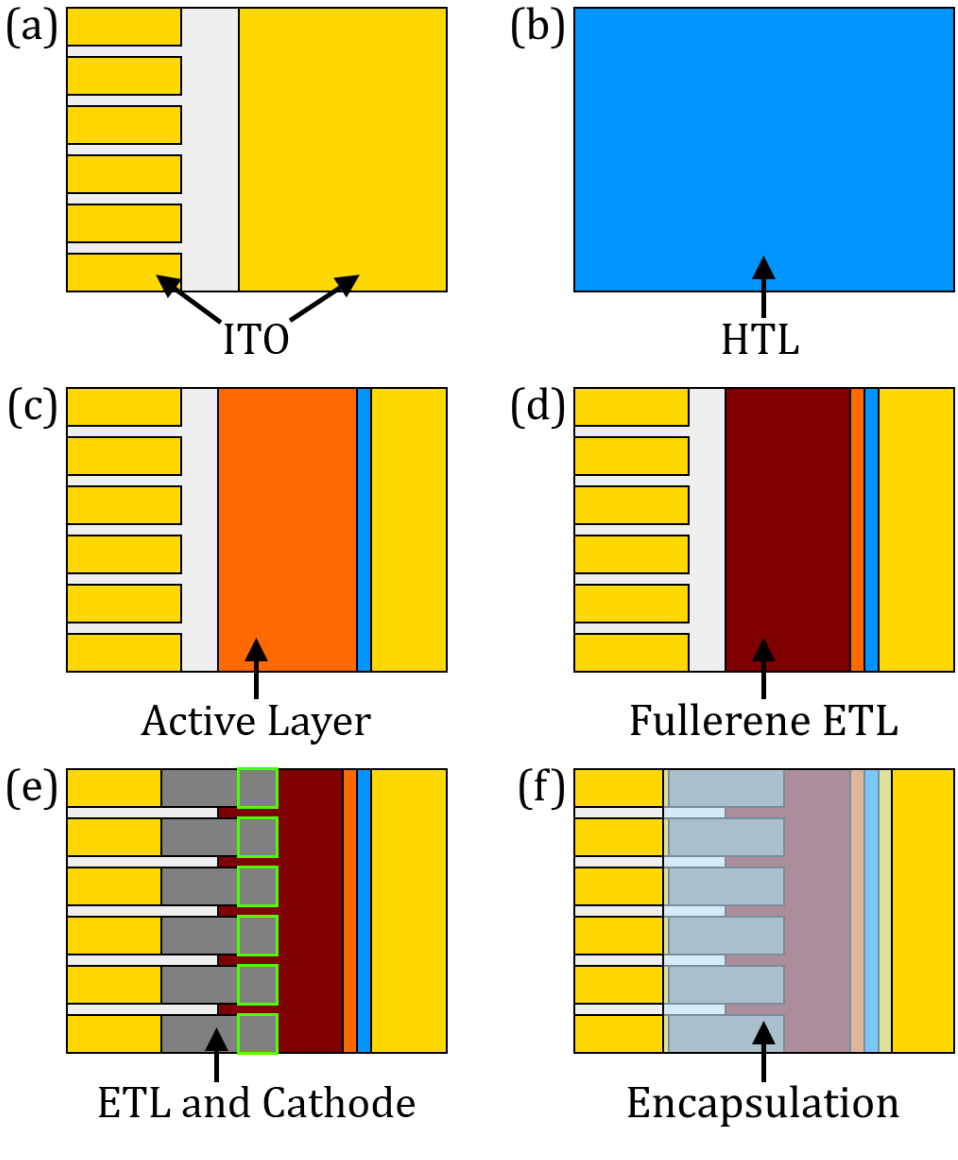

Figure 3.5: PSC device structure used and areas covered by each layer. The area highlighted in green in part (e) shows the active area of each device (2 x 2 mm).

The perovskite precursor was spin coated from solutions heated to 70°C and onto substrates heated to 90°C, creating 350 – 500 nm thick films. Both the solution and

substrate were heated on hot plates prior to deposition, so the actual temperatures during deposition were lower than those states. The films were then annealed at 90°C for 90 minutes to covert the precursor materials into a MAPI perovskite film. At the start of the anneal the perovskite and PEDOT:PSS films were removed from the substrate edges using DMF and a cotton bud whilst on a hotplate at 90°C. After annealing was complete, the substrates were removed from the hotplate and allowed to cool to room temperature. This was performed in a fume hood under yellow light. The perovskite films were transferred to a nitrogen filled glovebox before the next layer was deposited. $PC_{70}BM$ was spin coated at 1000 rpm for 30 s to give a 100 – 150 nm layer, and was removed from the substrate edges using CB as shown in Figure 3.5(d).

The ETL and cathode were deposited via thermal evaporation performed under vacuum at a pressure of $\sim 10^{-7}$ mbar. Here, the ETL was either a 2 nm layer of lithium fluoride, deposited at a rate of ~0.1 Å/s, or a 5 nm layer of Ca, deposited at a rate of ~0.2 Å/s. The cathode deposition and device encapsulation were performed using the same method as for the OPVs.

3.4: Device Characterisation

3.4.1: Current Density-Voltage Measurements

To perform power conversion efficiency (PCE) measurements, devices were mounted on a testing board and placed beneath a Newport 92251A-1000 AM1.5G solar simulator. The output light intensity of the solar simulator was adjusted to 100 mW/cm^2 using a calibrated silicon reference cell certified by the National Renewable Energy Laboratory (NREL). A shadow mask was used to define the active area of each device to 0.0256 cm^2. Measurements were performed using a computer controlled Keighley 237 source measure unit, recording the current response of the solar cell as a function of applied bias. PCE measurements of OPVs were performed from -1 to 1 V in steps of 0.01 V. For PSCs the measurements were performed first from -1 to 1 V, then 1 to -1 V at a rate of 0.4 V/s. The PSCs were then light-soaked for 20 minutes before the *J-V* sweeps were repeated. Space charge limited current measurements were performed in the dark from -1 to 15 V

in steps of 0.01 V. When reporting average values, the top 75% of devices, not including dead devices, were used for the calculation.

3.4.2: External Quantum Efficiency

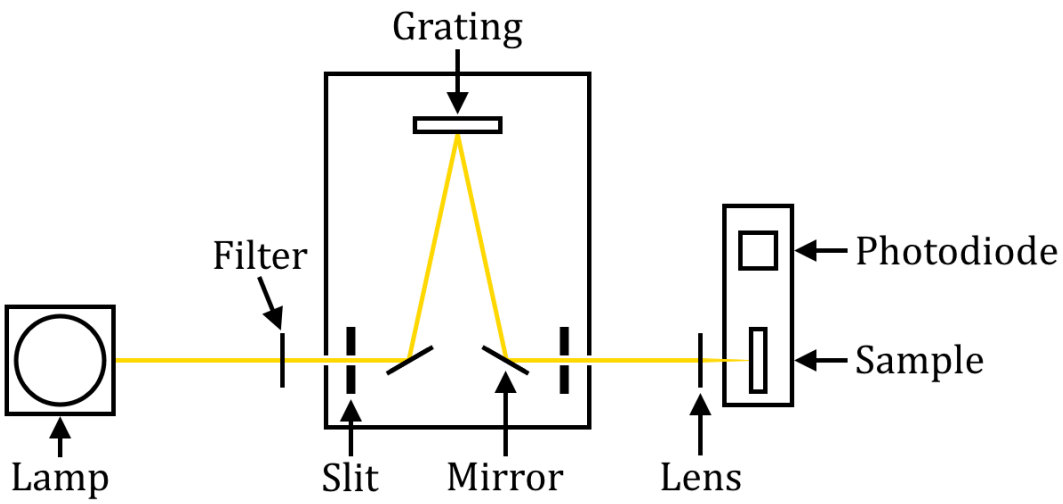

Figure 3.6: Schematic diagram of EQE set-up. The filter is either IR blocking or a 600 nm long pass filter, depending on the range of wavelengths being scanned.

To perform external quantum efficiency (EQE) measurements light from a LOT Oriel LSB117/5 tungsten lamp was passed through a Spectral Products DK240 monochromator, as shown in Figure 3.6. The light was focussed onto a reference silicon photodiode and the current response was measured using a Keighley 237 source measure unit over the desired wavelength range. The measurement was then repeated using the device under test. The EQE was then calculated from the ratio of the device current to the reference current, and normalised to the quantum efficiency of the reference photodiode at each particular wavelength.

3.4.3: Lifetime Testing

Lifetime measurements were performed using an Atlas Suntest CPS+, shown in Figure 3.7, which utilises a 1500 W xenon lamp and coated quartz filters to approximate the AM1.5G solar spectrum. Up to 8 devices were mounted on a custom-built test board by attaching metal 'legs', and placed in the centre of the testing chamber. The chamber was designed such that it provided uniform irradiance, with the temperature maintained at 35°C. A Keighley 2400 source measure unit and a multiplexing unit built by Ossila Ltd. were used to measure the

J-V response of the solar cells. J-V scans were performed from -1 to 1 V at 0.1 V/s, and between measurements the devices were held at open circuit. Shadow masks were not used due to the design of the test board. Before measurements were performed, the system was calibrated using software provided by Atlas. The system was set to run for at least 30 minutes during which time the calibration equipment measured the temperature and irradiance every 10 seconds and compared them to the values set on the system. These values were then entered into the Suntest CPS+ to correct the output of the system. The system was first set up and calibrated by Edward Bovill, who characterised the light output of the Atlas Suntest CPS+, which can be found in reference [9]. Here, it can be seen that a spectral mismatch exists between the xenon lamp of the Atlas system and AM1.5 solar spectrum, which is relatively small for 350 – 600 nm, but becomes greater at longer wavelengths.

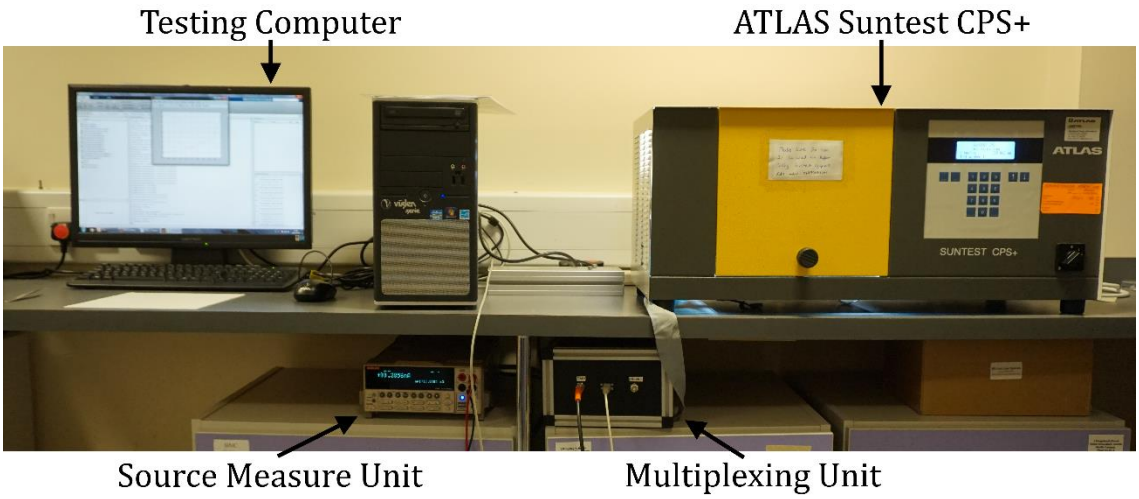

Figure 3.7: Lifetime testing set-up with key components labelled.

To determine the T_{80} lifetime of devices in this thesis a straight line was fit to the data, and the end time of the burn-in was increased until there was good agreement between the fit and the data, indicating that the linear decay region had been reached (see Section 2.3.6). From this data, and the straight line fit, the time taken for the device PCE to reach 80% of the value at the start of the linear section, the T_{80} lifetime, could be calculated.

3.5: Polymer Characterisation

3.5.1: Inductively Coupled Plasma Mass Spectrometry and Optical Emission Spectrometry

Inductively coupled plasma mass spectrometry (ICP-MS) and optical emission spectroscopy (ICP-OES) are high resolution elemental analysis techniques, able to detect elemental compositions in the parts per million (ppm) range. In both systems the sample was introduced as a liquid, which was then vaporised, atomised and ionised by an argon plasma torch. In ICP-MS, the ions are directed through a quadrupole mass filter to allow only ions with a single mass to charge (m/z) ratio to reach the mass spectrometer. In ICP-OES, the light emitted from the ionisation and recombination of the sample was used to determine elemental composition. Specific wavelengths are selected using a diffraction grating and detected by a CCD. The elemental concentration in the sample determines which technique is used, with ICP-MS used for concentrations <100 ppm, and ICP-OES used for concentrations >100 ppm. Analysis of polymer samples containing different Pd concentrations was done by Neil Bramall in the Department of Chemistry, University of Sheffield.

3.5.2: Cyclic Voltammetry

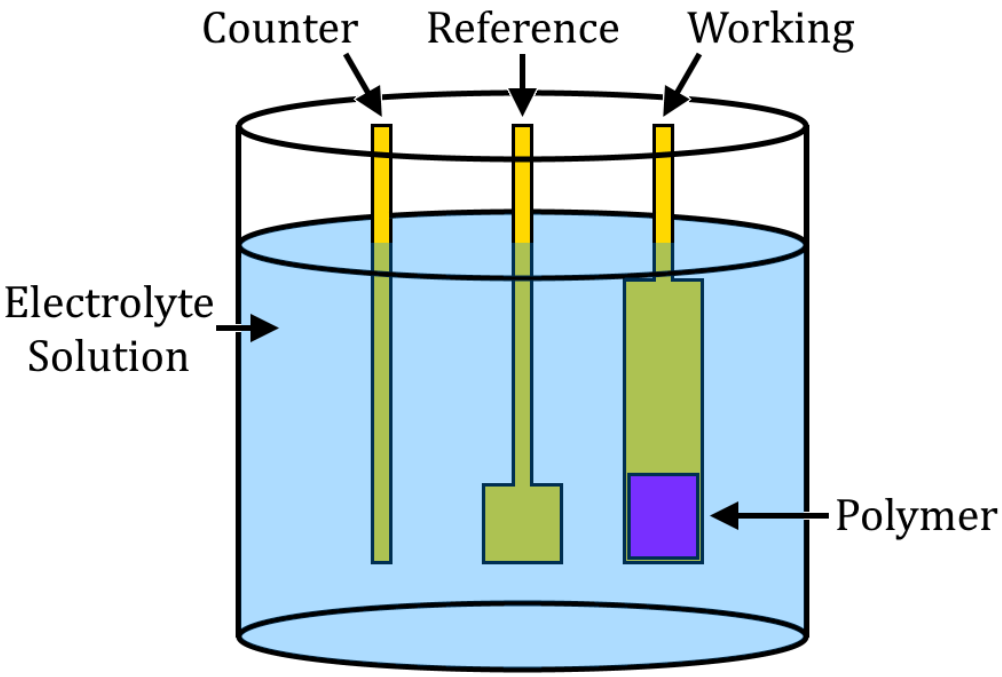

Figure 3.8: Schematic diagram of the cyclic voltammetry set-up, highlighting the working (platinum), reference (Ag/Ag+), and counter (platinum foil) electrodes. A potentiostat and current-voltage converter were connected to the electrodes to perform the measurements. The electrolyte was tetrabutylammonium hexafluorophosphate solution in acetonitrile.

As the HOMO and LUMO energy levels of a polymer are synonymous with the ionisation potential and electron affinity respectively, they can be estimated by measuring the reduction potential, E_{red}, and the oxidation potential, E_{ox}. These are determined through cyclic voltammetry (CV). This is a system consisting of three electrodes: the working, reference and counter electrodes, suspended in an electrolyte as shown in Figure 3.8. The polymer is coated onto the working electrode and the current response between the working and counter electrodes is measured whilst a linearly varied voltage is applied to the working and reference electrodes. From the resultant data the oxidation potential, E_{ox}, and reduction potential, E_{red}, can be extracted, and the energy of the HOMO and LUMO levels, E_{HOMO} and E_{LUMO} respectively, can then be calculated using the following equations (when using ferrocene as a reference) [10,11]:

$$E_{HOMO} = -e[E_{ox} + 4.4] \quad (3.3)$$

$$E_{LUMO} = -e[E_{red} + 4.4] \quad (3.4)$$

CV measurements on polymers of interest were performed by Hunan Yi in the Department of Chemistry, University of Sheffield.

3.5.3: Gel Permeation Chromatography

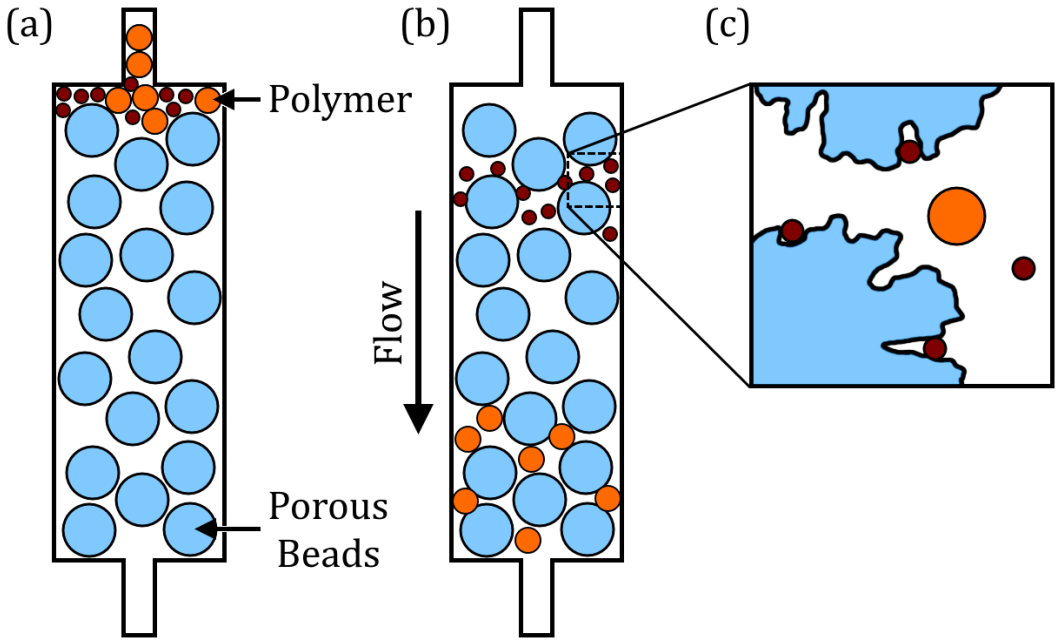

Figure 3.9: Gel permeation chromatography set-up (a) when the polymer is introduced, and (b) after time has passed, with different molecular weight components separated. (c) Zoomed in view of the porous beads, showing smaller polymer chains caught in the pours, resulting in increased transit time, whilst larger polymer chains are unimpeded.

The weight average and number average molecular weight (M_w and M_n respectively) of polymers were determined using gel permeation chromatography (GPC). As shown in Figure 3.9, the polymer is introduced into a column containing porous beads, and the time taken to traverse the column is determined by the molecular weight of the polymer. The shorter the polymer chain, the longer it will take to traverse the column due to increased interactions with the porous beads. Longer chains will pass through quicker due to fewer interactions. Once a polymer chain reached the end of the column a refractive index detector was used to record

the GPC curve, from which the M_w and M_n can be determined. GPC measurements on polymers of interest were performed by Hunan Yi in the Department of Chemistry, University of Sheffield.

3.6: Microscopy

3.6.1: Scanning Electron Microscopy

Scanning electron microscopy (SEM) is an imaging technique able to achieve very high resolution. A beam of electrons is focussed onto the surface of a sample and the resulting interactions can be used to form images. Inelastic scattering of the electrons results in the creation of secondary electrons emitted from the sample, which can be used to form images of a sample surface. This type of imaging is usually performed with a low energy electron beam. Elastic scattering of the electrons can be detected as backscattered electrons (BSE), which can form an image with greater penetration depth into the sample. Images created with BSE also have elemental contrast as the degree of scattering is dependent on the atomic number of the atom being imaged, with larger atomic numbers producing greater backscattered signal. This type of imaging is typically performed with higher energy electron beams.

For both types of imaging, materials were spin cast onto silicon oxide substrates to form 150 nm layers. A conductive silver paint was applied to the edges of the films to provide grounding electrodes and prevent electrostatic accumulation. A FEI Nova NanoSEM 450 was used to perform the imaging. For the BSE imaging, a 5 kV beam with a working distance of 5 mm was used, and the electrons were detected using a solid-state concentric backscatter detector. SEM was performed by Robert Masters in the Department of Materials Science and Engineering, University of Sheffield.

3.6.2: Atomic Force Microscopy

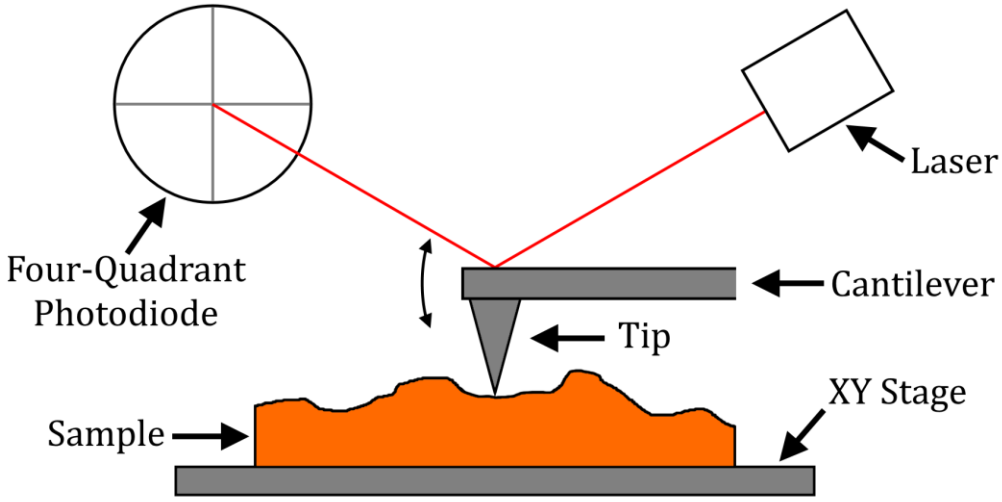

Figure 3.10: Schematic diagram of an atomic force microscope. In contact mode the tip is kept in contact with the surface whilst the sample is moved, whereas in tapping mode the tip is oscillated as indicated.

Atomic force microscopy (AFM) is a surface profiling technique with nanometre resolution achieved through the use of a very fine tip (several nm in size) on the end of a cantilever. Whilst scanning in a raster pattern, the tip is either kept in direct contact with the sample, known as contact mode, or the cantilever is oscillated at high frequency with the tip making intermittent contact with the sample, known as tapping mode. In both cases the displacement of the cantilever is measured through the reflection of a laser from its surface onto a four-quadrant photodiode. AFM images in this thesis were formed using tapping mode to avoid damaging the samples. For tapping mode, the cantilever is oscillated at close to its resonant frequency, with the tip making contact at maximum displacement. When the relative height of the sample changes as the tip is moved the maximum amplitude of oscillation measured by the photodiode changes. An electronic feedback loop monitors this signal and changes the height of the cantilever to maintain a constant oscillation amplitude. By recording the relative height at each position, a topographical image of the sample can be constructed. The sample is mounted on a piezoelectric XY stage to perform the raster scan and the cantilever is mounted on a piezoelectric Z stage to control height.

AFM measurements were performed using a Veeco Dimension 3100 AFM, and AFM tips used had a resonant frequency of 300 kHz, a spring constant of 40 N/m and were purchased from Budget Sensors (Tap300Al-G).

3.7: Spectroscopy

3.7.1: UV-Visible Spectroscopy

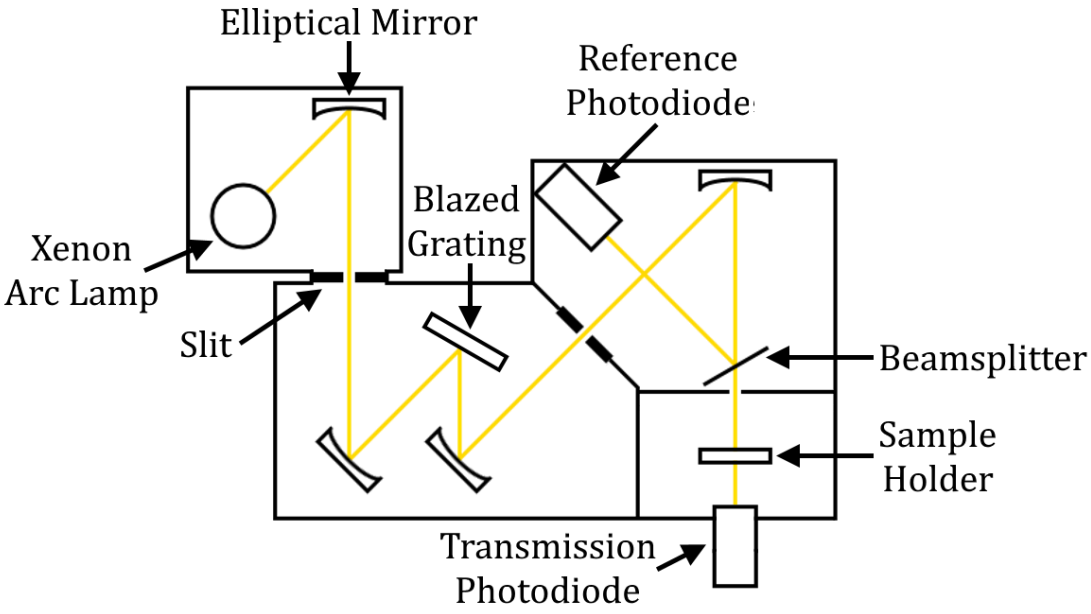

Figure 3.11: Schematic diagram of the interior workings of the Fluoromax.

Absorption spectroscopy measurements over the spectral range 300 nm to 900 nm were performed using a Horiba Fluoromax 4 spectrometer, shown schematically in Figure 3.11. A 150 W xenon arc lamp is used as a light source. The light is passed through a slit, used to control the light intensity, via an elliptical mirror into a Czerny-Turner monochromator [12]. Another mirror then collimates the light and directs it onto a blazed diffraction grating, which in turn reflects the diffracted light towards a third mirror. The wavelength of light directed to this mirror is dependent on the relative angle of the diffraction grating to the two mirrors. The light exits the monochromator through a second slit, and is directed towards the sample. Spectra were taken in transmission geometry, with light collected after passing through the sample, and normalised to incident light intensity collected via

a beam splitter located before the sample. The spectral resolution of this system is estimated to be 1 nm.

The transmittance, *T*, of the sample, and hence the absorbance, *A*, can be calculated using Equation (3.5) [13]:

$$T = \frac{I(\lambda)}{I_0(\lambda)} = 10^{-A} \tag{3.5}$$

Here, $I(\lambda)$ and $I_0(\lambda)$ are transmitted and incident light intensity respectively. The transmittance is the ratio of transmitted light to incident light and includes absorption, scattering and reflection caused by the sample. All measurements were normalised to blank reference substrates to account for reflection losses from the substrate.

3.7.2: Spatially Resolved Photoluminescence Spectroscopy

Spatially resolved photoluminescence measurements were used to acquire PL spectra from localised features in a film. To perform this a 100 mW, 532 nm laser was focussed onto the sample using a 100x Mitutoyo Plan Apo Infinity Corrected Long Working Distance objective lens, achieving a laser spot of approximately 5 μm diameter. The emitted PL was collected using the same lens and passed into a Jobin Yvon Triax 320 spectrometer. The spectrometer measured the spectra by reflecting the light with a diffraction grating onto a liquid nitrogen cooled CCD. A neutral density filter wheel was employed to control the laser intensity and a 532 nm long pass filter was used to prevent illumination from the laser from entering the spectrometer.

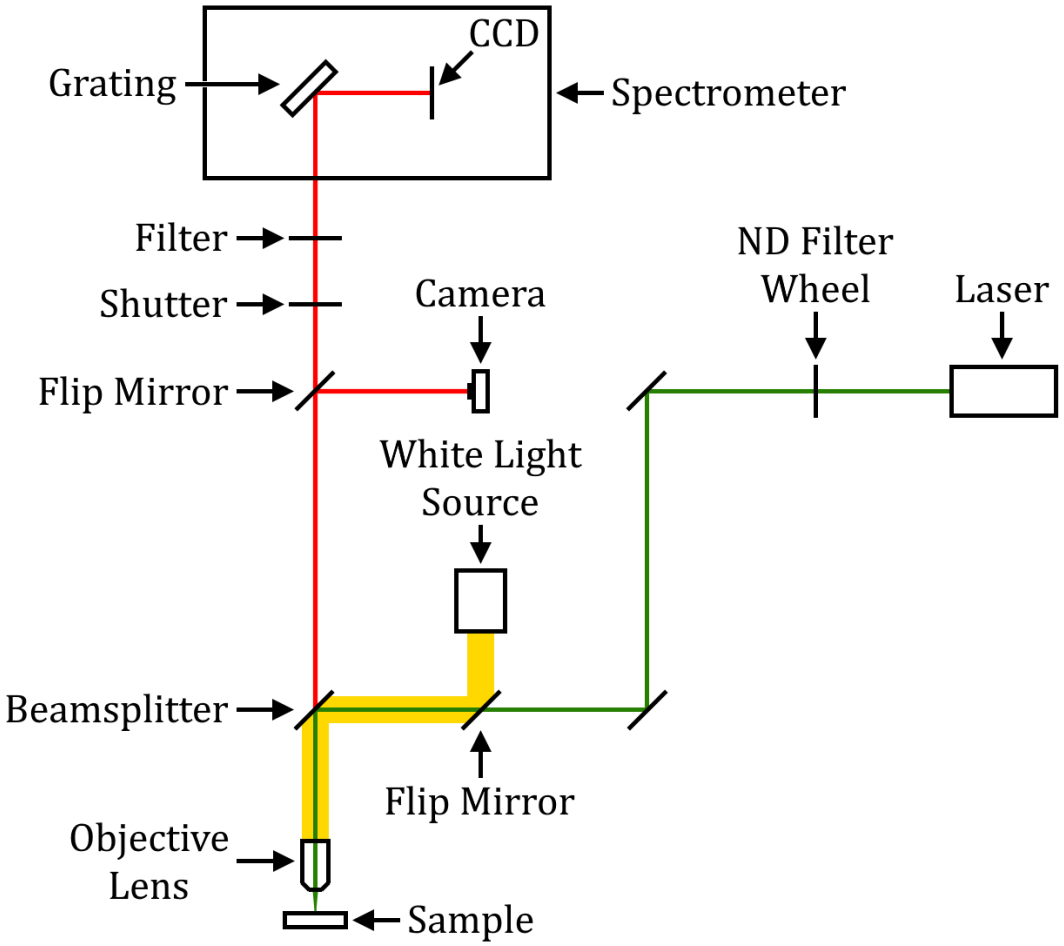

Figure 3.12: Schematic diagram of the spatially resolved photoluminescence set-up.

3.7.3: Time Resolved Photoluminescence Spectroscopy

Time resolved photoluminescence (TRPL) was performed using a 225 μW, 507 nm pulsed laser (2.5 MHz) connected to a single-photon counting system, as shown in Figure 3.13. The laser was focussed onto the sample at 45˚ and the PL emission was collected by a PicoQuant single photon avalanche diode. By measuring the relative intensity of the PL emission between each laser pulse, the charge carrier lifetime could be extracted. A 550 nm long pass filter was used to prevent laser light from entering the detector. Measurements were performed under vacuum of at least 10^{-3} mbar. TRPL data was taken by Benjamin Freestone, Department of Physics and Astronomy, University of Sheffield.

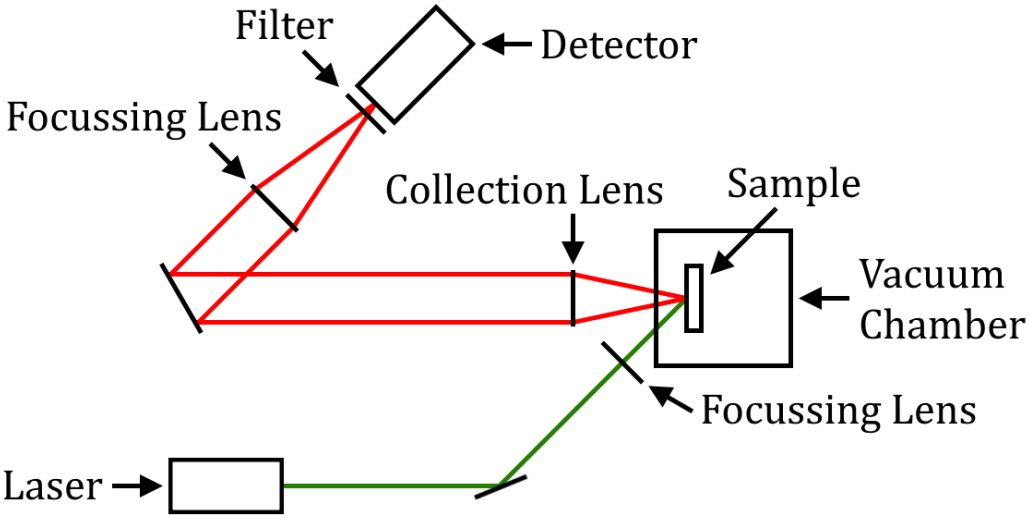

Figure 3.13: Schematic diagram of the time resolved photoluminescence set up.

3.8: Laser Beam Induced Current Mapping

Laser beam induced current (LBIC) mapping is a technique used to determine spatially resolved information about current generation within a device. To perform this, a laser is focussed onto the active layer of a device and scanned across the surface measuring the photocurrent at each point. The resolution of the system is based upon the size of the laser spot incident onto the device and the step size of the stages used to move the device or laser.

To explore both OPVs and PSCs a LBIC mapping system was developed having a spatial resolution of ~1 μm. A LabView program was written to control the motorised stages and a lock-in amplifier was used to record the photocurrent. The following section covers the design, development and calibration of the LBIC mapping system.

3.8.1: Experimental Set-up

In order to perform LBIC mapping, a few key components are required; a laser to excite the device, a lens to focus the beam onto the device, and an XY-stage to move the device so that an image can be constructed. The system is shown in Figure 3.14. Two lasers were employed, a 3mW, 405 nm laser and a 6mW, 670 nm laser. The use of two different wavelength lasers allows for different depths of a device to be

explored, based upon the relative absorption of the material at different wavelengths. By measuring the wavelength dependant refractive index of a material, the penetration depth of light, δ_p, the distance at which light intensity is reduced to 1/e (~37%) of its initial intensity, can be calculated for specific wavelengths using Equation 3.6:

$$\delta_p = \frac{1}{\alpha} = \frac{\lambda}{4\pi\kappa} \tag{3.6}$$

Here, α is the absorption coefficient and κ is the extinction coefficient (i.e. the imaginary part of the refractive index) [14]. The refractive index of $CH_3NH_3PbI_{3-x}Cl_x$ was measured by David Mohamad in the Department of Physics, University of Sheffield, via ellipsometry and gave κ of 1.1 and 0.23 for 405 nm and 670 nm respectively. Using these values with Equation 3.7 gave penetration depths of 30 nm and 230 nm for the 405 nm and 670 nm laser respectively.

The lasers were directed through a neutral density filter wheel and a ThorLabs optical chopper (MC2000-EC) before entering a spatial filter (see Section 3.8.2). Light reflected from the neutral density filter was directed onto a silicon photodiode to account for fluctuations in laser intensity. An iris was used to control the size of the beam exiting the spatial filter, before the beam was reflected into a microscope objective via a 50:50 beam splitter cube, and focussed onto the device. A 50x Mitutoyo infinity-corrected long working distance objective was used to create high-resolution images, and a 10x microscope objective was used for low-resolution images. The device was mounted on a computer controlled XY-stage, consisting of two Zaber X-LSM050A stages, with a ThorLabs MVS005/M manual Z stage used for focussing. Measurements were taken by moving the XY stage in a sawtooth pattern and measuring the current at each point. A Stanford Research Systems SR830 lock-in amplifier was used to maximise the signal.

A camera with a telephoto lens was attached to the system above the microscope objective to allow for easier focussing of the laser beam. Additionally, a white light source was used to enable the device to be viewed directly, allowing specific areas to be selected for measurement.

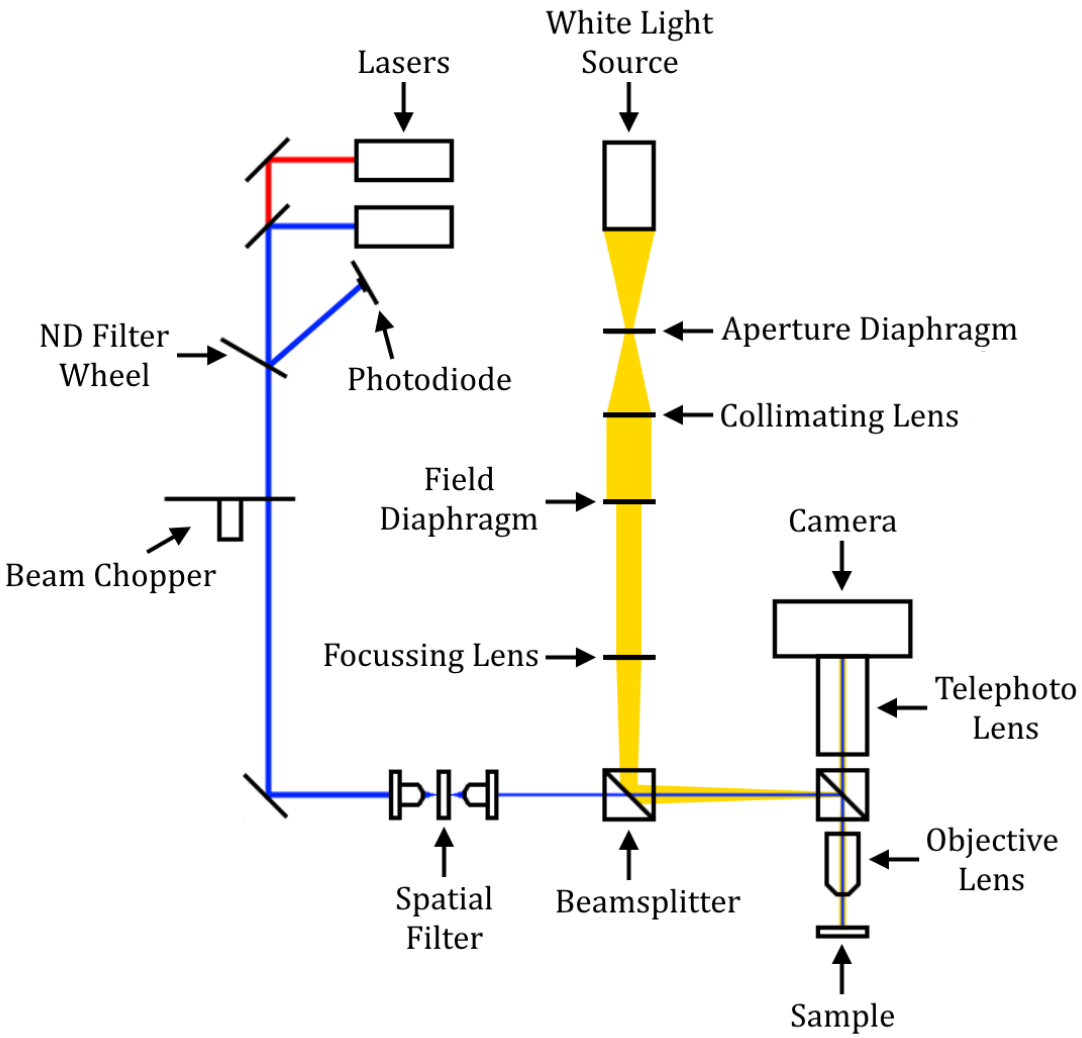

Figure 3.14: Schematic diagram of LBIC set-up. The laser power incident upon the device is 270 nW, with a spot size <1 μm.

3.8.2: LBIC Spatial Resolution

In order to achieve high spatial resolution, it was necessary to minimise the size of the laser spot that was focussed onto the sample surface. As the system is a microscope, the theoretical maximum resolution the system can be calculated using the Abbe diffraction limit [15]:

$$d = \frac{\lambda}{2n \sin\theta} \tag{3.6}$$

Here d is the Abbe limit, λ is the wavelength of light being focussed and $n \sin\theta$ is the numerical aperture (NA) of the objective lens. Initially, a 50x Mitutoyo infinity-corrected long working distance microscope objective was used to focus the laser.

This objective had a NA of 0.55, giving Abbe limits for light at 405 nm and 670 nm of 370 nm and 610 nm respectively. However, the beam emitted from the laser diode was bar-shaped having an uneven intensity profile, surrounded by scattered light and airy disks. This lead to problems when focussing the beam, due to diffraction and interference effects. In order to 'clean up' the beam, a spatial filter, shown in Figure 3.15 was employed. The beam was focussed using a microscope objective, typically resulting in a central spot surrounded by airy disks. A pinhole, with a diameter slightly greater than the central spot of the beam focus, was used to select the central spot, thereby removing the airy disks. The resultant light was collected and collimated using a second microscope objective, creating a circular beam with a Gaussian intensity profile.

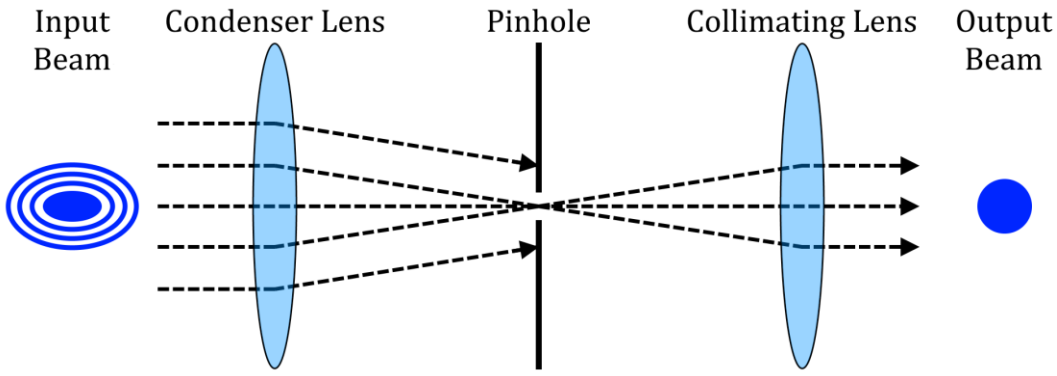

Figure 3.15: Schematic diagram of a spatial filter, showing the input beam before being focussed onto a pinhole, and the collimated output beam after passing through the pinhole.

As devices were imaged through the transparent device substrate internal reflection at the glass-air interface led to the formation of interference patterns, known as Newton's rings, effectively increasing the area being illuminated by the laser, as shown in Figure 3.16. This problem was solved by reducing the size of the beam upon leaving the spatial filter, effectively decreasing the NA of the objective and hence reducing the angle at which the beam was incident on the device. This process has the effect of reducing internal reflection within the device. This unfortunately had the adverse effect of increasing the diffraction limited resolution of the system.

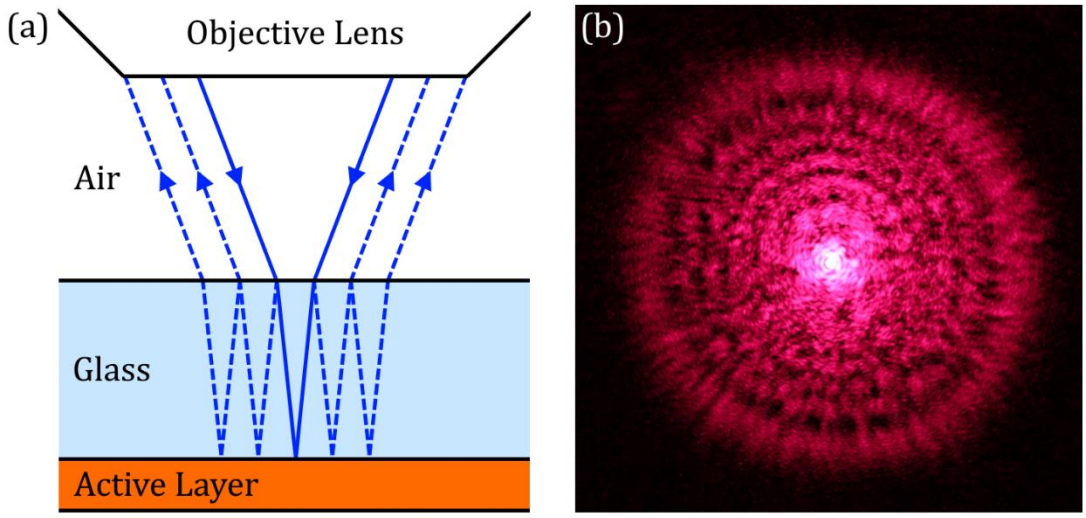

Figure 3.16: (a) Schematic diagram of internal reflection resulting in Newton's rings, and (b) an example of Newton's rings observed in a device.

To determine the size of the focussed laser spot, and hence determine the resolution of the system, the device was replaced with a silicon photodiode. An optical grid with a periodicity of 3 μm was placed above the photodiode. Line scans across the grid were then performed with step sizes of 1 and 0.5 μm, measuring the signal of the photodiode at each point. The scans are shown in Figure 3.17. It can be seen that the scan in 1 μm steps gave an approximate square wave with a period of 3 μm, whereas the 0.5 μm step scan gave a sinusoidal shape. This indicates that the practical resolution of the LBIC system is approximately 1 μm.

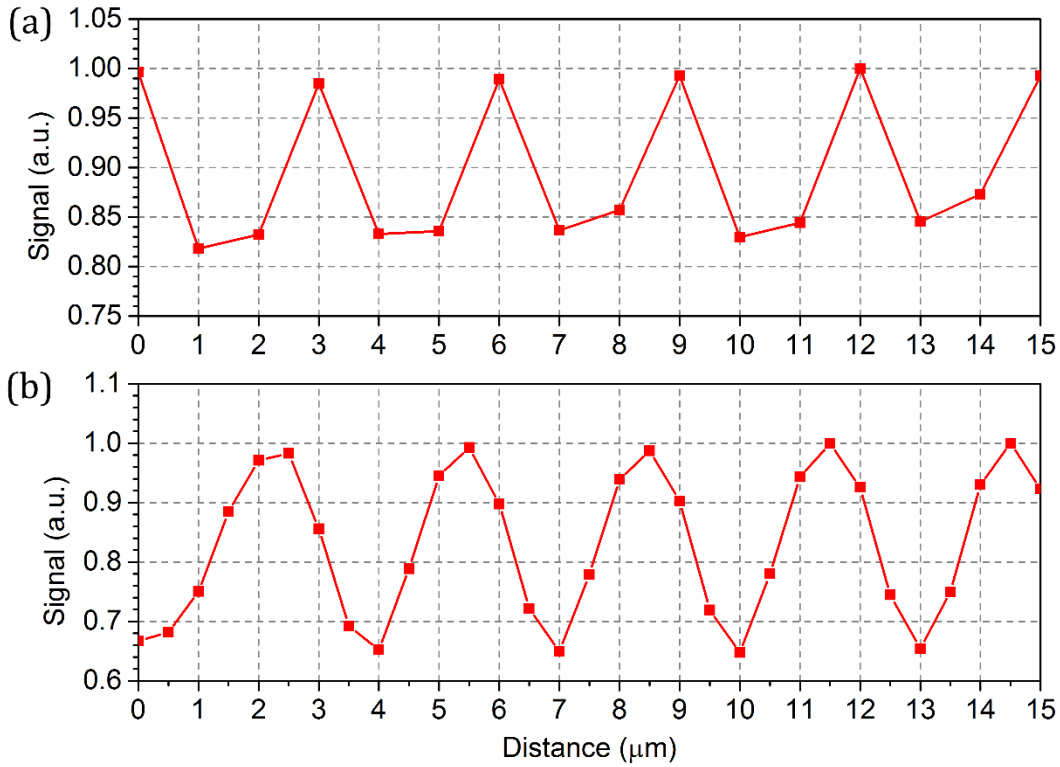

Figure 3.17: Line scans across a 3 μm grid with step sizes of (a) 1 μm and (b) 0.5 μm.

3.8.3: Imaging the Device

Prior to performing an LBIC measurement the system was first optimised by performing a line scan over the edge of a device. The focus of the device was adjusted until the current curve was as steep as possible at the point when the laser moved onto the device. By placing a camera behind the microscope objective, the laser spot could be viewed directly, making focussing faster and easier. The camera was equipped with a telephoto lens to collect the light as the 50x objective used was infinity corrected, meaning the light rays exiting the lens were parallel (collimated), effectively corresponding to an object that was placed at infinity. Telephoto lenses are designed for imaging at very long distances, and hence have long focal lengths, making them ideal for creating an image from infinity corrected light.

A ThorLabs quartz tungsten-halogen lamp (QTH10/M) emitting white light allowed a device to be imaged, allowing particular areas to be selected for study. This enabled the system to act as an optical microscope in reflected bright field

geometry. To illuminate the sample whilst it is in focus without focussing an image of the illumination source onto the same plane, the Köhler illumination technique was used. This is the illumination technique used in bright-field reflected and transmitted light microscopy, developed by August Köhler in 1894 [16]. Here the image of the lamp filament was focussed using a collector lens onto a diaphragm, known as an aperture diaphragm, which shares a conjugate plane with the rear focal plane of the objective. This diaphragm was used to control the intensity of the illumination without altering the field of illumination. Between the aperture diaphragm and the rear focal plane of the objective, the light was collimated and passed through a second diaphragm, known as the field diaphragm, which controls the size of the field of illumination without affecting the intensity. A final lens focussed the image of the filament to the rear focal plane of the objective, producing uniform illumination at the plane of the sample.

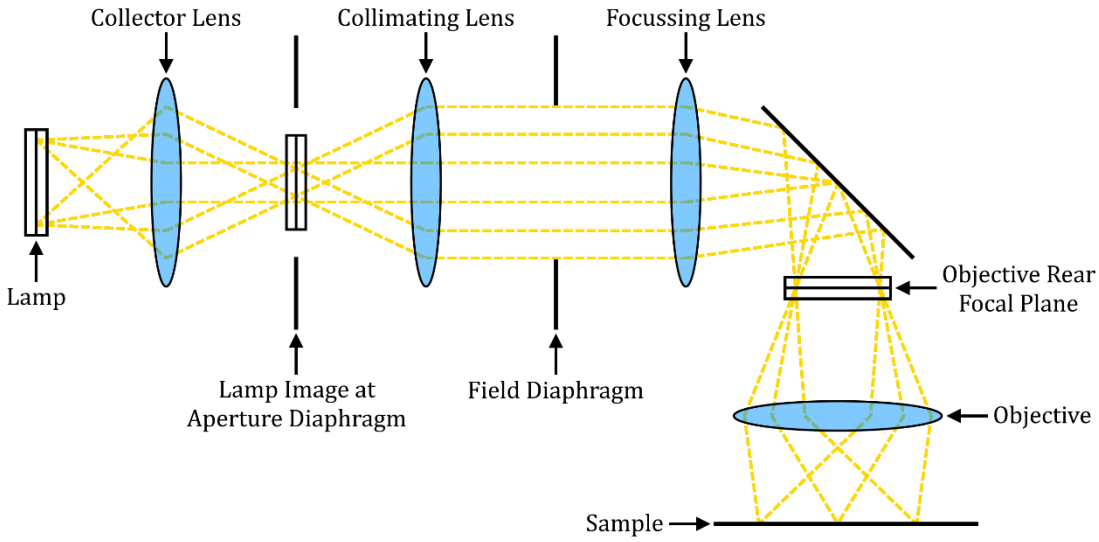

Figure 3.18: Path of light rays for Köhler illumination. The image of the

3.9: Summary

In this chapter, the experimental techniques used in this thesis have been described and explained. Section 3.1 outlined the spin and spray coating techniques for thin film deposition. Spin coating is used in all subsequent chapters, whilst spray coating is used only in Chapter 6. Section 3.2 described the materials used in and the fabrication of OPV devices, which will be used in Chapter 4. The

materials and fabrication of PSCs were covered in Section 3.3, and will be used in Chapters 5, 6, and 7. The techniques in Section 3.4, characterising photovoltaic devices, are relevant to all experimental chapters. The techniques for polymer characterisation described in Section 3.5 will be used in Chapter 4. Section 3.6 covered microscopy techniques, which will be used in Chapters 4 and 7. The spectroscopy techniques in Section 3.6 will be used in Chapters 4 and 5. Finally, Section 3.8 covered the design, set-up, and calibration of a laser beam induced current mapping system, which is used in all experimental chapters.

3.10: References

[1] Spin Coating: A Guide to Theory and Techniques - Ossila, (n.d.). https://www.ossila.com/pages/spin-coating (accessed January 8, 2017).

[2] F.C. Krebs, Fabrication and processing of polymer solar cells: A review of printing and coating techniques, Sol. Energy Mater. Sol. Cells. 93 (2009) 394–412.

[3] K.X. Steirer, M.O. Reese, B.L. Rupert, N. Kopidakis, D.C. Olson, R.T. Collins, D.S. Ginley, Ultrasonic spray deposition for production of organic solar cells, Sol. Energy Mater. Sol. Cells. 93 (2009) 447–453.

[4] R. Green, A. Morfa, A.J. Ferguson, N. Kopidakis, G. Rumbles, S.E. Shaheen, Performance of bulk heterojunction photovoltaic devices prepared by airbrush spray deposition, Appl. Phys. Lett. 92 (2008) 2006–2009.

[5] A.T. Barrows, A. Pearson, C. Kwak, A. Dunbar, A. Buckley, D.G. Lidzey, Efficient planar heterojunction mixed-halide perovskite solar cells deposited via spray-deposition, Energy Environ. Sci. 7 (2014) 1–7.

[6] J. Peet, M.L. Senatore, A.J. Heeger, G.C. Bazan, The role of processing in the fabrication and optimization of plastic solar cells, Adv. Mater. 21 (2009) 1521–1527.

[7] D.K. Mohamad, J. Griffin, C. Bracher, A.T. Barrows, D.G. Lidzey, Spray-Cast Multilayer Organometal Perovskite Solar Cells Fabricated in Air, Adv. Energy Mater. (2016) 1600994.

[8] G. Yu, J. Gao, J.C. Hummelen, F. Wudl, A.J. Heeger, Polymer Photovoltaic Cells: Enhanced Efficiencies via a Network of Internal Donor-Acceptor Heterojunctions, Science (80-.). 270 (1995) 1789–1791.

[9] E. Bovill, N. Scarratt, J. Griffin, H. Yi, A. Iraqi, a. R. Buckley, J.W. Kingsley, D.G. Lidzey, The role of the hole-extraction layer in determining the operational stability of a polycarbazole:fullerene bulk-heterojunction photovoltaic device, Appl. Phys. Lett. 106 (2015) 73301.

[10] J.L. Brédas, R. Silbey, D.S. Boudreux, R.R. Chance, Chain-Length Dependence of Electronic and Electrochemical Properties of Conjugated Systems: Polyacetylene, Polyphenyle, Polytiophene, and Polypyrrole, J. Am. Chem. Soc. 105 (1983) 6555–6559.

[11] L. Leonat, G. Sbarcea, I.V. Branzoi, Cyclic Voltammetry For Energy Levels Estimation of Organic Materials, U.P.B. Sci. Bull., Ser. B. 75 (2013) 111–118.

[12] C. Palmer, Diffraction Grating Handbook, Seventh ed, Newport Corporation, New York, 2014.

[13] E. Hecht, Optics, 5th ed., Pearson, Cambridge, 2016.

[14] H. Zimmermann, Integrated Silicon Optoelectronics, Second, Springer, Heidelberg, 2010.

[15] A. Lipson, S.G. Lipson, H. Lipson, Optical Physics, 4th ed., Cambridge University Press, Cambridge, 2010.

[16] A. Kohler, New Method of Illumination for Photomicrographical Purposes, J. R. Microsc. Soc. 14 (1894) 261–262.

Chapter 4

The Effects of Residual Palladium Catalyst on the Performance and Stability of Organic Photovoltaic Devices

4.0: Introduction

In this chapter, the effect of the residual catalyst palladium (Pd) on organic photovoltaic (OPV) devices is investigated for the semiconducting polymers PCDTBT and PFD2TBT-8. Excess Pd is intentionally introduced to the polymers via the processes given in section 4.1. The effects of this excess Pd on the device performance of both polymers will be presented and discussed. For the PCDTBT devices, a significant loss of power conversion efficiency (PCE) is observed for high palladium contents. This loss is explored through a variety of techniques and found to be a result of an increase in current shunts within the active layer. Increased Pd content is also found to increase PCE losses during the burn-in period of continuous operation. An increase in the density of current shunts, as well as oxidation reactions forming sub-bandgap states are believed to be the cause of this difference in the burn-in period. PFD2TBT-8 devices are found to be much more tolerant to Pd contamination, able to produce devices with comparable efficiencies at both low and high Pd concentrations. This is speculated to be a result of the solubilising alkyl chains preventing the Pd from pulling the polymer out of solution upon deposition, inhibiting the formation of short-circuits. The tolerance is also found to be reflected in the operational stability of such devices, where losses during the burn-in period are found to be much less severe.

4.0.1: Impurities in Organic Photovoltaic Devices

A key requirement in the preparation of semiconducting polymers for OPV devices and in the manufacture of solar cells is the need to minimise the presence of contaminants or impurities. Impurities in OPV devices come in many forms and can be introduced in a variety of ways. The most common form of impurity is palladium (Pd), a catalyst of the cross-coupling polymerisation reactions used to create the light-harvesting conjugated polymers for OPV devices [1–3]. This forms nanoparticles that bind to the polymers, remaining with them and introducing them into OPV devices unless specifically removed [4]. Impurities are also added intentionally to study their effects, for example [6,6]-phenyl-C_{84}-butyric methyl ester ($PC_{84}BM$) has been added to poly[N-90-heptadecanyl-2,7-carbazole-alt-5,5-(40,70-di-2-thenyl-20,10,30-benzothiadiazole)] (PCDTBT):$PC_{60}BM$ devices to act as an impurity [5], this fullerene is of the same family as $PC_{60}BM$ or $PC_{70}BM$, which are commonly used as an acceptor, but has a deeper HOMO and LUMO and so can act as a trapping site for free charges. Different impurities have different impacts of OPV devices through different mechanisms,

The overall performance of OPV devices is generally decreased by the presence of impurities, with deleterious effects observed in all device metrics [6–10]. Despite this polymers do have a tolerance to impurities [9,11], being unaffected below a certain threshold impurity concentration. This tolerance varies between polymers and is also dependant on the type of impurity [8] and knowledge of this is crucial to determine if inherent impurities, such as Pd, need to be removed after polymerisation in order to make functional OPV devices.

A loss of short circuit current density (J_{sc}) with increased impurity concentrations can be attributed to a significant drop in the EQE [7–9]. A reduction in this value can be due to either photons not being absorbed or charge carriers recombining whilst still an exciton or after dissociation. Impurities often have little effect on the absorption of an OPV device [8], certainly not enough to impact the EQE in such a significant way. This leaves the conclusion that the impurities act as trapping sites for charge carriers allowing them to recombine before reaching the electrodes. Transient absorption has further been used to confirm this behaviour. BHJs with impurities present much more rapid polaron decay indicating a decreased hole

population as a result of trap assisted Shockley-Read-Hall recombination [12]. From this state, thermal excitation is required for the electron to escape the localised state, otherwise the electron will recombine.

The polymer being studied influences the effect of the specific impurity, which will be illustrated by looking at the effect of residual Pd on various different polymer systems. When present in PPV (polyphenylenevinylene) or PPE (poly(phenyleneethynylene)) based materials, residual Pd was found to lower the shunt resistance of the active layer film [13,14], indicative of the creation of short circuits through the active layer. In PFB-co-FT (poly{[40-(9,9-bis(2-ethylhexyl)fluoren-2-yl)-20,10,30-benzothiadiazole-7,70-diyl]-co-[20-(9,9-bis(2-ethylhexyl)fluoren-2-yl)thien-7,50-diyl]), Pd resulted in the reduction of hole mobility within the polymer, as well as the creation of trapping states, leading to significant reductions in the fill factor (*FF*) and open circuit voltage (V_{oc}) of devices [10]. A similar effect was observed in P3HT (poly(3-hexylthiophene)) devices, where significant losses of PCE were attributed to reductions in charge mobility and an increase in traps, leading to deleterious effects on all device metrics [15]. An increase in the J_{sc} of PTB7 (poly[[4,8-bis[(2-ethylhexyl)oxy]benzo[1,2-b:4,5-b']dithiophene-2,6-diyl][3-fluoro-2-[(2-ethylhexyl)carbonyl]thieno[3,4-b]thiophenediyl]]) devices with 1 wt.% Pd content was observed before reducing at higher concentrations [11]. The increase is attributed to an increase in conductivity of the active layer film. However, despite the increase in the J_{sc}, the *FF* and V_{oc} of the device exhibit reductions at this concentration due to the Pd acting as charge trapping sites, resulting in lower PCEs.

Whilst $PC_{84}BM$ and Pd can act as trapping sites for charge carriers assisting in recombination, it is useful to examine other impurities as they can exhibit different mechanisms. 14,14,8,8-teracyanoquinodimethane (TCNQ) is another impurity that has been studied, it has the same general effect of reducing the PCE, *FF*, J_{sc}, and V_{oc} of OPV devices but operates in a different way. Instead of acting as a trapping site, TCNQ acts as a long-lived transfer state for excitons. This not only traps electrons in the TCNQ, but also immobilises the holes that are bound to them in excitons [8].

The presence of impurities can also affect the stability of devices, leading to reduced lifespans. It has been reported that significant reductions in J_{sc} can occur after a few weeks of storage in dark, inert conditions due to the presence of organic contaminants at significantly lower molecular weight than the average of the active material [16]. The lower molecular weight contaminants are speculated to diffuse through the active layer to the interface with the cathode with which it subsequently reacts. Indeed, this is supported by the S-shaped *J-V* curve observed after ageing, which is indicative of increased interfacial resistance [17].

There are also reports of impurities that can actually improve the performance of OPV devices. It has been shown that the addition of gold nanoparticles into a poly(3,4-ethylenedioxythiophene):poly(styrenesulfonate) (PEDOT:PSS) hole-transport layer can improve device performance by as much as 29% [18]. The improvement originates from the nanoparticles scattering incident light into the active layer via the amplification of the electrical field around it. Another study showed that introducing 2,3,5,6-tetrafl uoro-7,7,8,8-tetracyanoquinodimethane (F4-TCNQ) into the active layer can significantly increase the J_{sc} of a device by improving the absorption characteristics and hole mobility [19].

4.1: Polymer Preparation and Characterisation

4.1.1: Polymer Synthesis

A polymerisation reaction links monomers, the base units of a polymer, into a covalently bonded chain. As mentioned in section 4.0.1, most conjugated polymers used in OPV devices are synthesised via the Stille and Suzuki cross-coupling polymerisation reactions, which are catalysed by palladium [1–3]. Catalysts are materials that reduce the activation energy of a reaction, increasing its rate, but are not part of the final product. This can occur through the binding of the catalyst to the reagents (materials involved in the reaction), creating intermediate states which would not normally occur, or dissociating the reagents into more reactive forms.

In the Stille reaction, the Pd catalyst first binds with one monomer through oxidative addition, the transfer of two electrons from the Pd to the monomer. The

new compound then binds to the second monomer, which has tin based end groups, through transmetalation. Transmetalation is the process in which ligands, molecules attached to a metal, are transferred from one metal to another. Here, the monomer is transferred from the tin end group to the Pd catalyst. The Pd catalyst is then removed from the new compound through reductive elimination, the transfer of electrons from the compound to the Pd. The Pd catalyst can then be used in another reaction, so the cycle repeats until the polymerisation is complete [1,3].

The Suzuki reaction is similar, except uses boron instead of tin as the end groups on some of the monomers. There is also an addition metathesis step before the transmetalation [2], in which the bonds of two chemical species are exchanged, i.e.:

$$A\text{-}B + C\text{-}D \longrightarrow A\text{-}D + C\text{-}B$$

During either of these polymerisation reactions, there is the possibility of the Pd catalyst breaking down. If this occurs, the Pd forms nanoparticles which can bind to the polymer, remaining with it unless specifically removed [4,11,15].

4.1.2: Polymer Pollution

To achieve a higher Pd concentration in the polymers 1 g of the stock material was added to 50 ml of toluene and was placed in a 250 ml round bottom flask and then heated up to reflux for 3 hours under argon. The mixture was cooled down and to this mixture 16 ml of tetraethylammonium hydroxide (Et_4NOH), 21.8 mg of palladium acetate ($C_4H_6O_4Pd$) and 59.1 mg of tri(o-tolyl)phosphine ($(CH_3C_6H_4)_3P$) were added and then degassed. The mixture was heated to 93 °C overnight and cooled to room temperature. The PCDTBT was precipitated with methanol, collected by filtration and dried under vacuum, providing a 'polluted' polymer. This method is basically repeating the polymerisation reaction used to create the polymer. This produced a 'Pd polluted' polymer batch. The pollution procedure was performed by Hunan Yi, Department of Chemistry, University of Sheffield.

4.1.3: Polymer Cleaning

The Pd concentration of the polymers was lowered by dissolving 1 g of the stock material in 300 ml of chloroform (CF) and adding 300 ml of ammonium hydroxide

solution (28% in water)(NH_3(aq)). The solution was heated to reflux for 4 hours and left to cool overnight. Pd is soluble in NH_3(aq) whereas the polymers are not, so this will remove some of the Pd. The organic phase was separated from the NH_3(aq) through the addition of 300 ml of DI water, with which NH_3(aq) is miscible. 500 mg of ethylenediamine-tetraacetic acid disodium salt dehydrate (EDTA), Figure 4.1(a), was then added to the CF solution and stirred overnight.

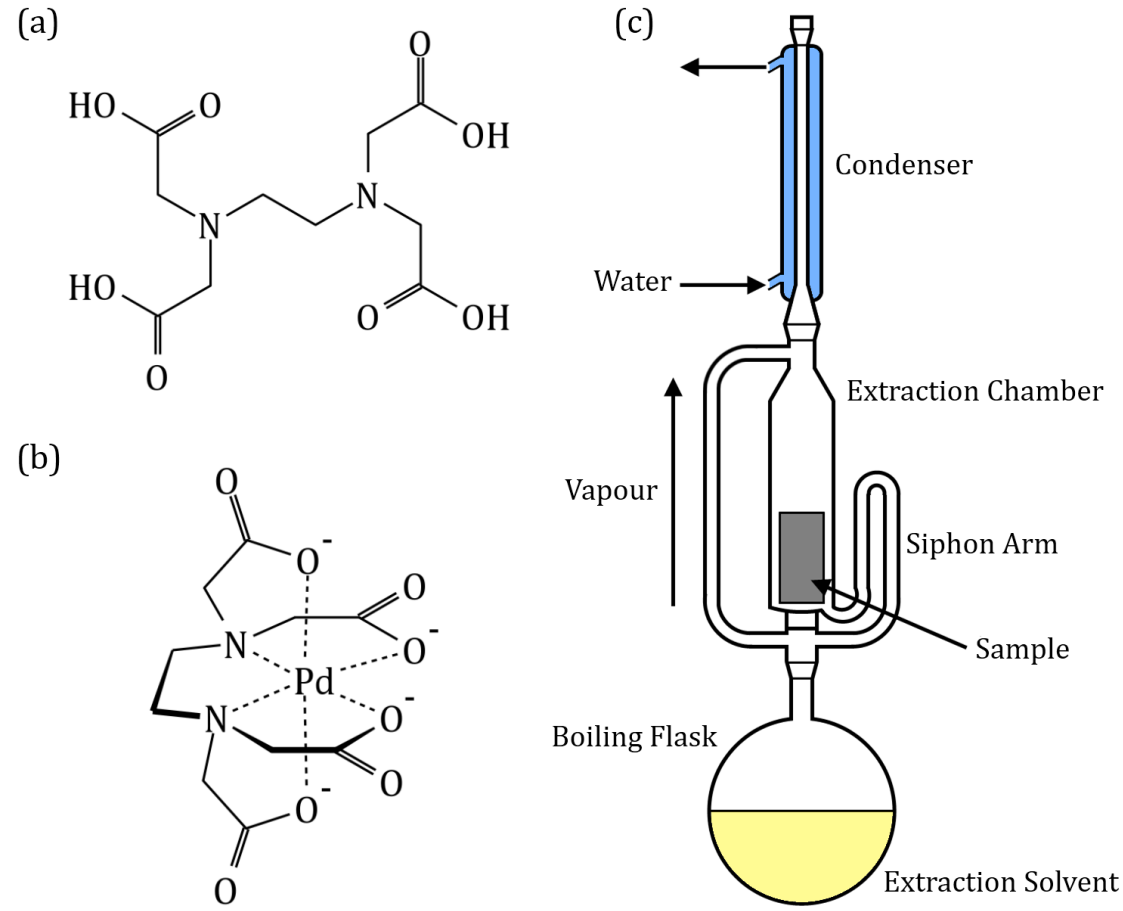

Figure 4.1: (a) EDTA, (b) EDTA-Pd, (c) Soxhlet extraction system.

EDTA has 4 single bond oxygen atoms and 2 central nitrogen atoms that bind strongly with metals, as shown in Figure 4.1(b), sequestering them and reducing their reactivity. It was removed through the addition of 300 ml of DI water in which it is soluble. A rotary evaporator was used to evaporate most of the CF, and the polymer was precipitated through the addition of methanol, collected by filtration and dried under vacuum. A series of Soxhlet extractions were performed using methanol, acetone, and hexane to remove any inorganic materials that may

have remained with the polymer. A Soxhlet extraction is a process of repeatedly 'washing' a sample with solvent to either remove impurities or extract a desired portion of the sample. To perform a Soxhlet extraction, the material is placed in a 'thimble' inside a special piece of glassware shown in Figure 4.1(c). The solvent being used for the extraction is added to a boiling flask at the bottom of the set-up to act as a reservoir and is heated to reflux. The solvent vapour rises to the condenser and is collected at the sample, dissolving the soluble portion. Once the collected solvent reaches the top of the siphon arm it returns to the reservoir. This process is repeated overnight to assure thorough removal of impurities. A final extraction using chlorobenzene (CB) was performed, and the polymer was precipitated with methanol, collected by filtration and dried under vacuum. This resulted in a 'clean' batch of polymer

4.1.4: Palladium Content and Molecular Weight of PCDTBT

The stock PCDTBT had a Pd concentration of 238 ppm and a molecular weight of 15,382 Da after synthesis. This was then put through both the pollution and cleaning procedures to create high and low Pd content batches.

The 'Pd polluted' PCDTBT batch, had a Pd concentration of 2570 ppm as measured by ICP-OES. This batch of PCDTBT had a molecular weight of 19,070 Da. This small apparent increase in molecular weight compared to the stock material (M_n = 15,382 Da) most likely resulted from additional coupling reactions during the pollution process, as some of the stock PCDTBT may still have had end-groups bearing either bromide or boronic ester. The pollution procedure was performed by Hunan Yi, Department of Chemistry, University of Sheffield.

This 'clean' batch of PCDTBT, had a Pd concentration of 0.1 ppm as measured by ICP-MS. The molecular weight of the cleaned PCDTBT was 15,755 Da; a value is in close agreement with that of the stock material (15,382 Da), indicating that the cleaning process does not result in chain scission. The Pd concentrations and molecular weights of the stock, clean, and polluted PCDTBT are given in Table 4.1. Importantly, the absorption and fluorescence properties of the stock PCDTBT (238 ppm), clean PCDTBT (0.1 ppm) and polluted PCDTBT (2570 ppm) are identical, shown in Figure 4.2, indicating that the pollution and cleaning processes did not

result in significant degree of chemical oxidation or the production of non-radiative defects.

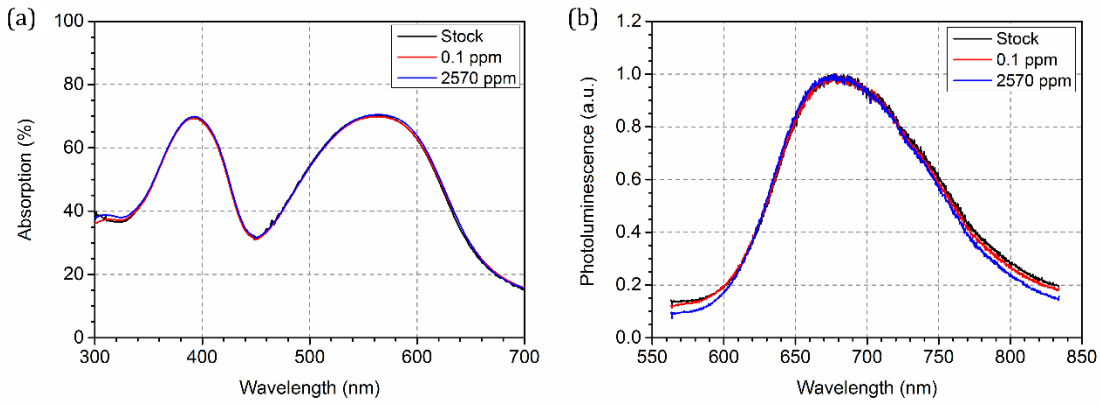

Figure 4.2: (a) Absorption and (b) photoluminescence spectra of thin films (~70 nm) of the stock PCDTBT and the PCDTBT with 0.1 and 2570 ppm Pd.

PCDTBT Batch	**Pd Concentration** (ppm)	**Molecular Weight** M_n (Da)
Stock	238	15,382
Cleaned	0.1	15,755
Polluted	2570	19,070

Table 4.1: The palladium concentrations and molecular weights for each batch of PCDTBT.

4.2: The Effects on PCDTBT:$PC_{70}BM$ Photovoltaic Devices

To explore the role of Pd concentration on device properties, a series of polymer samples were prepared by mixing the clean and polluted PCDTBT batches together at different concentrations. In particular the dry polymer materials were blended in ratios of 5:1, 4:2, 3:3, 2:4 and 1:5, creating a series of samples having assumed Pd concentrations of 0.1, 430, 860, 1290, 1710, 2140 and 2570 ppm. These polymer samples were used to fabricate a series of devices to determine how device operation is affected by the presence of excess Pd. Figure 4.3 shows the average *J-V* curves of these devices, with the average device metrics presented in Table 4.2, and plotted graphically as a function of Pd concentration in Figure 4.4.

Here, it can be seen that all device metrics experience a reduction as the Pd concentration increases, with PCE reduced by 47% at the highest Pd concentration explored (2570 ppm) compared to the devices with the lowest Pd concentration (2.42% and 4.55% respectively). This primarily originates from an increase in the series resistance (R_s) and a decrease in the shunt resistance (R_{sh}), leading to a decrease in the fill factor (*FF*) of the devices with increasing Pd content. As discussed in Section 2.2, R_s is dependent on the energy level alignment and charge mobility of a device, and R_{sh} is dependent on the recombination rate and presence of leakage pathways. These factors were therefore investigated to determine the primary mechanism at work.

Firstly, however, it should be noted that, as shown previously in Table 4.1, there is a ~20% difference between the molecular weights of the 0.1 ppm and 2570 ppm Pd containing polymer samples. It has been shown previously that for PCDTBT OPV devices, the PCE increases as the molecular weight increases, reaching a maximum at 21.5 kDa (after which the PCE reduces) [20]. Here, the opposite effect is observed; efficiency drops in devices based on higher molecular weight PCDTBT. This strongly suggests that the reduction in device efficiency observed here can be correlated with increased Pd concentration, rather than changes in the molecular weight of the polymer.

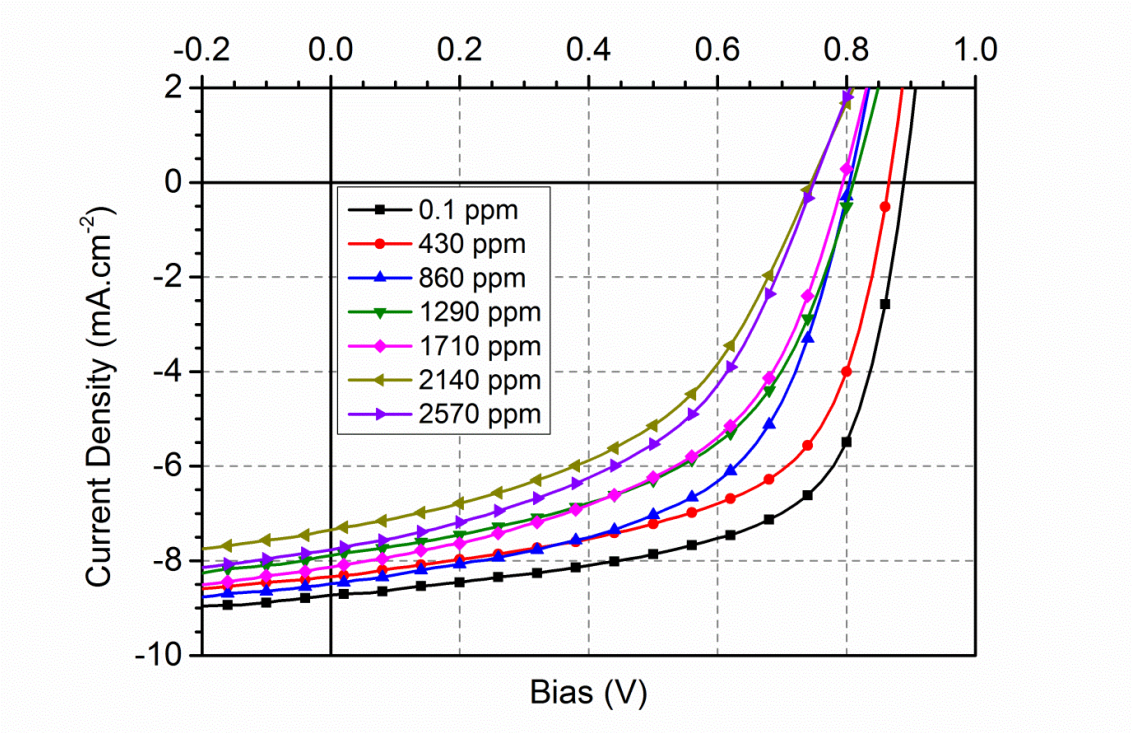

Figure 4.3: J-V curves of PCDTBT:$PC_{70}BM$ devices fabricated with different palladium concentrations.

Pd Content (ppm)	**PCE** (%)	**FF** (%)	**J_{sc}** (mA/cm²)	**V_{oc}** (V)	**R_{sh}** (Ωcm²)	**R_s** (Ωcm²)
0.1	4.6 ± 0.3	60 ± 3	-8.6 ± 0.1	0.89 ± 0.002	700 ± 40	12 ± 1
430	4.0 ± 0.4	57 ± 4	-8.2 ± 0.2	0.85 ± 0.03	660 ± 40	15 ± 2
860	3.4 ± 0.2	53 ± 1	-8.3 ± 0.1	0.78 ± 0.02	510 ± 100	20 ± 3
1290	3.0 ± 0.3	49 ± 2	-7.9 ± 0.1	0.77 ± 0.02	420 ± 80	25 ± 3
1710	2.8 ± 0.4	47 ± 4	-8.0 ± 0.1	0.77 ± 0.02	380 ± 50	25 ± 3
2140	2.3 ± 0.3	45 ± 2	-7.3 ± 0.1	0.71 ± 0.04	380 ± 10	34 ± 1
2570	2.4 ± 0.3	45 ± 3	-7.7 ± 0.1	0.71 ± 0.03	340 ± 30	30 ± 1.0

Table 4.2: Mean device results and standard deviations for power conversion efficiency, fill factor, short circuit current density, open circuit voltage, and shunt and series resistance, extracted from *J-V* curves for PCDTBT containing a range of palladium concentrations. 12 devices were used to calculate the mean and standard deviations for each Pd content.

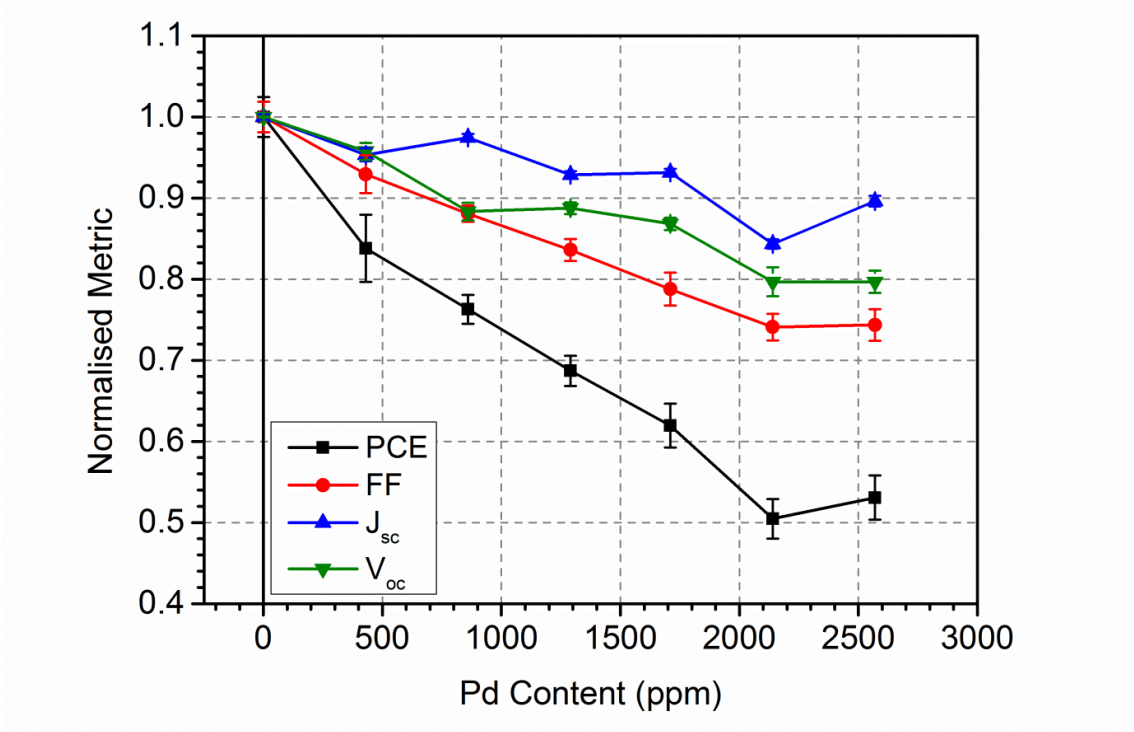

Figure 4.4: Changes in device metrics plotted as a function of palladium content, with data normalised to metrics determined from devices containing the lowest concentration of Pd. The lines are a guide for the eye.

To check whether reductions in device efficiency result from modification of the electronic-structure of the polymer caused by chemical reactions with Pd, which would result in changes of the energy level alignment within the device, cyclic voltammetry was used to determine the energetic position of the highest occupied molecular orbital (HOMO) and lowest unoccupied molecular orbital (LUMO) energy levels, as shown in Figure 4.5. A small difference in the HOMO levels (by 0.08 eV) and a negligible difference in LUMO levels between polymers containing either 0.1 ppm or 2570 ppm Pd was found, indicating that significant changes in electronic structure of the polymer do not occur as a result of Pd contamination. Therefore, the increases in R_s are not a result of significant changes to energy level alignment within the device.

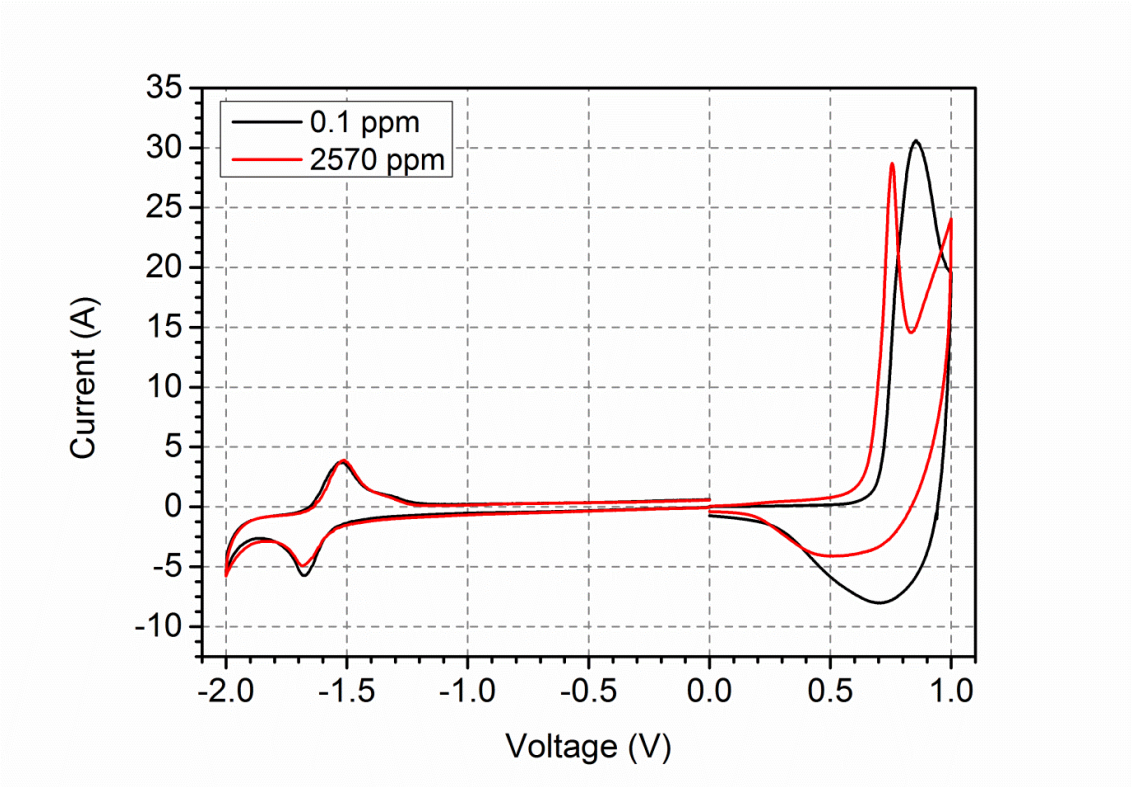

Figure 4.5: Cyclic voltammetry plots of PCDTBT film with 0.1 and 2570 ppm Pd. Ferrocene was used as a reference redox system.

Furthermore, it appears that the Pd does not result in significant changes in the ability of the PCDTBT to transport charge; single carrier devices were fabricated in order to determine the hole and electron mobility of PCDTBT:$PC_{70}BM$ blends at the extremes of Pd content. This data is shown in Figure 4.6, and gave extracted hole mobilities of [3.7 ± 0.1] x 10^{-4} cm^2/Vs and [3.2 ± 0.1] x 10^{-4} cm^2/Vs, and electron mobilities of [1.00 ± 0.04] x 10^{-3} cm^2/Vs and [0.99 ± 0.06] x 10^{-3} cm^2/Vs for the 0.1 ppm and 2570 ppm Pd devices respectively. This suggests that significant changes in hole or electron carrier mobility do not occur as a result of the presence of the Pd catalyst. This further implies no significant increase in charge carrier traps, which would lead to an increase in the recombination rate of the device.

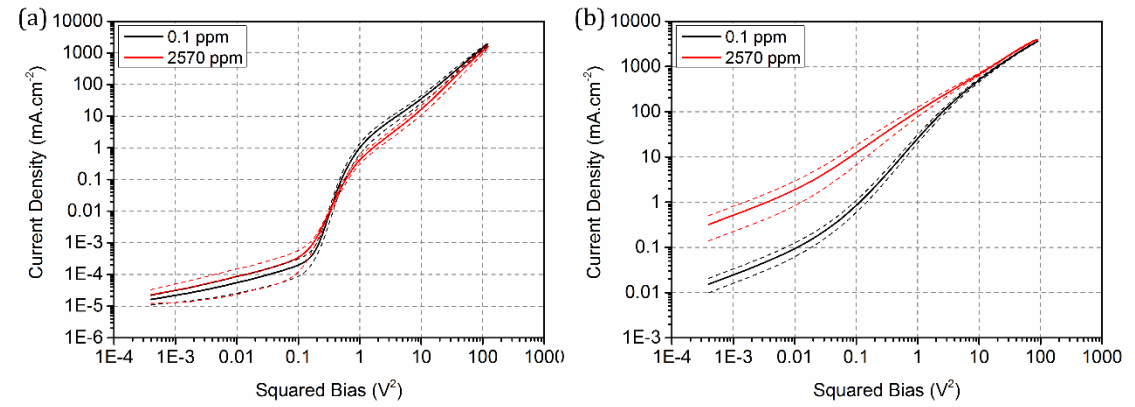

Figure 4.6: J-V curves for (a) hole-only devices and (b) electron-only devices. The dashed lines show the standard deviation of the solid lines.

As the energy level alignment and charge mobility do not significantly change with Pd content, it is therefore speculated that the changes in R_s and R_{sh} as Pd content increases are a result of increased current shunt density within devices. These current shunts create short circuits and leakage pathways within the device, allowing charges to flow between the electrodes. Indeed, previous work has also correlated an increase in R_s and a reduction in R_{sh} and *FF* (which decreased by 26% in devices containing 2570 ppm Pd) with an increased density of shorts circuits within an OPV device [13,21].

To confirm the presence of an increased density of short-circuits in devices containing a large fraction of Pd, laser beam induced current (LBIC) mapping was used. This technique utilises a laser that is focussed to a spot of 5 μm diameter on the device surface and then raster scanned whilst the photocurrent (PC) is recorded. Figures 4.7(a), (b) and (c) show optical micrographs of PCDTBT:$PC_{70}BM$ films that contain 0.1 ppm, 1290 ppm and 2570 ppm Pd respectively, while Figures 4.7(d), (e) and (f) show LBIC maps recorded from the same areas of the film as shown in parts (a) to (c).

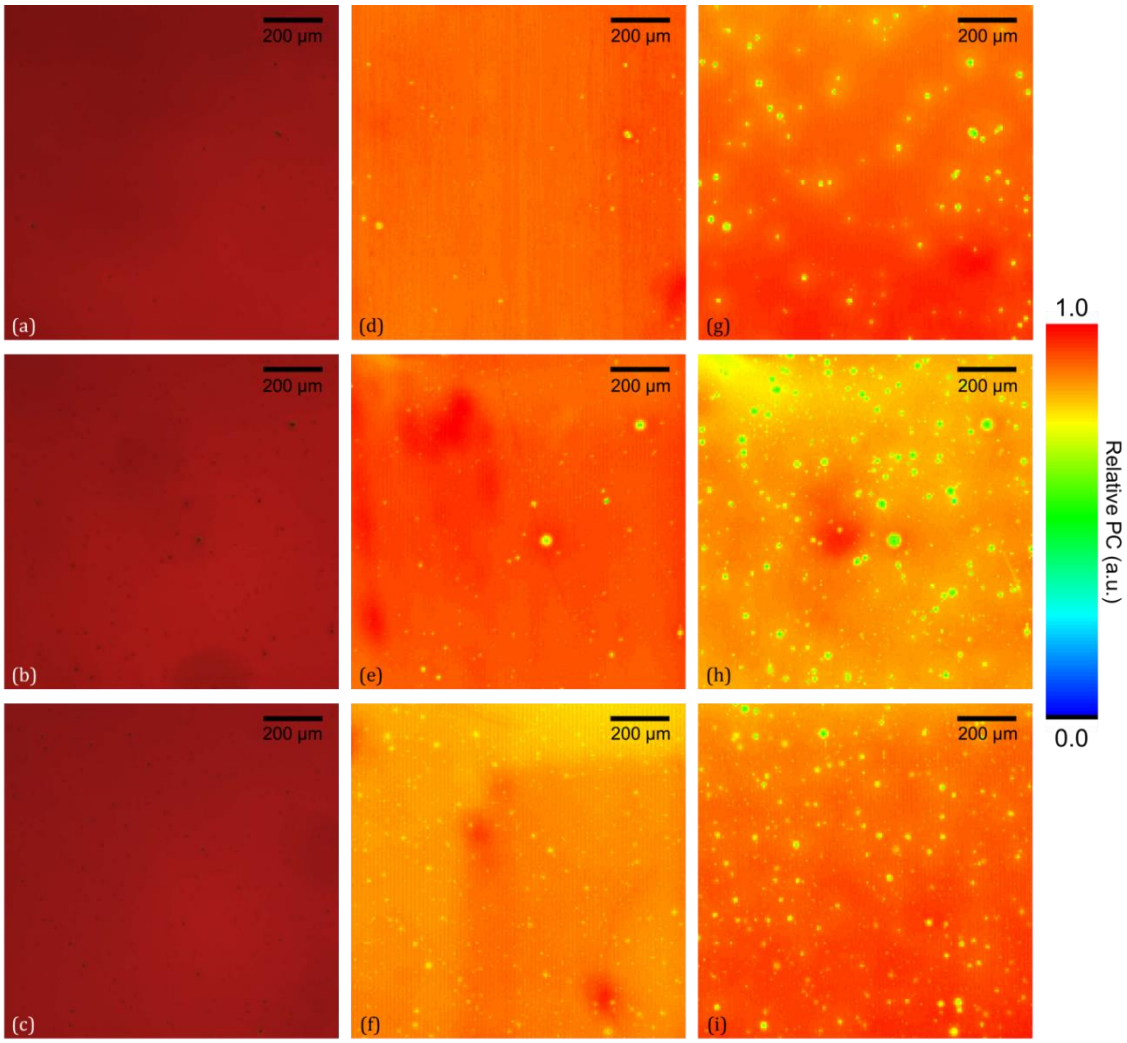

Figure 4.7: Parts (a), (b), and (c) are optical microscope images of 0.1 ppm, 1290 ppm, and 2570 ppm Pd PCDTBT:$PC_{70}BM$ films respectively. Parts (d), (e) and (f) are laser beam induced current maps of the films whose images are shown in parts (a), (b), and (c) respectively. Parts (g), (h), and (i) are laser beam induced current maps of the same areas that have been subjected to 140 hours of continuous illumination. The maps are normalised individually to the peak value in the image.

It can clearly be seen that as the Pd concentration increases, there is a concomitant increase in the relative density of 'dark' spots in the optical microscope images that are associated with reduced photocurrent in the LBIC images. These current 'cold-spots' have a diameter between 5 and 35 microns, and in many cases are larger than the overall thickness of the active polymer:fullerene layer (70 nm). In the film containing 0.1 ppm, 1290 ppm and 2570 ppm Pd, these current 'cold-spots' are estimated to appear at a surface density of 51, 195 and 250 mm^{-2} respectively.

Considering the relatively large size of these features, together with their relatively high density, it is likely that such current shunts are responsible for the reduced FF and PCE of these devices. It can be seen that the density of such cold-spots does not scale linearly with Pd concentration. The reason for this is currently unclear, however SEM imaging (vide infra) indicates that only a fraction of the available Pd forms large defects responsible for the current cold-spots, with the remainder of the Pd being distributed throughout this film at a level that presumably does not cause a current short. It is also apparent that such cold-spots appear overlaid on a background that has fluctuations in PC that occur over lengths scales of 200 microns. These long range fluctuations in PC are likely associated with variations in film thickness and polymer:$PC_{70}BM$ mixing ratio.

To probe the nature of such features within films containing a high concentration of Pd, scanning electron microscopy (SEM) using backscattered electrons has been performed and is shown in Figure 4.8(a) and (b). Here, typical images of two large defects observed in a PCDTBT:$PC_{70}BM$ film containing a 2570 ppm mass fraction of Pd are shown. The feature shown in part (a) has a lateral dimension of approximately 1 μm, with the feature in part (b) being more diffuse in nature, having a lateral size of around 6 μm.

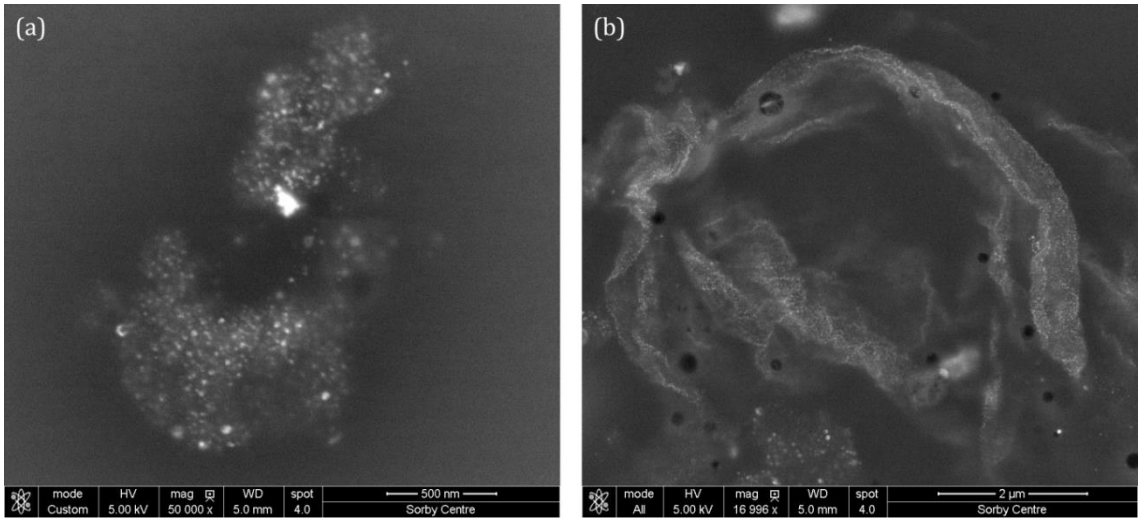

Figure 4.8: SEM images of aggregates using backscattered electrons. The width of the image shown in part (a) (left) has a size of ~1 micron, whereas the image part (b) (right) has a width of 6 microns.

In both cases, these defects are found to be composed of a sub-structure consisting of particles having a size of around 15 to 45 nm. Imaging using backscattered electrons probes the entire depth of the sample, rather than just the surface, indicating that these particles are distributed *throughout* the defect. These nanoscale particles are believed to be composed of Pd; a conclusion confirmed by the fact that the large nuclear charge in Pd nuclei scatters electrons more strongly than the PCDTBT polymer and as such Pd particles produce a larger backscattered signal. Indeed, previous work has shown that palladium nanoparticles bind to conjugated polymers during their synthesis [4] and thus the large aggregates observed in Figure 4.8 are likely composed of both PCDTBT and Pd.

A white light optical image of a typical defect is shown in Figure 4.9(a). As observed in the SEM images presented above, it can be seen that the defect is characterised by a central Pd-containing core that is surrounded by a polymer:fullerene layer of varying thickness, forming a typical "comet" structure. Photoluminescence (PL) spectroscopy has been used to explore the composition of such defects. Here, the PL was excited using light from a 532 nm diode laser focused in a dark-field configuration onto the active layer of an encapsulated device. Emission was collected using a microscope objective lens, with PL spectra being recorded with a spatial resolution of ~5 μm. The PL spectrum recorded from the Pd defect is shown in Figure 4.9(b), with PL spectra recorded from two different areas of the film marked with arrows shown in Figures (c) and (d).

It can be seen that the emission from the defect is significantly different from that recorded from other regions of the film. Figure 4.10 shows the PL emission from a PCDTBT film (Pd concentration of 0.1 ppm) and a thin $PC_{70}BM$ prepared by spin-casting. It appears that PL emitted from the defect is almost identical with that of PCDTBT. The significant similarity between the PL emitted from the defect (shown in Figure 4.9(b), and that of PCDTBT indicate that the defects are composed primarily of PCDTBT and Pd, with little to no $PC_{70}BM$ present. In contrast the emission spectra recorded from other points across the film (see Figures 4.9(c) and (d)) is similar to that of pure $PC_{70}BM$. This behaviour was observed in films over the entire range of Pd concentrations and is consistent with effective

quenching of excitons in PCDTBT, with residual emission occurring from excitons that reside on fullerene aggregates [22].

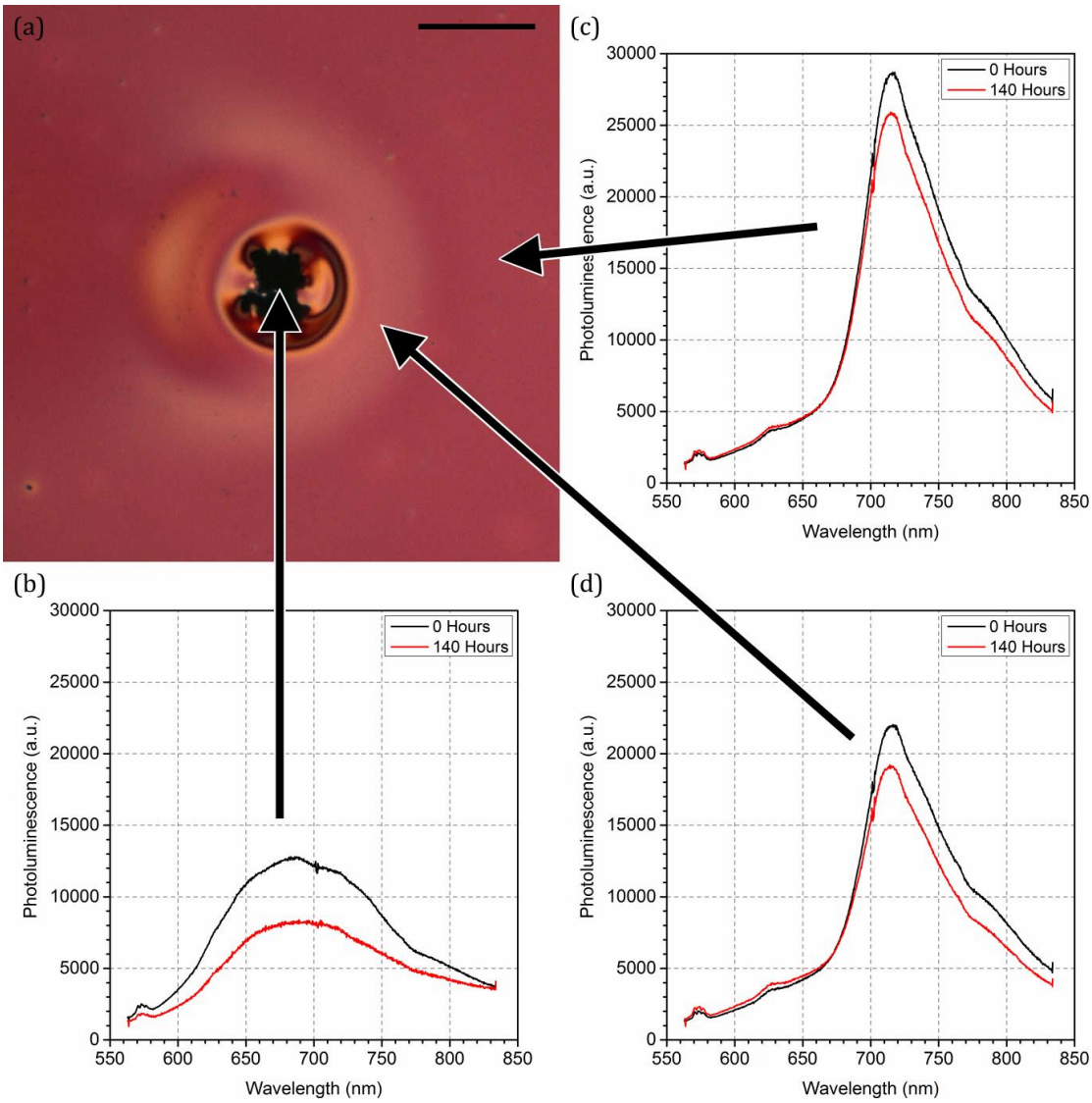

Figure 4.9: (a) Optical microscope image of a defect, with scale bar representing 100 µm. (b) PL spectrum of the defect before and after 140 hours of illumination. (c) and (d) PL spectra of the surrounding film before and after 140 hours of illumination.

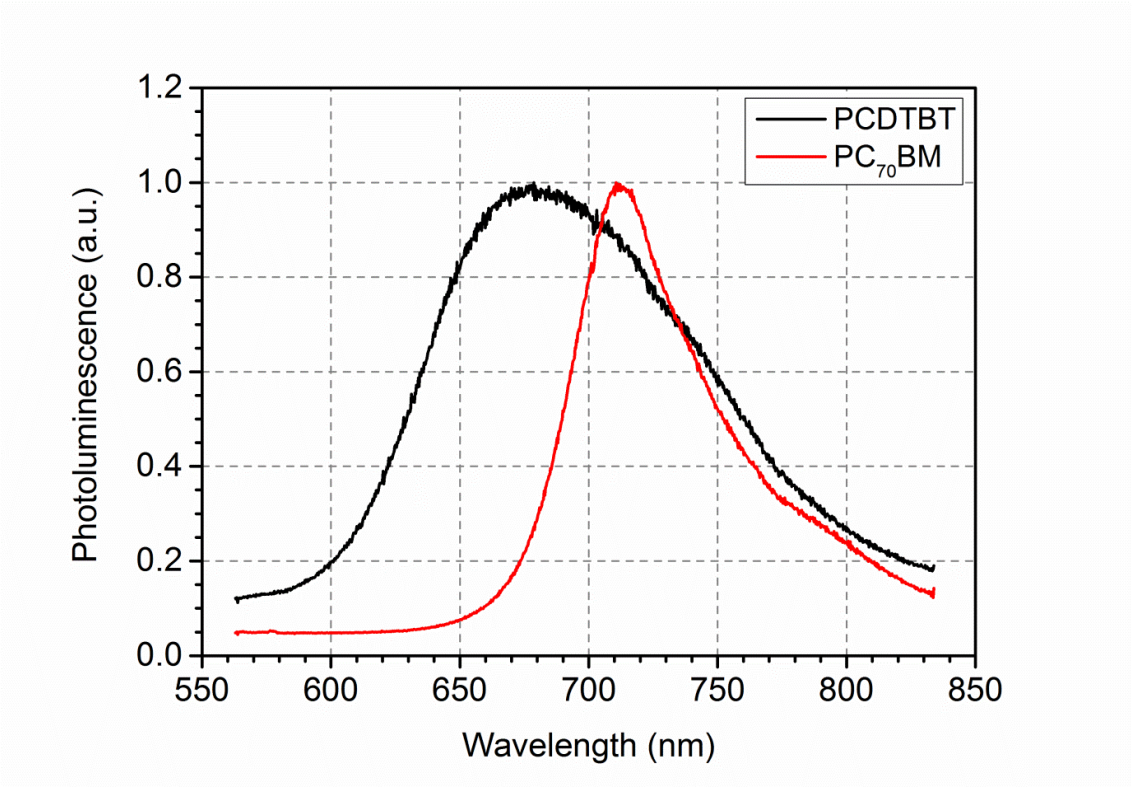

Figure 4.10: Normalised photoluminescence spectra for a PCDTBT thin film and $PC_{70}BM$ thin film.

Therefore it is speculated that when a Pd-contaminated PCDTBT:$PC_{70}BM$ solution is prepared, some PCDTBT polymer-chains become bound to the Pd nanoparticles. On casting a film, the PCDTBT-Pd aggregate "falls out" of solution before the blend film undergoes vitrification, resulting in the formation of a mesoscopic polymer-Pd aggregate structure. The composition of such aggregates therefore appears significantly different from that of the bulk film, and contains a significantly reduced fraction of $PC_{70}BM$.

It has been shown that the presence of the Pd nanoparticles reduces the efficiency of the OPV devices, principally by reducing device *FF* as a result of the generation of localised current shunts. The reduced efficiency of photocurrent generation around the Pd nanoparticles is also likely to result from a reduced probability of exciton dissociation resulting from increased demixing between PCDTBT and $PC_{70}BM$. Indeed, the relative fluorescence emission intensity from films containing a high concentration of Pd is found to be increased (see spectra in Figure 4.11), indicating a relatively higher proportion of $PC_{70}BM$ in these films.

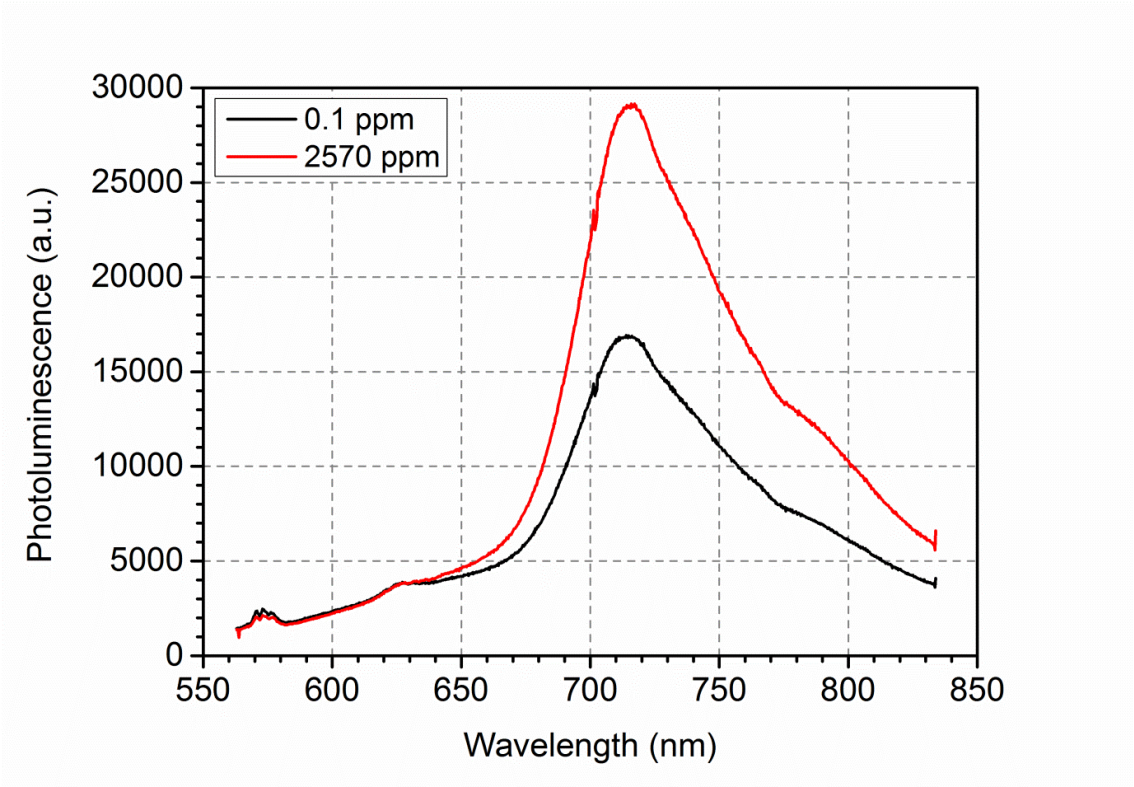

Figure 4.11: Photoluminescence spectra of PCDTBT:$PC_{70}BM$ thin film with 0.1 and 2570 ppm Pd.

It is interesting to determine whether such shunts have any consequence for device operational stability. To explore this issue, an ATLAS Suntest CPS+ lifetime tester (approximating AM1.5 radiation) was used to track OPV device performance over a period of 140 hours of continuous illumination as shown in Figure 4.12 and Figure 4.13. Specifically, Figure 4.12(a) shows the relative (normalised) PCE of devices having a varying concentration of Pd as a function of continuous illumination. This decay in PCE is commonly divided into two regions; a 'fast' initial 'burn-in' period (extending here to 60 hours, as determined using the method in Section 3.4.3) during which the device undergoes rapid degradation. This period is followed by a period in which device degradation is more linear (here shown in Figure 7(b)). It can be seen that the presence of Pd has a significant effect on the initial 'fast burn-in' period, with devices having a higher Pd concentration generally undergoing a larger initial loss in PCE. (Note the device having the highest Pd concentration (2570 ppm) appears slightly more stable than that having a Pd concentration of 2140 ppm. A high degree of significance is not given to this observation and assign this to experimental uncertainty).

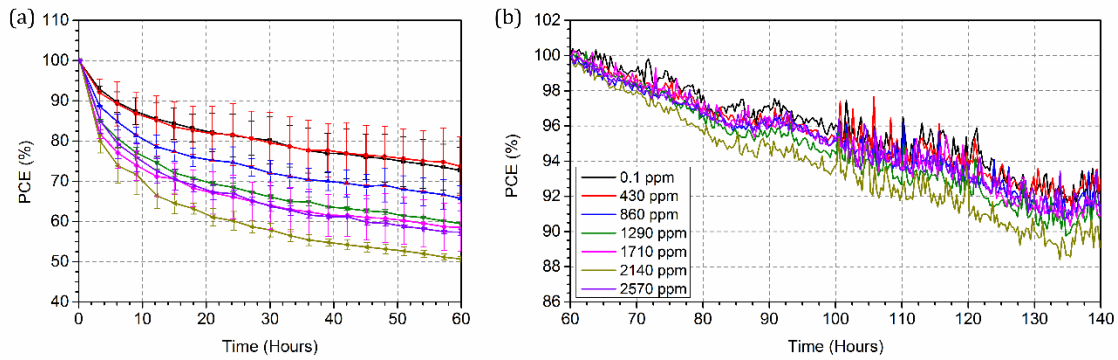

Figure 4.12: (a) PCE over 60 hours of continuous illumination normalised with respect to the initial PCE, corresponding to the burn-in period. (b) PCE from 60 to 140 hours of continuous illumination normalised with respect to the PCE after the burn-in period.

From the more linear decay region (60 to 140 hours), (see Figure 4.12(b)), the Pd content is observed to not have a significant effect on the stability in the more linear period beyond fast burn-in. Indeed, this linear part of the decay-trace is used to calculate the device T_{80} lifetime, defined as the time taken for the device PCE to drop to 80% of its PCE determined after the initial burn-in period. Here, the T_{80} lifetime is estimated to be 274 ± 9 hours in devices containing 0.1 ppm Pd, a value similar to that determined for devices containing 2570 ppm (250 ± 21 hours). This data is summarised in Figure 4.14. Note that the T_{80} lifetimes determined here are reduced compared to previous lifetime studies on PCDTBT devices incorporating a MoO_x anode, where a T_{80} lifetime of 650 – 1000 hours was recorded [23]. The apparently shorter lifetimes observed here is believed to result from the fact that the degradation of devices was only followed over a relatively short time-scale (140 hours), and that some degree of device burn-in was still in progress even at the end of this measurement, making a long-term extrapolation unreliable. Indeed, further measurements are required to explore whether excess Pd concentration plays a role in degradation over time-scales of 1000's of hours. Despite this uncertainty, the results show that devices containing high levels of Pd undergo most rapid degradation in the initial fast burn-in period, with degradation in the period beyond burn-in being less sensitive to the effect of residual palladium catalyst.

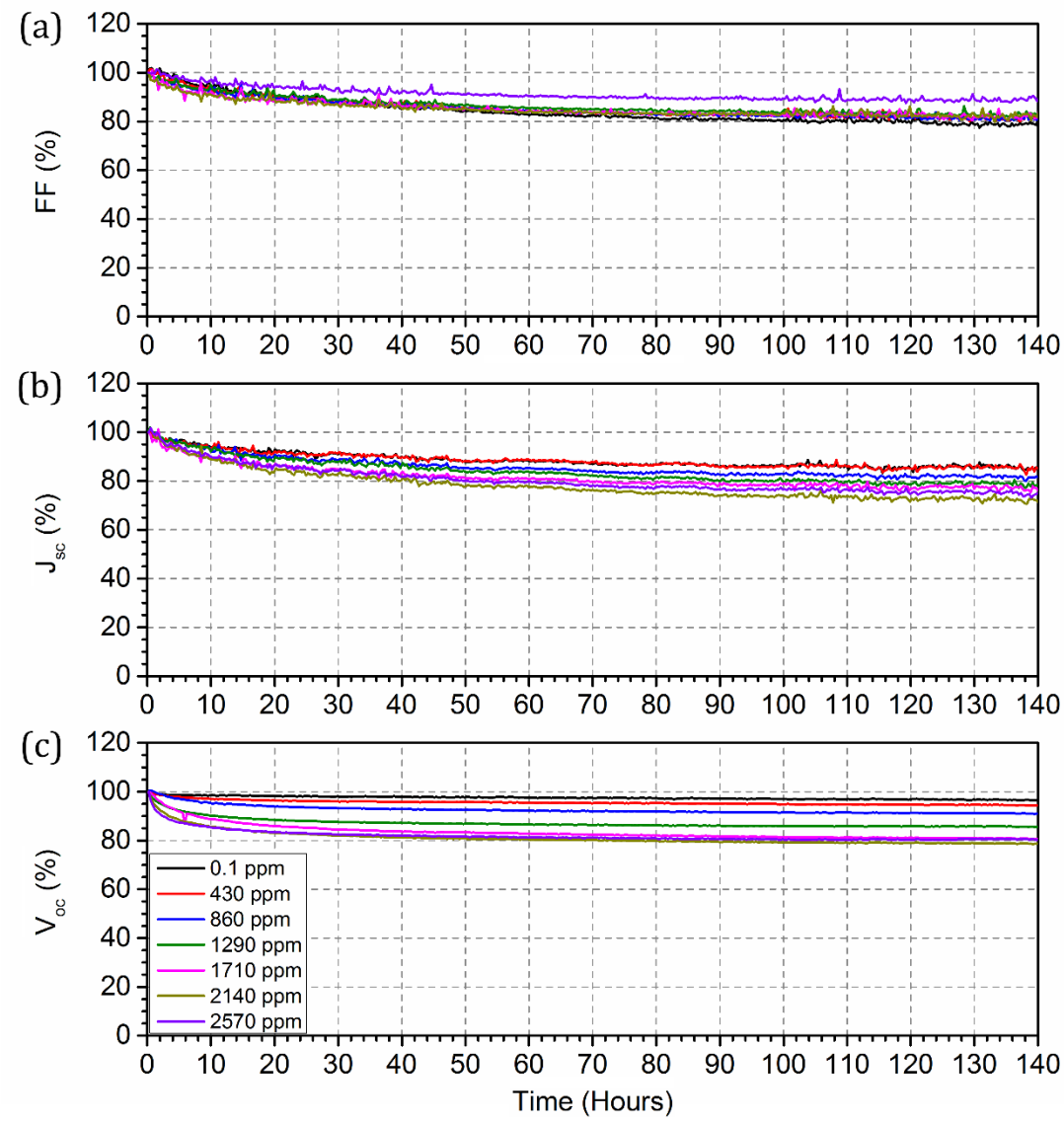

Figure 4.13: Lifetime traces for (a) *FF*, (b) J_{sc}, and (c) V_{oc} of PCDTBT OPV devices with a range of Pd concentrations over 140 hours of continuous illumination.

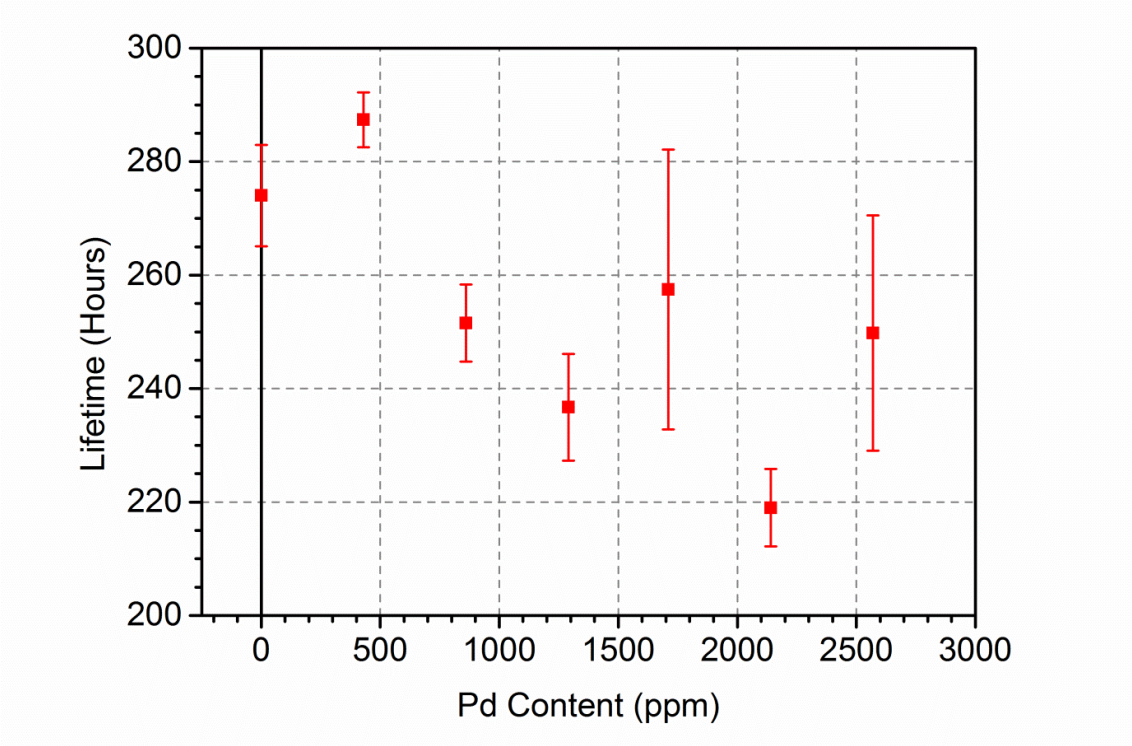

Figure 4.14: T_{80} lifetimes for different palladium content PCDTBT devices calculated from the PCE lifetime curves.

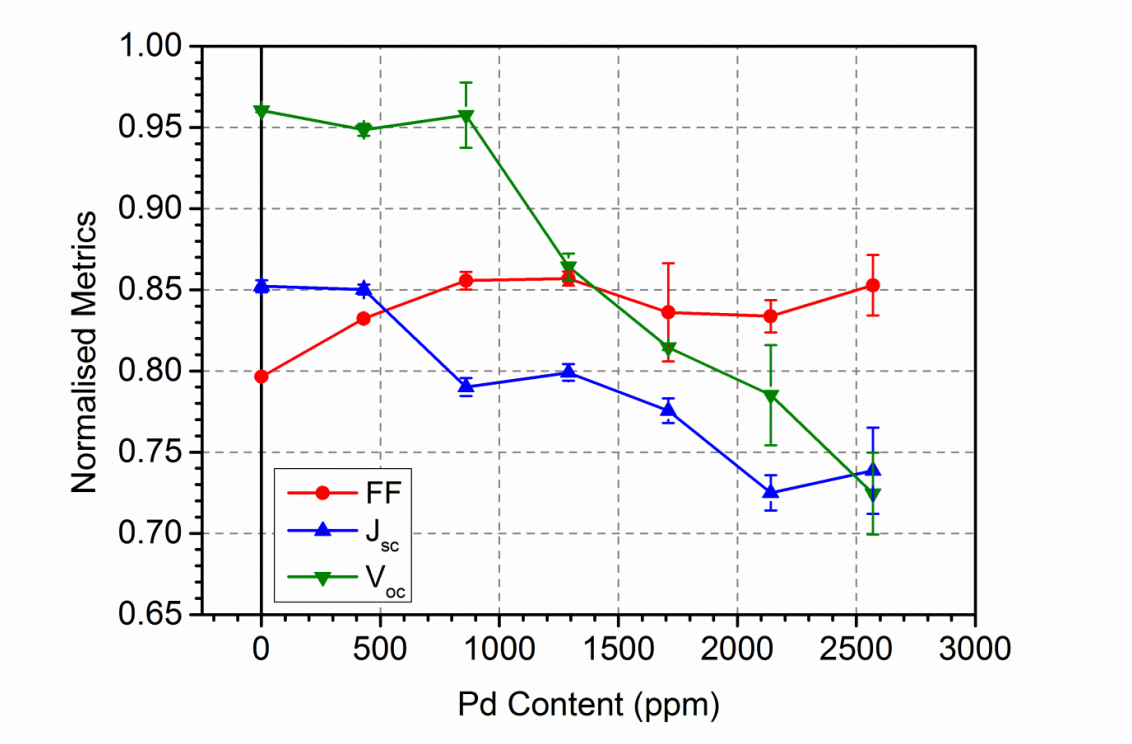

Figure 4.15: Device metrics after 140 hours of continuous illumination relative to initial values. The lines are a guide for the eye.

Pd Content (ppm)	**FF** (%)	**J_{sc}** (mA/cm²)	**V_{oc}** (V)
0.1	48 ± 0.1	-7.34 ± 0.03	0.85 ± 0.001
430	47 ± 0.1	-6.98 ± 0.03	0.81 ± 0.003
860	43 ± 0.3	-6.57 ± 0.05	0.72 ± 0.015
1290	41 ± 0.2	-6.28 ± 0.04	0.67 ± 0.006
1710	40 ± 1.4	-6.22 ± 0.06	0.63 ± 0.001
2140	37 ± 0.4	-5.27 ± 0.80	0.56 ± 0.022
2570	38 ± 0.8	-5.70 ± 0.21	0.51 ± 0.018

Table 4.3: Mean and standard deviations of device metrics after 140 hours of continuous illumination. 8 devices were used to calculate the average and standard deviation for each Pd content.

To quantify the reduced efficiencies of the Pd containing devices, the relative changes in device after 140 hours are plotted in Figure 4.15, normalised to values determined at t = 0. Absolute values are given in Table 4.3. For devices characterised by a low Pd concentration (0.1 – 860 ppm), the observed reduction in PCE in aged devices mainly results from a reduction in device *FF* and J_{sc}. For aged devices characterised by higher Pd concentrations (above ~1000 ppm), a strong reduction in device V_{oc} also contributes to a reduction in OPV efficiency.

To explore this process further, LBIC images were recorded of devices that have been aged by exposure to AM1.5 radiation for 140 hours (see Figures 4.7(g), (h), and (i)). Here, it is apparent that the number density of cold-spots increases by around 20% in all of the aged devices. From normalised line profiles taken across such defects before and after 140 hours of illumination (as shown in Figure 4.16) variation in the evolution in shunt structure is observed. Specifically, it is found that larger shunts do not change appreciably in their size or depth; however, a population of smaller shunts emerges during the ageing process. Such smaller shunts can grow rapidly in size, increasing in diameter by between 2 and 4 times. The origin of the "new" current shunts observed in the aged devices is as yet

unclear. When the polymer:fullerene film is first cast, there exists a 'background' level of Pd nanoparticles that are dispersed within the film that co-exist with the larger nanoparticle aggregates; an example of this can be seen in Figure 4.17, where several spots can be seen outside of the defect. It is speculated that on ageing such devices under the solar simulator, the nanoparticles are able to undergo slow thermally-assisted diffusion and aggregation within the film (perhaps assisted by the field within the device), eventually reaching a size whereby they are also able to act as current shunts; a process likely to contribute to the observed loss in PCE. It is possible that the larger shunts do not change size due to a locally decreased Pd content in the film immediately surrounding the, as the Pd from this area has already been incorporated into the shunt upon the casting of the film. This would prevent the accumulation of further Pd if the nanoparticles cannot diffuse large distances through the film.

To explore whether the photoactive material is modified by its proximity to a Pd-containing defect, PL spectra was recorded at different distances (from 0 to 250 microns) from a single aggregate after 140 hours of AM1.5 irradiation, as shown in Figures 4.9(b), (c) and (d). Interestingly, the PL emission spectra do not change shape after the ageing process, however they all undergo a decrease in intensity (by around 10% for the film, 30% for the defect), an observation consistent with photo-oxidation [23].

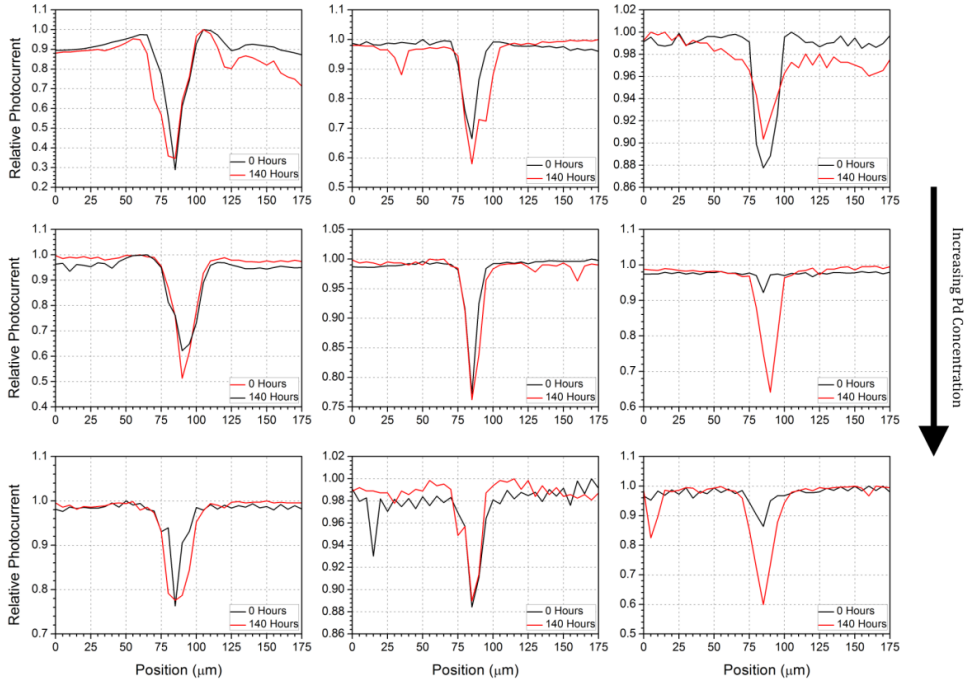

Figure 4.16: Line profiles of current shunts in LBIC images before and after ageing.

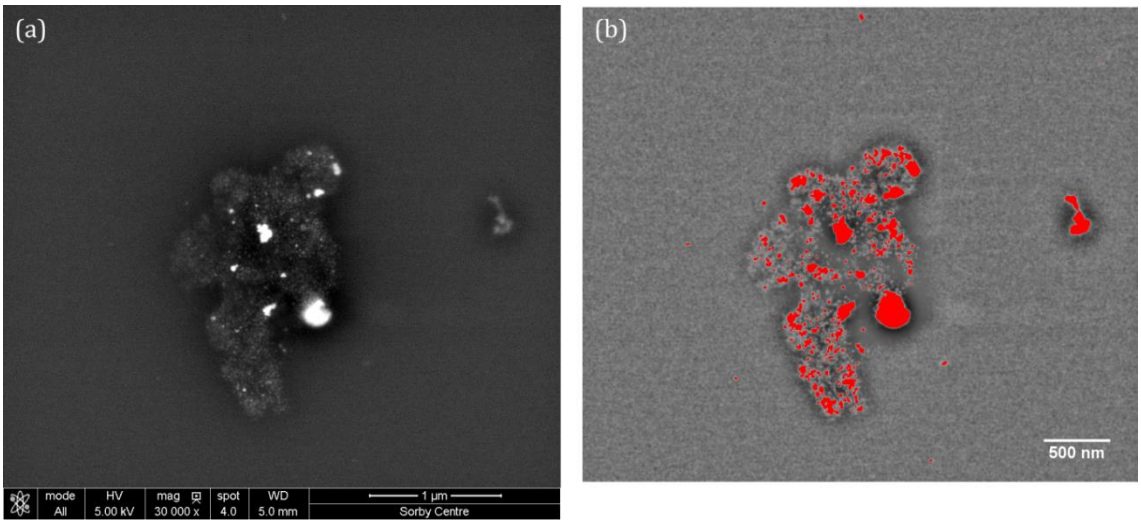

Figure 4.17: (a) SEM image of an aggregate and surrounding film using backscattered electrons. (b) The same image after FFT and thresholding with nanoparticles highlighted.

The measurements suggest therefore that there are two contributory factors to the loss in device efficiency during the fast burn-in period. Firstly, the appearance of additional Pd defects acting as current shunts are likely to reduce device efficiency. Secondly however, the observed reduction in the PL emission intensity that is

observed in regions far from the Pd defect and accompanied by a reduction of V_{oc} and *FF* indicates an accompanying oxidation process that is consistent with the formation of sub-bandgap states. It has been shown previously that the generation of such states is a primary mechanism for the burn-in loss of PCDTBT:$PC_{70}BM$ solar cells [24]. These sub-bandgap states are therefore likely to be independent of Pd content, and is the main cause of the burn-in for low Pd content devices.

4.3: The Effects on PFD2TBT-8:$PC_{70}BM$ Photovoltaic Devices

In order to highlight the need to investigate individual polymers when determining the effects of residual catalyst on photovoltaic performance, another polymer system, poly[9,9-dioctylfluorene-4,7-alt-(5,6-bis(octyloxy)-4,7-di(2,2′-bithiophen-5-yl)benzo[c][1,2,5]thiadiazole)-5,5-diyl] (PFD2TBT-8) was investigated. Here, a stock batch of polymer with a Pd concentration of 630 ppm was polluted and cleaned using the same methods as with the PCDTBT, producing a 'Pd polluted' batch having a Pd concentration of 3300 ppm and a 'clean' batch having a Pd concentration of 4 ppm.

As with the PCDTBT, the different batches were mixed in varying ratios to produce intermediate Pd concentrations. Specifically, the cleaned and stock batch were mixed in ratios of 4:1, 3:2, 2:3, and 1:4, creating samples assumed to have 130, 250, 380, and 505 ppm Pd respectively. Additionally, the stock and polluted batch were mixed at a ratio of 1:1, creating a sample with 1970 ppm Pd. These polymer samples, along with the clean, stock, and polluted batches were used to fabricate OPV devices (4 for each Pd content). The average *J-V* curves for these devices are shown in Figure 4.18, with the extracted device metrics presented in Table 4.4. The device metrics are further plotted in Figure 4.19 as a function of Pb concentration, normalised to the values at the lowest concentration.

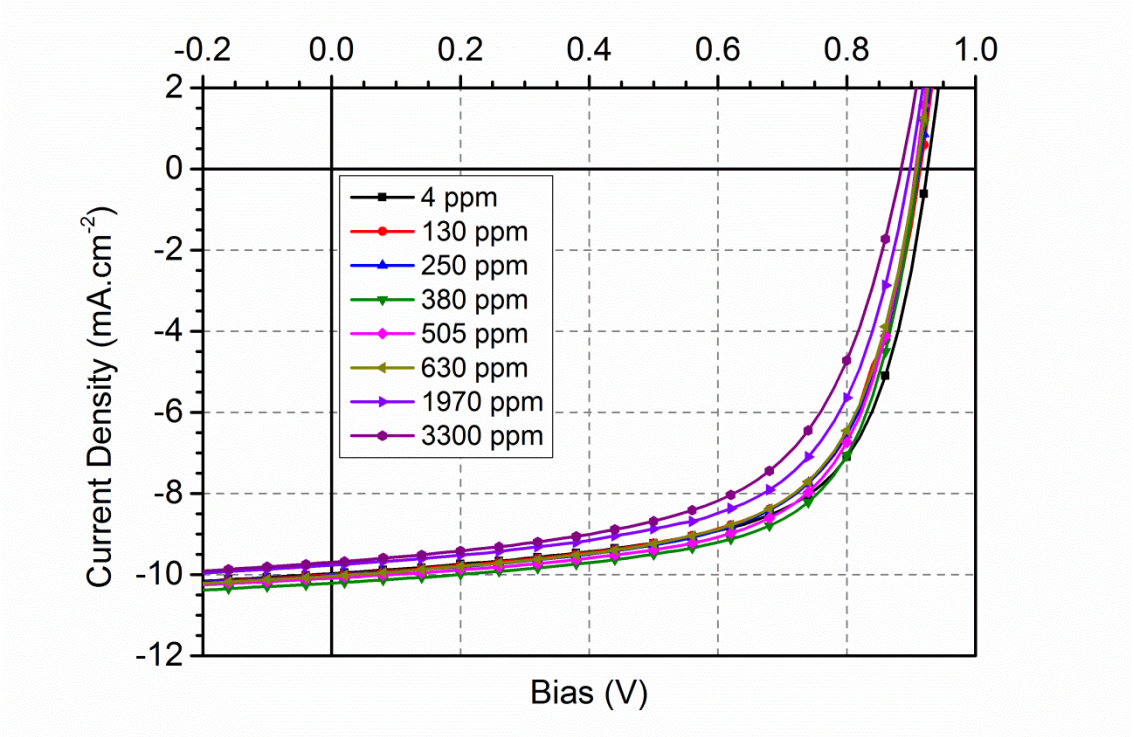

Figure 4.18: J-V curves of PFD2TBT-8:$PC_{70}BM$ devices fabricated with different palladium concentrations.

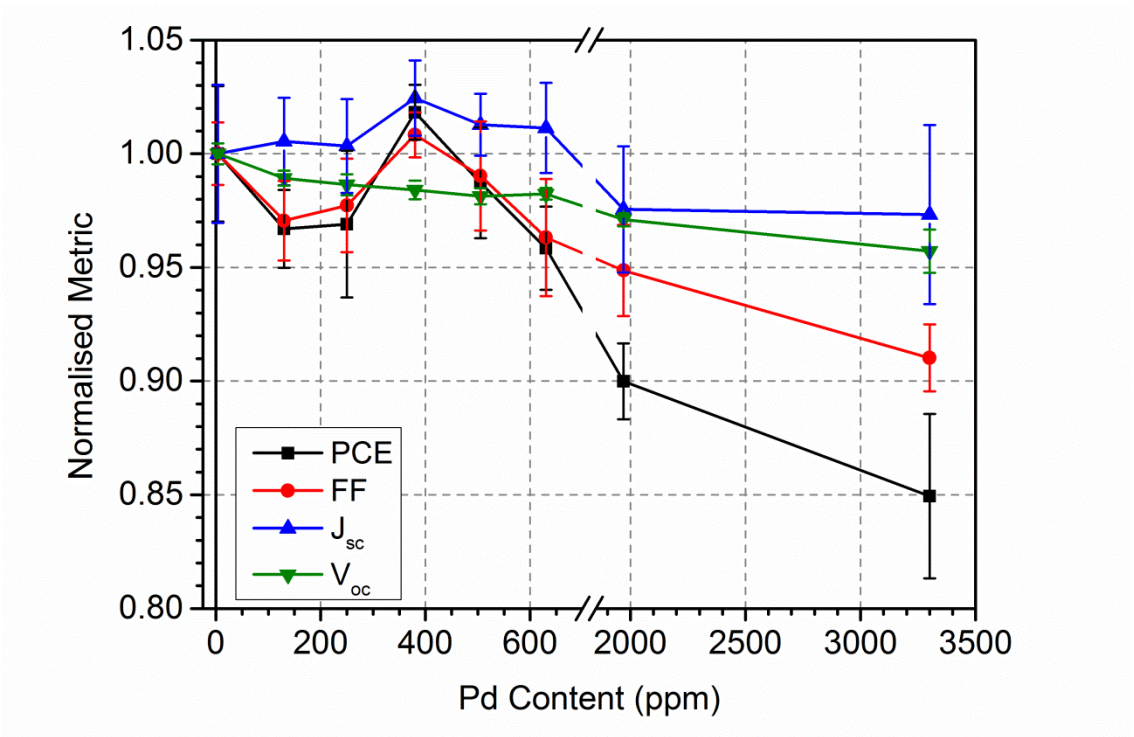

Figure 4.19: Changes in device metrics plotted as a function of palladium content, with data normalised to metrics determined from devices containing the lowest concentration of Pd. The lines are a guide for the eye.

Pd Content (ppm)	**PCE** (%)	**FF** (%)	**J_{sc}** (mA/cm²)	**V_{oc}** (V)	**R_{sh}** (Ωcm²)	**R_s** (Ωcm²)
4	6 ± 0.2	65 ± 1	-10.0 ± 0.3	0.92 ± 0.004	1060 ± 80	9.0 ± 0.2
130	5.8 ± 0.1	63 ± 1	-10.0 ± 0.2	0.91 ± 0.003	1040 ± 80	9.7 ± 0.3
250	5.8 ± 0.2	63 ± 1	-10.0 ± 0.2	0.91 ± 0.004	1000 ± 90	9.4 ± 0.3
380	6.1 ± 0.1	66 ± 1	-10.2 ± 0.2	0.91 ± 0.004	1070 ± 90	8.4 ± 0.4
505	5.9 ± 0.2	64 ± 2	-10.1 ± 0.1	0.91 ± 0.003	1070 ± 50	9.1 ± 0.7
630	5.7 ± 0.1	63 ± 2	-10.1 ± 0.2	0.91 ± 0.002	1020 ± 100	9.6 ± 0.2
1970	5.4 ± 0.1	62 ± 1	-9.7 ± 0.3	0.9 ± 0.003	940 ± 80	11.0 ± 0.6
3300	5.1 ± 0.2	59 ± 1	-9.7 ± 0.4	0.89 ± 0.009	860 ± 70	12.8 ± 0.6

Table 4.4: Mean device results and standard deviations for power conversion efficiency, fill factor, short circuit current density, open circuit voltage, and shunt and series resistance, extracted from *J-V* curves for PFD2TBT-8 containing a range of palladium concentrations. 12 devices were used to calculate the mean and standard deviations for each Pd content.

In contrast to PCDTBT, the metrics of PFD2TBT-8 devices with Pd concentrations below 630 ppm do not significantly differ, and the PCE of the highest Pd concentration (3300 ppm) is only reduced by ~15% relative to PCE of the lowest Pd concentration (5.08% and 5.98% respectively), compared to the ~50% reduction of PCDTBT. The losses occur in the same device metrics as with PCDTBT, and the R_{sh} and R_s are the most affected device metrics, suggesting, as discussed in Section 2.2, increased shunt pathways, recombination rates, or changes in energy level alignment through the high Pd devices. Regardless of which mechanisms are at work, it is apparent that Pd has significantly less of an effect on PFD2TBT-8 than PCDTBT.

This suggests that PDF2TBT-8 has a much greater tolerance of to the presence of the Pd than PCDTBT. Indeed, this is further evidenced by the lack of aggregation observed in PFD2TBT-8 devices, as can be seen in Figure 4.20. It is possible that the solubilising alkyl chains present on the benzothiadiazole of PFD2TBT-8 inhibit

the Pd from pulling the polymer out of solution, preventing the formation of polymer aggregates and short circuits within the devices.

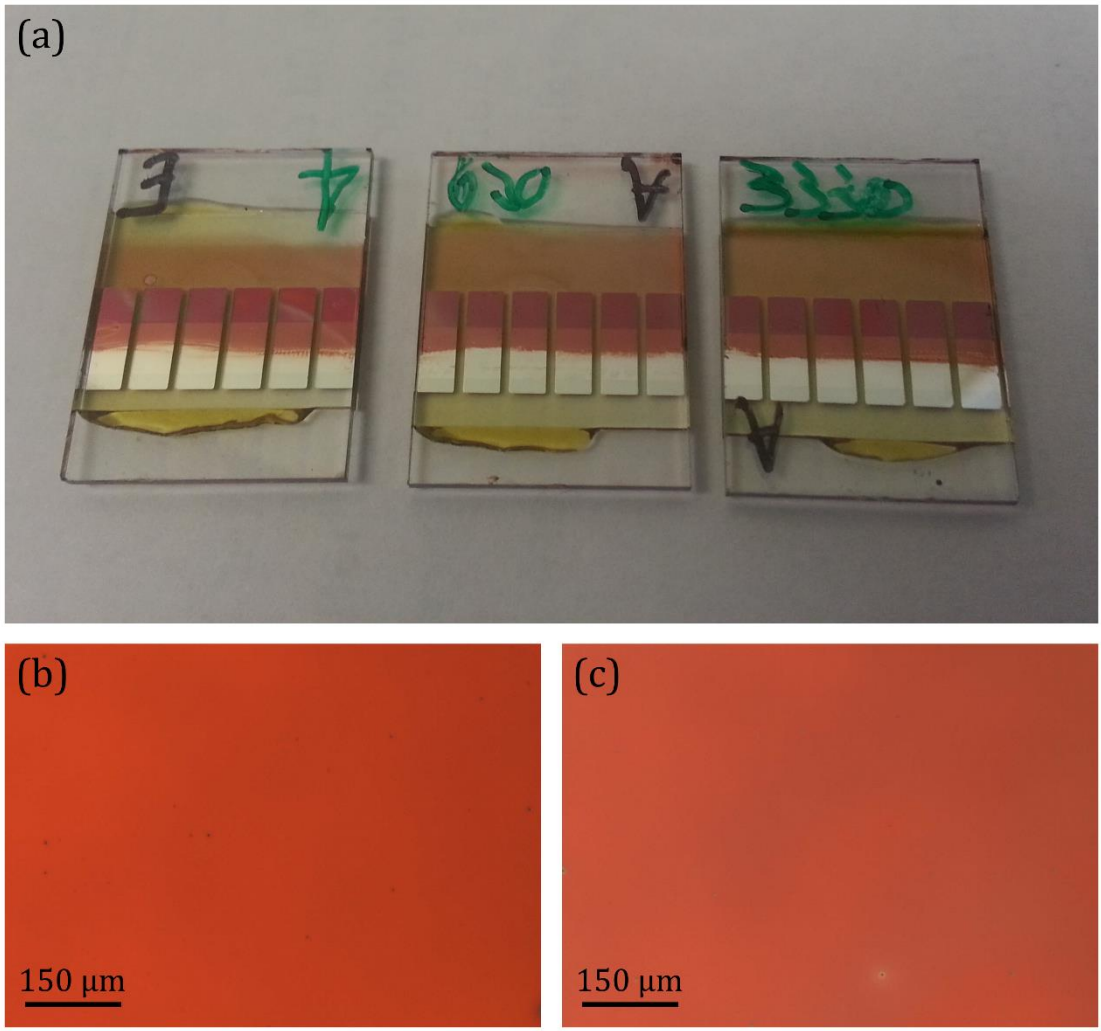

Figure 4.20: (a) Photograph of PFD2TBT-8 OPV devices containing 4, 630, and 3300 ppm Pd from left to right respectively. (b) and (c) optical microscope images PFD2TBT-8:$PC_{70}BM$ films containing 4 and 3300 ppm Pd respectively.

This tolerance is also seen in stability measurements of PFD2TBT-8 based OPV devices. In Figure 4.21, the evolution of the PCE, *FF*, J_{sc}, and V_{oc} of PFD2TBT-8:$PC_{70}BM$ OPV devices over 300 hours of continuous illumination is presented. It can be seen in figure 4.21(a) that the PCE for lower Pd concentrations (<630 ppm) degrades by ~70%, whilst the PCE for higher Pd concentrations (>630 ppm) decreases by ~80%. As with PCDTBT, this difference primarily arises during the

burn-in period (the first 125 hours), however the effect is significantly less pronounced for PFD2TBT-8.

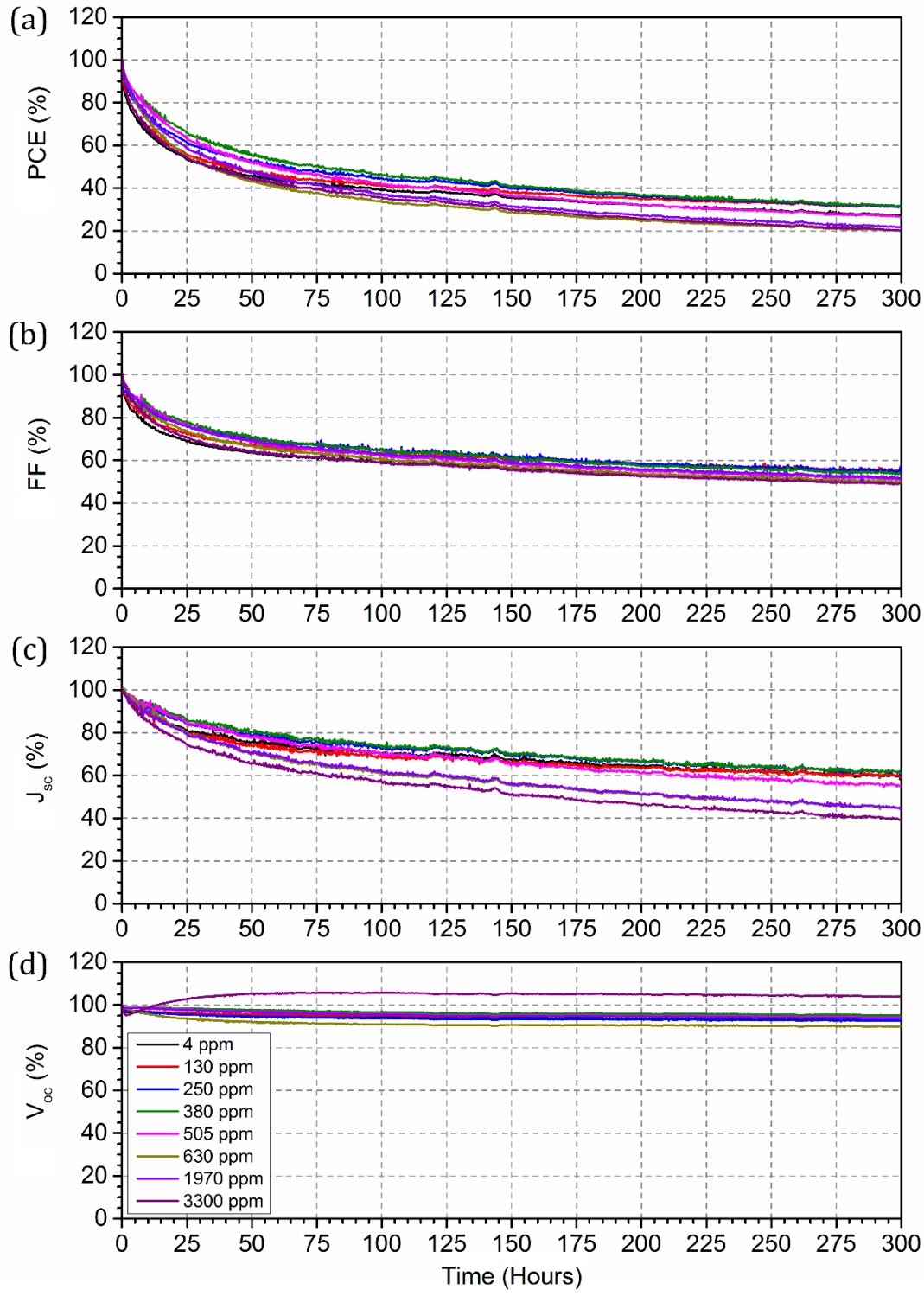

Figure 4.21: (a) PCE, (b) *FF*, (c) J_{sc}, and (d) V_{oc} of PFD2TBT-8:$PC_{70}BM$ OPV devices with a range of Pd concentrations over 300 hours of continuous illumination.

In contrast to PCDTBT, the metric influencing this difference is the J_{sc}, with decreases of 60% for high Pd concentrations and only 40% for low Pd concentrations. As discussed in Section 2.3.6, this indicates an increase in the rate of photobleaching of devices containing higher Pd concentrations, reducing the absorption characteristics of devices. Interestingly, the V_{oc} of the device containing the highest concentration of Pd (3300 ppm) actually increases over the first 50 hours (after an initial rapid decrease) to ~105% of the initial value before stabilising. This has been seen previously for OPV devices using PEDOT:PSS as a hole transport layer, where it was speculated to be caused by changes in the work function of PEDOT:PSS due to charge transfer [23]. It is possible that the PFD2TBT-8 film can only contain a certain quantity of Pd, and the excess may undergo diffusion to the PEDOT:PSS during ageing, potentially resulting in changes to the work function of the hole transporting layer.

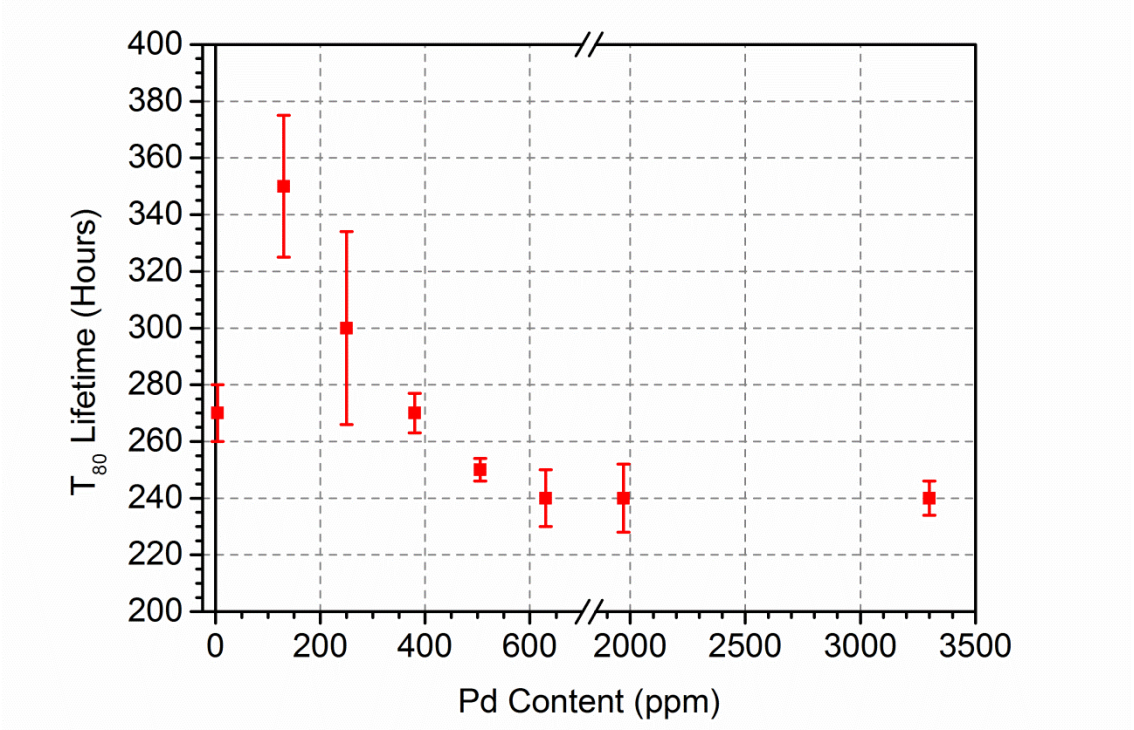

Figure 4.22: T_{80} lifetimes for different palladium content PFD2TBT-8 devices calculated from the PCE lifetime curves.

As with the PCDTBT devices, T_{80} lifetimes have been calculated from the lifetime data of PFD2TBT-8 devices with differing Pd concentrations. This data is shown in Figure 4.22. Similarly to PCDTBT, the presence of Pd does not appear to have a

significant impact on the T_{80} lifetime of PFD2TBT-8 devices, with lifetimes of 270 ± 10 hours for the lowest Pd content (4 ppm) and 240 ± 10 hours for the highest Pd content (3300 ppm). Interestingly, devices with a small amount of Pd (130 ppm) exhibit the longest T_{80} lifetimes, giving 350 ± 30 hours.

4.4: Conclusions

The effect of residual palladium-catalyst left over from the synthesis of the polymers PCDTBT and PFD2TBT-8 on their efficiency when fabricated into polymer:fullerene solar cells has been explored. It was found that the Pd has a significant effect of device efficiency, with PCE reduced by almost 50% from 4.55% to 2.42% due to the presence of 2570 ppm of Pd (relative to the mass of PCDTBT). This is attributed to the presence of the Pd that self-assembles into 15 nm nanoparticles that are then bound by the PCDTBT polymer into larger sized aggregates (>10 μm). Laser beam photocurrent mapping was used to demonstrate that such aggregates are associated with reduced photocurrent within the device and thus act as short-circuits that result in additional leakage pathways between the anode and cathode that conduct charge. On ageing the devices, a number of additional current shunts appear; an effect that believed to contribute to a loss in device efficiency. Larger shunts do not change in size during ageing, a process that likely results from the immediately surrounding film having a locally reduced Pd content due to having already been incorporated into the shunt.

PFD2TBT-8, however, showed a much greater tolerance to the presence of a residual palladium catalyst, with PCE decreasing by only 15% from 5.98% to 5.08% at a Pd concentration of 3300 ppm. With concentrations below 630 ppm, however, there was no significant decrease in the PCE of devices. This is speculated to be due to the improved solubility of PFD2TBT-8 preventing the Pd from pulling the polymer out of solution and forming aggregates that act as short-circuits. Furthermore, the operational stability of PFD2TBT-8 devices is not affected by the presence of Pd as significantly as PCDTBT, with slightly decreased stability of the J_{sc}.

These measurements thus highlight the need to remove Pd from PCDTBT after polymer synthesis, as it is responsible for both reduced device efficiency and

enhanced device degradation, as well as the need to investigate individual polymers for their tolerance to impurities.

4.5: References

[1] B. Carsten, F. He, H.J. Son, T. Xu, L. Yu, Stille polycondensation for synthesis of functional materials., Chem. Rev. 111 (2011) 1493–528.

[2] A. Suzuki, Organoborates in New Synthetic Reactions, Accounts Chem. Reseach. 15 (1982) 178–184.

[3] D. Milstein, J.K. Stille, A General, Selective, and Facile Method for Ketone Synthesis from Acid Chlorides and Organotin Compounds Catalyzed by Palladium, J. Am. Chem. Soc. 100 (1978) 3636–3638.

[4] K.T. Nielsen, K. Bechgaard, F.C. Krebs, Removal of Palladium Nanoparticles from Polymer Materials, Macromolecules. 38 (2005) 658–659.

[5] W.L. Leong, G. Hernandez-Sosa, S.R. Cowan, D. Moses, A.J. Heeger, Manifestation of carrier relaxation through the manifold of localized states in PCDTBT:PC60BM bulk heterojunction material: the role of PC84BM traps on the carrier transport., Adv. Mater. 24 (2012) 2273–7.

[6] A. Saeki, M. Tsuji, S. Seki, Direct Evaluation of Intrinsic Optoelectronic Performance of Organic Photovoltaic Cells with Minimizing Impurity and Degradation Effects, Adv. Energy Mater. 1 (2011) 661–669.

[7] W.L. Leong, G.C. Welch, L.G. Kaake, C.J. Takacs, Y. Sun, G.C. Bazan, A.J. Heeger, Role of trace impurities in the photovoltaic performance of solution processed small-molecule bulk heterojunction solar cells, Chem. Sci. 3 (2012) 2103.

[8] L. Kaake, X.-D. Dang, W.L. Leong, Y. Zhang, A. Heeger, T.-Q. Nguyen, Effects of impurities on operational mechanism of organic bulk heterojunction solar cells., Adv. Mater. 25 (2013) 1706–1712.

[9] S.R. Cowan, W.L. Leong, N. Banerji, G. Dennler, A.J. Heeger, Identifying a Threshold Impurity Level for Organic Solar Cells: Enhanced First-Order

Recombination Via Well-Defined PC84BM Traps in Organic Bulk Heterojunction Solar Cells, Adv. Funct. Mater. 21 (2011) 3083–3092.

[10] N. Camaioni, F. Tinti, L. Franco, M. Fabris, A. Toffoletti, M. Ruzzi, L. Montanari, L. Bonoldi, A. Pellegrino, A. Calabrese, R. Po, Effect of residual catalyst on solar cells made of a fluorene-thiophene-benzothiadiazole copolymer as electron-donor: A combined electrical and photophysical study, Org. Electron. 13 (2012) 550–559.

[11] M.P. Nikiforov, B. Lai, W. Chen, S. Chen, R.D. Schaller, J. Strzalka, J. Maser, S.B. Darling, Detection and role of trace impurities in high-performance organic solar cells, Energy Environ. Sci. 6 (2013) 1513.

[12] J. a. Carr, S. Chaudhary, The identification, characterization and mitigation of defect states in organic photovoltaic devices: a review and outlook, Energy Environ. Sci. 6 (2013) 3414.

[13] F.C. Krebs, B. Nyberg, M. Jørgensen, A.B.S. Energy, M. Sol, Influence of Residual Catalyst on the Properties of Conjugated Polyphenylenevinylene Materials : Palladium Nanoparticles and Poor Electrical Performance, Chem. Mater. 16 (2004) 1313–1318.

[14] K.T. Nielsen, H. Spanggaard, F.C. Krebs, Synthesis, Light Harvesting, and Energy Transfer Properties of a Zinc Porphyrin Linked Poly(phenyleneethynylene), Macromolecules. 38 (2005) 1180–1189.

[15] P. a. Troshin, D.K. Susarova, Y.L. Moskvin, I.E. Kuznetsov, S. a. Ponomarenko, E.N. Myshkovskaya, K. a. Zakharcheva, A. a. Balakai, S.D. Babenko, V.F. Razumov, Impedance Measurements as a Simple Tool to Control the Quality of Conjugated Polymers Designed for Photovoltaic Applications, Adv. Funct. Mater. 20 (2010) 4351–4357.

[16] W.R. Mateker, J.D. Douglas, C. Cabanetos, I.T. Sachs-Quintana, J. a. Bartelt, E.T. Hoke, A. El Labban, P.M. Beaujuge, J.M.J. Fréchet, M.D. McGehee, Improving the long-term stability of PBDTTPD polymer solar cells through material purification aimed at removing organic impurities, Energy Environ. Sci. 6 (2013) 2529.

[17] B.Y. Finck, B.J. Schwartz, Understanding the origin of the S-curve in conjugated polymer/fullerene photovoltaics from drift-diffusion simulations, Appl. Phys. Lett. 103 (2013) 1–4.

[18] D. Kozanoglu, D.H. Apaydin, A. Cirpan, E.N. Esenturk, Power conversion efficiency enhancement of organic solar cells by addition of gold nanostars, nanorods, and nanospheres, Org. Electron. 14 (2013) 1720–1727.

[19] Y. Zhang, H. Zhou, J. Seifter, L. Ying, A. Mikhailovsky, A.J. Heeger, G.C. Bazan, T.-Q. Nguyen, Molecular Doping Enhances Photoconductivity in Polymer Bulk Heterojunction Solar Cells, Adv. Mater. 25 (2013) 7038–7044.

[20] J.W. Kingsley, P.P. Marchisio, H. Yi, A. Iraqi, C.J. Kinane, S. Langridge, R.L. Thompson, A.J. Cadby, A.J. Pearson, D.G. Lidzey, R. a. L. Jones, A.J. Parnell, Molecular weight dependent vertical composition profiles of PCDTBT:PC71BM blends for organic photovoltaics, Sci. Rep. 4 (2014) 1–7.

[21] S. Günes, H. Neugebauer, N.S. Sariciftci, Conjugated polymer-based organic solar cells., Chem. Rev. 107 (2007) 1324–38.

[22] T. Wang, A.J. Pearson, A.D.F. Dunbar, P. a. Staniec, D.C. Watters, H. Yi, A.J. Ryan, R. a L. Jones, A. Iraqi, D.G. Lidzey, Correlating structure with function in thermally annealed PCDTBT:PC70BM photovoltaic blends, Adv. Funct. Mater. 22 (2012) 1399–1408.

[23] E. Bovill, N. Scarratt, J. Griffin, H. Yi, A. Iraqi, a. R. Buckley, J.W. Kingsley, D.G. Lidzey, The role of the hole-extraction layer in determining the operational stability of a polycarbazole:fullerene bulk-heterojunction photovoltaic device, Appl. Phys. Lett. 106 (2015) 73301.

[24] C.H. Peters, I.T. Sachs-Quintana, W.R. Mateker, T. Heumueller, J. Rivnay, R. Noriega, Z.M. Beiley, E.T. Hoke, A. Salleo, M.D. McGehee, The mechanism of burn-in loss in a high efficiency polymer solar cell., Adv. Mater. 24 (2012) 663–8.

Chapter 5

The Operational Stability of Inverted Architecture Perovskite Solar Cells

5.0: Introduction

As discussed in Chapter 2 (section 2.4), perovskite solar cells (PSCs) have now reached power conversion efficiencies (PCEs) in excess of 20% [1], a value comparable to commercial silicon solar cells. This has caused an increased interest in the stability and lifetime of PSCs, as this is one of the most important steps towards the commercialisation of the technology. Most of this work, however, has been conducted on 'standard' architecture devices (Chapter 2, section 2.4.1.3). In this chapter, work is presented on the lifetime of the mixed halide perovskite, $CH_3NH_3PbI_{3-x}Cl_x$, in 'inverted' architecture devices utilising materials commonly used for this architecture (full device structure: ITO/PEDOT:PSS/Perovskite/$PC_{70}BM$/LiF/Al). Devices are subjected to 670 hours (4 weeks) of continuous illumination, during which the PCE was found to decrease significantly. A variety of techniques were employed to determine the cause of the degradation. This was attributed to the decomposition of the perovskite through reactions with oxygen and water, resulting in the formation of trap states within the perovskite.

5.1: Stability Measurements

In Figure 5.1, the power conversion efficiency (PCE), fill factor (*FF*), short circuit current density (J_{sc}), and open circuit voltage (V_{oc}) of four $CH_3NH_3PbI_{3-x}Cl_x$ devices are plotted as a function of irradiance time. The data represented by lines was recorded using the Atlas CPS+ lifetime tester, whilst the data represented by symbols was taken using the calibrated Newport solar simulator (AM1.5, 100 mW/cm^2). All of the data is normalised to its initial value. As mention in Chapter 3, it is important to note that a spectral mismatch exists between the xenon lamp of the Atlas system and the solar spectrum, and no aperture mask was used when performing measurements, therefore the data is used only to highlight trends, with all *J-V* curves presented being taken using the Newport solar simulator.

Over the course of the 670 hour test, the average PCE of devices decreased by approximately 80%, with the loss primarily originating from a ~70% reduction in the J_{sc}. The *FF* and V_{oc} were affected to a lesser extent, decreasing by 10 – 20% and 25 – 30% respectively. The trends seen in the data recorded using the Newport solar simulator are similar to those recorded using the Atlas system, although some difference in the *FF* was observed when recorded using the different systems. This is believed to originate from the fact that the temperature of the devices recorded using the Atlas system is slightly higher (37 vs 25 °C) [2].

The T_{80} lifetime of the devices are presented in Table 5.1, defined as the time taken to reach 80% of the PCE immediately after the burn-in period (160 hours), calculated from the data measured using the Atlas Suntest CPS+ system and the calibrated Newport solar simulator. It can be seen that the calculated T_{80} lifetimes determined by the two systems are in statistical agreement. The results indicate therefore that the devices have a T_{80} lifetime of 280 ± 20 hours. This is a shorter lifetime than those seen by Leitjins et al. [3], who observed 45% loss of PCE after 200 hours of ageing, followed by very slow degradation over the subsequent 800 hours, and Guarnera et al. [4], who observed a 5% decrease in PCE over 350 hours. However, these studies were conducted on standard architecture devices utilising a mesoporous scaffold, whilst the measurements here are for planar inverted architecture devices, with the only material in common between these studies being the perovskite, with differing charge transport layers and electrodes.

Burn-in time (hours)	**PCE after Burn-in** (%)	**PCE loss over Burn-in** (%)	**PCE loss over 670 hours** (%)	**T_{80} Atlas** (hours)	**T_{80} Newport** (hours)
160	6.0 ± 0.6	39.0 ± 0.5	78 ± 2	260 ± 10	280 ± 20

Table 5.1: PCE loss over burn-in period and whole test, and T_{80} lifetimes calculated using data from both the Atlas Suntest CPS+ and the calibrated Newport solar simulator.

The *J-V* curves used to plot the data-symbols in Figure 5.1 are plotted in Figure 5.2(a). The average device metrics before and after ageing are presented in Table 5.2. It can be seen that a large decrease in the shunt resistance (R_{sh}) (from 1100 ± 150 Ωcm^2 to 460 ± 20 Ωcm^2). As discussed in Section 2.2, this is indicative of an increase in leakage pathways and an increase in the energetic barriers to charge extraction. The change in Rs, along with the significant decrease in J_{sc} (-15.8 ± 0.4 mA/cm^2 to -6.1 ± 0.3 mA/cm^2), indicating the creation of trap states within the active layer. Indeed, the decrease in V_{oc} (0.92 ± 0.01 V to 0.69 ± 0.02 V) indicates an increase in charge carrier recombination rate within the device. It can also be observed that there is an increase in the level of hysteresis during the first week (168 hours), due to changes in the J_{sc} between forward and reverse scans, further indicating increases in interfacial recombination and the migration of ionic species within the active layer, as discussed in Section 2.4.6 [5–10].

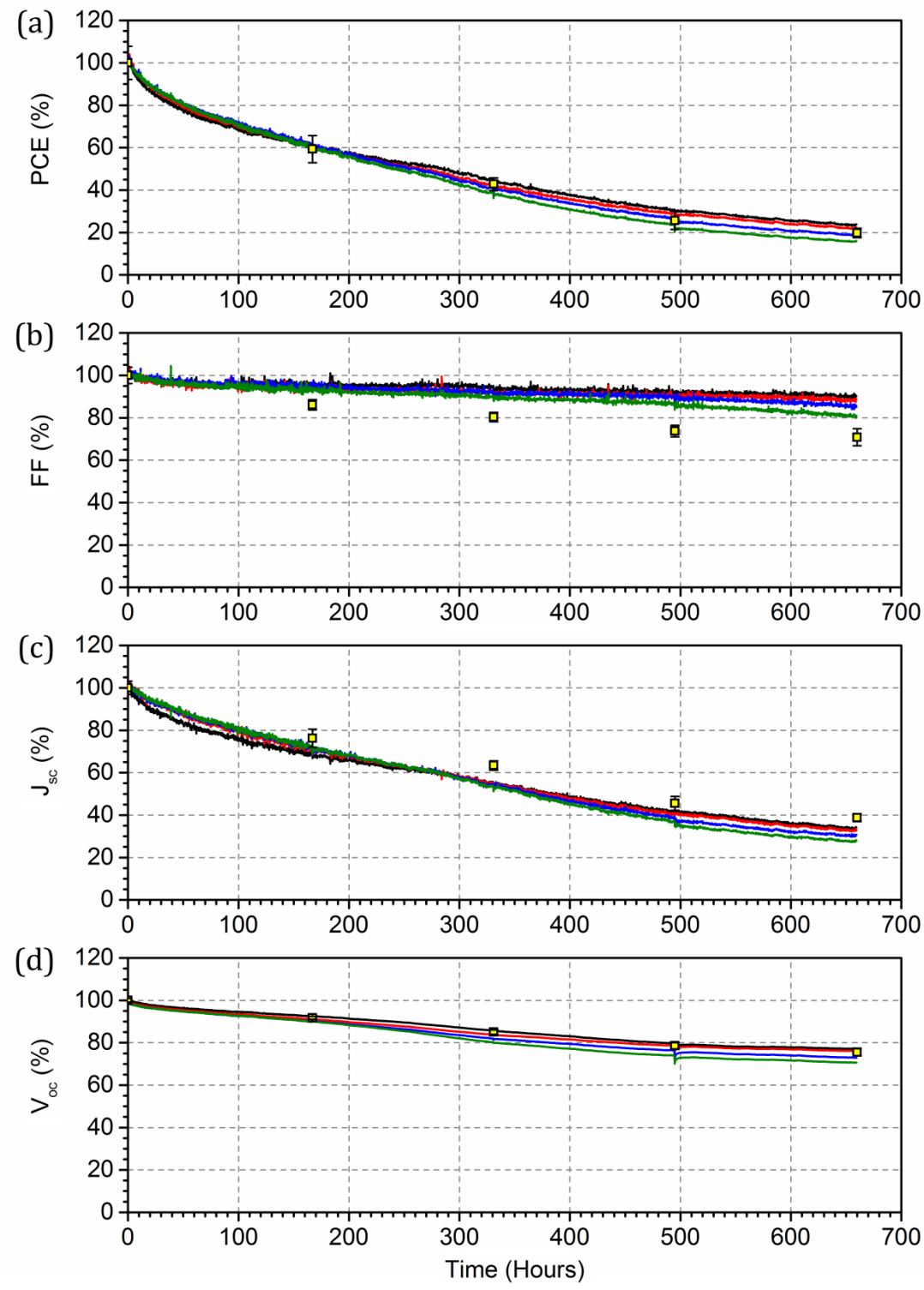

Figure 5.1: (a) PCE, (b) *FF*, (c) J_{sc}, and (d) V_{oc} of four $CH_3NH_3PbI_{3-x}Cl_x$ devices over 670 hours of continuous illumination. Solid points are data taken using a calibrated solar simulator. All *J-V* scans were performed from -1 to 1 V.

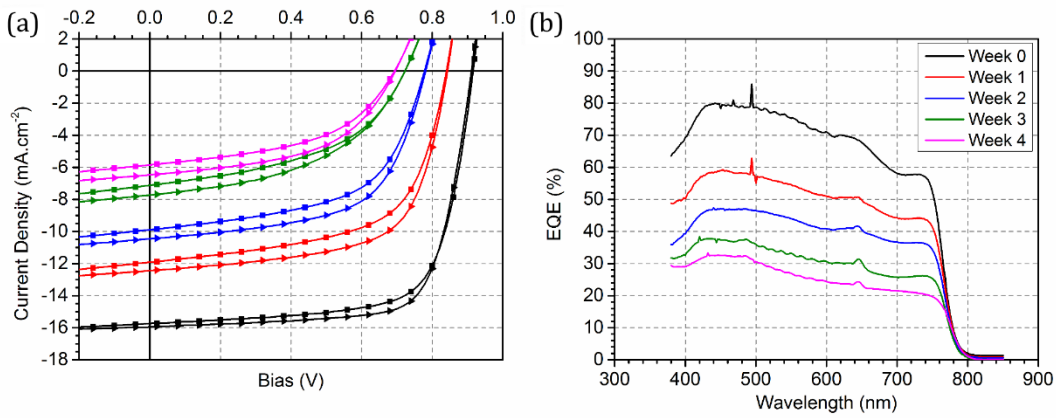

Figure 5.2: (a) *J-V* curves and (b) EQE measurements for devices at different stages of the lifetime study. Squares in part (a) represent forwards scans, triangles represent backwards scans.

Time (Hours)	**Scan Direction**	**PCE** (%)	**FF** (%)	**J_{sc}** (mA/cm^2)	**V_{oc}** (V)	**R_{sh}** (Ω cm^2)	**R_s** (Ω cm^2)
0	Forwards	10.2 ± 0.5	70 ± 2	-15.8 ± 0.4	0.92 ± 0.01	1100 ± 150	5.6 ± 0.3
	Backwards	10.6 ± 0.4	73 ± 1	-16.0 ± 0.4	0.91 ± 0.01	1360 ± 350	6.0 ± 0.5
670	Forwards	2.0 ± 0.2	50 ± 3	-6.1 ± 0.3	0.69 ± 0.02	460 ± 20	25 ± 6
	Backwards	2.3 ± 0.4	52 ± 3	-6.7 ± 0.3	0.69 ± 0.02	530 ± 20	23 ± 5

Table 5.2: Mean device metrics and standard deviations for open circuit voltage, short circuit current density, fill factor, power conversion efficiency, and shunt and series resistance, extracted from *J-V* curves, for devices before and after ageing. 12 devices were used to calculate the mean and standard deviations.

Concomitant with the decrease in J_{sc}, a decrease in the external quantum efficiency (EQE) of the devices is observed, as shown in Figure 5.2(b), with the peak EQE value dropping from 80% to 33%. As discussed in Section 2.2, the EQE is dependent upon the absorption efficiency or charge transport and extraction properties of the perovskite, suggesting potential photobleaching or detrimental changes in the perovskite structure. The shape of the EQE curve also changes with time, as can be seen in Figure 5.3(a), with the peak photocurrent wavelength shifting from 468 nm to 432 nm. This is also accompanied by a shift in the band edge, shown in Figure 5.3(b), indicating changes in the energetic structure of the

perovskite, or possibly the introduction of new materials in the device with a smaller band gap than the perovskite, in turn impacting the absorption characteristics of the solar cell. Indeed, the relative loss of EQE at wavelengths greater than 500 nm is characteristic of an increase in the relative levels of PbI_2 within the device [11]. The peak EQE and the corresponding wavelengths are detailed in Table 5.3, along with the integrated and measured J_{sc}.

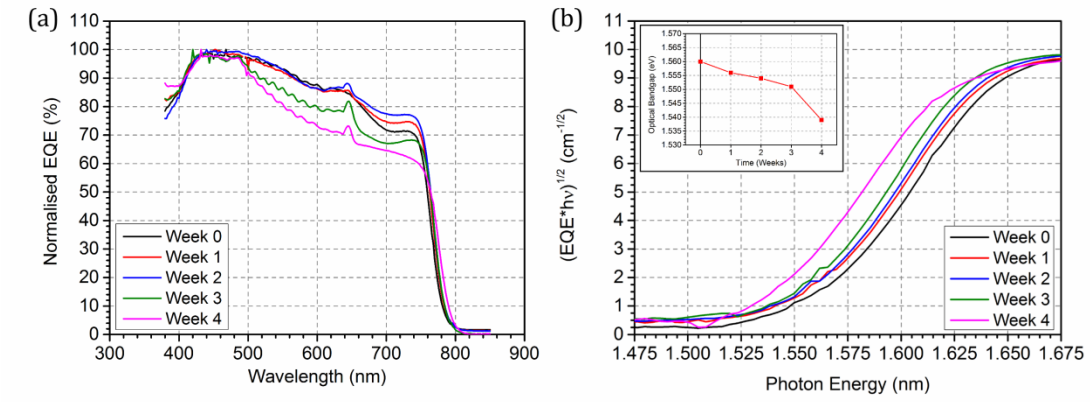

Figure 5.3: (a) EQE data normalised to the peak value each week, highlighting the relative change in shape and loss of EQE at wavelengths longer than 500 nm. (b) Tauc plot of EQE band edge. Inset are the estimated values for the optical bandgap for each week.

Time (Weeks)	**Peak EQE** (%)	**Wavelength** (nm)	**Integrated J_{sc}** (mA/cm^2)	**Measured J_{sc}** (mA/cm^2)
0	81	468	16.8	16.0
1	59	452	12.5	12.5
2	47	440	10.1	10.6
3	38	420	7.6	7.8
4	33	432	6.3	6.7

Table 5.3: Peak EQE and integrated J_{sc} taken each week during the lifetime study.

5.2: Determination of the Degradation Mechanisms

Time resolved photoluminescence (TRPL) measurements were recorded on encapsulated films based on the structure ITO/PEDOT:PSS/$CH_3NH_3PbI_{3-x}Cl_x$ both before illumination, and again after one and two weeks of continuous illumination as shown in Figure 5.4(a). Here, it can be seen that there is a drop in the charge carrier lifetime after one week (168 hours) of illumination. This effect could result from several different processes, including an increase in the density of trap states within the material, an increase in recombination rate and a decrease charge-carrier mobility [12–14]. Each of these could result from a change in the chemical structure of the perovskite and the potential introduction of trap states that would result from this, particularly if the perovskite were to decompose into other materials, such as PbI_2 as indicated by the change in EQE.

A preliminary study regarding the effectiveness of the encapsulation system was also performed. Images of an unencapsulated and an encapsulated ITO/PEDOT:PSS/$CH_3NH_3PbI_{3-x}Cl_x$ film are shown in Figure 5.4(b) and (c) respectively. After 16 hours of illumination, it can be seen that the unencapsulated films became yellow; a process characteristic of complete degradation of the $CH_3NH_3PbI_{3-x}Cl_x$ to PbI_2 [11,15]. In contrast the encapsulated films retained their original dark-brown colour characteristic of $CH_3NH_3PbI_{3-x}Cl_x$ after two weeks of illumination. This illustrates that encapsulation is critical to preventing the complete device failure that would occur if the perovskite was exposed to ambient air and light, leading to decomposing into PbI_2.

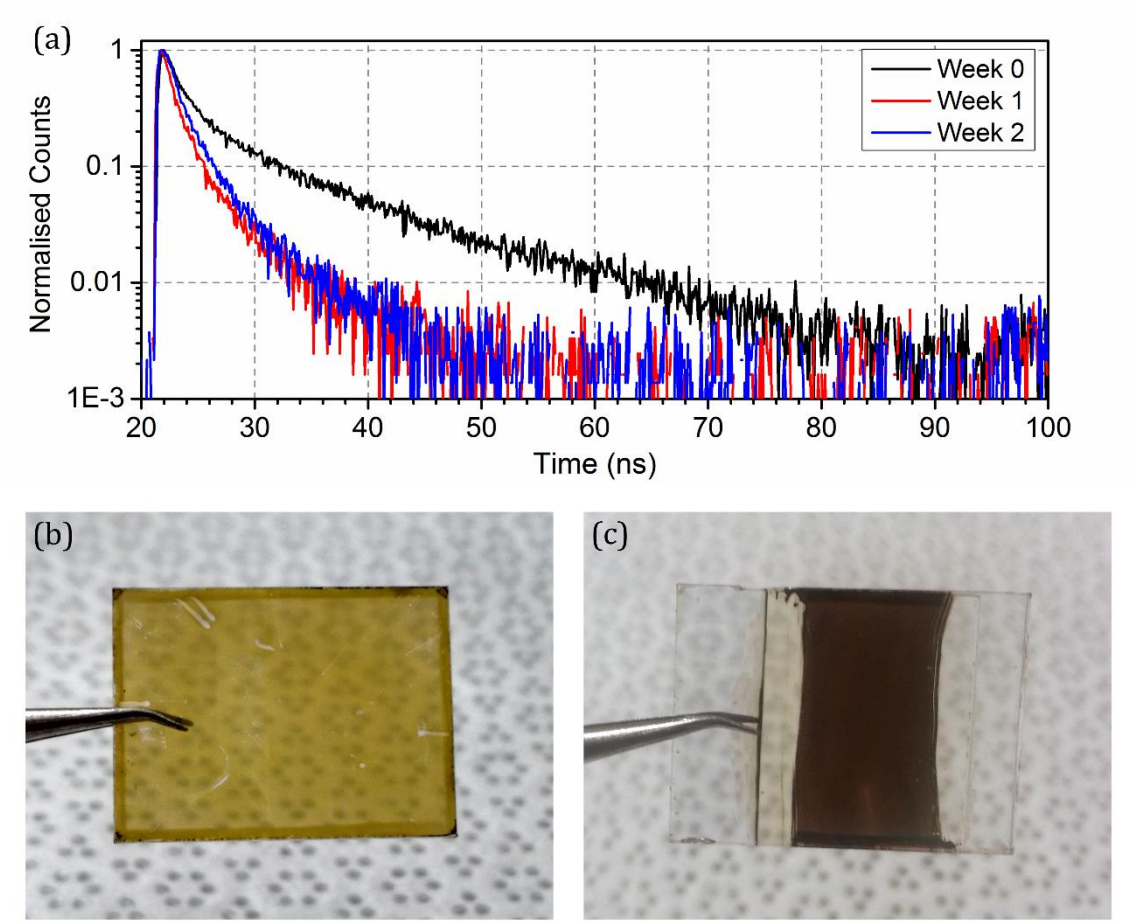

Figure 5.4: (a) Time resolved photoluminescence data for encapsulated ITO/PEDOT:PSS/ $CH_3NH_3PbI_{3-x}Cl_x$ films taken before illumination and after one and two weeks of continuous illumination. (b) Unencapsulated ITO/PEDOT:PSS/$CH_3NH_3PbI_{3-x}Cl_x$ after 16 hours of illumination. (c) Encapsulated ITO/PEDOT:PSS/$CH_3NH_3PbI_{3-x}Cl_x$ after 330 hours of illumination.

Optical images of the device before and after 670 hours of continuous illumination are shown in Figure 5.5(a) and (d) respectively. No obvious difference can be seen here, indicating no large scale morphological changes as a result of continuous operation. To probe the films for changes in spatially resolved photocurrent generation, laser beam induced current mapping was used before and after the ageing measurements with typical data plotted in Figure 5.5. Here, Figure 5.5(b) and (e) were recorded using a 405 nm laser before and after 670 hours of simulated solar irradiation. Figure 5.5(c) and (f) similarly plot data recorded using a 670 nm laser both before and after irradiation respectively. Unfortunately, the spatial location on the device surface of the measurements recorded 670 hours

apart is different. The photocurrent maps can, however, be analysed by plotting a histogram of the photocurrent recorded across the device, with all histograms normalised to their peak photocurrent. This is shown in Figure 5.5(g) and (h) for devices imaged at 405 and 670 nm respectively, with each figure plotting histograms for devices both before and after irradiation.

It can be seen that there is a decrease in the uniformity of current generation, with the standard deviation of the photocurrent data increasing from 4.2 ± 0.7% to 7.4 ± 0.9%, and 4.0 ± 0.3% to 7.2 ± 0.9% when imaged at 405 and 670 nm respectively. Furthermore, it can be seen in Figure 5.5(i) and (j), histograms of the absolute values of the LBIC data, that there is a significant drop in the photocurrent of the device after ageing for both wavelengths, concomitant with the decrease in J_{sc} observed in Figure 5.1. This reveals that degradation of the perovskite occurs equally both towards the PEDOT:PSS interface and within the bulk of the film, indicating that the degradation is a bulk process. It is apparent, however, that the degradation is not uniform across the film, with some areas more susceptible to degradation than others. It is possible that this is due to thickness variation within the film. Larger scale LBIC images covering whole devices were recorded after ageing and are shown in Figure 5.6. The photocurrent was found to be relatively homogeneous across most devices, however an area at the edge of one device exhibited very low current generation, possibly due to complete degradation of the perovskite. To check whether damage to the LiF/Al cathode occurred during the lifetime test, images of the cathode were recorded using an optical microscope both before and after imaging, shown in Figure 5.7, however no obvious delamination or formation of pin-holes was observed.

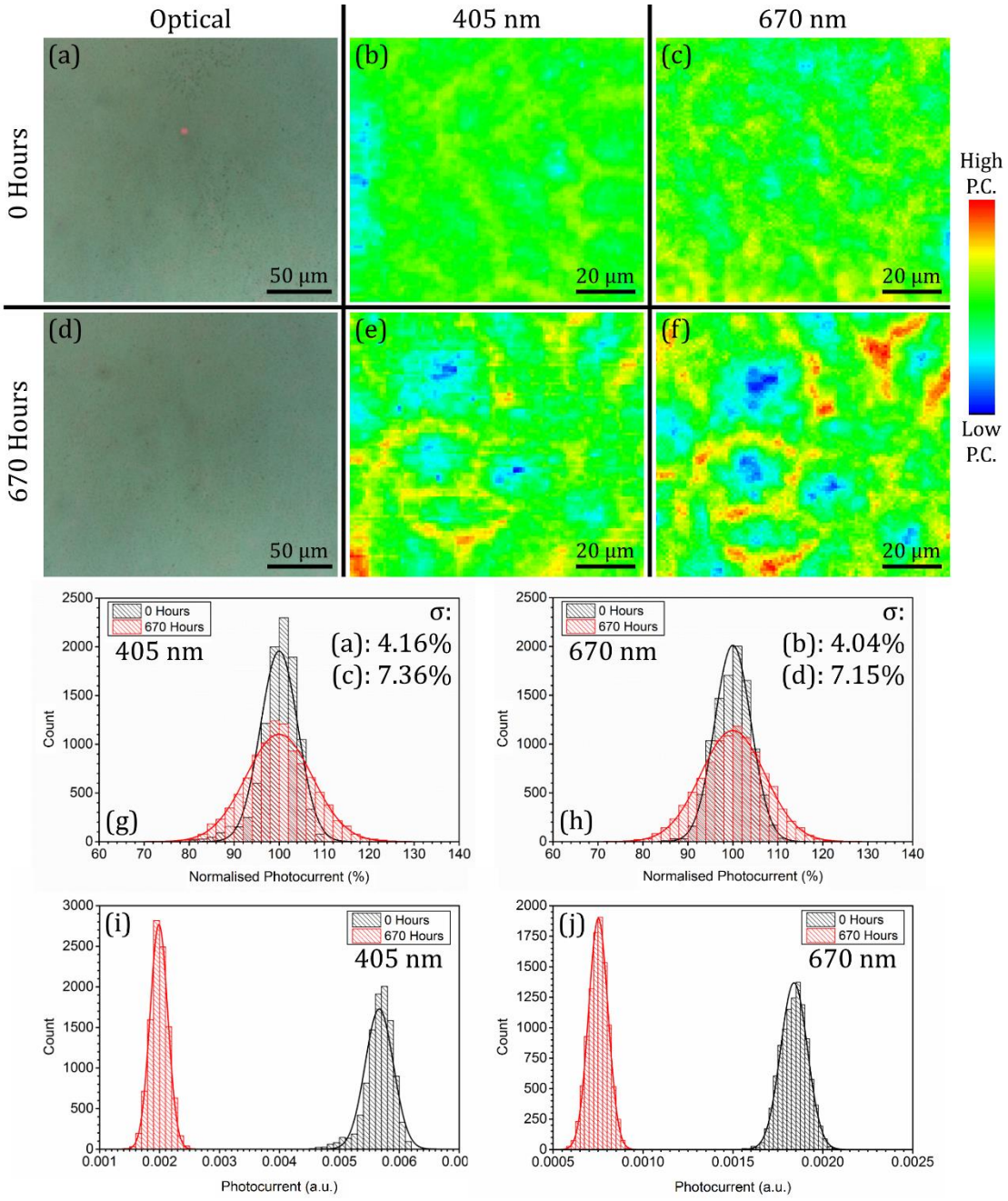

Figure 5.5: Laser beam induced current maps of devices before and after 670 hours of operation. Parts (a) and (d) show optical images of films before and after ageing respectively. Parts (b) and (e) were acquired using a 405 nm laser, before and after ageing respectively. Parts (c) and (f), were acquired using a 670 nm laser, before and after ageing respectively. Parts (g) and (h) are histograms of the normalised data shown in parts (b) and (e), and (c) and (f) respectively. The data in parts (g) and (h) are shown without normalisation in parts (i) and (j) respectively.

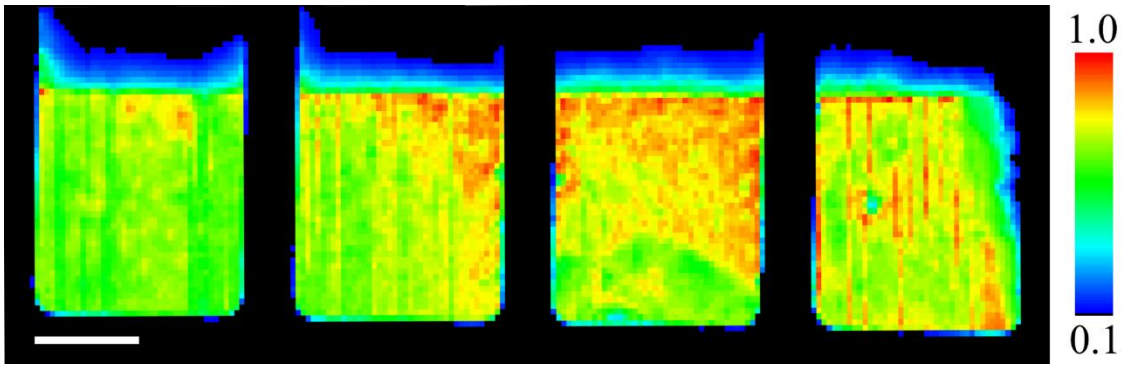

Figure 5.6: Laser beam induced current maps of four devices after the 670 hour stability test, taken using a 405 nm laser and normalised to the peak photocurrent. The scale bar represents 1 mm. A 10x microscope objective was to create a 10 µm laser spot, and the stages were moved in 50 µm increments.

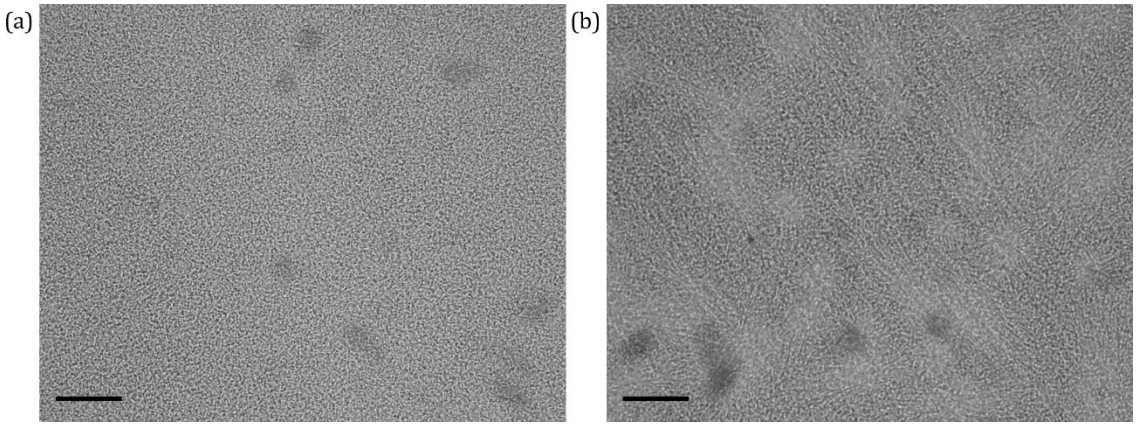

Figure 5.7: 10x microscope images of the Al cathode of (a) fresh and (b) aged devices. The scale bar represents 10 µm.

Due to the significant decrease in J_{sc}, reduction of the EQE primarily at wavelengths >500 nm, and decrease in charge carrier lifetime, the main cause of degradation is attributed to reactions with water and oxygen in the presence of light, resulting in the decomposition of the perovskite into methylamine (CH_3NH_2), hydroiodic acid (HI), iodine, water, and PbI_2 [15–18]. As the observed degradation occurs over a much longer period of time for encapsulated devices than it does for un-encapsulated devices, the water and oxygen required for this degradation process are concluded to be present in the device before encapsulation. Indeed, polymer:fullerene devices using calcium/aluminium cathodes have previously been reported as having lifetimes over 1 year when using the same encapsulation system, making it unlikely that the degradation catalysts are entering the device

through the encapsulation [19]. Furthermore, the devices would have shown more degradation at the edges than the centre if the catalysts were diffusing through the encapsulation, which is not seen in Figure 5.6. This inherent moisture could be strongly bound in the PEDOT:PSS, which is known to be highly hygroscopic [20], and may be released during the test due to the light and elevated temperatures, as shown in Figure 5.8. It has also been reported that $CH_3NH_3PbI_{3-x}Cl_x$ perovskite can contain hygroscopic methylammonium lead chloride, as described in Section 2.4.7, which would introduce another source of water within the device [21]. As the changes in spatially resolve current are similar for both the surface and bulk of the perovskite, it is possible that the water can travel along grain boundaries of the perovskite crystals before reacting and decomposing the perovskite. It should be noted that as methylamine and HI are soluble in water and volatile, they would normally escape an unencapsulated $CH_3NH_3PbI_{3-x}Cl_x$ film leaving a PbI_2 film. However, the encapsulation used here is likely to significantly reduce the rate at which these species escape, allowing them to remain in the film. As they remain in the film, they can act as charge trapping sites, which could explain the observed reduction in charge carrier lifetime in Figure 5.4. Indeed, the highest occupied state of methylamine and the lowest occupied state of HI exist within the band gap of the perovskite [22], enabling the trapping of holes and electrons respectively.

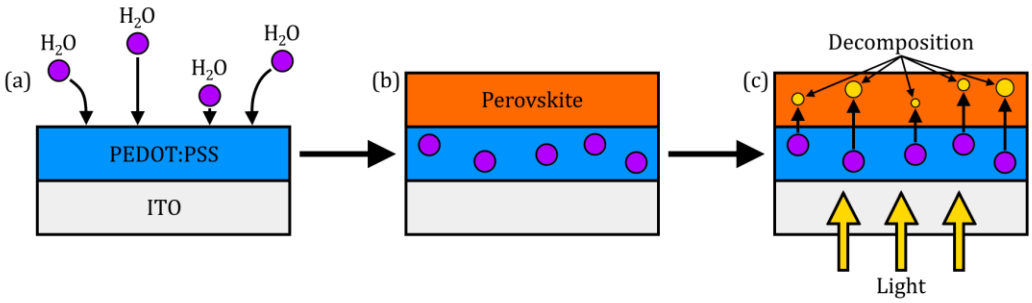

Figure 5.8: Schematic diagram of proposed degradation mechanism. (a) Water is absorbed into the PEDOT:PSS after deposition and strongly bound there. (b) The perovskite deposited onto the PEDOT:PSS traps the water in the layer during the subsequent steps of device fabrication. (c) Light heats up the device, enabling the water to diffuse into the perovskite and react, causing decomposition.

5.3: Conclusions

It has been shown that the operation stability of encapsulated $CH_3NH_3PbI_{3-x}Cl_x$ based perovskite solar cells utilising an inverted architecture is approximately 280 hours. The main cause of the degradation is likely to result from a reaction with water and oxygen that was introduced into the device during fabrication, probably strongly bound in the hygroscopic PEDOT:PSS hole-extraction layer. This water was then able to diffuse into the perovskite layer due to the elevated temperature of the continuous illumination. After reaching the perovskite, the water, together with residual oxygen is assumed to facilitate the decomposition of the perovskite into methylamine, hydoiodic acid, iodine, water, and PbI_2. As the escape of methylamine and hydoiodic acid from the device will be hindered due to the encapsulation, they may also act as a non-radiative recombination centres, reducing charge transport properties and thus reducing device J_{sc}. The data in this chapter will be referred to in the subsequent chapters as a point of comparison.

5.4: References

[1] M.A. Green, K. Emery, Y. Hishikawa, W. Warta, E.D. Dunlop, Solar cell efficiency tables (version 47), Prog. Photovolt Res. Appl. 24 (2016) 3–11.

[2] L.K. Ono, S.R. Raga, S. Wang, Y. Kato, Y. Qi, Temperature-dependent hysteresis effects in perovskite-based solar cells, J. Mater. Chem. A. 3 (2014) 9074–9080.

[3] T. Leijtens, G.E. Eperon, S. Pathak, A. Abate, M.M. Lee, H.J. Snaith, Overcoming ultraviolet light instability of sensitized TiO2 with meso-superstructured organometal tri-halide perovskite solar cells., Nat. Commun. 4 (2013) 2885.

[4] S. Guarnera, A. Abate, W. Zhang, J.M. Foster, G. Richardson, A. Petrozza, H.J. Snaith, Improving the long-term stability of perovskite solar cells with a porous Al2O3 buffer layer, J. Phys. Chem. Lett. 6 (2015) 432–437.

[5] H.J. Snaith, A. Abate, J.M. Ball, G.E. Eperon, T. Leijtens, N.K. Noel, S.D. Stranks, J.T.-W. Wang, K. Wojciechowski, W. Zhang, Anomalous Hysteresis in Perovskite Solar Cells, J. Phys. Chem. Lett. 5 (2014) 1511–1515.

[6] Y. Shao, Z. Xiao, C. Bi, Y. Yuan, J. Huang, Origin and elimination of photocurrent hysteresis by fullerene passivation in CH3NH3PbI3 planar heterojunction solar cells, Nat. Commun. 5 (2014) 1–7.

[7] Y. Zhao, C. Liang, H. min Zhang, D. Li, D. Tian, G. Li, X. Jing, W. Zhang, W. Xiao, Q. Liu, F. Zhang, Z. He, Anomalously large interface charge in polarity-switchable photovoltaic devices: an indication of mobile ions in organic-inorganic halide perovskites, Energy Environ. Sci. 0 (2015) Advance.

[8] W. Tress, N. Marinova, T. Moehl, S.M. Zakeeruddin, N. Mohammad K., M. Grätzel, M.K. Nazeeruddin, M. Grätzel, Understanding the rate-dependent J–V hysteresis, slow time component, and aging in CH3NH3PbI3 perovskite solar cells: the role of a compensated electric field, Energy Environ. Sci. 8 (2015) 995–1004.

[9] H. Zhang, C. Liang, Y. Zhao, M. Sun, H. Liu, J. Liang, D. Li, F. Zhang, Z. He, Dynamic interface charge governing the current-voltage hysteresis in perovskite solar cells, Phys. Chem. Chem. Phys. 17 (2015) 9613.

[10] P. Calado, A.M. Telford, D. Bryant, X. Li, J. Nelson, B.C. O'Regan, P.R.F. Barnes, Evidence for ion migration in hybrid perovskite solar cells with minimal hysteresis, Nat. Commun. 7 (2016) 13831.

[11] S. Ito, S. Tanaka, K. Manabe, H. Nishino, Effects of Surface Blocking Layer of Sb2S3 on Nanocrystalline TiO 2 for CH3NH3PbI3 Perovskite Solar Cells, J. Phys. Chem. C. 118 (2014) 16995–17000.

[12] Q. Chen, H. Zhou, T. Bin Song, S. Luo, Z. Hong, H.S. Duan, L. Dou, Y. Liu, Y. Yang, Controllable self-induced passivation of hybrid lead iodide perovskites toward high performance solar cells, Nano Lett. 14 (2014) 4158–4163.

[13] O. Gunawan, T.K. Todorov, D.B. Mitzi, Loss mechanisms in hydrazine-processed Cu2ZnSn(Se,S)4 solar cells., Appl. Phys. Lett. 97 (2010) 233506.

[14] C.S. Ponseca, T.J. Savenije, M. Abdellah, K. Zheng, A. Yartsev, T. Pascher, T. Harlang, P. Chabera, T. Pullerits, A. Stepanov, J.P. Wolf, V. Sundstr??m, Organometal halide perovskite solar cell materials rationalized: Ultrafast

charge generation, high and microsecond-long balanced mobilities, and slow recombination, J. Am. Chem. Soc. 136 (2014) 5189–5192.

[15] N. Aristidou, I. Sanchez-Molina, T. Chotchuangchutchaval, M. Brown, L. Martinez, T. Rath, S.A. Haque, The Role of Oxygen in the Degradation of Methylammonium Lead Trihalide Perovskite Photoactive Layers, Angew. Chemie - Int. Ed. 54 (2015) 8208–8212.

[16] Y. Han, S. Meyer, Y. Dkhissi, K. Weber, J.M. Pringle, U. Bach, L. Spiccia, Y.-B. Cheng, Degradation observations of encapsulated planar CH3NH3PbI3 perovskite solar cells at high temperatures and humidity, J. Mater. Chem. A. 3 (2015) 8139–8147.

[17] J.M. Frost, K.T. Butler, F. Brivio, C.H. Hendon, M. Van Schilfgaarde, A. Walsh, Atomistic origins of high-performance in hybrid halide perovskite solar cells, Nano Lett. 14 (2014) 2584–2590.

[18] A.J. Pearson, G.E. Eperon, P.E. Hopkinson, S.N. Habisreutinger, J.T.W. Wang, H.J. Snaith, N.C. Greenham, Oxygen Degradation in Mesoporous Al2O3/CH3NH3PbI3-xClx Perovskite Solar Cells: Kinetics and Mechanisms, Adv. Energy Mater. 6 (2016) 1–10.

[19] Y. Zhang, E. Bovill, J. Kingsley, A.R. Buckley, H. Yi, A. Iraqi, T. Wang, D.G. Lidzey, PCDTBT based solar cells : one year of operation under real-world conditions, Sci. Rep. 6 (2016) 21632.

[20] A. Elschner, S. Kirchmeyer, W. Lovenich, U. Merker, K. Reuter, PEDOT: Principles and Applications of an Intrinsically Conductive Polymer, CRC Press, 2010.

[21] F.X. Xie, D. Zhang, H. Su, X. Ren, K.S. Wong, M. Grätzel, W.C.H. Choy, Vacuum-Assisted Thermal Annealing of CH3NH3PbI3 for Highly Stable and Efficient Perovskite Solar Cells, ACS Nano. 9 (2015) 639–646.

[22] P. Delugas, A. Filippetti, A. Mattoni, Methylammonium fragmentation in amines as source of localized trap levels and the healing role of Cl in hybrid lead-iodide perovskites, Phys. Rev. B - Condens. Matter Mater. Phys. 92

(2015) 1–11.

Chapter 6

The Effects of Hydroiodic Acid Additive on the Performance and Stability of Spray and Spin Coated Perovskite Solar Cells

6.0: Introduction

Spin coating is the primary fabrication method used for the fabrication of perovskite solar cells (PSCs), however, the ideal fabrication technique would be a more scalable technique, compatible with roll-to-roll manufacturing. Due to the high power conversion efficiencies exhibited by state-of-the-art PSCs (over 20%, see Chapter 2, section 2.4), it has become important to investigate the possibility of using such techniques to produce efficient and stable PSCs. In this chapter, work is presented on the stability of 'inverted' architecture devices (using the same structure as the devices in Chapter 5) in which the mixed halide perovskite $CH_3NH_3PbI_{3-x}Cl_x$ has been deposited via ultrasonic spray coating, a roll-to-roll compatible deposition technique. Two different precursor solutions were used for the perovskite layer, the first being the standard solution for air processing, albeit at a lower concentration (optimised for spray coating), and the second containing 1 vol% hydroiodic acid (HI) as an additive in an attempt to improve the solubility of the precursor materials. The PSCs were subjected to 670 hours (4 weeks) of continuous illumination, with *J-V* curves taken using a calibrated solar simulator and EQE measurements performed every week. Similar experiments were then performed for devices fabricated via spin coating, to find out if the improvements observed in spray coated devices transferred to other deposition methods. The results in this chapter will be compared to those for spin coated PSCs presented in Chapter 5 to enable evaluation of spray coating and use of the HI additive.

6.1: Spray Coating

All of the devices in this chapter had a perovskite layer deposited via a PRISM ultrasonic spray coater from Ultrasonic Systems Inc. Substrates with a 100 nm pre-patterned layer of ITO and a 35 nm spin coated PEDOT:PSS layer were placed on a 70°C hotplate beneath the spray coater. A 1:3 $PbCl_2$:MAI perovskite precursor solution with a total solid concentration of 200 mg/ml was fed onto the tip of the spray coater, which was vibrated at 35 kHz and held 40 mm above the substrates during deposition. A gas pressure of 10 psi was used to direct and planarise the spray generated by the ultrasonic tip as the spray head was passed over the substrates. A single pass of 150 mm at a speed of 220 mm/s was used to form the perovskite precursor film before the substrates were transferred to a hotplate held at 90°C for annealing. All other layers in the devices were fabricated as described in Chapter 3. Devices with a spray coated perovskite layer were fabricated by David Mohamad of the Department of Physics and Astronomy, University of Sheffield.

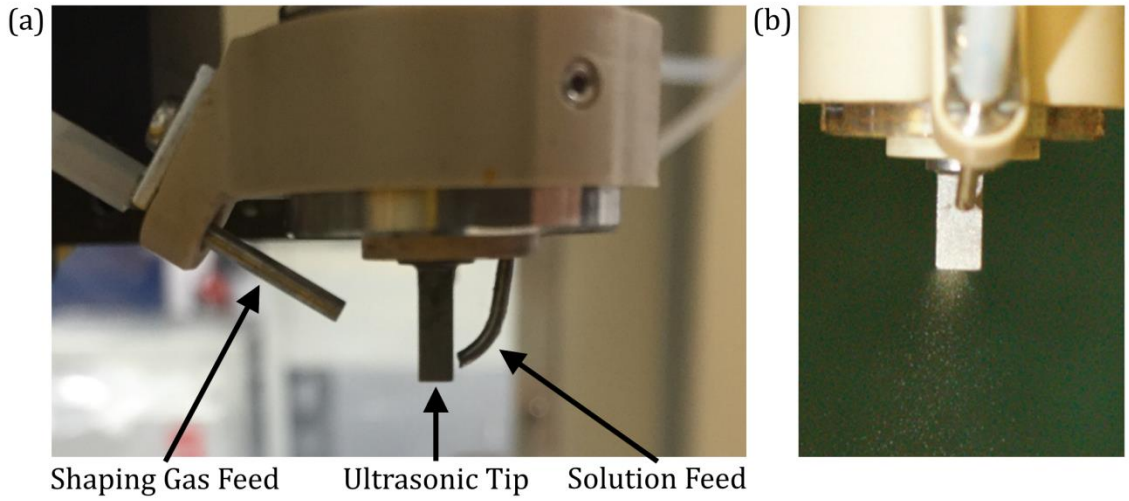

Figure 6.1: (a) The head of the spray coater with the ultrasonic tip, and solution and shaping gas feeds highlighted. (b) Spray coater head in operation.

6.2: Initial Spray Coated Device Performance

Initial attempts to spray coat the $CH_3NH_3PbI_{3-x}Cl_x$ were met with very variable results and poor surface coverage. It was noticed that solutions heated for longer periods of time often performed better, hinting at possible solubility issues of the

precursor materials causing the variation in results. The addition of HI to the precursor solution of formamidinium lead triiodide perovskite has been shown to improve the performance in standard architecture devices due to improved surface coverage. This was speculated to be due to improved solubility of the precursor materials [1]. Therefore it was decided to try adding HI to the precursor solution of $CH_3NH_3PbI_{3-x}Cl_x$ to see if improved device performance could be attained for spray and spin coated inverted architecture devices. It should be noted that the added HI was a 57% solution with DI water.

In Figure 6.2(a) and (b), the average *J-V* curves of PSCs fabricated via spray coating without and with a HI additive respectively are presented. The metrics corresponding to these curves are given in Table 6.1. With the addition of HI there is an improvement in the PCE from 8.4 ± 0.4% to 10.4 ± 0.3%, a value comparable to the performance of the spin coated devices in Chapter 5. This enhancement is primarily a result of an increased short circuit current density, J_{sc}, from -13.5 ± 0.1 to 16.7 ± 0.1 mA/cm^2 with the addition of HI. Increases in J_{sc} can be attributed to improved light absorption of the active layer [2,3], or improved charge carrier generation, transport, and extraction efficiency [4]. Interestingly, the *FF* slightly decreased with the addition of HI, indicating that the improved J_{sc} is more a result of improved absorption than charge carrier dynamics, due to the dependence of the *FF* on the electronic properties of a device (such as R_{sh} and R_s, see Section 2.2).

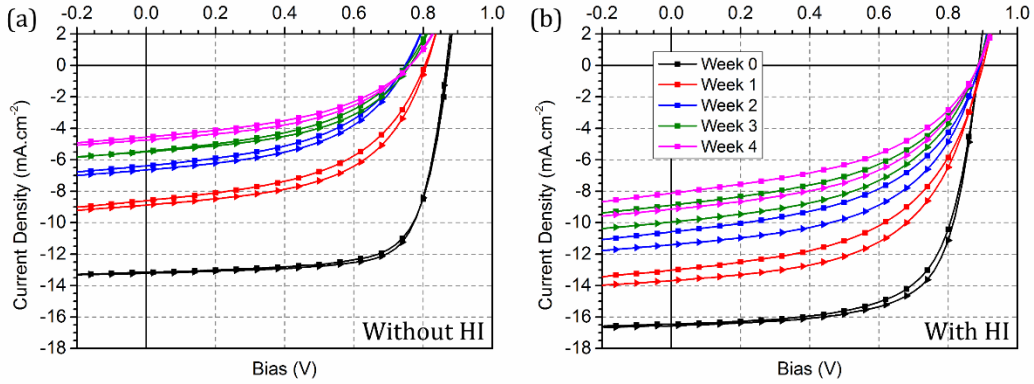

Figure 6.2: J-V curves of spray coated PSCs (a) without and (b) with the HI additive at different stages during the lifetime study. Squares represent forwards scans, triangles represent backwards scans.

Additive	Scan Direction	PCE (%)	FF (%)	J_{sc} (mA/cm²)	V_{oc} (V)	R_{sh} (Ω cm²)	R_s (Ω cm²)
No	Forwards	8.2 ± 0.4	72 ± 2	-13.4 ± 0.1	0.87 ± 0.01	1380 ± 230	6.0 ± 0.2
	Backwards	8.4 ± 0.4	73 ± 1	-13.5 ± 0.1	0.87 ± 0.01	1880 ± 500	5.9 ± 0.2
Yes	Forwards	10.0 ± 0.3	68 ± 2	-16.7 ± 0.1	0.89 ± 0.01	1850 ±750	5.2 ± 0.3
	Backwards	10.4 ± 0.3	70 ± 2	-16.7 ± 0.1	0.89 ± 0.01	2190 ± 620	5.0 ± 0.2

Table 6.1: Mean device metrics and standard deviations for open circuit voltage, short circuit current density, fill factor, power conversion efficiency, and shunt and series resistance, extracted from *J-V* curves, for spray coated devices without and with the HI additive. 12 devices were used calculate the mean and standard deviations for both device types.

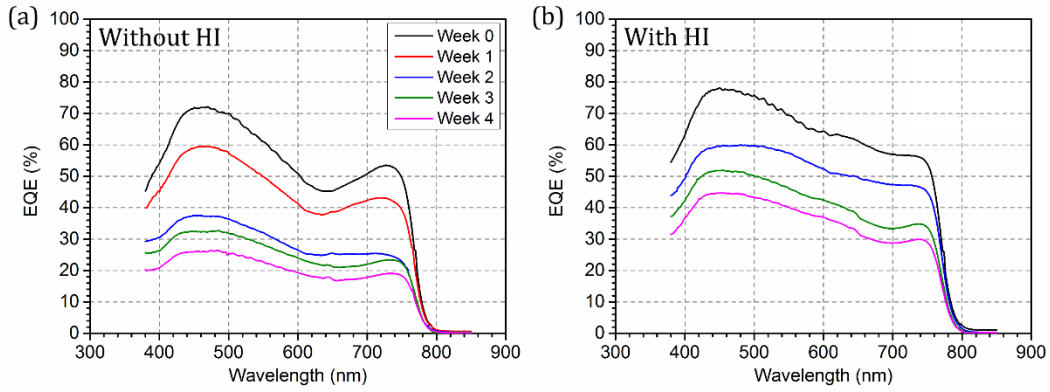

Figure 6.3: EQE of spray cast devices (a) without and (b) with the HI additive at different stages during the lifetime study.

Concomitant with the increases in J_{sc}, there is an increase in the external quantum efficiency (EQE) of the devices with HI over those without, as shown in Figure 6.3. In particular, there is a large dip in the EQE spectrum for spray cast devices without HI at approximately 640 nm which is not present in the EQE of devices with HI. Given this strong spectral difference between the EQE measurements, it is apparent that light absorption efficiency plays a larger role than changes to the charge carrier dynamics in the observed improvement of the J_{sc}, suggesting that

the addition of HI to the precursor solution leads to improved light absorption for the subsequent perovskite film.

The improved light absorption observed in PSCs fabricated with the HI additive could arise from improved conversion of the precursor materials into perovskite crystals. Indeed, this may account for the observed dip in the EQE spectrum of devices without the additive. This could be a result of the additive improving the solubility of the precursors, enabling better control over the material ratios which are deposited. This improved solubility could be a result of the additional HI altering the Hansen Solubility Parameters of the solvent mixture, making them more favourable for dissolution of MAI and $PbCl_2$ [5,6]. Surface coverage of the perovskite layer may also be increased, which would improve the overall absorption efficiency of the device, and hence the J_{sc} and EQE [7]. Indeed, this is consistent with the findings for use of the additive in standard architecture formamidinium lead triiodide perovskite solar cells [1]. Furthermore, this has also been observed with the additive 1-chloronaphthalene, where the absorption was enhanced through the reduction of pinholes and voids in the film [8] and with the addition of 1,8-diiodooctane, which improved the crystallisation of the perovskite [9].

Optical images of spray coated perovskite films fabricated without and with the HI additive are shown in Figure 6.4(a) and (d) respectively. It can be seen that there is a significant difference between these films, with what appears to be a large scale structure existing in the film fabricated without HI. In the film fabricated with HI the film appears to be more uniform, indicating that the addition of HI significantly impacts the formation of the perovskite film, potentially enabling more favourable crystal formation. It does not appear that the surface coverage is affected on a large scale, as no pinholes or voids are visible in either of the images. However, this may still have occurred on a smaller length scale, and would need to be investigated using a higher resolution technique, such as SEM.

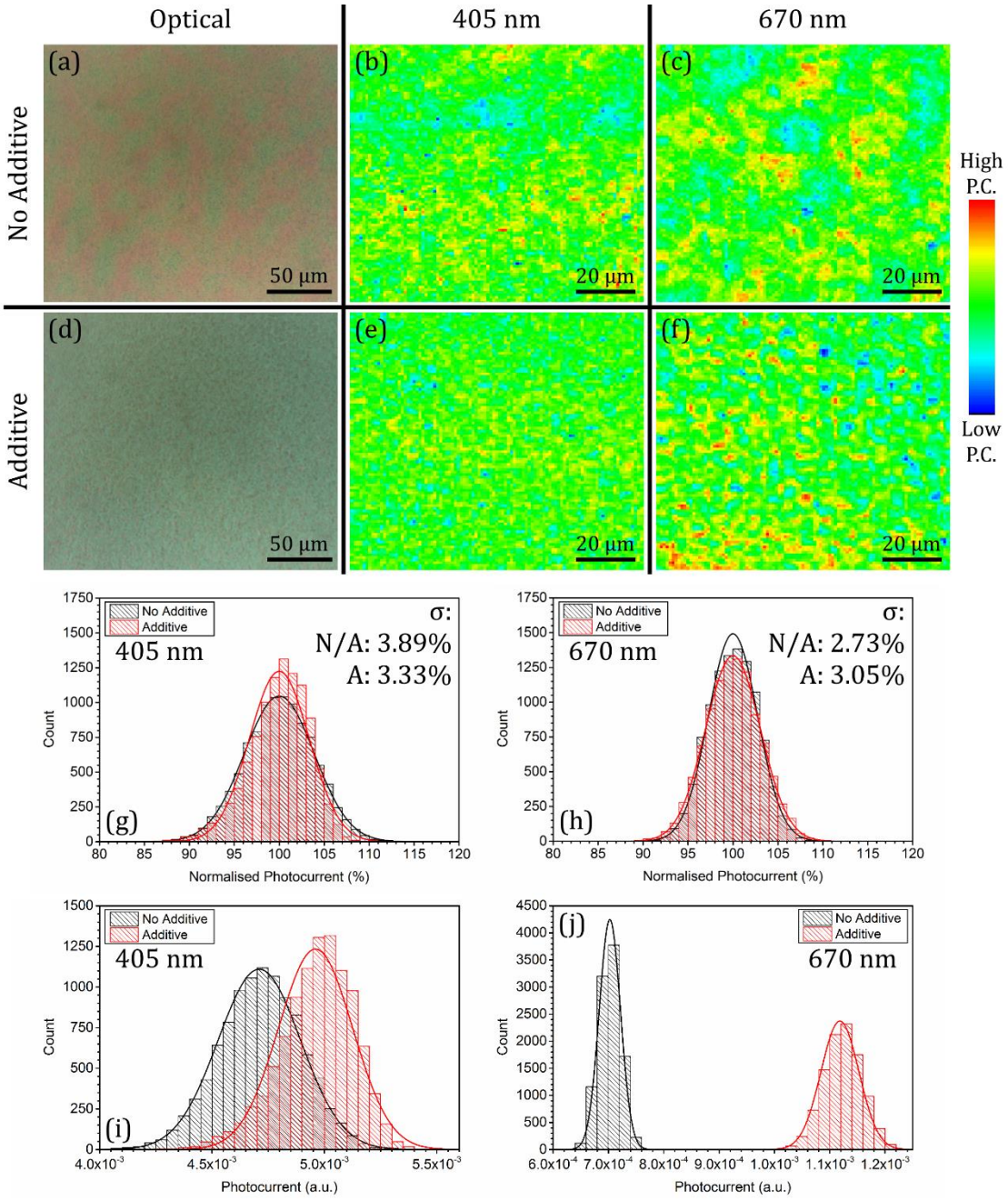

Figure 6.4: Laser beam induced current maps for spray cast devices. Parts (a) and (d) show optical images of films fabricated without and with HI respectively. Parts (b) and (e) were acquired using a 405 nm laser, without and with HI respectively. Parts (c) and (f), were acquired using a 670 nm laser, without and with HI respectively. Parts (g) and (h) are histograms of the normalised data shown in parts (b) and (e), and (c) and (f) respectively (N/A = No Additive, A = Additive). The data in parts (g) and (h) are shown without normalisation in parts (i) and (j) respectively.

Laser beam induced current (LBIC) mapping was used to investigate differences in spatially resolved photocurrent generation of the PSCs, and is plotted in Figure 6.4. A 405 nm laser was used to collect the data in Figure 6.4(b) and (e), corresponding to devices without and with the HI additive respectively. The data in Figure 6.4(c) and (f) was acquired using a 670 nm laser, and similarly corresponds to devices without and with the HI additive respectively. Histograms of the data for the 405 nm and 670 nm laser are shown in Figure 6.4(g) and (h) respectively to allow clearer comparison between the different devices.

It can be seen that there is a small increase in the uniformity of current generation at 405 nm for the devices with the additive over those without, with the standard deviation of the data decreasing from 3.9 ± 0.1% to 3.3 ± 0.1% respectively. Interestingly, this is not true at 670 nm, with uniformity of current generation appearing to decrease slightly for devices with the additive, with the standard deviation increasing from 2.7 ± 0.1% to 3.1 ± 0.04% for devices without and with the additive respectively. This implies that the HI may be introducing recombination pathways whilst improving the surface coverage. The histograms in Figure 6.4(i) and (j) are of the absolute values for the LBIC data. It can clearly be seen that there is an increase in the photocurrent when HI is added to the precursor solution. This increase is significantly greater in the bulk of the perovskite than near the PEDOT:PSS interface, consistent with the changes observed in the EQE spectra, further suggesting improvements in the optical and electronic properties of the perovskite, as discussed in Section 2.2.

It is important to note, however, that despite being able to achieve comparable performance to spin coated PSCs, spray coated PSCs fabricated with HI suffer from film uniformity issues. This is highlighted in Figure 6.5, where LBIC maps of devices with the perovskite deposited through spin coating and spray coating taken using a 405 nm laser are compared. Here, Figure 6.5(a) and (b) show large area, low resolution (50 μm per point) LBIC maps for spin and spray coated devices respectively, with line profiles through the centre of each set of devices shown in Figure 6.5(e).

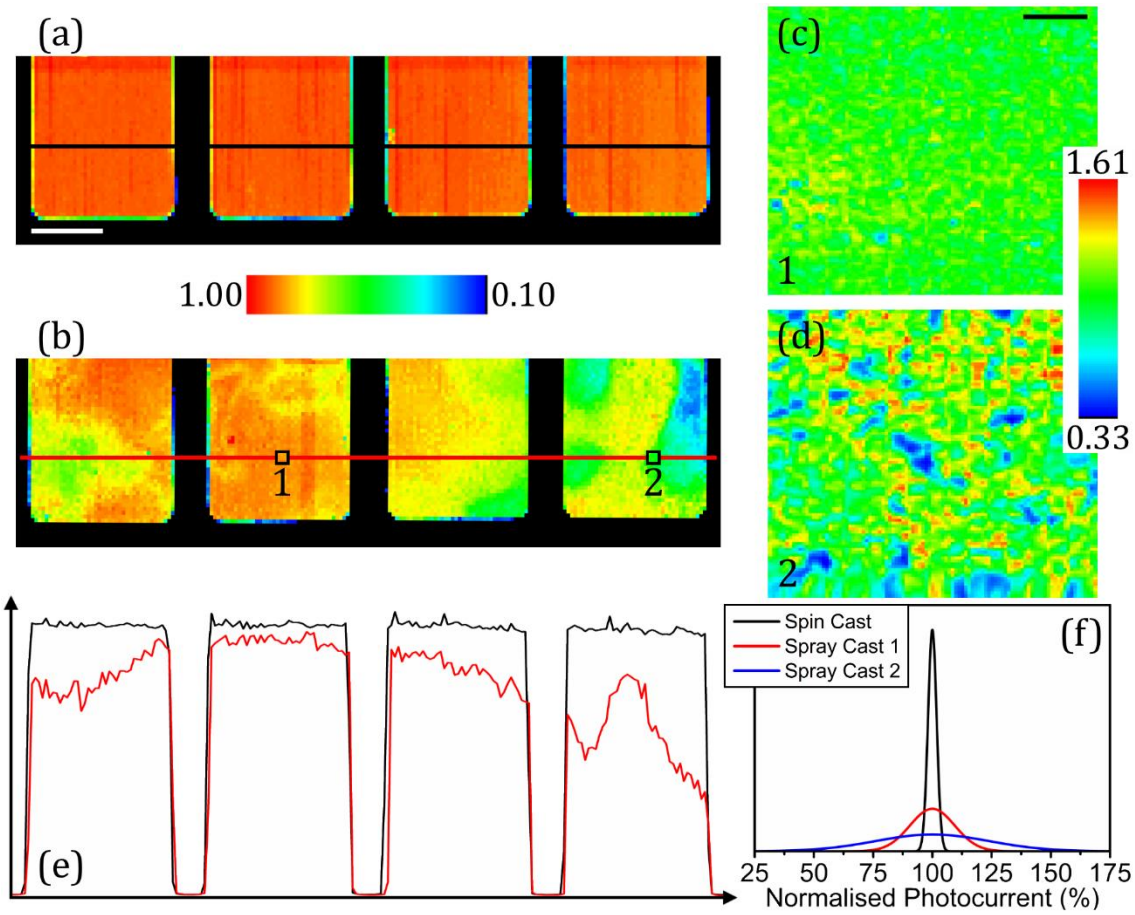

Figure 6.5: (a) and (b) are low resolution (scale bar represents 1 mm) LBIC maps over 4 devices for spin and spray coated devices respectively. (c) and (d) are high resolution (scale bar represents 20 μm) LBIC maps of the marked areas in (b). Line profiles of (a) and (b) are shown in (e). A histogram of the data in (c), (d), and a spin coated device, is shown in (f).

It can clearly be seen that the photocurrent generation across the spin coated devices is relatively uniform, whilst there is significant variation across the spray coated devices. These fluctuations can be seen on a smaller scale in Figure 6.5(c) and (d), which show high resolution (1 μm per point) LBIC maps of the labelled areas of the spray cast device in Figure 6.5(b). This data is summarised and compared with data from a spin coated device in the histogram in Figure 6.5(f). The standard deviation of the data for the spin coated device was 1.8%, whilst the standard deviations of the data for the spray coated devices in Figure 6.5(c) and (d) were 9.4% and 24% respectively. It is speculated that such large-scale fluctuations in the spray coated perovskite films result from local thickness

variations in the initial precursor film, caused by turbulence in the air flow used to direct the spray onto the substrate. This film is unable to reorganise due to the fast drying rates required when using this deposition technique, resulting in the thickness fluctuations being effectively set into the final dry film [10]. It therefore appears that the electrical properties of the spray cast films fabricated with HI are superior to those of the spin cast films, as the device performances are comparable despite the significant inhomogeneity of photocurrent generation in the spray cast film.

6.3: The Stability of Spray Coated Perovskite Solar Cells

The PCE, *FF*, J_{sc}, and V_{oc} of spray coated PSCs fabricated with and without the additive are plotted as a function of irradiance time in Figure 6.6. Similarly to Chapter 5, the data represented by lines was taken using the Atlas CPS+ lifetime testing system, whilst the data represented by points was recorded using a calibrated Newport solar simulator (AM1.5, 100 mW/cm^2), with all data normalised to their initial values.

During the 670 hours of illumination the average PCE of spray coated devices without HI decreased by 79 ± 2%, whereas the PCE of those with HI decreased by 72 ± 2%. For both sets of devices, the observed losses were primarily caused by a 67 ± 1% decrease in the J_{sc}. The improved stability of the spray coated devices utilising the HI additive originates from increased stability of the *FF* and V_{oc}. Here, *FF* decreases by 13 ± 4% and the V_{oc} by 3 ± 1% over the 670 hour period, whereas in the spray coated devices without HI the *FF* and V_{oc} degrade by 25 ± 1% and 12 ± 2% respectively. As with the spin coated devices in Chapter 5, the PCE and V_{oc} taken using both the Atlas lifetime tester and Newport solar simulator are in good agreement, whilst there is some difference in the *FF* and J_{sc}. Again, this is likely a result of differences in the temperature of the two systems [11].

The T_{80} of the spray coated devices both with and without HI is difficult to quantify as the lifetime PCE plot is curved for almost the entire duration of the test. Despite this, it is clear that spray coated devices, like the spin coated devices in Chapter 5, have short lifetimes and will likely completely degrade within a matter of months.

The evolution of the *J-V* curves corresponding to the points in Figure 6.6 are shown in Figure 6.2, with device metrics at the end of the lifetime test presented in Table 6.2. It can be seen that R_s increases for devices both with and without the additive. The increase is much more significant in the devices without the additive, (39.9 ± 3.7 Ω cm^2), than in those without (18.1 Ω cm^2), indicating the formation of fewer trapping sites within the perovskite fabricated using HI. It should be noted that whilst HI can act as a trapping site, it is volatile and is removed from the perovskite during the annealing process. Indeed, as the V_{oc} as measured by the calibrated Newport solar simulator after continuous illumination is identical to the value before the test (0.89 ± 0.01 V), it is more likely that the increase in R_s for devices with HI originates from an increase of interfacial resistance between the transport layers and the perovskite. Therefore, it appears that the perovskite fabricated with HI exhibits a greater degree of chemical stability than the perovskite fabricated without HI, as the decomposition products, such as methylamine and HI, have been shown to act as trapping sites [12], leading to losses of V_{oc} and increases of R_s.

Additive	**Scan Direction**	**PCE** (%)	**FF** (%)	**J_{sc}** (mA/cm^2)	**V_{oc}** (V)	**R_{sh}** (Ω cm^2)	**R_s** (Ω cm^2)
No	Forwards	1.4 ± 0.2	43 ± 1	-4.6 ± 0.2	0.77 ± 0.02	540 ± 70	43.6 ± 3.6
	Backwards	1.5 ± 0.3	45 ± 1	-4.7 ± 0.1	0.77 ± 0.02	610 ± 60	39.9 ± 3.7
Yes	Forwards	3.4 ± 0.2	47 ± 1	-8.1 ± 0.4	0.89 ± 0.01	380 ± 20	20.4 ± 0.8
	Backwards	4.0 ± 0.1	49 ± 1	-9.1 ± 0.4	0.89 ± 0.01	440 ± 30	18.1 ± 0.6

Table 6.2: Mean device metrics and standard deviations for open circuit voltage, short circuit current density, fill factor, power conversion efficiency, and shunt and series resistance, extracted from *J-V* curves, for spray coated devices without and with the HI additive. 12 devices were used calculate the mean and standard deviations for both device types.

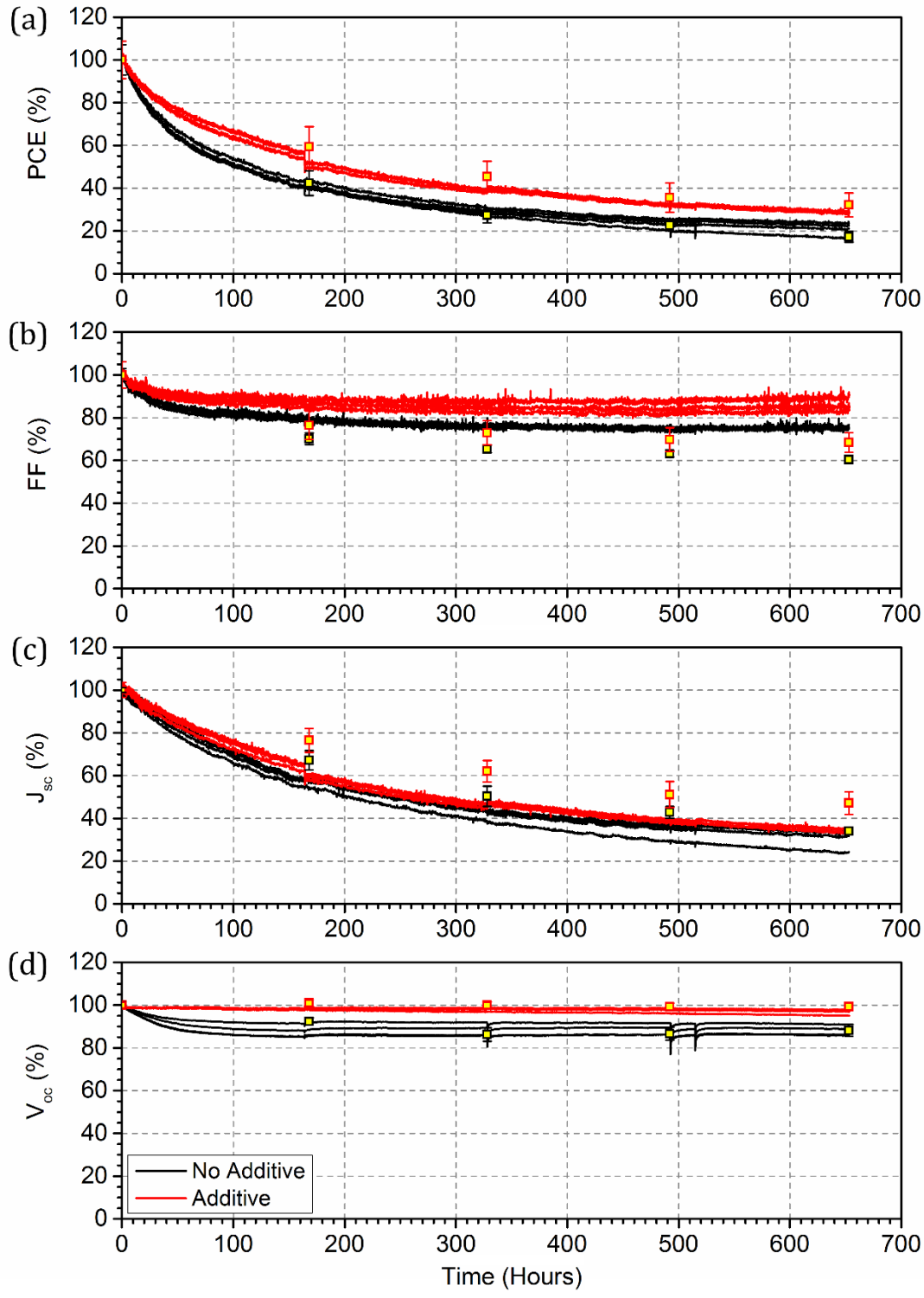

Figure 6.6: (a) PCE, (b) *FF*, (c) J_{sc}, and (d) V_{oc} of spray coated PSCs without and with the HI additive over 670 hours of continuous illumination. Solid points are data taken using a calibrated solar simulator. All *J-V* scans were performed from -1 to 1 V.

Interestingly, there is an increase in the level of hysteresis of *J-V* curves for the PSCs fabricated with the additive, which does not occur for the devices fabricated without HI. The hysteresis arises from a ~10% difference in the J_{sc} for forward and reverse J-V scans, indicative of increases in interfacial recombination and ionic species migration within the active layer [13–18], as discussed in Section 2.4.6.

Figure 6.3 presents the evolution of the EQE over the course of the lifetime study. For devices both with and without the additive, the peak EQE decreases over the 670 hours of continuous illumination. However, the relative decrease is much greater for devices without the additive, where the peak EQE decreased by ~65% after 670 hours, than those with the additive, where the peak EQE decreased by ~45%. The evolution of the spectral shape also differs between the devices, as shown in Figure 6.7, with the shape remaining approximately the same for devices without the additive, whilst there are relative losses in the EQE at higher wavelengths (>600 nm) for devices with the additive. As explained in Chapter 5, losses in EQE at wavelengths greater than 500 nm are indicative of chemical breakdown of the perovskite crystal into PbI_2, among other compounds [19].

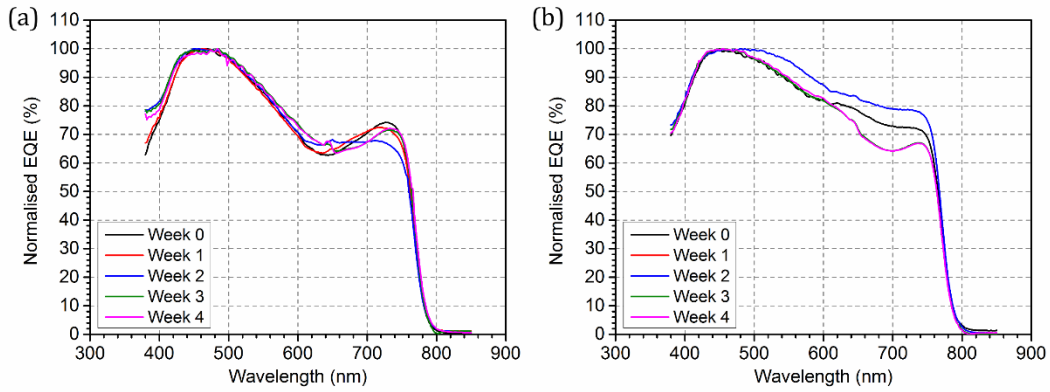

Figure 6.7: Normalised EQE curves for spray coated devices fabricated (a) without and (b) with the HI additive.

Comparing these devices to those fabricated using spin coating in Chapter 5, it is interesting that the spray coated devices utilising the HI additive proved to be the most stable. Whilst the spin coated devices ended the lifetime test with a PCE of 2.3 ± 0.4% (~20% of initial performance), spray coated devices with HI retained 4.0 ± 0.1% (~40% of initial performance). This is due to greater stability of the J_{sc} and

V_{oc} of the spray coated devices over the spin coated devices. As with the differences observed between spray coated devices with and without the additive, this may be due improved precursor conversion due to the presence of HI, affording the perovskite a greater degree of chemical stability. This would also explain the comparable efficiencies of spray coated devices utilising HI and spin coated devices, despite the observed large scale uniformity issues. It is therefore possible that using the HI additive in spin coated devices could improve over performance, as well as potentially improving the stability of such devices.

6.4: The Effects of the Additive on Spin Coated Devices

Due to the success of the HI additive in spray coated devices, it was used in spin coated devices to see if similar improvements could be achieved. As with the spray coated devices, 1 vol% HI was added to the perovskite precursor solution before deposition. The average *J-V* curve for the resultant devices is shown in Figure 6.8, with average metrics presented in Table 6.3. It can be seen that the PCE is significantly improved, increasing from 10.6 ± 0.4% (see Chapter 5) to 13.2 ± 0.6%. Similarly to the spray coated devices, this is primarily due to an enhancement of the J_{sc} to -18.8 ± 0.2 mA/cm^2, a 17.5% increase compared to devices fabricated without the additive in Chapter 5. There are also small improvements in the V_{oc} and R_s, indicating reduced charge trapping and recombination within the perovskite film.

Again, the improvements in the J_{sc} can be seen in the EQE of these devices over those in Chapter 5, with increases in EQE across all wavelengths, as shown in Figure 6.9(a). It is worth noting that a small dip in the EQE around 700 nm present in the EQE of devices without HI (Chapter 5) is reduced with the addition of the HI additive. This is similar to the improvements in the spray coated devices, and likely arises from the same mechanisms as with the spray coated devices; improved perovskite formation or surface coverage due to better precursor material control.

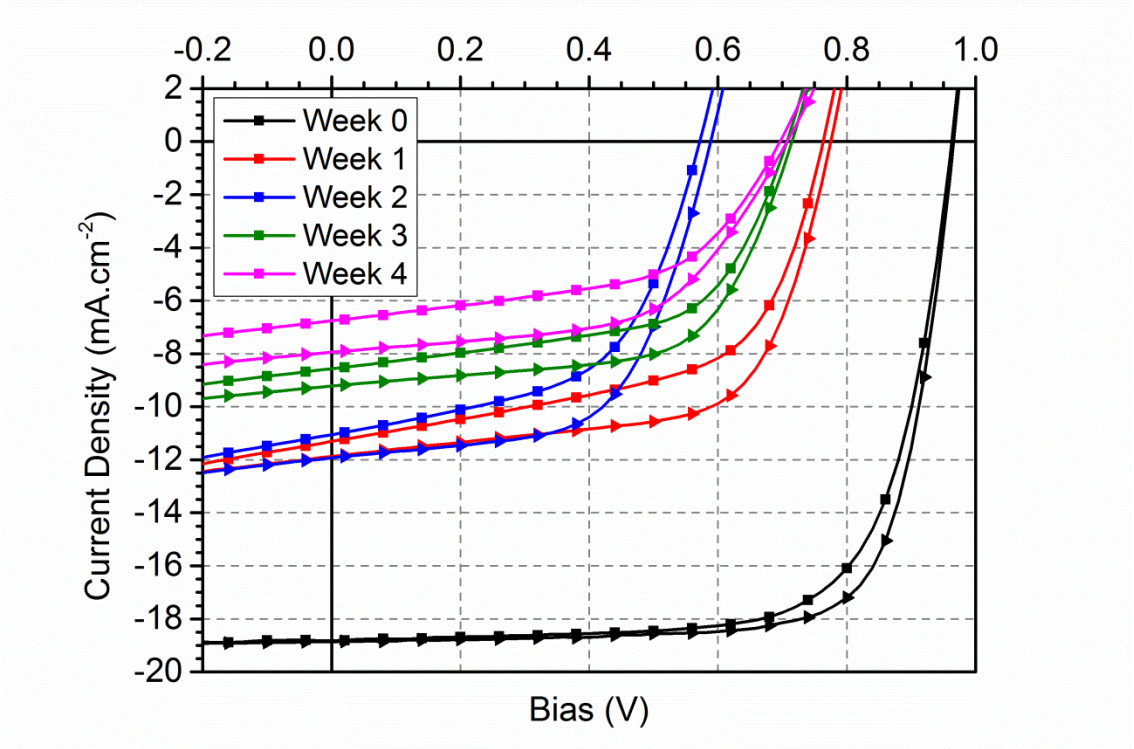

Figure 6.8: J-V curves of spin coated PSCs with the HI additive at different stages during the lifetime study. Squares represent forwards scans, triangles represent backwards scans.

Time (Hours)	**Scan Direction**	**PCE** (%)	**FF** (%)	**J_{sc}** (mA/cm²)	**V_{oc}** (V)	**R_{sh}** (Ω cm²)	**R_s** (Ω cm²)
0	Forwards	12.4 ± 0.9	69 ± 4	-18.8 ± 0.2	0.96 ± 0.01	1580 ± 540	5.1 ± 0.3
	Backwards	13.2 ± 0.6	73 ± 3	-18.8 ± 0.2	0.96 ± 0.01	2120 ± 700	5.3 ± 0.5
670	Forwards	2.5 ± 0.3	54 ± 1	-6.8 ± 0.9	0.69 ± 0.01	350 ± 20	21.5 ± 2.0
	Backwards	3.0 ± 0.3	57 ± 1	-7.6 ± 1.0	0.72 ± 0.03	560 ± 310	22.2 ± 1.0

Table 6.3: Mean device metrics and standard deviations for open circuit voltage, short circuit current density, fill factor, power conversion efficiency, and shunt and series resistance, extracted from *J-V* curves, for spin coated devices with the HI additive. 8 devices were used to calculate the mean and standard deviation.

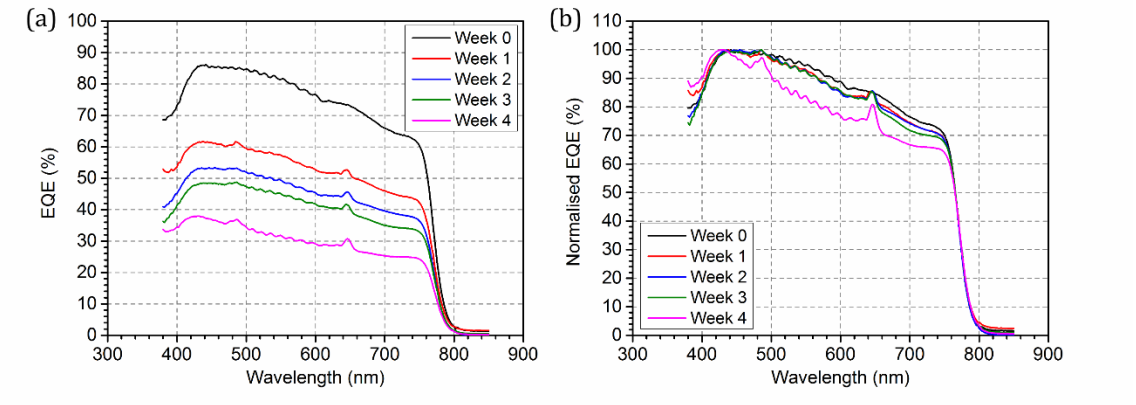

Figure 6.9: (a) EQE and (b) normalised EQE of spin coated devices fabricated with the HI additive at different stages of the lifetime study.

An optical microscope image of the spin cast perovskite fabricated with the HI additive is shown in Figure 6.10. Here, it can be seen that the perovskite has a needle-like structure that was not seen in the images in Figure 5.5 (see Section 5.2), indicating that the HI has a significant impact on the conversion of the precursor materials and the formation of the perovskite crystal, as seen with the spray coated films in Figure 6.4.

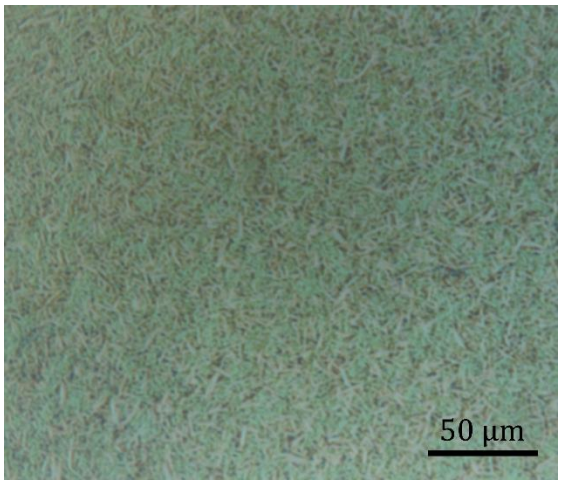

Figure 6.10: Optical microscope image of a spin cast perovskite film fabricated with HI.

In Figure 6.11, the PCE, *FF*, J_{sc}, and V_{oc} over 670 hours of continuous operation for four spin coated devices fabricated with the HI additive are presented. Data represented by lines were taken using the Atlas CPS+ lifetime tester, and data represented by points were measured using a calibrated Newport solar simulator.

It can be seen that whilst the PCE decreases by 79 ± 4%, the same losses as the devices in Chapter 5, the behaviour of the decay is slightly different. The V_{oc} decays by ~20% over the first 150 hours before becoming significantly more stable, whereas without the additive the V_{oc} decreased by the same amount over the course of the entire study. Here, the *FF* of most devices increases after 100 hours of continuous illumination for 100 hours, reaching 109 ± 2% of the initial value, before decaying back to the starting value over the remainder of the test. The J_{sc} is, again, the primary area of loss, decreasing by 70 ± 9% during the study. Interestingly, one device showed much greater stability of the J_{sc} than the others, decreasing by only 57% over the study. This was, however, balanced out by decreased stability of the *FF*, which did not undergo the increase that was exhibited by the other devices, resulting in a PCE only slightly more stable than the others. It is unclear as to why this occurred, however this highlights that it may be possible to achieve a more stable J_{sc} in devices utilising the HI additive.

The separation between burn-in period and linear decay period is also much more distinct than for the devices in Chapter 5, with the burn-in lasting approximately 200 hours before the decay of the PCE becomes linear. From this linear decay, the T_{80} lifetime was calculated to be approximately 360 ± 40 hours for the data from both the Atlas CPS+ lifetime tester and calibrated Newport solar simulator, as given in Table 6.4. Whilst this is longer than the T_{80} of the devices in Chapter 5 (280 ± 20 hours), the losses during the burn-in period are much greater for the devices fabricated with the HI additive, resulting in a lower PCE at the start of the linear decay region (4.9 ± 0.8% and 6.0 ± 0.6% for devices with and without the HI additive respectively). It is possible the difference in structure of the perovskite observed in Figure 6.10 alters the rate at which reactions with water and oxygen occur, resulting in the greater losses during the burn-in period. Another possibility may be that the water in the HI solution that was added to the precursor solution does not leave the film after deposition, instead being trapped in voids between crystals or even becoming bound in the PEDOT:PSS. This may result in a greater quantity of water available to degrade the perovskite at the start of the lifetime test and hence greater degradation during the burn-in.

Burn-in time (hours)	**PCE after Burn-in** (%)	**PCE loss over Burn-in** (%)	**PCE loss over 670 hours** (%)	**T_{80} Atlas** (hours)	**T_{80} Newport** (hours)
200	4.9 ± 0.8	59.9 ± 0.5	75 ± 8	360 ± 20	360 ± 40

Table 6.4: PCE loss over burn-in period and whole test, and T_{80} lifetimes calculated using data from both the Atlas Suntest CPS+ and the calibrated Newport solar simulator.

The *J-V* curves corresponding to the points in Figure 6.11 are presented in Figure 6.8, with the device metrics at the end of the test given in Table 6.3. Whilst the absolute values for these metrics are higher than those for devices without HI, proportionally the losses are the same. The only exception is the losses in *FF*, which are 29% for the devices in Chapter 5, and 22% for the devices with the HI additive. Hysteresis also saw a much larger increase for the devices fabricated using HI, with large differences in J_{sc} (-6.8 ± 0.9 mA/cm^2 and -7.6 ± 1.0 mA/cm^2), and smaller differences in the *FF* (54 ± 1% and 57 ± 1%) and V_{oc} (0.69 ± 0.01 V and 0.72 ± 0.03 V) for forwards and backwards voltage sweeps respectively. The losses in V_{oc} and increased R_s (from 5.3 ± 0.5 Ω cm^2 to 22.2 ± 1.0 Ω cm^2) indicate that this is likely due to increases in trapping states within the perovskite [13,14,18]. It should be noted that it is unclear as to why the V_{oc} of the devices in the second week were the lowest measured, it is possible that light soaking was not performed for long enough before measurements were taken as light soaking often improves the V_{oc} of devices [20].

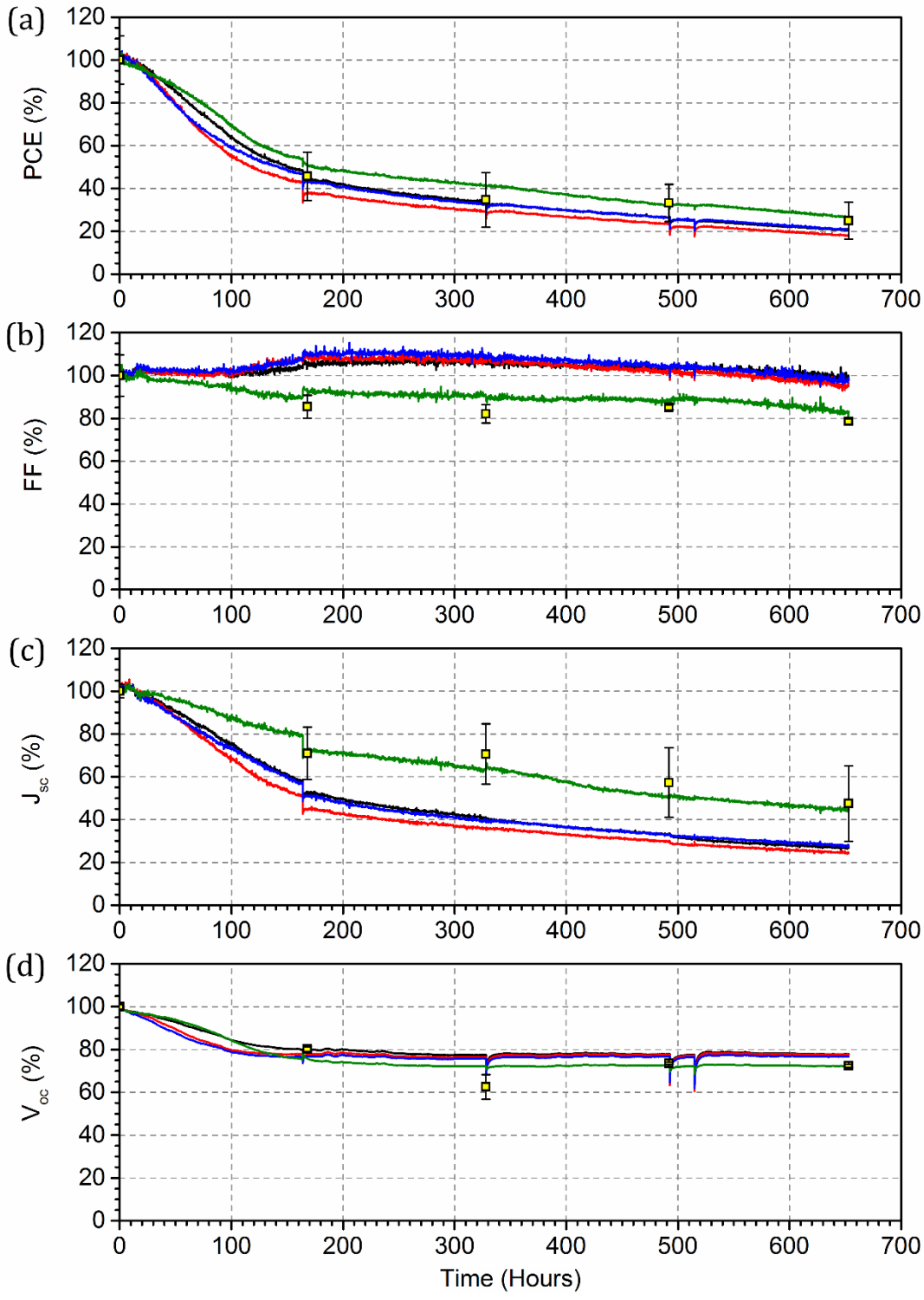

Figure 6.11: (a) PCE, (b) *FF*, (c) J_{sc}, and (d) V_{oc} of spin coated PSCs with a HI additive over 670 hours of continuous illumination. Solid points are data taken using a calibrated solar simulator. All *J-V* scans were performed from -1 to 1 V.

The evolution of the EQE over the lifetime test is presented in Figure 6.9(a), with normalised data given in Figure 6.9(b). It can be seen that the EQE is more stable when the HI additive is used, with peak EQE dropping from 86% to 38% over 670 hours of continuous illumination. The decrease in EQE at longer wavelengths, indicating decomposition of the perovskite into PbI_2, is also less severe, with significant changes only occurring towards the end of the study. Therefore, it appears that $CH_3NH_3PbI_{3-x}Cl_x$ perovskite has greater chemical stability when fabricated with a HI additive for both spin and spray coating.

6.5: Conclusions

It has been shown that the addition of a small quantity of hydroiodic acid to the precursor solution of spray coated $CH_3NH_3PbI_{3-x}Cl_x$ significantly improves perovskite solar cell performance, with PCE increasing from 8.4% to 10.4%, a value comparable to devices with a spin coated perovskite layer. This improvement originated from an increase in the uniformity of the external quantum efficiency, removing a large dip in the spectral response of the PSC between 600 and 700 nm, and hence increasing the J_{sc} of the devices. It is speculated that the additive improves the solubility of the precursor, allowing greater control over material ratios and better conversion during annealing, leading to the altered structure seen observed in optical microscopy. This results in better optical absorption and electronic properties of the perovskite, potentially improving them beyond those of the spin cast films. Despite these improvements, spray coated devices suffered from film uniformity issues, most likely caused by turbulence of the air during deposition affecting the generated spray. When subjected to 670 hours of continuous illumination, devices utilising the HI additive proved more stable, with PCE decreasing by ~70% compared to ~80% losses exhibited by devices that did not use the additive. Losses primarily occurred in J_{sc} for both types of device, with the J_{sc} of devices fabricated with HI displaying slightly better stability. This, along with the improved stability observed for the V_{oc} and R_s suggest a slower rate of decomposition reactions with oxygen and water than observed in devices without the additive.

The HI additive was also used to fabricate spin coated devices, which resulted in PCE increased to 13.2% due to improvements of the J_{sc}. This is attributed to the same mechanisms speculated for the spray coated devices due to similar changes in the EQE. Lifetime testing for 670 hours revealed changes in the stability of devices that contained HI, improving the T_{80} lifetime to 360 hours. The increase in lifetime arises from improved chemical stability revealed by EQE measurements during the test. Despite these improvements, losses during the burn-in period were much greater than for the devices in Chapter 5, resulting in lower PCE at the start of the linear decay period.

6.6: References

[1] G.E. Eperon, S.D. Stranks, C. Menelaou, M.B. Johnston, L.M. Herz, H.J. Snaith, Formamidinium lead trihalide: a broadly tunable perovskite for efficient planar heterojunction solar cells, Energy Environ. Sci. 7 (2014) 982.

[2] J. Yin, H. Qu, J. Cao, H. Tai, J. Li, N. Zheng, Light absorption enhancement by embedding submicron scattering TiO 2 nanoparticles in perovskite solar cells, RSC Adv. 6 (2016) 24596–24602.

[3] Q. Lin, A. Armin, R. Chandra, R. Nagiri, P.L. Burn, P. Meredith, Electro-optics of perovskite solar cells, Nat. Photonics. 9 (2014) 106–112.

[4] M.-C. Wu, S.-H. Chan, M.-H. Jao, W.-F. Su, Enhanced short-circuit current density of perovskite solar cells using Zn-doped TiO2 as electron transport layer, Sol. Energy Mater. Sol. Cells. 157 (2016) 447–453.

[5] C.M. Hansen, Hansen Solubility Parameters: A User's Handbook, Second, CRC Press, 2007.

[6] F. Machui, S. Langner, X. Zhu, S. Abbott, C.J. Brabec, Determination of the P3HT:PCBM solubility parameters via a binary solvent gradient method: Impact of solubility on the photovoltaic performance, Sol. Energy Mater. Sol. Cells2. 100 (2012) 138–146.

[7] S. Lilliu, T.G. Dane, J. Griffin, M. Alsari, A.T. Barrows, M.S. Dahlem, R.H. Friend, D.G. Lidzey, J.E. Macdonald, Mapping Morphological and Structural

Properties of Lead Halide Perovskites by Scanning Nanofocus XRD, (2016).

[8] X. Song, W. Wang, P. Sun, W. Ma, Z.K. Chen, Additive to regulate the perovskite crystal film growth in planar heterojunction solar cells, Appl. Phys. Lett. 106 (2015).

[9] P.W. Liang, C.Y. Liao, C.C. Chueh, F. Zuo, S.T. Williams, X.K. Xin, J. Lin, A.K.Y. Jen, Additive enhanced crystallization of solution-processed perovskite for highly efficient planar-heterojunction solar cells, Adv. Mater. 26 (2014) 3748–3754.

[10] D.K. Mohamad, J. Griffin, C. Bracher, A.T. Barrows, D.G. Lidzey, Spray-Cast Multilayer Organometal Perovskite Solar Cells Fabricated in Air, Adv. Energy Mater. (2016) 1600994.

[11] L.K. Ono, S.R. Raga, S. Wang, Y. Kato, Y. Qi, Temperature-dependent hysteresis effects in perovskite-based solar cells, J. Mater. Chem. A. 3 (2014) 9074–9080.

[12] P. Delugas, A. Filippetti, A. Mattoni, Methylammonium fragmentation in amines as source of localized trap levels and the healing role of Cl in hybrid lead-iodide perovskites, Phys. Rev. B - Condens. Matter Mater. Phys. 92 (2015) 1–11.

[13] H.J. Snaith, A. Abate, J.M. Ball, G.E. Eperon, T. Leijtens, N.K. Noel, S.D. Stranks, J.T.-W. Wang, K. Wojciechowski, W. Zhang, Anomalous Hysteresis in Perovskite Solar Cells, J. Phys. Chem. Lett. 5 (2014) 1511–1515.

[14] Y. Shao, Z. Xiao, C. Bi, Y. Yuan, J. Huang, Origin and elimination of photocurrent hysteresis by fullerene passivation in CH3NH3PbI3 planar heterojunction solar cells, Nat. Commun. 5 (2014) 1–7.

[15] Y. Zhao, C. Liang, H. min Zhang, D. Li, D. Tian, G. Li, X. Jing, W. Zhang, W. Xiao, Q. Liu, F. Zhang, Z. He, Anomalously large interface charge in polarity-switchable photovoltaic devices: an indication of mobile ions in organic-inorganic halide perovskites, Energy Environ. Sci. 0 (2015) Advance.

[16] W. Tress, N. Marinova, T. Moehl, S.M. Zakeeruddin, N. Mohammad K., M.

Grätzel, M.K. Nazeeruddin, M. Grätzel, Understanding the rate-dependent J–V hysteresis, slow time component, and aging in CH3NH3PbI3 perovskite solar cells: the role of a compensated electric field, Energy Environ. Sci. 8 (2015) 995–1004.

[17] H. Zhang, C. Liang, Y. Zhao, M. Sun, H. Liu, J. Liang, D. Li, F. Zhang, Z. He, Dynamic interface charge governing the current-voltage hysteresis in perovskite solar cells, Phys. Chem. Chem. Phys. 17 (2015) 9613.

[18] P. Calado, A.M. Telford, D. Bryant, X. Li, J. Nelson, B.C. O'Regan, P.R.F. Barnes, Evidence for ion migration in hybrid perovskite solar cells with minimal hysteresis, Nat. Commun. 7 (2016) 13831.

[19] S. Ito, S. Tanaka, K. Manabe, H. Nishino, Effects of Surface Blocking Layer of Sb2S3 on Nanocrystalline TiO 2 for CH3NH3PbI3 Perovskite Solar Cells, J. Phys. Chem. C. 118 (2014) 16995–17000.

[20] C. Zhao, B. Chen, X. Qiao, L. Luan, K. Lu, B. Hu, Revealing Underlying Processes Involved in Light Soaking Effects and Hysteresis Phenomena in Perovskite Solar Cells, Adv. Energy Mater. (2015) 1500279.

Chapter 7

The Effects of Additional Annealing and Deposition Temperatures on the Stability of Perovskite Solar Cells

7.0: Introduction

In this chapter two different lifetime experiments on perovskite solar cells (PSCs) are presented. In section 7.1, the effects of an additional anneal of the perovskite layer at an elevated temperature after conversion of the precursors is completed are examined. This is performed as an attempt to remove oxygen and moisture that is potentially absorbed into the device during fabrication. PSCs are fabricated using $CH_3NH_3PbI_{3-x}Cl_x$ films that have been subjected to further annealing in ambient air or in a nitrogen filled glove box. These are then exposed to 335 hours (2 weeks) of continuous illumination, along with control devices fabricated without the additional annealing step. The PSCs with additional annealing are found to have decreased initial performance, with those annealed under nitrogen performing worst. Optical microscopy, atomic force microscopy (AFM), and laser beam induced current (LBIC) mapping are used to investigate these losses. Upon ageing, the annealed devices are found to have improved stability over devices without the additional anneal, with those annealed in air ending the test with the highest power conversion efficiency (PCE).

In section 7.2, the effects of substrate and solution temperature when depositing the precursor solution of $CH_3NH_3PbI_{3-x}Cl_x$ perovskite on the stability of PSCs are investigated. Here, three different temperatures have been used: room temperature, 90°C substrate and 70°C solution, and 120°C substrate and solution. PSCs with the perovskite deposited at a higher temperature are found to have

improved initial performance, but are found to degrade faster over 335 hours (2 weeks) of continuous illumination. Despite having the lowest initial performance, devices with perovskites deposited at the lowest temperatures end the test with the highest performance.

Both of these results highlight the need to optimise PSCs for stability rather than chasing incrementally higher efficiencies, as the most efficient devices are not necessarily the most stable, and much longer lifetimes are required for PSCs to become commercially viable.

It is important to note that all PSCs in this chapter used Ca instead of LiF as an electron transport layer, otherwise the structure is the same as used in Chapter 5.

7.1: The Effects of Additional Annealing on Stability

As discussed in Chapter 5, the main causes of degradation for the encapsulated 'inverted' architecture PSCs are reactions with oxygen and water, resulting in the decomposition of the perovskite into methylamine, hydroiodic acid, iodine, water, and lead iodide [1–4]. The water and oxygen required for these reactions likely either enter the device by slow ingress though the encapsulation or are already present within the device, possibly absorbed by the hygroscopic PEDOT:PSS. In an attempt to limit this decomposition, two sets of devices were subjected to an additional anneal on a hotplate at 110°C for 15 minutes performed after the annealing step, either in ambient air or a nitrogen filled glove box, to remove moisture that may have been trapped in the device. This temperature was chosen for the initial experiment as it was high enough to enable the removal of moisture from the film, but hoped to not cause too much damage to the perovskite as might occur at higher temperatures.

In Figure 7.1 the average *J-V* curves are shown for control PSCs without the additional annealing step, PSCs annealed in ambient air, and PSCs annealed in a nitrogen filled glove box. The corresponding device metrics are presented in Table 7.1. It can be seen that the additional annealing step causes a decrease in the PCE from 10.4 ± 0.3% to 8.7 ± 0.6% for PSCs annealed in air, and 6.9 ± 0.3% for PSCs annealed under nitrogen. These losses result from decreases in all device metrics,

with the most significant losses occurring in the fill factor (*FF*) and open circuit voltage (V_{oc}), and relatively minor losses in the short circuit current density (J_{sc}). In particular, the V_{oc} of the PSCs which were annealed under nitrogen decreases significantly from 0.87 ± 0.004 V to 0.75 ± 0.04 V. The loss of V_{oc} indicates an increase of the charge carrier recombination rate [5], however there is only a small increase in the series resistance (R_s) (from 5.4 ± 0.3 Ω cm^2 to 6.8 ± 0.7 Ω cm^2), possibly suggesting that recombination is not the only mechanism leading to this decrease. The V_{oc} is also dependent on the energy levels of the perovskite, indicating that possible chemical changes in the perovskite are occurring [6]. Indeed, it has been shown that $CH_3NH_3PbI_3$ is thermally unstable, with its constituents decomposing when exposed to temperatures above 85°C, albeit over a period of 24 hours [7]. It is possible that decomposition of the perovskite occurred here, as 110°C was used for the additional annealing step, potentially resulting in an increased reaction rate, allowing noticeable changes to occur during the 15 minutes of annealing.

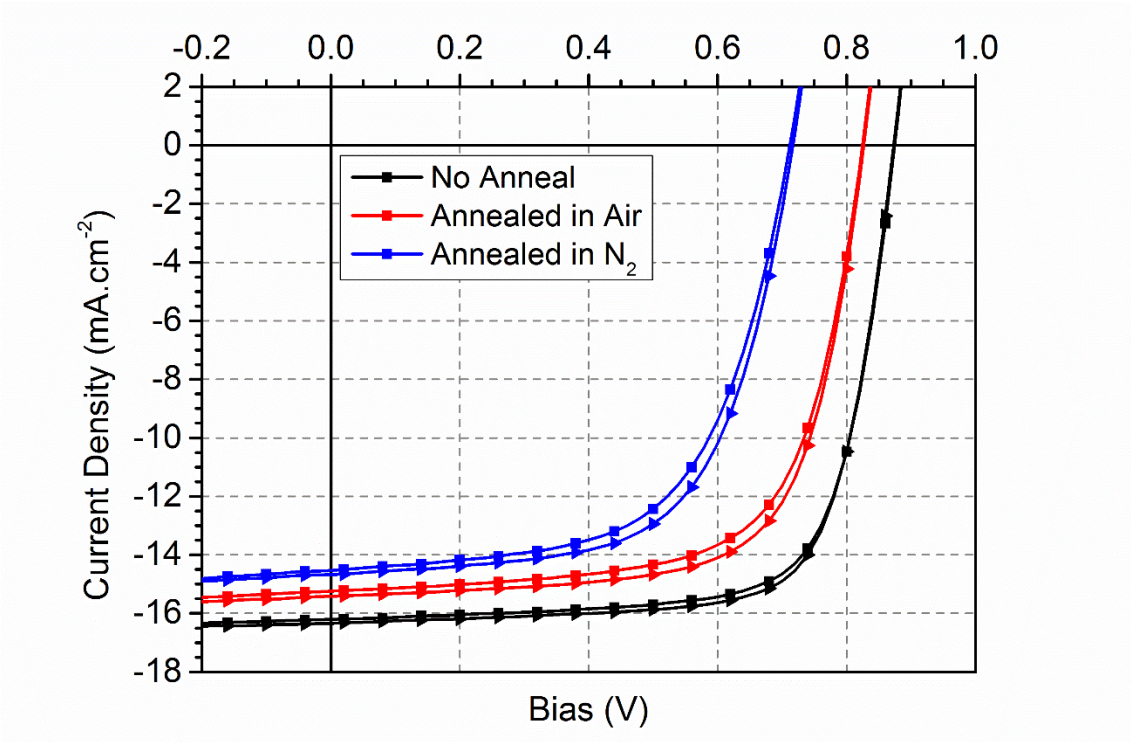

Figure 7.1: Initial *J-V* curves for PSCs with and without the additional annealing step. Squares represent forwards scans, triangles represent reverse scans.

Extra Anneal	Scan Direction	PCE (%)	FF (%)	J_{sc} (mA/cm^2)	V_{oc} (V)	R_{sh} (Ω cm^2)	R_s (Ω cm^2)
None	Forwards	10.2 ± 0.3	73 ± 1	-16.1 ± 0.3	0.87 ± 0.004	1570 ± 200	5.3 ± 0.6
	Backwards	10.4 ± 0.3	74 ± 1	-16.1 ± 0.4	0.87 ± 0.004	1540 ± 320	5.4 ± 0.3
Air	Forwards	8.4 ± 0.5	67 ± 2	-15.2 ± 0.3	0.82 ± 0.01	1030 ± 220	6.0 ± 0.5
	Backwards	8.7 ± 0.6	69 ± 2	-15.3 ± 0.4	0.82 ± 0.01	1110 ±180	5.8 ± 0.5
N_2	Forwards	6.5 ± 0.3	61 ± 1	-14.3 ± 0.4	0.75 ± 0.05	790 ± 180	7.4 ± 0.9
	Backwards	6.9 ± 0.3	63 ± 1	-14.5 ± 0.3	0.75 ± 0.04	910 ± 180	6.8 ± 0.7

Table 7.1: Mean device metrics and standard deviations for open circuit voltage, short circuit current density, fill factor, power conversion efficiency, and shunt and series resistance, extracted from *J-V* curves, for control PSCs without any additional anneal, and PSCs annealed in air or under nitrogen. 12 devices were used to calculate the mean and standard deviation for each device type.

External quantum efficiency (EQE) curves for devices with and without the additional annealing step are presented in Figure 7.2. Here, it can be seen that the devices which have undergone the additional anneal have reduced EQE at all wavelengths, but particularly for wavelengths below 600 nm. This is consistent with the reduced J_{sc} observed in the *J-V* curves of the devices with the additional annealing step. It is speculated that the reductions arise from damage to the perovskite crystal caused by the high temperature of the additional anneal.

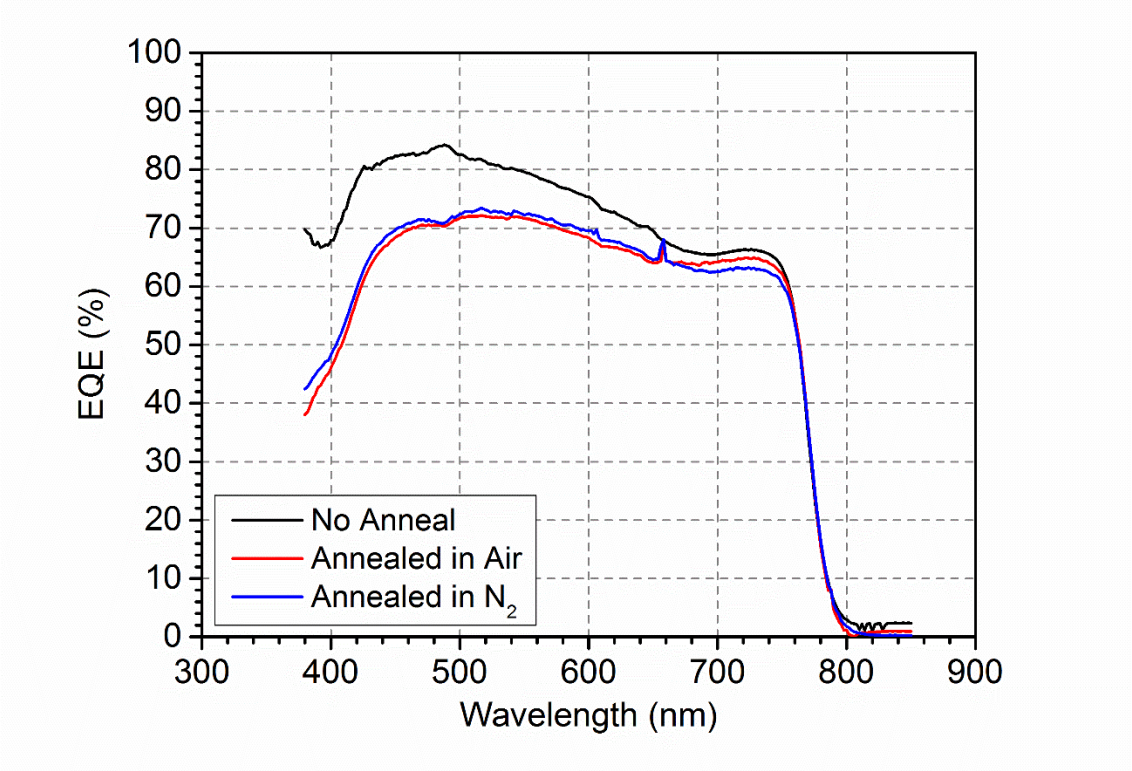

Figure 7.2: EQE curves for PSCs with and without the additional annealing step.

To determine if the additional annealing step caused morphological changes to the perovskite, optical and atomic force microscopy (AFM) were employed. Figure 7.3(a) shows an optical micrograph of the control perovskite, and in Figure 7.3(b) an optical micrograph of a perovskite film that was annealed in air. The two images are very similar, with no obvious large scale morphological differences between the perovskites with and without the additional anneal. In Figure 7.3(c) and (d), the films in (a) and (b) respectively are examined in higher resolution using AFM. Again, no major differences in structure can be seen between the two films. However, there is a difference in the roughness of the films, with the films annealed in air exhibiting a slightly rougher surface (17.8 ± 2.6 nm) than the control films (15.8 ± 2.5 nm).

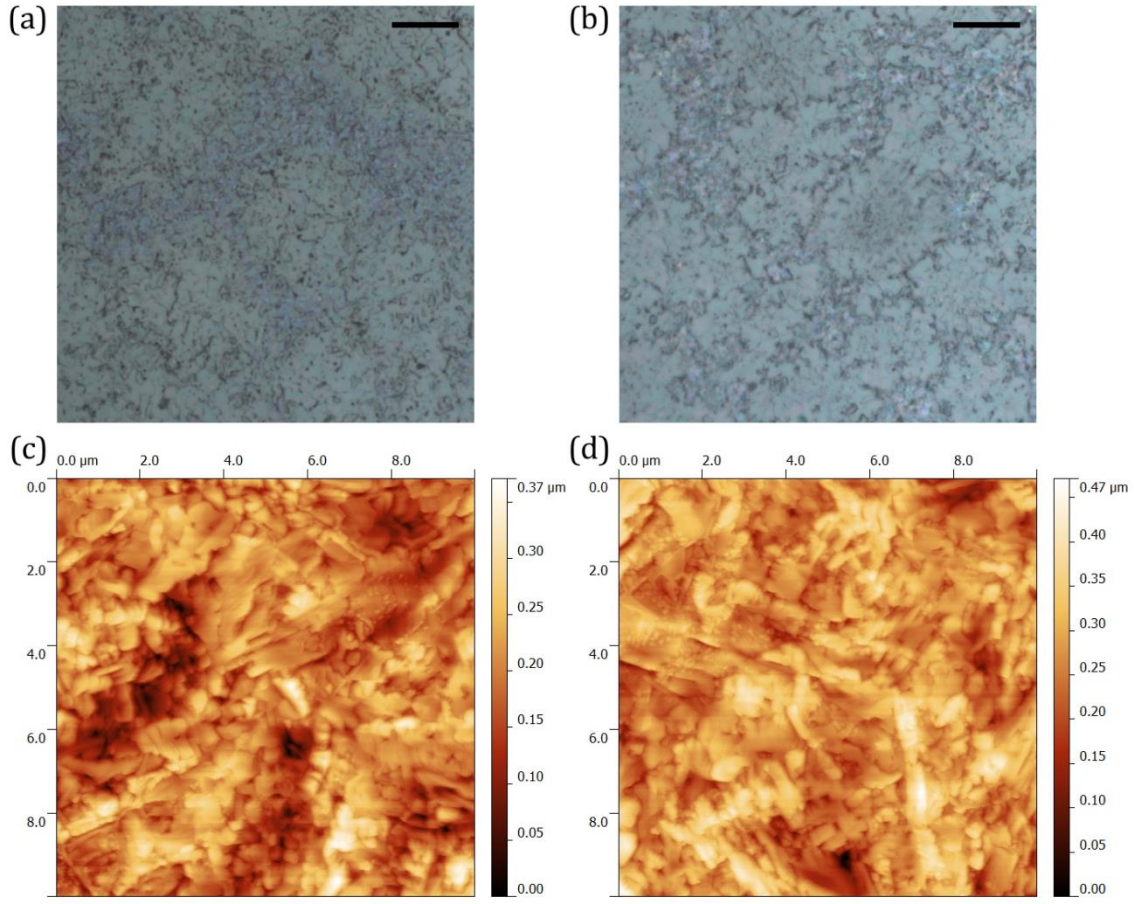

Figure 7.3: (a) and (b) are optical micrographs of perovskite films without additional annealing and with annealing in air respectively. The scale bars represent 10 µm. (c) and (d) are AFM images of the films in (a) and (b) respectively.

However, when the devices are examined using laser beam induced current (LBIC) mapping, as shown in Figure 7.4(a), (b), and (c), differences in the spatial uniformity of photocurrent generation become apparent. Here it can be seen that there appears to be larger scale structure in the photocurrent of the perovskites which have been subjected to the additional anneal. In Figure 7.4(g), a histogram of the data in Figure 7.4(a), (b), and (c) is presented, highlighting the decrease of photocurrent uniformity in the perovskites with the additional anneal. The standard deviation increases from 7.1 ± 0.2% in control PSCs, to 10.8 ± 0.3% and 13.1 ± 0.4% in PSCs that were annealed in air and under nitrogen respectively. This change in homogeneity indicates some electronic or structural change within the perovskite. As mentioned previously, it is possible that this is caused by

damage to the perovskite crystal due to the high temperature of the additional annealing step. This would result in poorer absorption and charge carrier transport properties, limiting the photovoltaic performance in the areas affected.

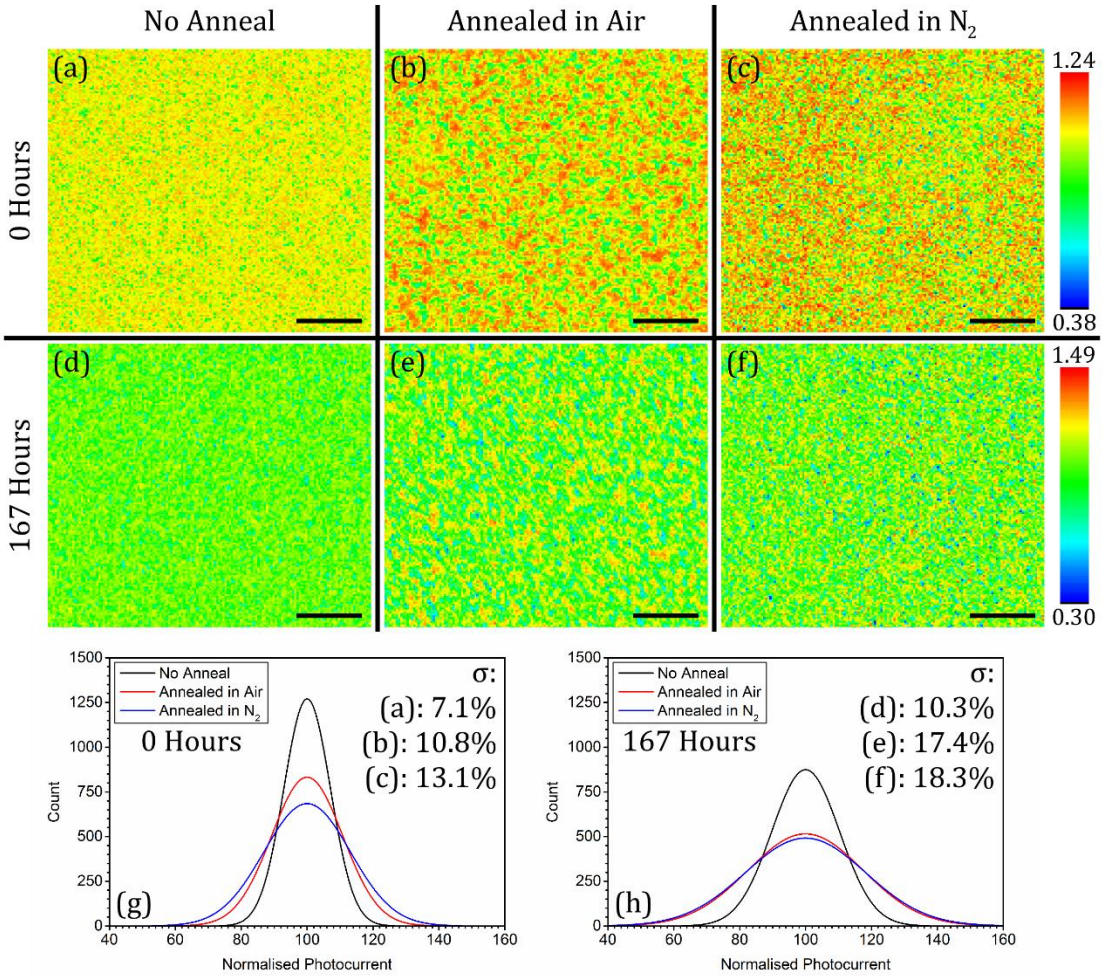

Figure 7.4: LBIC maps of PSCs (a) without extra annealing, (b) annealed in air, and (c) annealed under nitrogen. (d), (e), and (f) are LBIC maps of the devices in (a), (b), and (c) respectively after 167 hours of continuous illumination. The scale bars represent 150 μm. (g) and (h) are histograms of the data in (a) – (c) and (d) – (f) respectively.

Whilst it is currently unclear why the performance of devices annealed under nitrogen is reduced more significantly than those annealed in air, it could be a result of the pre-cursor solution and materials used to form the perovskite. The pre-cursor solution used was methylammonium iodide (MAI) and lead chloride ($PbCl_2$) in dimethylformamide (DMF), which has been optimised to create efficient

perovskite films when deposited and annealed in ambient conditions, requiring ~30% RH for optimal films. It is therefore possible that annealing at an elevated temperature in a moisture free environment could cause deleterious effects on the chemical structure of the perovskite, impacting both its physical structure and electronic properties.

In Figure 7.5 the PCE, *FF*, J_{sc}, and V_{oc} of control PSCs, and with annealing in air or nitrogen, is plotted as a function of irradiance time for 335 hours (2 weeks) of continuous illumination. Over the 335 hour test, the PCE of the control PSCs, fabricated without the additional annealing step, decreased by 63 ± 1% (from 10.4 ± 0.3% to 3.9 ± 0.5%). Devices that were annealed under nitrogen were more stable, with PCE decreasing by 53 ± 2% (from 6.9 ± 0.3% to 3.6 ± 0.1%). However, devices that were annealed in air proved the most stable, with PCE degrading by only 44 ± 3% (the decrease is ~35% for data taken using the calibrated Newport solar simulator, with PCE decreasing from 8.7 ± 0.3% to 5.9 ± 0.2%), resulting in a higher PCE after the lifetime test than that of the control devices. The improved stability for both of the device sets with additional annealing originates from more stable J_{sc} and V_{oc}, whilst the *FF* degrades by a similar amount for all of the devices (~20%).

The T_{80} lifetimes of the devices are shown in Table 7.2, along with the length of the burn-in period and the PCE losses during this time and over the whole test. The burn-in period, the region of rapid performance degradation before the decay becomes linear, was determined to be 200 hours, using the method described in Section 3.4.3. Devices fabricated without the additional annealing step gave the shortest T_{80} lifetimes with 370 ± 30 hours, whilst those that were annealed in air show the longest lifetimes with 490 ± 40 hours. This is significantly longer than the T_{80} lifetime exhibited by the PSCs in Chapter 5 (280 ± 20 hours), which could be attributed to the annealing step removing oxygen and water from the device, slowing down the rate at which the perovskite decomposition reactions could occur.

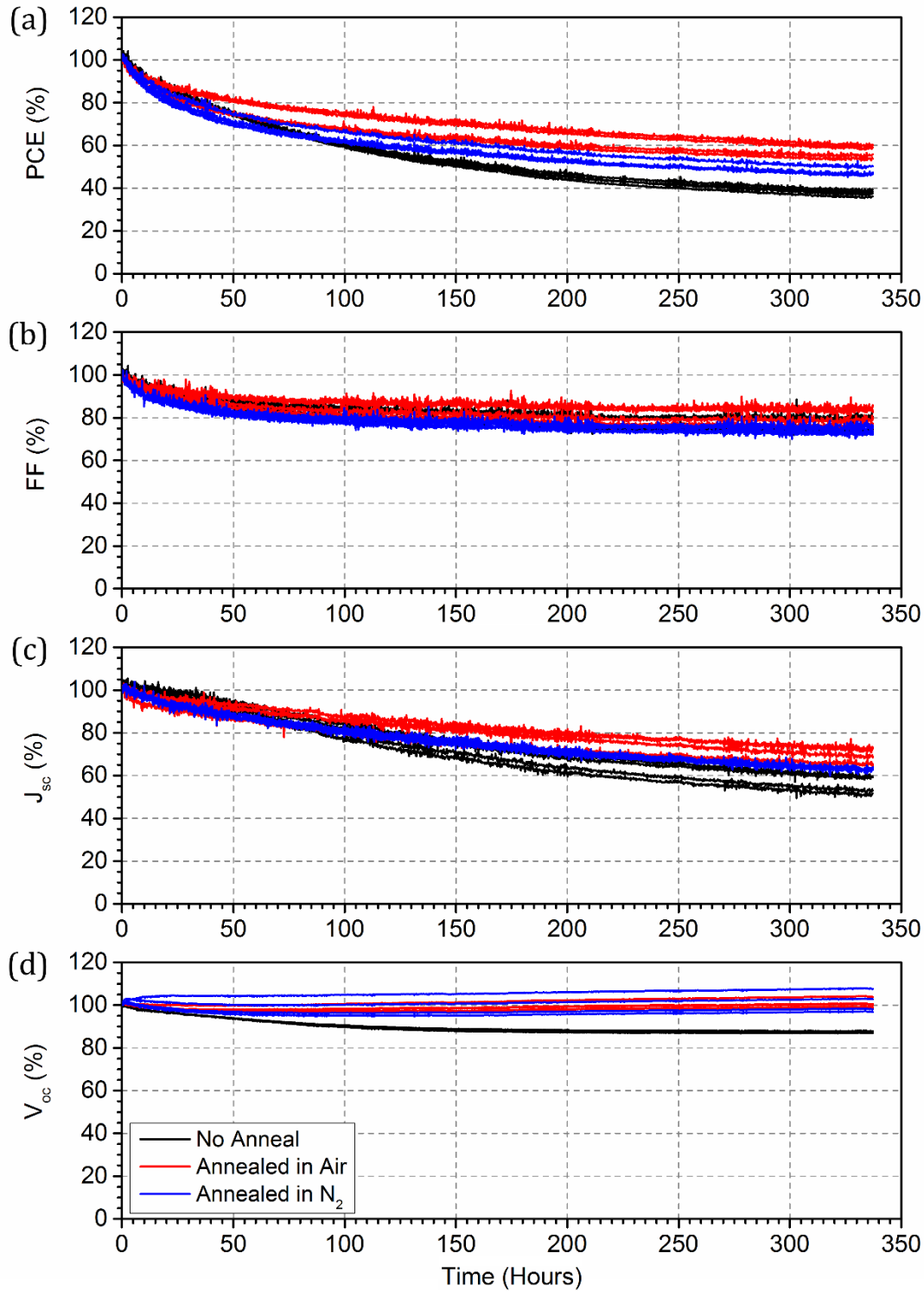

Figure 7.5: (a) PCE, (b) *FF*, (c) J_{sc}, and (d) V_{oc} of $CH_3NH_3PbI_{3-x}Cl_x$ PSCs without additional annealing and with additional annealing in air or under nitrogen over 335 hours of continuous illumination. All *J-V* scans were performed from -1 to 1 V.

Extra Anneal	Burn-in time (hours)	PCE loss over burn-in (%)	PCE loss over 335 hours (%)	T_{80} Lifetime (hours)
None	200	56 ± 1	63 ± 1	370 ± 30
Air	200	39 ± 4	44 ± 3	490 ± 40
N_2	200	48 ± 2	53 ± 2	430 ± 10

Table 7.2: PCE loss over burn-in period and whole test, and T_{80} lifetimes calculated using data from the Atlas Suntest CPS+.

The *J-V* curves performed at the end of the lifetime test using a calibrated Newport solar simulator are presented in Figure 7.6, with the corresponding device metrics given in Table 7.3. It can be seen that the V_{oc} of the PSCs that were annealed in air remained stable throughout the test (0.82 V), whilst the V_{oc} of the control devices degraded to a similar value (0.81 ± 0.01 V). Interestingly, the V_{oc} of the devices annealed under nitrogen increases from 0.75 ± 0.04 V to 0.78 ± 0.01 V. This suggests improved energy level alignment between the perovskite and the transport layers, facilitating the extraction of photogenerated charge carriers [8]. The J_{sc} of the devices which were not subjected to additional annealing also proved to be the least stable, decreasing to -10.6 ± 1.2 mA/cm^2, whilst the J_{sc} of devices annealed under nitrogen decreased to -11.3 ± 0.1 mA/cm^2, and those annealed in air decreased to -13.5 ± 0.3 mA/cm^2. The losses of these metrics for the devices in Chapter 5 were a result of the perovskite decomposing, producing methylamine and hydroiodic acid which acted as charge trapping sites within the perovskite. As the degradation of these metrics is reduced, along with improved R_{sh} and R_s after the lifetime test, it indicates an improved degree of chemical stability in devices subjected to additional annealing after conversion of the precursor materials, both in air and under nitrogen. Indeed, it has been reported that perovskites formed using MAI and $PbCl_2$ as the precursor can contain methylammonium chloride (MACl), which readily absorbs water from the air, enabling moisture to enter the device [9]. Here, the authors report that annealing at 60°C whilst under vacuum (instead of the usual anneal in air) reduces the quantity of MACl in the final perovskite. When subjecting unencapsulated devices that had undergone the vacuum anneal to continuous testing over 10 hours, no losses of PCE were

observed, whereas devices without the vacuum degraded completely within 2 hours. Therefore the improvement in the stability of devices with an additional annealing step seen here could in part be due to removal MACl, as well as any water which had been absorbed into the film.

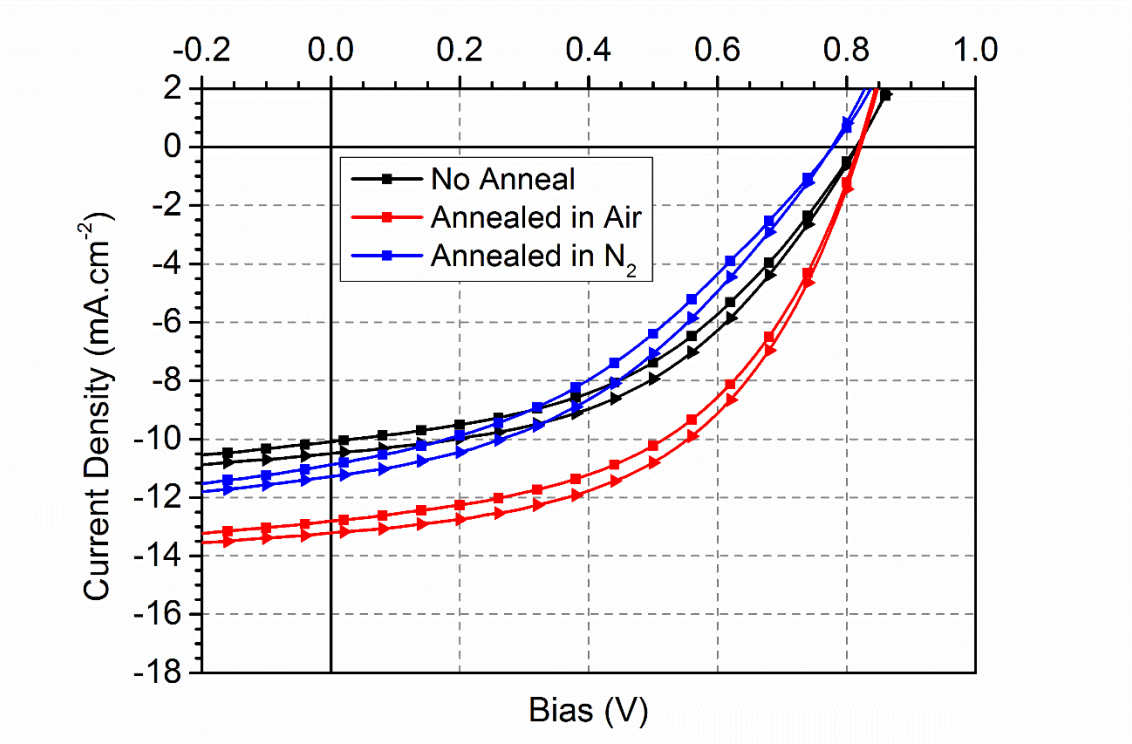

Figure 7.6: J-V curves for PSCs with and without the additional annealing step after 335 hours of continuous illumination. Squares represent forwards scans, triangles represent reverse scans.

Extra Anneal	Scan Direction	PCE (%)	FF (%)	J_{sc} (mA/cm²)	V_{oc} (V)	R_{sh} (Ω cm²)	R_S (Ω cm²)
None	Forwards	3.7 ± 0.4	45 ± 3	-10.2 ± 1.2	0.81 ± 0.01	410 ± 80	28.1 ± 3.8
	Backwards	3.9 ± 0.5	47 ± 4	-10.6 ± 1.2	0.81 ± 0.01	490 ± 100	25.7 ± 4.7
Air	Forwards	5.6 ± 0.2	51 ± 2	-13.1 ± 0.4	0.82 ± 0.003	480 ± 60	13.3 ± 1.7
	Backwards	5.9 ± 0.2	53 ± 2	-13.5 ± 0.3	0.83 ± 0.003	560 ± 60	13.4 ± 1.8
N_2	Forwards	3.3 ± 0.1	38 ± 1	-10.9 ± 0.1	0.78 ± 0.01	270 ± 10	32.8 ± 0.9
	Backwards	3.6 ± 0.1	41 ± 1	-11.3 ± 0.1	0.78 ± 0.01	330 ± 50	28.3 ± 1.2

Table 7.3: Mean device metrics and standard deviations for open circuit voltage, short circuit current density, fill factor, power conversion efficiency, and shunt and series resistance, extracted from *J-V* curves, for control PSCs without any additional anneal, and PSCs annealed in air or under nitrogen after 335 hours of continuous illumination. 8 devices were used to calculate the mean and standard deviation for each device type.

To determine the differences in the evolution of the spatially resolved photocurrent, LBIC mapping was performed after 1 week (167 hours) of continuous illumination. This data is shown in Figure 7.3(d), (e), and (f). Despite suffering the greatest rate of degradation of the three sets of devices, PSCs not subjected to additional annealing still exhibit the greatest degree of uniformity (σ = 10.3 ± 0.6%), whilst both of the devices with additional annealing display similar levels (σ = 17.4 ± 0.4% and 18.3 ± 0.8% for the devices annealed in air and under nitrogen respectively).

7.2: The Effects of Deposition Temperature on Stability

Another perovskite stability investigation was performed looking at the effect of the substrate and solution temperature during the deposition of the $CH_3NH_3PbI_{3-x}Cl_x$ perovskite precursor (MAI:$PbCl_2$) on the stability of PSCs. Three different sets of temperatures were used: room temperature substrate and solution (referred to as 'cold'), 90°C substrate and 70°C solution (the standard temperatures used, referred to as 'medium'), and 120°C substrate and solution (referred to as 'hot'),

and are summarised in Table 7.4. It should be noted that these values are the temperature of the hotplates which the substrates and solutions were kept on immediately prior to film deposition, therefore the actual temperatures during deposition will have been slightly lower. This study was motivated by the observation that perovskite films deposited at different temperatures showed different stability when stored in air for one day, as shown in Figure 7.7. Here, it can be seen that films deposited cold almost entirely degraded into PbI_2, with the amount of decomposition decreasing as deposition temperatures increased. This difference in stability likely arises from improved film coverage and larger grains when the precursors are deposited at higher temperatures, slowing the ingress of water and oxygen into the bulk of the perovskite film and hence reducing the rate at which the degradation reactions occur [10].

Label	**Substrate Temperature** (°C)	**Solution Temperature** (°C)
Cold	Room Temp	Room Temp
Medium	90	70
Hot	120	120

Table 7.4: Summary of hotplate temperatures used to heat the substrates and solutions for each batch of devices and the corresponding labels.

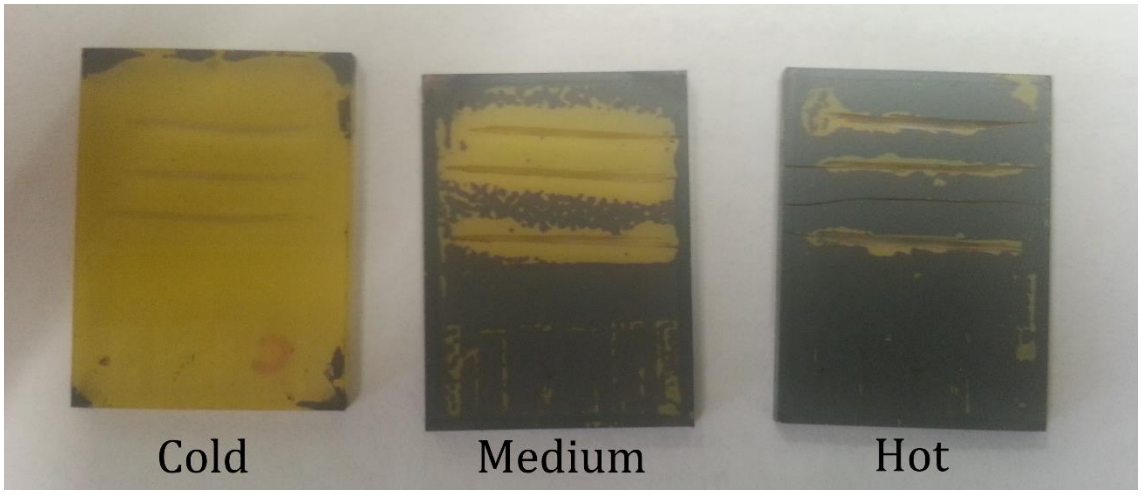

Figure 7.7: Photograph of perovskite films deposited from different temperature substrates and solutions after being stored in air for the same amount of time.

Encapsulated PSCs were fabricated using the perovskite films deposited at the different temperatures and the initial *J-V* curves for these devices are presented in Figure 7.8, with the extracted metrics given in Table 7.5. It can be seen that the PCE of devices increased from 9.9 ± 0.4% to 11.6 ± 0.3% as substrate and solution temperature increased, resulting from improved J_{sc} and V_{oc}. The improved J_{sc}, increased from -15.2 ± 0.5 mA/cm^2 to -16.6 ± 0.4 ma/cm^2, is again speculated to be due to improved surface coverage of the perovskite leading to improved absorption efficiency and the increased grain size providing better charge transport [11]. Improvements in the V_{oc}, from 0.90 ± 0.01 V to 0.95 ± 0.01 V, could originate from decreased charge carrier recombination rates within the perovskite deposited at 'hot' temperature [5], or alternatively differences in the energy levels of the perovskites deposited at different temperatures [6].

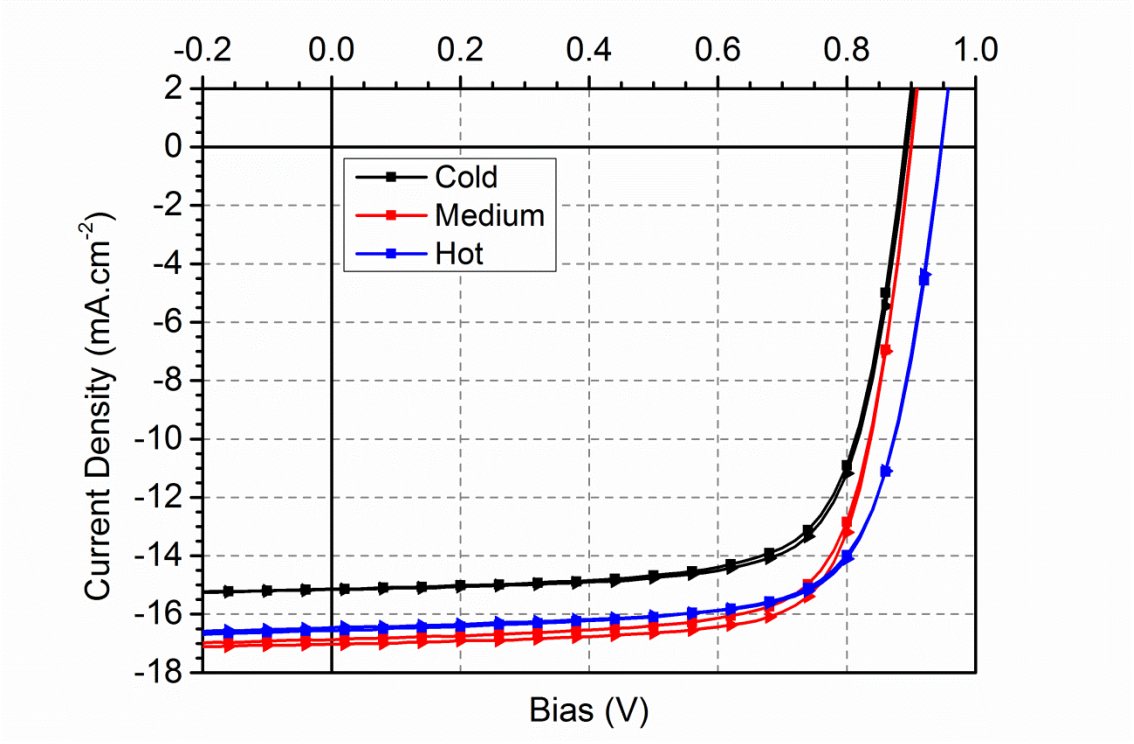

Figure 7.8: Initial *J-V* curves for PSCs with different temperatures for perovskite precursor deposition. Labels in the legend correspond to those in Table 7.4. Squares represent forwards scans, triangles represent reverse scans.

Deposition Temp	Scan Direction	PCE (%)	FF (%)	J_{sc} (mA/cm²)	V_{oc} (V)	R_{sh} (Ω cm²)	R_S (Ω cm²)
Cold	Forwards	9.7 ± 0.4	72 ± 2	-15.1 ± 0.5	0.89 ± 0.01	2200 ± 680	5.3 ± 0.6
	Backwards	9.9 ± 0.4	73 ± 2	-15.2 ± 0.5	0.90 ± 0.01	3100 ± 930	5.7 ± 0.7
Medium	Forwards	11.1 ± 0.2	73 ± 1	-16.9 ± 0.4	0.90 ± 0.01	2130 ± 1390	4.9 ± 0.1
	Backwards	11.4 ± 0.2	75 ± 1	-17.0 ± 0.3	0.90 ± 0.02	2530 ± 1230	5.0 ± 0.3
Hot	Forwards	11.3 ± 0.3	72 ± 1	-16.6 ± 0.4	0.95 ± 0.01	1770 ± 820	5.4 ± 0.3
	Backwards	11.6 ± 0.3	73 ± 1	-16.6 ± 0.4	0.95 ± 0.01	1470 ± 250	6.1 ± 0.2

Table 7.5: Mean device metrics and standard deviations for open circuit voltage, short circuit current density, fill factor, power conversion efficiency, and shunt and series resistance, extracted from *J-V* curves, for PSCs fabricated using different substrate and solution temperatures. 8 devices were used to calculate the mean and standard deviation for each device type.

The PCE, *FF*, J_{sc}, and V_{oc} of PSCs with perovskite layers deposited at different temperatures over 335 hours of continuous illumination and operation are presented in Figure 7.9. In contrast to the degradation seen in Figure 7.7, where higher substrate and solution temperatures resulted in more stable films, PSCs utilising perovskites prepared 'hot' showed the lowest stability, with PCE decreasing by 70 – 80% over the 335 hour period. PSCs fabricated using 'medium' temperatures were more stable with PCE degrading by ~60%. However, the devices with a 'cold' perovskite layer proved the most stable, with PCE decreasing by only 40 – 50% during the test. For all deposition temperatures, the primary losses occur to the J_{sc}, which decreases by 60 – 80% for 'hot' devices, 40 – 50% for 'medium' devices, and ~30% for 'cold' devices. Interestingly, the *FF* of the 'hot' devices was the most stable, increasing over the first 100 hours to 105 – 110% of the initial value, whereas the *FF* of 'medium' and 'cold' devices reduced by 10 – 20% over the course of the illumination. There was no significant difference in the stability of V_{oc} between the different deposition temperatures.

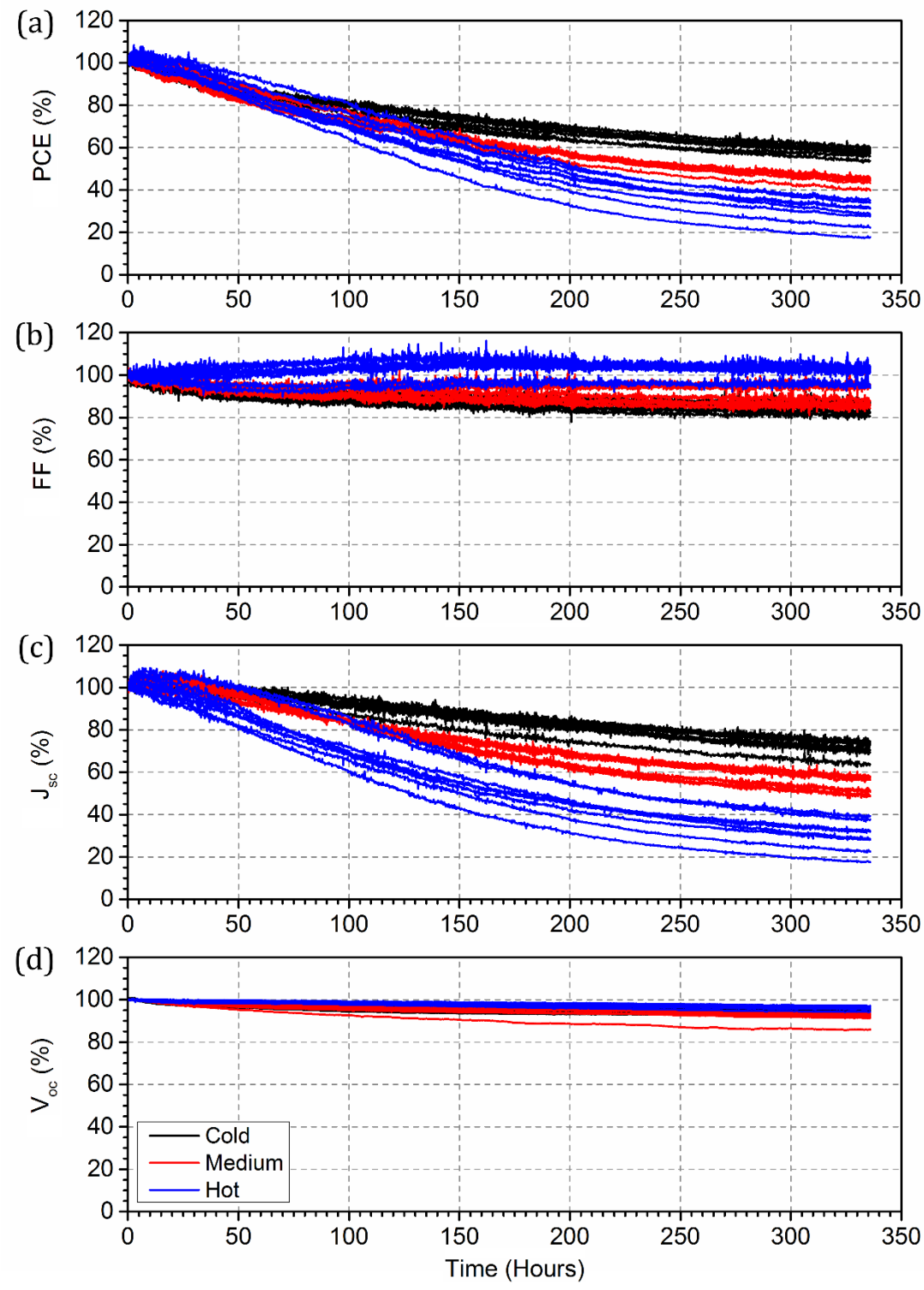

Figure 7.9: (a) PCE, (b) *FF*, (c) J_{sc}, and (d) V_{oc} of $CH_3NH_3PbI_{3-x}Cl_x$ PSCs with different substrate and solution temperatures for perovskite precursor deposition over 335 hours of continuous illumination. All *J-V* scans were performed from -1 to 1 V. Labels in the legend correspond to the temperatures given in Table 7.4.

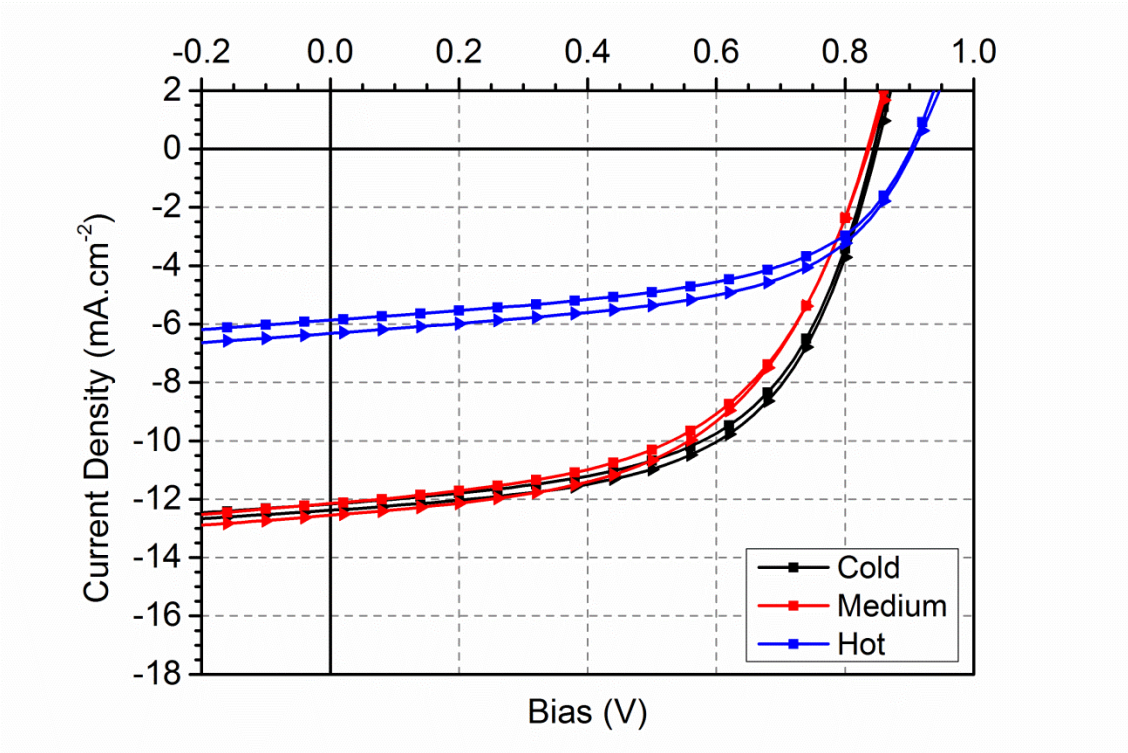

Figure 7.10: J-V curves for PSCs with different substrate and solution temperatures for perovskite precursor deposition after 335 hours of continuous illumination. Squares represent forwards scans, triangles represent reverse scans.

In Figure 7.10 the *J-V* curves, measured using a calibrated Newport solar simulator, of devices with different perovskite deposition temperatures after the 335 hour lifetime test are presented, with the metrics shown in Table 7.6. Despite having the lowest initial PCE, the 'cold' devices were measured to have the highest final PCE at 6.1 ± 0.3%. 'Medium' devices had a slightly lower PCE of 5.6 ± 0.5%, and 'hot' devices had the lowest PCE at 3.4 ± 0.5%. These values are in reasonable agreement with the data taken using the lifetime testing system. As seen in the lifetime data, the J_{sc} was the most significantly affected metric, decreasing to -7.0 ± 1.2 mA/cm^2 for 'hot' devices, whilst in 'medium' and 'cold' devices the J_{sc} decreased to -12.6 ± 1.4 mA/cm^2 and -12.4 ± 0.4 mA/cm^2 respectively. This indicates a greater reduction in absorption and charge transport properties for 'hot' devices compared to 'medium' and 'cold' devices. Indeed, the resultant R_s after 335 hours of illumination was increased to 22.6 ± 0.4 Ω cm^2, suggesting increased barriers to charge extraction from the perovskite. It is likely that this originates from a greater

rate of decomposition into PbI_2. All of the devices saw an increase in hysteresis owing to differences in the measured J_{sc} when scanning forwards and backwards.

Deposition Temp	Scan Direction	PCE (%)	FF (%)	J_{sc} (mA/cm²)	V_{oc} (V)	R_{sh} (Ω cm²)	R_s (Ω cm²)
Cold	Forwards	5.9 ± 0.3	57 ± 1	-12.2 ± 0.4	0.85 ± 0.01	620 ± 3	11.3 ± 0.1
	Backwards	6.1 ± 0.3	58 ± 2	-12.4 ± 0.4	0.85 ± 0.01	700 ± 50	11.6 ± 0.02
Medium	Forwards	5.5 ± 0.5	54 ± 1	-12.1 ± 1.5	0.84 ± 0.02	550 ± 10	13.1 ± 0.9
	Backwards	5.6 ± 0.5	54 ± 2	-12.6 ± 1.4	0.84 ± 0.02	550 ± 2	14.4 ± 1.1
Hot	Forwards	3.1 ± 0.7	54 ± 5	-6.5 ± 1.2	0.90 ± 0.01	670 ± 120	20.6 ± 0.9
	Backwards	3.4 ± 0.5	55 ± 2	-7.0 ± 1.2	0.90 ± 0.01	610 ± 60	22.6 ± 0.4

Table 7.6: Mean device metrics and standard deviations for open circuit voltage, short circuit current density, fill factor, power conversion efficiency, and shunt and series resistance, extracted from *J-V* curves, for PSCs fabricated using different substrate and solution temperatures after 335 hours of continuous illumination. 8 devices were used to calculate the mean and standard deviation for each device type.

7.3: Conclusions

In conclusion, it has been shown that additional annealing of $CH_3NH_3PbI_{3-x}Cl_x$ perovskite films at an elevated temperature, in this case 110°C, after conversion of the precursor materials results in PSCs with an improved degree of operational stability, with PCE decreasing by only 35% over 335 hours of continuous illumination. However, this extra anneal resulted in a reduction in initial PCE of ~20% for films annealed in ambient air, and ~30% for films annealed in a nitrogen glove box. Optical microscopy and AFM revealed no major morphological differences between films, however LBIC mapping revealed decreased uniformity in the spatial photocurrent generation of devices with a perovskite layer subjected to an additional anneal. The improved stability observed in the PSCs with additional annealing of the perovskite layer was a result of reduced degradation of the V_{oc} and J_{sc}, indicating a greater degree of chemical stability in these devices. It is

possible that this is due to the removal of water or oxygen absorbed into the device during fabrication, slowing down the rate at which the decomposition reactions seen in Chapter 5 can occur. Unwanted products of the fabrication process, such as methylammonium chloride could also have been removed, improving the stability.

It has also been shown that the temperature of the substrate and solution when depositing the perovskite precursors has a significant impact on the stability of PSCs. Despite an increase in initial performance as deposition temperatures increased, this performance degraded significantly faster than in devices with perovskites deposited at lower temperatures, with PCE decreasing by ~75% and ~45% for 'hot' and 'cold' devices respectively. This originated from more rapid decay of the J_{sc} in devices deposited at high temperatures and a greater increase of the series resistance, suggesting a similar degradation mechanism to that of the devices in Chapter 5, with the perovskite decomposing into PbI_2 due to reactions with oxygen and water, albeit at a faster rate.

7.4: References

[1] J.M. Frost, K.T. Butler, F. Brivio, C.H. Hendon, M. Van Schilfgaarde, A. Walsh, Atomistic origins of high-performance in hybrid halide perovskite solar cells, Nano Lett. 14 (2014) 2584–2590.

[2] A.J. Pearson, G.E. Eperon, P.E. Hopkinson, S.N. Habisreutinger, J.T.W. Wang, H.J. Snaith, N.C. Greenham, Oxygen Degradation in Mesoporous Al2O3/CH3NH3PbI3-xClx Perovskite Solar Cells: Kinetics and Mechanisms, Adv. Energy Mater. 6 (2016) 1–10.

[3] D. Bryant, N. Aristidou, S. Pont, I. Sanchez-Molina, T. Chotchunangatchaval, S. Wheeler, J.R. Durrant, S.A. Haque, Light and oxygen induced degradation limits the operational stability of methylammonium lead triiodide perovskite solar cells, Energy Environ. Sci. 9 (2016) 1655–1660.

[4] N. Aristidou, I. Sanchez-Molina, T. Chotchuangchutchaval, M. Brown, L. Martinez, T. Rath, S.A. Haque, The Role of Oxygen in the Degradation of Methylammonium Lead Trihalide Perovskite Photoactive Layers, Angew. Chemie - Int. Ed. 54 (2015) 8208–8212.

[5] J. You, Y. (Michael) Yang, Z. Hong, T.-B. Song, L. Meng, Y. Liu, C. Jiang, H. Zhou, W.-H. Chang, G. Li, Y. Yang, Moisture assisted perovskite film growth for high performance solar cells, Appl. Phys. Lett. 105 (2014) 183902.

[6] S. Ryu, J.H. Noh, N.J. Jeon, Y.C. Kim, W.S. Yang, J. Seo, S. Il Seok, Voltage Output of Efficient Perovskite Solar Cells with high Open-Circuit Voltage and Fill Factor, Energy Environ. Sci. 7 (2014) 2614–2618.

[7] B. Conings, J. Drijkoningen, N. Gauquelin, A. Babayigit, J. D'Haen, L. D'Olieslaeger, A. Ethirajan, J. Verbeeck, J. Manca, E. Mosconi, F. De Angelis, H.G. Boyen, Intrinsic Thermal Instability of Methylammonium Lead Trihalide Perovskite, Adv. Energy Mater. 5 (2015) 1–8.

[8] E. Bovill, N. Scarratt, J. Griffin, H. Yi, A. Iraqi, a. R. Buckley, J.W. Kingsley, D.G. Lidzey, The role of the hole-extraction layer in determining the operational stability of a polycarbazole:fullerene bulk-heterojunction photovoltaic device, Appl. Phys. Lett. 106 (2015) 73301.

[9] F.X. Xie, D. Zhang, H. Su, X. Ren, K.S. Wong, M. Grätzel, W.C.H. Choy, Vacuum-Assisted Thermal Annealing of CH3NH3PbI3 for Highly Stable and Efficient Perovskite Solar Cells, ACS Nano. 9 (2015) 639–646.

[10] S. Lilliu, T.G. Dane, J. Griffin, M. Alsari, A.T. Barrows, M.S. Dahlem, R.H. Friend, D.G. Lidzey, J.E. Macdonald, Mapping Morphological and Structural Properties of Lead Halide Perovskites by Scanning Nanofocus XRD, (2016).

[11] Z. Liang, J. Ding, S.-H. Zhang, X. Xu, N. Wang, J. Wang, X. Wang, Z. Bi, G. Xu, N. Yuan, A large grain size perovskite thin film with dense structure for planar heterojunction solar cells via spray deposition under ambient condition, RSC Adv. 5 (2015) 60562–60569.

Chapter 8

Conclusions

In this thesis, the stability of common materials used in both organic photovoltaic devices and perovskite solar cells have been examined. This has been used to determine the effects of intrinsic impurities, device architectures, and deposition techniques and temperature on the performance and long-term viability of these two relatively new photovoltaic technologies.

In Chapter 4, the effects of the residual catalyst palladium (Pd) on PCDTBT:$PC_{70}BM$ and, to a lesser extent, PFD2TBT-8:$PC_{70}BM$ organic photovoltaic devices were explored. The Pd catalyst originated from the polymerisation reaction used to synthesise the polymers, where it broke down and formed into nanoparticles, remaining with the polymer unless specifically removed. In PCDTBT:$PC_{70}BM$ solar cells the presence of these Pd nanoparticles was observed to cause significant reductions in device performance, even at low concentration. Using laser beam induced current mapping and scanning electron microscopy (SEM), this was discovered to be due to the Pd nanoparticles binding the PCDTBT into large aggregates, forming short-circuits that result in leakage pathways between the anode and cathode. To determine the long-term effects of Pd contamination, the device were subjected to operational stability tests for 140 hours. Here, the increased Pd content was found to increase efficiency losses during the burn-in period of rapid decay. This was attributed to the appearance of additional short-circuits within the device during ageing, formed by Pd nanoparticles not already bound in the large aggregates, but distributed throughout the active layer. Devices

with the active layer PFD2TBT-8:$PC_{70}BM$ were found to be significantly more tolerant to the presence of Pd, able to achieve comparable performance at both low and high Pd contents. This was speculated to be due to the improved solubility of PFD2TBT-8, preventing the Pd from pulling the polymer out of solution before the film formed. As with PCDTBT, PFD2TBT-8 devices were subjected to operational stability tests, where the improved tolerance was seen again. Here, the main differences observed were slightly less stable short-circuit current densities for the highest Pd contents.

In Chapter 5, the operational stability of $CH_3NH_3PbI_{3-x}Cl_x$ perovskite solar cells in an inverted architecture was investigated. The devices were observed to degrade relatively quickly, presenting low T_{80} lifetimes. A change in the spectral shape of the external quantum efficiency of the devices was consistent with the decomposition of the perovskite into lead iodide through reactions with water or oxygen, which also produced methylamine, hydroiodic acid, iodine, and water. The highest occupied and lowest unoccupied states of methylamine and hydroiodic acid respectively exist within the band gap of the perovskite. Both of these materials are volatile and would normally escape the device, however the encapsulation here prevented this, causing them to act as charge trapping sites. This lead to an increase in the level of hysteresis in the current density-voltage scans, and a decrease in charge carrier lifetime observed through time-resolved photoluminescence. The water and oxygen required for this degradation process were believed to be present in device upon fabrication, bound into the hygroscopic PEDOT:PSS layer, or in methylammonium chloride left over from device fabrication.

In Chapter 6, the effects of a hydroiodic acid additive on the performance and stability of perovskite solar cells with a spray coated active layer were examined. It was found that devices utilising the HI additive performed significantly better than those without the additive, having power conversion efficiencies comparable to devices with a spin coated perovskite layer. The improvement was primarily a result of increased short circuit current density and external quantum efficiency, indicating better absorption efficiency by the active layer. This was speculated to be a result of the additive improving the solubility of the precursor materials, enabling the formation of a better perovskite film due to greater control over material ratios.

When subjected to 670 hours of continuous illumination, PSCs utilising the additive proved to be more stable, due to increased stability of the short-circuit current density, open circuit voltage, and series resistance. Therefore it was speculated that devices fabricated using the HI additive had a greater degree of chemical stability, with decomposition reactions occurring at a slower rate than in devices fabricated without the additive. These experiments were then performed for spin coated devices, which exhibited similar improvements in power conversion efficiency, short circuit current density, and external quantum efficiency. The operational stability was also improved over devices in Chapter 5, however losses during the burn-in period were greater for devices fabricated with HI, resulting in lower power conversion efficiency at the end of the burn-in period than devices without HI.

In Chapter 7, the stability measurements of Chapter 5 were built upon. Firstly, the devices were subjected to an additional annealing step, either in air or a nitrogen filled glove box, at an elevated temperature after conversion of the precursor materials in an attempt to remove moisture or oxygen present within the device. Here, a 20% loss of initial performance was observed for the devices with the additional annealing step performed in air due to differences in spatially resolved photocurrent generation. However, this loss was countered with a significant improvement to the operational stability of the devices, degrading by only 35% over 335 hours. This improvement was speculated to be due to the removal of the degradation catalysts, oxygen and water, from the perovskite and PEDOT:PSS layers, reducing the speed at which the degradation reactions can occur. It is also possible that hygroscopic by-products of the formation of the perovskite crystal, most notably methylammonium chloride, are removed by the additional annealing step, reducing the probability of water reabsorbing into the device after the main annealing step. Secondly, the effect of substrate and solution temperature when depositing the perovskite precursor solution on the stability of devices was investigated. Devices with perovskite films deposited at the highest temperatures gave the highest initial performance most likely due to improved surface coverage, however, they proved to be the least stable when subjected to 335 hours of continuous illumination.

8.1: Further Work

With the work presented in this thesis, it is hoped that an insight has been provided on the importance of studying polymer contamination, the operational stability of perovskite solar cells and the factors affecting their lifetime. There are several ways in which the work presented here could be taken further. As the lifetime test of Pd contaminated PCDTBT:$PC_{70}BM$ photovoltaic devices was only for 140 hours, it would be interesting to see the impact of Pd over a much longer time period. Further investigation into the effects of Pd on PFD2TBT-8:$PC_{70}BM$ solar cells is important to determine the actual mechanisms behind any performance losses, such as short-circuit limited current measurements to determine any effect to charge carrier mobility, as well as the observed tolerance to certain levels of contamination.

With regards to perovskite solar cell stability, alternate materials could be used for the electrodes and charge transport layers, as well as different perovskite materials, to see if stability could be improved. PEDOT:PSS is known to be highly hygroscopic, so utilising less hygroscopic materials for the hole transport layer may improve the stability of devices. The recently reported $Cs_5(MA_{0.17}FA_{0.83})_{95}Pb(I_{0.83}Br_{0.17})_3$ [1] has been found to be remarkably stable in standard architecture devices, so it would be interesting to see how it performs in inverted architecture devices. Different forms of encapsulation, such as a cover slide containing a desiccant could also be used to try and improve the stability of perovskite solar cells. Furthermore, it has been seen in Chapter 5 that when the perovskite decomposes, the products are trapped within the device by the encapsulation. Therefore, it would be interesting to see if any performance could be recovered by annealing the device after some decomposition has occurred, potentially allowing the perovskite crystal to reform from the components and recover some of the lost performance.

For the hydroiodic acid additive examined in Chapter 6, further experiments should be performed to determine the exact mechanism behind the improved device performance. Steady-state and time-resolved photoluminescence could be used to determine how well the precursor materials covert into perovskite crystals, as well as differences in the charge carrier recombination rates which could be affecting the open circuit voltage of such devices. It would also be useful to determine the

optimum quantity of hydroiodic acid to add to precursor solutions to provide the greatest device performance and stability.

The experiments in Chapter 7 should be repeated with additional experiments performed, such as Raman spectroscopy, energy dispersive x-ray spectroscopy, external quantum efficiency, and both steady-state and time-resolved photoluminescence, to determine the mechanisms behind the improved operational stability that was observed. These experiments would give insight into any chemical changes that could be occurring as a result of additional annealing steps or depositing at different temperatures, for both the initial state, and after continuous illumination and operation. It would also be useful to find the optimum temperature and time for the additional anneal, as it may be possible to achieve even longer lifetimes than observed in this thesis.

8.2: References

[1] M. Saliba, T. Matsui, J.-Y. Seo, K. Domanski, J.-P. Correa-Baena, N. Mohammad K., S.M. Zakeeruddin, W. Tress, A. Abate, A. Hagfeldt, M. Gratzel, Cesium-containing Triple Cation Perovskite Solar Cells: Improved Stability, Reproducibility and High Efficiency, Energy Environ. Sci. 9 (2016) 1989–1997.